Development of Near-IR and Beam Shaping of

Mid-IR Lasers

by

Elijah Loyiso Maweza

Dissertation presented for the degree of

Doctor of Philosophy

in the Faculty of Science at Stellenbosch University

Supervisor: Dr Hencharl J. Strauss

Co-supervisor: Prof. Erich G. Rohwer

April 2019

DECLARATION

By submitting this dissertation electronically, I declare that the entirety of the work contained therein is my own original work, that I am the sole author thereof (save to the extent explicitly otherwise stated), that reproduction and publication thereof by Stellenbosch University will not infringe any third party rights and that I have not previously in its entirety or in part submitted it for obtaining any qualification.

Signed: ………………………………………..

DECLARATION

ii

The development and writing of the papers (presented in conferences, published and unpublished) were the principal responsibility of myself and, for each of the cases where this is not the case, a declaration is included in the dissertation indicating the nature and extent of the contributions of co-authors.

iii

ABSTRACT

This study seeks to produce short-pulsed laser output with high peak and average powers to meet the demand for industrial ranging applications. Q-switched lasers are suitable for this due to their ability to produce high energy, high average power, high peak power, short pulses and high efficiency at high pulse repetition rates.

This research seeks to develop an actively Q-switched 100 kHz source that emits peak powers of ~10 kW with pulse widths in the 1 ns range. To obtain these parameters, a diode end-pumped laser was constructed and two Q-switching devices were investigated, namely Acousto-Optic Modulators (AOMs) and Electro-Optic Modulators (EOMs).

An AOM uses an RF-generated acoustic grating to diffract light out of the cavity, inducing a variable loss, which Q-switches it. The advantages are that AOMs do not require high voltages, are usually polarisation insensitive and are well understood. However, the switching speed is limited by the speed of sound in the material and their restricted modulation depth often causes hold-off problems.

EOMs require high voltages for their operation. However, when EOMs are not shielded, the high voltages cause electromagnetic interference (EMI) noise, as well as ringing, which result in undesired losses during Q-switching. Electro-optic Q-switching with solid state lasers mostly uses the Pockels effect to rotate beam polarisation and this, together with polarising elements, causes a varying loss within the cavity. This makes it possible to switch the cavity losses quickly since the switching time depends mainly on the high-voltage source-switching speed. EOM Q-switched are also compact, they have high extinction ratios and do eliminate the hold-off problems typically seen in AOMs.

A Nd:YVO$_4$ pulsed laser was developed using an AOM as a Q-switch element and its outputs measured. This laser produced pulses of ~2 ns widths and peak powers of over 10 kW at the pulse repetition frequency of 140 kHz. The observations on the AOM Q-switch results show that pulse widths of ~1 ns could not be reached. Double pulsing, which occurred due to slow switching speeds, was also observed at high peak powers.

A comparative study was initiated to see if EOMs cannot solve these challenges that are experienced with AOMs. A new method to use these EOMs to Q-switch lasers was subsequently developed. Although the results were similar to those of the AOM, they showed significant potential for further improvement. The results of this research indicate that high peak powers and short pulse widths can be obtained using both methods. The performance and suitability of both the AOM and EOM Q-switch methods were compared in miniature, short-pulsed high-PRF lasers.

The second part of this research involved beam shaping of mid-IR light in the 2 µm region. The mid-IR light has the advantages of having both high atmospheric transmission and being considered eye safe, thus making it suitable for free-space communication applications. The advancement of beam shaping, from using physical optics to using digital systems in the visible spectrum, has prompted interest in investigating the same in the mid-IR region. In order to implement a mid-IR communication link that uses spatial modes, suitable encoding and decoding techniques need to be implemented. Two of the techniques that are currently in use are detection using modal decomposition and detection using spiral phase plates. The advantage of the former is that it is dynamic and operates in real time. However, it is only optimised for low powers. The latter has the advantage of being able to operate at high power. Its disadvantage, however, is that it requires the synthesis of a number of optics so as to generate different orbital angular momenta.

During this research we employed techniques based on Spatial Light Modulator (SLM) to implement modal decomposition on our structured 2 µm light to extract the modal weightings and intermodal phases. This allowed us to reconstruct the optical fields of interest as well as perform wavefront reconstruction. This work models far-field detection before the next phase of outdoor implementation. Both the detection of the optical fields and wavefront reconstruction by modal decomposition were achieved.

This work is dedicated to my beloved wife, Fezeka,

our precious children, Sibabalwe, Luxolo and Blessing,

as well as our parents.

ACKNOWLEDGEMENTS

I am sincerely indebted to God for the completion of this work, because He provided me with great support from a significant number of people. Since I cannot list all the people that helped and walked with me at different stages of this journey, I would like to thank them all. However, I will mention only a few that can be accommodated in these pages.

My thanks and sincere gratitude and acknowledgement of contribution go to:

- The CSIR National Laser Centre for sponsoring my formal studies and affording me the time to complete this dissertation.
- Stellenbosch University for evaluating, ensuring the quality of the work we did over the period of this study and subsequently awarding me the PhD degree upon successful completion.
- The Novel Lasers group members at the NLC for their technical ideas and contributions, particularly:
  - o Cobus Jacobs for making extra effort to explain specialised techniques that were useful in this research
  - o Gary King for technical assistance
  - o Dr Wayne Koen for useful discussions
- Posthumously, Dr Lourens Botha for allowing me to come to the National Laser Centre at the CSIR.
- My fellow students at the National Laser Centre for the times we spent together on student issues and also reading some parts of my work.
- My supervisors, Dr Hencharl Strauss and Prof. Erich Rohwer. Your knowledge, encouragement and assistance have helped me to grow in the field of laser research.
- Dr Angela Dudley, for her special guidance in the mid-IR beam-shaping research.
- Prof. Andrew Forbes for his insight in developing the mid-IR beam-shaping concept.
- My extended family: grandparents (posthumously), parents, kids, and siblings. Also my church family for the encouragement, prayers and support that have helped me in this long journey.

Lastly and very importantly, I thank my wife (Fezeka) for the special support she has given me throughout my study period. May God bless you my Love, Thandolwam! Now I have completed this work and I highly appreciate your contribution.

vii

All credit goes to God for giving me strength to hold on and all these wonderful people who have contributed to my growth. Indeed, in Your light we have seen light.

"*For with You is a fountain of life: in Your light shall we see light.*" [Pslams 36:9 (KJV2000)]

Table of Contents

xi

1.   Table of Figures

xxiii

2. Table of Tables

List of Symbols and Abbreviations

AMD	Azimuthal Modal Decomposition
AOI	Angle of Incidence
AOM	Acousto-Optic Modulator
AR	Anti-reflection
BR	Back Reflector
CCD	Charge-Coupled Device
CGH	Computer-Generated Hologram
CW	Continuous Wave
DP	Density Plot
EMI	Electromagnetic Interference
EOM	Electro-Optic Modulator
ESA	Excited-State Absorption
f	Thermal Boltzmann factor
FCLD	Fibre-Coupled Laser Diode
FOM	Figure of Merit
FWHM	Full Width Half Maximum
g_0	Small signal gain coefficient
$GdVO_4$	Gadolinium Orthovanadate
h	Planck's constant

HD	High Definition
Ho	Holmium
HR	High Reflection
HT	High Transmission
LADAR	Laser Detection And Ranging
L	Lens
LASER	Light Amplification through Stimulated Emission of Radiation
LG	Laguerre-Gaussian
LIDAR	Light Detection And Ranging
LLF/LuLiF/LuLF	Lutetium Lithium Fluoride
M	Mirror
M^2	Beam Quality Factor
Mid-IR	mid-infrared
MIL-STD	Military Standard
NA	Numerical Aperture
Nd	Neodymium
OC	Output Coupler
OAM	Orbital Angular Momentum
PAAMD	Phase-and-Amplitude Modal Decomposition
POMD	Phase-Only Modal Decomposition
PRF	Pulse Repetition Frequency

xxix

PSST	Photonics Simulation Software for Teaching
PT	Partial Transmission
RADAR	Radio Detection And Ranging
RF	Radio Frequency
RTP	Rubidium Titanyl Phosphate ($RbTiOPO_4$)
SLM	Spatial Light Modulator
TEM_{00}	Transverse Electromagnetic Mode (Fundamental mode)
TeO_2	Tellurium dioxide
Tm	Thulium
v	Frequency
VSWR	Voltage Standing Wave Ration
YAG	Yttrium Aluminium Garnet
YLF/YLiF	Yttrium Lithium Fluoride
YVO_4	Yttrium Orthovanadate
λ	Wavelength
σ_a	Effective absorption cross-section
σ_e	Effective stimulated emission cross-section

xxx

Chapter 1

1. Introduction

This research consists of two parts. The first study seeks to develop a pulsed laser system that can be used in fast ranging applications. This was done with solid-state laser systems that were pumped with laser diode sources at the wavelength of ~800 nm and emitted laser outputs at the wavelength of 1 μm. Nd^{3+} doped crystals were used because this element is well known for its stability and ability to generate stimulated emission and reach high power outputs with a number of host materials suitable for use in high-power laser systems [1]. Several compact high repetition-rate pulsed lasers as well as a new Q-switched technique that exploits the thermal lensing properties of uniaxial materials were demonstrated.

The second part of this study attempted to establish in a lab environment a basis to exploit mid-IR laser systems for free-space communication. This study demonstrated, for the first time, the usage of mid-IR laser beam shaping to determine the integrity of signals at the far-field as mimicked in the lab. This was carried out through two techniques, the creation and detection of modes, and wavefront reconstruction through modal decomposition.

1.1   Part 1: Compact Q-switched 1 μm lasers

1.1.1 Laser Application Requirements

Many applications in industry require compact pulsed lasers that are characterised by short durations, high update rates, high energy and high peak powers. These parameters are important to various applications such as laser drilling, scribing, ranging, etc. The laser that was built in this research was for ranging and mapping applications. For ranging, short pulses provide precise distance measurements and the ability to distinguish between measured objects. This research aimed to answer the following research questions:

- Are AOM or EOM Q-switches more suitable for nanosecond sources with repetition rates in the range of 100 kHz?

1

- How can nanosecond and 100 kHz pulses be efficiently obtained from a miniature laser source?

- Are there novel ways to Q-switch lasers?

1.1.2 Background and Chapter Overview

The Part 1 study was initiated on a request from a client for miniature nanosecond lasers for a laser ranging application. While several pulsed laser systems have been investigated and reported in literature, none of the systems at that time available on the market suited the requirements for the laser and physical parameter that the client requested.

Various options were considered to develop such systems. A dedicated literature study is presented in Chapter 2 that investigated the power levels (both average and peak powers), the pulse durations and energies that have been achieved with different pulsed laser systems. In the study the conditions of operation such as design and repetition rates was considered. Eventually the decision was made to develop compact Q-switched solid-state systems. The study also includes a closer look at the applications a laser of this nature can be used for, particularly ranging. The study of pulsed laser systems helped us identify active Q-switching as the laser technique that can most likely generate the desired results. In particular, literature reports the most comparable results with acousto-optic and electro-optic active Q-switching techniques. Other techniques, however, were shown to satisfy only one or two conditions while falling short on the rest, and others were not applicable with regard to the required application. In the case where not all conditions were satisfied, the possibility of amplification was also looked at; otherwise those that did not meet the requirements could safely be set aside.

The most challenging decision was to choose between using Acousto-Optic Modulator (AOM) and Electro-Optic Modulator (EOM) Q-switches, because literature shows that both can meet the operational conditions sought by the client. Initially AOM Q-switching was considered to be the most promising technology because it is not sensitive to the Electro Magnetic Interference (EMI) that would potentially develop when using Electro-Optic Q-switches. As such, AOM Q-switched laser systems that were optimised for short duration, high peak, power pulse emission at high repetition rates were developed to set a prototype for parallel comparison. Although significant problems such as low efficiency and double pulsing were experienced with these systems, the client chose to go ahead with this technology due to the lack of EMI in AOM systems. It became clear

2

that EOM Q-switches could solve some of the inherent limitations encountered. A parallel study was therefore commissioned to study the differences between AOM and EOM Q-switching for high resolution ranging applications. This study forms the basis of roughly two thirds of this thesis.

Following the literature study in Chapter 2, Chapter 3 presents the theoretical background of Q-switched laser systems. This chapter discusses specifically the general laser system and the operation thereof, including the properties of laser materials, pumping of laser systems and laser performance. The general theory of active Q-switching is also discussed in this chapter, including that which is based on acousto-optic and electro-optic modulators. The chapter finally compares the two techniques by focusing on advantages and disadvantages.

In Chapter 4, a base laser setup was constructed, consisting of the fibre-coupled laser diode, the pump relay optics and a cavity with a water-cooled $Nd:YVO_4$ crystal as a laser material. The input face of this crystal served as one of the cavity mirrors. The other mirror was a flat 70% reflective output coupler that completed the first cavity of this project. The author was initially part of the team that designed the laser, but later took the lead in respect of assembly, component and system testing, as well as taking measurements. When needed, a team of electronics engineers, laser experts and technical personnel supported the early stages of the experiments with specialist knowledge such as the mounting of laser diodes and assembling the electronic equipment used for driving both the AOMs and the EOMs. For example, the author made laser design decisions, by analysing the pump light absorption by $Nd:YVO_4$ crystals of different dimensions and dopant concentrations to select the suitable laser material. While assisted by technicians to mount the crystal, the author was responsible for further laser cavity development. The author took the lead in the assembly of the laser system and in most of the experiments (measurements and data analysis) that followed by testing AOM and EOM Q-switches in various configurations.

Chapter 5 presents the insertion of an AOM Q-switch in the cavity, measurements and the corresponding results as well as the inherent limitations of this technique. In Chapter 6 various EOM Q-switching configurations were introduced and evaluated against the requirements of the client. As these conventional techniques were found to be insufficient due to some engineering problems that were encountered, a new electro-optic Q-switch technique with a Pockels cell is presented. The technique makes use of the known properties of uniaxial gain materials, in particular, the varying thermal lens effects along is different axes, to facilitate the EOM Q-switch process. Chapter 6 also theorised that this technique could solve some of the problems encountered

3

with conventional EOM Q-switch methods in short cavities. This technique was developed, used and shown to lead to successfully Q-switched pulsed laser output with results that are comparable to the AOM Q-switch laser developed in Chapter 5.

In Chapter 7 we seek to compare the results we obtained with AOM and EOM Q-switching respectively with the best results obtained in literature. Limitations were encountered in AOM Q-switching, but the design measures undertaken (such as selecting a short Nd:YVO$_4$ crystal for a laser material, pumping it with a fibre-coupled laser diode and Q-switching the resulting short cavity laser system with a high-performance TeO$_2$ acousto-optic modulator) resulted in a pulsed output of 10.48 kW of peak power, 1.87 ns of pulse durations and 20 µJ of energy achieved at a 140 kHz repetition frequency. With EOM Q-switching, the same laser material and output coupler were used to construct a short cavity laser system where the new technique was implemented, and an output of 7.7 kW of peak power and 3.4 ns of pulse duration was obtained at the pulse repetition frequency of 100 kHz. Both these sets of results successfully obtained outputs with high peak powers, short durations, and high energy pulses that, according to our knowledge, have not been achieved before in such combinations in compact solid-state lasers.

1.2 Part 2: Mid-IR Beam Shaping

Beam shaping has for some time now used to enhance the properties of laser light, mostly in the visible and near-IR wavelength bands to fit specific applications. Since little beam shaping has been conducted in the mid-IR region, with this research it is implemented in the form of modal decomposition and wavefront reconstruction to exploit the 2 µm light for free-space communication. This was meant to extract modal weightings and intermodal phases of this light's optical fields and to consequently reconstruct their intensity profile.

We aimed to investigate, identify and report on the following:

- The implementation of beam-shaping techniques for the first time in the mid-IR region
- The limitations associated with the resolution of mid-IR sensors
- What to do to mitigate the challenges encountered

This work aimed to identify and solve several problems and answer questions in beam shaping in the mid-IR region. To the best of our knowledge, this is the first shaping of mid-IR laser beams with a spatial light modular. The aim of the work was to address some of the problems that have

4

hindered beam shaping in the mid-IR region through the use of spatial light modulators. To achieve this, a two-SLM and lens optical setup was used in the laboratory environment to mimic an out-door free-space communication link. The process involved creating laser modes (beams) that carry orbital angular momentum (OAM), propagated them through a 4-f telescope, before subjecting them to modal decomposition for detection or wavefront reconstruction. With the OAM, the beams exhibit rotating phase structures as they propagate and are capable of transferring their momenta onto the target objects, a phenomenon that makes them useful for several applications.

1.2.1   The Concept

The concept of Part 2 of this thesis employs the modal decomposition of the mid-IR light into modes that contain the resolution needed to reconstruct the field. The process decomposes an unknown light field into a superposition of its constituent modes that are described by the characteristic orthonormal basis functions, in order to determine the constituent components that make up the optical field of interest [2]. Modal decomposition is employed in the detection of the modes that constitute the field at far-field in Chapter 8 and the detection of the wavefront of the field at far-field in Chapter 9.

1.2.2   Background and Chapter Overview

Part 2 of this research is focused on the implementation of mid-IR laser beam shaping in the creation, reconstruction and detection of orbital angular momentum-carrying laser beams. While Part 1 was developed for an airborne ranging application, Part 2 manipulates a mid-IR beam with high atmospheric transmission from a laser source for free-space communication. While both parts deal with airborne applications, they can be treated as separate.

It is well-known that mid-IR light is well-suited to free-space communication applications. The wavelength (2.1 µm in this case) transmits well through the atmosphere; it is eye safe and currently more secure than higher frequency light. For this reason, the creation and detection of higher-order spatial modes of light was investigated in the mid-IR region, since it can prove useful for high-bandwidth information encoding in free-space communication links. To the best of our knowledge, the shaping and measuring of 2 µm light with Spatial Light Modulators has yet to be achieved.

Chapter 8 presents the theory and the implementation of a special technique of beam shaping called modal decomposition. This technique is used to decompose an unknown field into a superposition of modes and then determine the modes that constitute it. This was achieved by measuring the modes that underlie the field and using computer-generated holograms encoded on a mid-IR coated dynamic spatial light modulator (SLM) to decompose different spatial modes onto and from a 2 μm laser light beam. Two cases are presented – decomposition into a phase-only basis and decomposition into a phase-and-amplitude basis – described as Laguerre-Gaussian beams. Chapter 9 presents the implementation of this modal decomposition tool on mid-IR wavefront reconstruction. Both chapters 8 and 9 present the physical setup of how this technique was implemented and tested in a laboratory environment, and also the results thereof.

1.3   Conclusion

This chapter presents an overview of a systematic investigation into the suitability and feasibility of different Q-switching techniques for miniature ranging lasers. It also presents the motivation for the investigation into the shaping and measuring of 2 μm light spatial modes.

Part 1: Compact Q-switched 1 µm Lasers

Chapter 2

2. Motivation for Laser Pulsing Technique Selection

2.1 Introduction

The objective of this research was to develop a diode-pumped solid-state 1064 nm laser system that generates short-pulsed ($\lesssim$ 2 ns) and high-peak power ($\geq$ 10 kW) laser output at high pulse repetition rates ($\geq$ 100 kHz), and to do so with the most efficient and affordable design. Chapter 2 first shows why this combination of laser parameters was chosen for a specific ranging application and then evaluates several pulsed laser technologies to determine which is most suitable to generate these outputs.

2.2 Distance Ranging with Pulsed Lasers

Laser-based Detection And Ranging (LADAR) devices have become topical in recent years because of their optical remote sensing capability that can rapidly measure distances to targets by illuminating them with laser light [3]. It is an active and non-contact ranging system that operates by emitting an electromagnetic (optical) radiation [4]. Commonly used LADAR transmitters operate in available atmospheric propagation windows. The exploited propagation windows currently include the 1.06 µm wavelength, where Nd:YAG has been used, the 1.5 µm wavelength for erbium-doped laser material, and the 9 to 11 µm band for CO_2. The research in hand focused on lasers radiating wavelengths around 1.06 µm where solid-state lasers can be used because they are dominant in the laser industry, where they can

7

be assembled into compact systems, and where they have the potential to satisfy the research objectives of this study [1].

A LADAR device emits laser radiation to a measured object that in turn reflects it back to the detector. The detector, which is also part of the LADAR device, determines the properties of the detected laser light on its return after reflection [4]. LADAR devices can be classified according to their characteristic transmitted waveforms (i.e. continuous, modulated, or pulsed waves), their detection schemes (direct or coherent detections), or their intended measurements (range, velocity, backscatter, or spectral absorption) [3]. The fundamental parameter of interest is range measurement of stationary or mobile target objects that can either be small (< 1 m) or big (~10 m or more) in size, hard or soft, and regular or irregular. The range describes the distance between the emitter/sensor of a LADAR device and the target object [5].

LADAR optical systems have certain advantages over other detection technologies, in that they emit a highly collimated and easily focused laser light with short duration and high energy pulses [5]. As a result they are more appropriate for applications that require high spatial resolution and the illumination of small areas or volumes, and they are useful for measurements in confined areas [6]. These advantages make LADAR systems suitable for concealment and useful in higher countermeasure resistance [7], target object identification and range determination in the automotive industry, with military as well as robotics applications. This is possible because of the use of optical signals that measure distances without the need for physical contact with the target [8]. LADARs can however be easily attenuated by environmental conditions such as optically thick clouds and precipitation on cloudy and rainy days respectively, making them less effective in search missions over a wide area.

The typical operation of LADAR devices depends on the properties of emitters and sensors. The laser light that the devices emit needs to be examined to determine if the lasers can

operate efficiently in different surrounding environments. The following parameters must be measured or specified [9]:

- Dimensions of the transmitter and receiver together with its field of view
- Receiver minimum detectable power density
- Target reflectance, ideally also in terms of bi-directional reflectance-distribution function
- Beam diameter and divergence (the desired parameters are small and well-collimated beams with low divergence)
- Output properties such as wavelength, pulse peak power, duration, and repetition frequency
- Distance
- Environmental conditions (relative humidity, temperature, precipitation, atmospheric composition and visibility)

For LADAR mapping devices, the emitted pulsed laser beam is scanned over the target object by making lines of length (l_scan) across (perpendicular to) the flight direction, traversing a total angle of θ_{scan} at a speed (θ/t_scan) and measuring properties of interest. Laser pulses that are emitted by the LADAR device and detected on their return, measure how far the target object is at specific times. The performance of a system like this can be evaluated in terms of single-point measurement of the time of flight, spatial resolution along (longitudinal) and perpendicular (transverse) to the optical path, as well as long-term stability [10].

Pulsed LADAR mapping devices effectively determine the range or distance to target objects by measuring the round trip time of flight (t_L) of collected reflections [5]. Figure 2.1 is a schematic diagram of laser scanning and ranging processes where an airborne laser-based scanning device is flown along one direction at a slow constant speed while it rapidly scans the target object across the flight direction with an emitted pulsed laser light at a known high repetition rate. The scanned object scatters the light that falls on it into different directions. As the reflected light also falls back on the detector of the scanning device (the LADAR), the desired measurement is recorded.

9
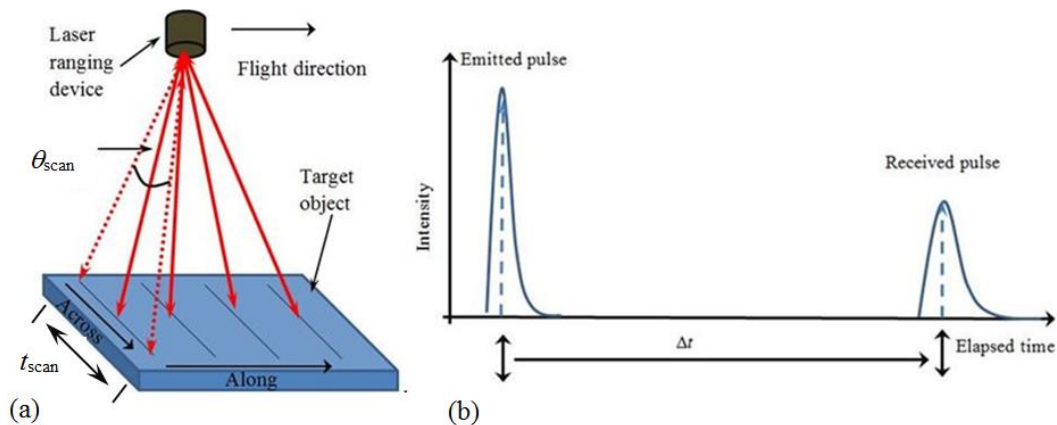
Figure 2.1. (a) An ideal airborne ranging device showing flying to the right while scanning a target object across its flight direction. (b) A typical laser pulse that is emitted and received.

The measurement gives the distance that each emitted laser pulse travels to the target object and is defined by Equation (2.1) [5] as

$$R = \frac{1}{2}ct_{\text{L}}$$ (2.1)

where c is the speed of light. The range (R) is related to the time of flight (t_{L}) of the pulse, which is the time interval between its emission and detection, thus giving a direct measurement of the round-trip distance to the target [10].

The amplitude of every pulse (related to its energy and intensity) that is emitted and detected (received), gets reduced and the width lengthened on its return because of several factors that are discussed below. More specifically, the nature of the return pulse when detected specifies the nature of the target object it encountered, that is how far it is and what shape it is. Figure 2.2 illustrates several scenarios that show the different cases that can be encountered when evaluating laser ranging/scanning. These practical scenarios demonstrate the interaction of laser light with different but simplified target object types, namely, a hard-irregular target object, rain drops or a cloud. In each of the cases presented in Figure 2.2, the range can be calculated, and as that is done, both the longitudinal (also called range resolution) and the

10

transverse resolution (Δl_{scan} indicating the measurement point density) are evaluated. Laser pulses are used to determine the longitudinal spatial resolution by calculating the difference (ΔR) between two close targets that are observed [4]. This is done by timing laser pulses as they travel to and from the target objects [10]. Equation (2.2), expresses the longitudinal spatial resolution as

$$\Delta R = \frac{1}{2}c\Delta t_{\mathrm{L}} \qquad\qquad \textbf{(2.2)}$$

And defines the range the range resolution, where $\Delta t_{\mathrm{L}} = \frac{t_{\mathrm{rise}}}{\mathrm{S/N}}$ is the time resolution. The rise time is the time the pulse takes to reach its peak intensity and the S/N describes the ratio of the pulse power or intensity to the noise. This indicates that measurement ambiguity can be reduced and high range resolution (low ΔR) achieved with pulsed LADAR sources, by having lasers where rise times are short (high time resolution) and signal-to-noise ratios are high [4].

Figures 2.2 (a) and (b) demonstrate how high and low the pulse repetition rate emissions of narrow, collimated and short pulse duration laser beams should be when emitted by airborne laser sources onto different (hard or soft), usually irregular surfaces. For example, one measurement point can give an instantaneous distance measurement, while two measurement points can measure the speeds at which target objects are moving, as well as give a rough indication of their size. If few measurement points (about 10 or less) are taken with the ranging device, the outline of target objects can be determined. When many points (about 100) are taken, the measurement can indicate (or reconstruct) with high resolution the nature of the target object. High resolution measurements can also give early warnings and enable the execution of early counter or escape measures.

Figure 2.2 (a) in particular shows that the emission of a short-pulsed incident laser beam at high repetition rate results in indistinguishable return pulses with slightly reduced amplitudes and durations that are still short, but slightly elongated due to environmental attenuation. Furthermore, the high repetition rate ensures that the measurement points are close to each

11

other (high measurement-point density) along the scan line (across the airborne laser source flight direction).
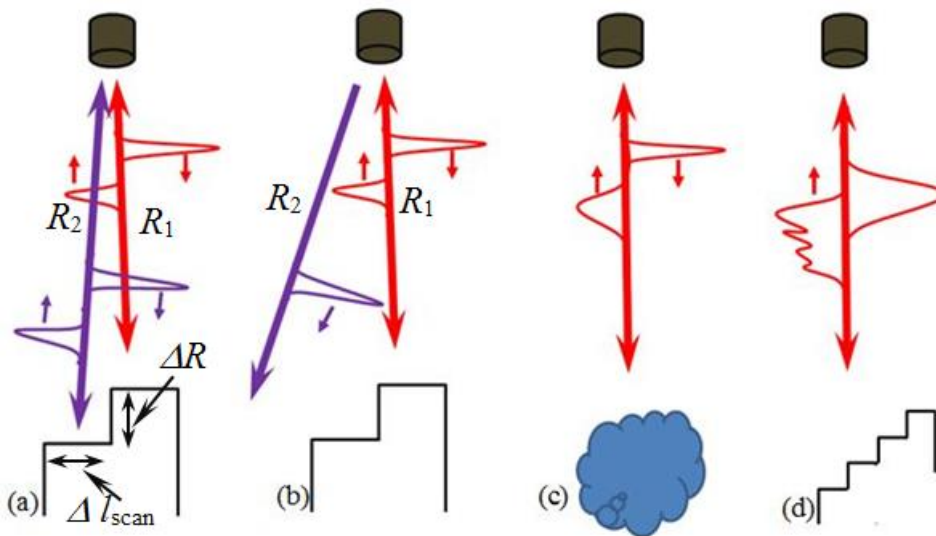
Figure 2.2. Different practical ranging scenarios showing both the physical and optical conditions. The scenarios first illustrate a narrow, collimated and short pulsed laser beam emitted towards (a) an irregular but hard surface at high pulse repetition frequency, (b) an irregular but hard surface at low pulse repetition frequency, (c) a cloud, (d) a narrow and collimated, but long pulsed beam emitted towards an irregular but hard surface.

The high point density together with short duration or sharp rising (short rise time) pulses result in high resolution and precise measurements of the target objects. Also, high repetition rates enable the detection of slight distance (range) changes (ΔR) [4] and the measurement of multiple ranges on uneven target surfaces. In contrast, available lasers could be those that are stable at low pulse repetition frequencies, which when used for scanning (ranging) purposes emit measurement pulses that are far apart. This is demonstrated in Figure 2.2 (b), where the spacing between the pulses, even if they are short, is so wide that immediate changes on the target object's surfaces are missed, thus giving less accurate measurements.

12

Meanwhile, Figure 2.2 (c) and (d) show two cases where the return pulses are severely distorted – to such a degree that they become long and deformed respectively. Figure 2.2 (c) demonstrates the interaction of a short-pulsed laser beam with a cloud, mist, rain or any soft surface that may absorb, scatter or reflect it at multiple surfaces. Because of this, the return pulse has an elongated duration and reduced amplitude (lower energy) when compared to the incident. To ensure strong signals are detected, high energy pulses need to be emitted. In addition, pulsed laser sources must emit short duration pulses (in the ns range) so as to distinguish between hard and soft surface target objects by measuring the pulse width of the return pulse. Meanwhile, Figure 2.2 (d) illustrates a situation where the LADAR device initially emits a long-pulsed laser light on an irregular surface at a given pulse repetition frequency. In this case, portions of the incident pulse arrive at an uneven target's object surface at different times. Subsequently, the pulse that gets reflected from the different surfaces of the target object at different times becomes even longer and shows multiple peaks. This indicates that pulsed laser scanning can distinguish between smooth and irregular surfaces.

In each of these cases, the signal power is still high at the detection point, but the precision of the reflected signal can vary from least error (higher accuracy and high signal-to-noise) in Figure 2.2 (a), to highest error (low accuracy and low signal-to-noise) in Figure 2.2 (d). Efficient laser-ranging devices require that one determines the desired properties of the laser that will be used. Such properties are the combination of short pulse durations, low to non-divergent laser beam [4], the ability to operate at high repetition rates and high peak power. This is because some target objects do not have laser retro-reflectors with them, and as a result ranging devices would require high instant laser power (or peak power) to still receive sufficient laser signals after long-distance range-finding measurement [11].

Considering much of the discussion above, one can deduce that the reliability of ranging measurements is determined by their ability to achieve high resolution and precision. This can be achieved by using laser emission with high PRF and short duration or short rise time pulse respectively. To demonstrate this, one consider a scanning process of an l [m] wide target

13

object with a τ_{pw} [ns] duration pulsed laser light at the PRF of Y [kHz], and from a height of h [m], thus making a maximum scan angle of $\theta_{\text{s-max}}=\arcsin(0.5\ l/h)$ [revolutions or revs] at the start of a single scan line. If the scan speed is given by $\dot{\theta}_s$, the angle varies from maximum at the start of the scan line, through the middle (at 0 revs), to maximum again at the other end.

To apply this, a single scan line on a target object is shown in Figure 2.3, with one measurement point representing all others that fell on it. To detect and read the information detected by the ranging device (the target object dimensions and the time of flight) used with high precision and strong signal, a short-pulsed and high-peak power laser-emitting source at high repetition rates is required. When reflected, some return pulses get scattered, while others are detected by the detector back at the LADAR device.
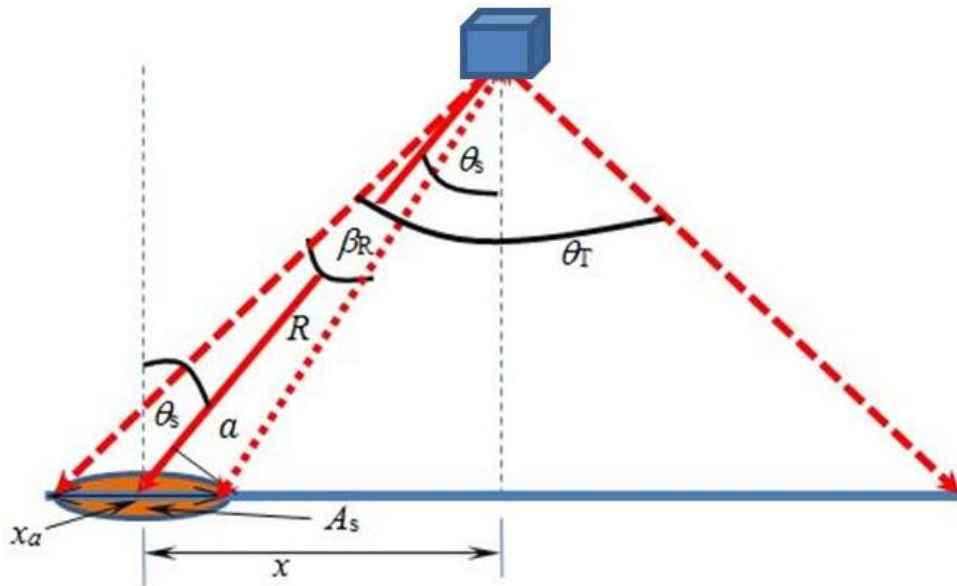
Figure 2.3. This is a scan line showing one-shot measurement. The symbols (R, A_s θ_s, x_a, a and β_R) shown on the diagram respectively represent the range [m], the laser footprint at the target/background [m^2], the angle between the normal of the target surface and the line joining the target and receiver centres, the diameter of the target object, a line normal beam, and the receiver's point of view, which here is approximated to the beam's divergence.

14

If the scanning device detects (captures) N measurement pulses along the scan line at a typical scan speed of $\dot{\theta} = \theta_T/t_T$, the total pulses that would land on the target objects over the given length can be calculated. The number of emitted pulses to a target object that get detected by the LADAR upon reflection can be assumed to be distributed evenly. Their on-surface and angular positions (N points on the target object) can be determined by using simple geometry ($R^2 = x^2 + h^2$) and trigonometry ($\sin \theta_s = x/R$) formulas. These formulae indicate that the number of measurements points on the target object is dependent on the scanning process with the LADAR.

A cubic mirror emitter can be used to maximise the number of measurement points so that for each revolution, the pulse emission can be four times. To demonstrate this scanning process, one can consider a LADAR device that emits short (ns) pulses at 100 kHz of PRF from 100 m perpendicular distance from the target surface of 10 m wide. In such a case, the total scan angle would be $\theta_T \cong 2.86°$ (= 0.016 revs). The number of measurement points that can be accommodated in such a narrow angle at 100 kHz was calculated, quadrupled and found to be approximately 55 when the scan speed was 6900 revs/min. In this case, the measurement points would be about 18 cm apart, which gives a fairly high transverse (on-surface) spatial resolution (Δl_{scan}). These calculations also show that laser emission at higher PRFs can allow laser sources scanning at high rotational speeds to accommodate even more measurement points. For example, a laser emission at a PRF of 160 kHz and scanning at 10 000 revs/min can accommodate over 61 measurement points. In this case, the spatial resolution was calculated to be $\Delta l_{\text{scan}} = 16.4$ cm. Since it is difficult to even maintain long-term stable pulse emission at these high PRFs, 100 kHz was found to be sufficient.

Several different cases can be considered, namely stationary sources versus a moving measured object (towards or away) or having both the source and the measured object be mobile (towards or away from each other, or one towards and the other moving away). One simple example would be one where the source is stationary or slow, versus a fast-approaching measured object that is unaware of the source's existence. If the measured object with a 10 m outline surface is first detected at 100 m away and is immediately scanned with a

15

stationary 100 kHz emitting LADAR device, the distance it would travel after every scan can be determined. Simple calculations show that a measured object that is travelling at 1000 km/h toward a LADAR device that is scanning at a speed of 6900 revs/min will travel a distance of approximately 4 mm after every scan, which takes approximately 140 µs. This indicates that such a device can be useful in providing an immediate and early warning that can prompt the evasion of an accident. This makes such lasers invaluable tools and has drawn the attention of this research, where a 100 kHz emitting laser source with nanosecond and high peak power pulses is to be developed.

To achieve these characteristics, the laser research community has also developed several laser sources that emit pulsed outputs and use unique pulsing techniques, namely cavity dumping, gain switching, Q-switching, etc. This chapter continues to investigate from literature what these techniques have achieved, and aims to identify those that can produce short pulse, high peak power pulsed output at high repetition rates. The discussion above looked at the properties that determine the reliability of ranging measurements. If both pulse repetition frequencies and scan speeds are known, the number of measurement points that meet the target object, together with their spacing from each other along the scan lines, can be determined and, in turn, the range resolution can be found. This discussion so far looked at laser properties that are required to develop a reliable ranging device that will give trusted and useful measurements. The literature review that follows looks at how several researchers have developed laser systems when ranging is the intended application.

Table 2.1 illustrates general design parameters (columns 1 to 4) that need to be selected to obtain the result parameters (columns 5 to 9) that this research seeks to obtain. Based on the discussion above, it can be deduced that high repetition rates, short duration and high peak power pulses are required to take high resolution, high precision and long-range distance measurements. Meanwhile, high pulse energies are required for strong signal detection.

16

Table 2.1. The design and results question that literature has sought to answer, as investigated through the literature review in this chapter. In later chapters this research is used to outline another contribution in response to the market demand.

Pump source/ scheme, Power [W], wavelength [nm], radius [µm]	Gain medium Doping	Crystal Geometry	Cavity length	PRF [kHz]	Pulsed Average power [W]	Pulse Energy [µJ]	Pulse Width [ns]	Peak Power [kW]
End, 808, 7, 100	x at.% Nd:General	Shortest, high gain, good thermal stability	Short	100	>1	⪆ 10	~ 1	~10

2.3   Merits and Demerits of Different Laser Pulsing Techniques

Different laser pulsing techniques generate outputs that are intended for or limited to specific value ranges that are highlighted in this section. The example presented in Section 2.2 shows that optimum laser output parameters, that are suitable for ranging applications, should be pulsed at repetition rates of ~100 kHz, with pulse durations of ~1 ns and peak powers of ~10 kHz.

This section maps out a series of output parameter values for different techniques that have been obtained by different researchers. In doing so, Table 2.2 lists a few common laser pulsing techniques, giving an overview of each by highlighting the value brackets (minima and maxima) of their output parameters − in particular the pulse repetition frequencies, pulse widths and peak powers. While these laser pulsing techniques could be applied to other laser forms, this research focused on solid-state and pulsed fibre lasers as well as on amplifiers. This was because they can be assembled such that they are small, compact, and rugged. Table 2.2 can also be used to select techniques that can generate the desired output parameters or eliminate those that are irrelevant to the intended output parameters.

First, the Table 2.2 lists solid-state based laser pulsing techniques such as gain switching, cavity dumping, mode-locking, and Q-switching. In addition, the table also mentions fibre and amplified laser systems. It describes the output scope of laser pulses in each technique, including pulse generation from low to high repetition frequencies, the corresponding pulse durations, and peak powers. Gain-switched and cavity-dumped laser research accounts were found to generate pulses that included 100 kHz of PRF, few nanosecond and few kW pulses. Pulses generated by gain-switched lasers have been found to range from sub-nanoseconds to hundreds of nanoseconds, while cavity-dumped lasers generate pulses within a narrow nanosecond range (≤ 10 ns) as well as high peak power ranges. As a result, in the following sections we study the published results of several of these techniques to establish the operational conditions of the corresponding lasers.

18

Table 2.2. An overview of the merits of different laser pulsing techniques, focusing on pulse repetition frequency, pulse widths and peak powers.

Pulsing technique	Pulse repetition rate range, [Hz]	Pulse width range, [ns], [ps], [fs].	Peak Power range, [W], [kW]
Gain switching:	100 to 106 [12], [13]	$0.08 < \tau_{pw} < 409$ ns [14]	$0.07W \lesssim P_{pk} \lesssim 4$ kW [15]
Cavity dumping: Pulse pumped, CW pumped	$50 \leq PRF \leq 1500$ kHz, [16]	$3 < \tau_{pw} < 10$ ns, [17]	$0.5 \lesssim P_{pk} \lesssim 70$ kW [18],
Mode locking:	GHz to THz	Pico to Femtoseconds	>10 W
Passive Q-switching:	4 few kHz to 2 MHz [12]	$2.2 < \tau_{pw} < 45$	$0.5 \lesssim P_{pk} \lesssim 30$
Active Q-switching: AOM	10 - 100 kHz	$2 < \tau_{pw} < 20$ ns	$0.2 \lesssim P_{pk} \lesssim 30$
Active Q-switching: EOM	7 - 300 kHz	$\sim 1 < \tau_{pw} < 18$ ns	$0.7 < P_{pk} < 300$ kW
Q-switched fibre lasers	100s Hz to 100 kHz [19], [20]	few to few 100s of nanoseconds [19], [20]	Few Watts to 1 kW [19]
Scaled lasers	10s to 500 kHz	~ 20 ps $< \tau_{pw} < 50$ ns	1 kW $\lesssim P_{pk} \lesssim 10$ MW
Fibre lasers	$\leq$ few kHz to 8 MHz	$19 < \tau_{pw} \leq 109$ ns	$0.05 \lesssim P_{pk} \lesssim 0.12$ W

The table also mentions mode-locking as another laser pulsing technique that is currently being researched and within its parameter ranges. It is a process where the oscillating modes are set to maintain equal frequency spacing related to each other with a fixed phase and to have a well-defined output as a function of time. The PRF range is in the GHz to THz, with the corresponding pulse widths in the pico- to femtosecond range. While the compactness and reliability that also characterise mode-locked lasers are attractive, the extremely high repetition rates and excessively short pulses eliminate them as alternative techniques for our research.

19

Table 2.2 also lists Q-switching techniques as other important laser pulsing techniques that have been highly researched in recent times ([19], [20]). These techniques exist in passive and active forms. Passively, Q-switching is operated at pulse repetition frequencies of 4 kHz to 2 MHz, with s pulse duration that includes few nanoseconds and few kW of peak power. Because of the possibility of designing passively Q-switched lasers to satisfy the objectives of this research, the literature of passively Q-switched lasers is further studied and discussed later in the chapter. This technique can be compared to active Q-switching.

The two major active Q-switching techniques that currently compete more than any other for use in applications that require high peak power, short pulsed laser output properties at high pulse repetition, are based on acousto-optic and electro-optic modulators respectively. Literature reports several accounts that investigate both these techniques and Table 2.2 lists both, highlighting the output scope of each. Literature reports on both techniques report in some cases the combination of high PRF ($\gtrsim 100$ kHz), short duration ($\lesssim 2$ ns) and high peak power. This made these laser systems strong candidates for further investigation in literature and possibly experimentation.

Other techniques that are worth mentioning include pulsed fibre lasers that are doped with rare-earth active ions, which have been shown to potentially generate short duration, high peak power pulsed outputs. For example, high gain pulsed fibre lasers that produce pulses with peak powers in the order of a few to tens of kW and durations of several ns have been reported ([21], [22]). Because of the advances of fibre lasers to the extent of having an established commercial version on the market, a brief review is presented in Subsection 2.4.6. Because of the limitations that other techniques have, including pulsed fibre lasers, the study was continued with amplified lasers. Amplifiers have a parameter range that includes the objectives of this research.

Section 2.4 discusses different laser pulsing techniques, including the design properties and operating conditions of laser systems, as well as the pulsed output results generated.

2.4   Different Laser Pulsing Techniques as Reported in Literature

This section presents several laser design summaries and the corresponding results that are reported in literature under different pulsing techniques. The literature study of each of these laser pulsing techniques highlights both their design and corresponding results to determine whether they can achieve ~1 ns, ~10 kW pulses at high PRFs of 100 kHz or better, and whether they are suitable for the intended applications of our research.

First we discussed gain-switched, followed by cavity-dumped, Q-switched (passive and active) and pulsed fibre laser systems. The investigation also looked at laser power-scaling techniques that can augment the limitations of some of the techniques. In each case, we looked at the results range, definition and the description of each technique. Furthermore, we looked at whether the operation and the results of the technique can satisfy the research objectives of this dissertation. While other techniques exist as presented, active Q-switching is further divided into a few sub-techniques. Acousto-optic and electro-optic modulator-based active Q-switching were selected because of their suitability for fast Q-switching. Following this, we also looked at the physical requirements of the laser system that fit the set requirements of the ranging applications, such as compactness (few tens of millimetres in size), ruggedness (to survive harsh environmental conditions), as well as lifespan. In addition to case, design and output parameters are presented and listed in tables placed in Appendix A, which serve to highlight what different researchers used in designing their laser systems and how they optimised them to satisfy their requirements within limitations. The results that were obtained from literature and considered for this study are comparable to those intended for the current research. The best among them were noted and used to compare their design with the current research.

This analysis was used to select the technique(s) that can best achieve the desired results. The techniques that were selected in this study are investigated in the following chapters.

2.4.1   Gain Switching

Gain switching is one of the laser pulsing techniques that is used to generate short pulsed laser outputs (generally from sub-nanoseconds to a few hundreds of nanoseconds) with high peak powers (≤ 5 kW), and several research accounts have reported on the different results they obtained. Gain switching can be implemented by sufficiently pumping the laser material used (for example solid-state laser materials: micro-chip, thin and long slab crystals) with a fast-pulsed source, such that the population inversion increases and reaches a considerably larger value – much larger than the threshold before the cavity photons can have a chance to deplete it. In addition, gain-switched lasers can generate short pulses at high PRFs when their laser materials (micro-chips) are pumped intensely to achieve high gain and short pulse build-up times [12]. A simplified gain-switching process selects the first transient pulse of the laser oscillation by blocking the pump light until after the pulse is emitted [23]. Pumped with pulsed sources, usually a passively Q-switched laser (discussed in Subsection 2.4.4), gain-switched lasers are well-known for generating stable pulse widths and for their ability to reproduce pulse amplitudes [23]. In addition, one of the advantages of gain-switched lasers is that their switching elements are not inserted in the cavity, and that leads to reduced losses, as well as shorter and rugged lasers [15].

Several gain-switching research accounts are listed in Table A.1 in Appendix A, spanning three decades. Literature shows that gain switching has been implemented mostly with micro-chip or thin slab gain media, and reveals the technique has been implemented at both low and high PRF conditions. At low PRFs (< 25 kHz), the laser systems generated long pulses (16 to 65 ns) even though they had 3 and 4 kW peak powers [15], and this condition was a disadvantage for this technique. In addition, at the desired high PRF (100 kHz), the system yields even longer-pulsed (130 ns, 45 ns and 40 ns) outputs [23] with low energy, which results in low peak powers. The shortest pulse width that was reported with this technique was 16 ns, generated by a diode pumped Nd:YVO_4 thin rod at the PRF of 25 kHz. This limits the chances of gain switching to be considered as an alternative for the intended ranging applications.

22

2.4.2 Cavity Dumping

Cavity dumping is a laser pulsing technique that is used to generate radiation sources with short (nanosecond) pulses, essentially independently of gain and repetition rate, by replacing a permanent optical output coupler with a time-varying output coupler [17]. The cavity-dumping process consists of three stages, namely the pumping, Q-switching, and dumping stages. During the pumping stage (also called the high-loss cavity state), lasing is prevented to allow energy in the laser material to accumulate by keeping the output coupler reflection at zero [24]. The Q-switch stage of the cavity-dumping technique can be carried out with an acousto-optic or electro-optic modulator. The latter has an advantage over the former due to its fast switching times, thus it achieves high and superior optical efficiencies as well as short nanosecond pulse oscillators. The last stage, which occurs after the intracavity Q-switch pulse has reached its maximum intensity, is dumping the high-intensity stored energy out of the cavity. This occurs when the reflection of the output coupler turns to zero again [17]. If the output coupling-switching time is fast enough, and within one round-trip time thereafter, the entire intracavity energy is dumped rapidly out of the cavity in the form of a giant output pulse [24], with durations that are equivalent to the round-trip transit time inside the cavity [1]. As a result, the produced pulse is independent of the laser material gain [24] and pulse repetition frequency, but is essentially defined by the cavity length and the opening time of the dumping optics. In addition, higher repetition rates do not elongate the pulse durations as the available gain for each Q-switched pulse decreases. This allows one to increase the pump spot area and thereby reach higher pump powers to achieve high peak powers with reduced thermal limitations [17].

Table B.1 in Appendix B lists several investigations on cavity-dumped laser systems that have been conducted in the past ([17], [18], [24], [25], [26]) in view of comparing their design parameters and results with the intended design parameters and results of our research for this dissertation. From this table one can deduce that cavity dumping could favourably be considered as an alternative because a 3.8 ns pulse (not far from the desired ~1 ns), where over 30 kW of peak powers (much higher than the intended ~10 kW) were reported at high PRFs of ~100 kHz. However, due to the independence of cavity-dumped laser output from gain, and the lack of demand on cavity lengths (which tend to be long), LADAR devices that

23

can be made with such laser systems may be susceptible to misalignment. This has led to design limitations for developing small, compact and rugged devices, and has made us look for another pulsing technique. This is their physical and major drawback. In Appendix B, the listed cavity-dumping research accounts give us other conditions and results that can be obtained with this technique. The closest of these to the intended results was compared to the ultimate technique that was selected for this research.

Cavity dumping does provide results that ranging applications require; as a result, it can be considered suitable for table-top applications in spacious environments and in ground-to-sky ranging, but not in concealed and confined fittings on aircrafts. Suitable devices aircraft fitting must be small, compact and rugged to remain aligned when subjected to rapid movements and when taking measurements at the same time.

2.4.3 Q-switching

The Q-switching pulsing technique is a repetitive process which, as the name suggests, involves two state cycles where the cavity Quality (Q-factor) is switched from a low to a high value. It occurs by means of a type of shutter that can either be closed or open. The shutter introduces losses while it is closed to keep the cavity at a low Q-state and thus prevents laser action from taking place. When certain processes during the low Q-state are fulfilled, a sudden opening of the shutter switches the laser cavity to a high Q-state. During the high Q-state, the cavity emits a giant laser pulse of short duration (from the nanosecond to the picosecond range) and high peak powers. The cycles occur and Q-switch pulses are emitted repeatedly at pulse repetition rates that range from a hertz to a few mega-hertz in range, and always much lower than the cavity round-trip frequency [27].

Common Q-switched lasers generate pulses with durations that vary depending on factors such as the gain in the laser material, the output coupler coating and the pulse repetition frequencies. Q-switching can either be passively or actively implemented. Passively, intracavity saturable absorbers are used as pulsing components, whereas active Q-switching

requires an externally controlled intracavity device such as acousto-optic or electro-optic modulators. Both passive and active Q-switching techniques are discussed below.

Over the past two decades, high repetition rate Q-switched diode-pumped lasers have become known as important sources of high peak power laser radiation with uses in a wide range of applications [28] such as micro-machining (which requires knowledge of the fundamental laws that influence laser radiation and matter interaction) [29], ranging, remote sensing, and micro-surgery.

2.4.4   Passive Q-switching

The passive Q-switch laser operation is a process that occurs in an optically pumped laser system where the shutter is an intracavity saturable absorber. Passively Q-switched laser cavities are simple to fabricate since they consist of laser materials such as Nd:YAG micro-chips and saturable absorbers mounted between two mirrors. The resulting cavities are also simple to operate because they do not require high voltage or radio frequency (RF) drivers. Possible saturable absorbers include the colour centre crystal $LiF:F_2^+$, Cr^{4+} doped YSGG and YAG crystals, as well as bulk semiconductors, anti-resonant Fabry-Perot saturable absorbers (A-FPSA), and polymer and plastic films [30]. When the laser system is pumped, intensity increases and this causes a saturable absorber to bleach, thus introducing losses in the cavity and thereby preventing lasing from taking place [27]. The bleaching of the saturable absorber significantly spoils and keeps the cavity Q-factor low until the average population inversion density within the cavity reaches a critical threshold. At that instant, laser oscillation starts and produces a high intensity optical field in the cavity. At the same time, the optical losses due to the saturable absorber are reduced, thereby increasing the Q-factor of the cavity. With carefully selected components, passively Q-switched lasers can generate pulsed outputs with peak powers in the kilowatt range and pulse durations in the sub-nanosecond levels [31].

Passive Q-switching is attractive and suitable for scientific and industrial applications that do not require accurate repetition rates [31]. Table C.1 lists several passive Q-switching laser

25

research accounts demonstrated in literature ([24], [26], [17], [18] and [25]). These studies report several advantages that passive Q-switching offers apart from its simplicity, namely compactness [30], low cost [32] and reliability [31]. In addition, they are small in size and very power efficient [33]. However, passively Q-switched lasers are limited by the lack of an external precision-trigger system and have outputs lower than electro-optic or acousto-optic versions of Q-switched lasers. The lower passive Q-switch outputs are caused by the high insertion loss that results from the residual absorption of the saturated passive Q-switch [1]. In addition, the photo-chemical degradation is a problem and the main drawback from which dye saturable absorbers suffer when exposed to high intensities.

The output parameters include pulse repetition frequencies, pulse widths and peak powers. The shortest reported pulse widths were obtained with short cavity lasers (between 2 and 7 mm) with reasonably high repetition rates of ~80 kHz, thus yielding close to 6 ns pulse with low peak powers of < 0.5 kW [32]. This low peak power can be attributed to the high insertion losses that we have just mentioned. Such lasers can be used for reasonably high resolution (high precision) and short-range purposes. Also, at a low PRF of 4 kHz, a 2.2 ns pulse output was reported with reasonably high peak powers of 5.6 kW [30]. This indicates that such passive Q-switched lasers can be suitable for ranging applications that require high precision and long range with less emphasis on resolution. This indicates that passive Q-switched lasers do not possess all the parameters at the required range, since at least one of them always falls off.

Due to their simplicity and affordability, passively Q-switched lasers can be used for low-budget projects that may require short range or low-resolution applications. This discussion indicates that together with cavity dumping, passive Q-switching can be an alternative technique for obtaining the desired results.

26

2.4.5   Active Q-switching

Two active Q-switched techniques, based on acousto-optic and electro-optic modulators, are the leading techniques in the research and industrial market. They differ from the passively Q-switched lasers in that the shutter is an optical element that performs the switching processes through an external trigger [1]. Several reports that were studied and discussed for each of these techniques were selected for their relevance, where they either have one of the parameters (the PRF, pulse durations, and peak power falling in the desired range such as the 50 to 150 kHz range of PRF), or lower than a 10-nanosecond pulse duration with peak powers of approximately 10 kW and above.

2.4.5.1   Acousto-optic Q-switched lasers

An acousto-optic modulator (AOM) is an active Q-switch optical (crystal) element that is mounted on the path of an optical beam inside the cavity. The AOM crystal serves to diffract the beam when an acoustic wave, triggered externally, is propagated through it and transmits it when no acoustic wave is propagated. The literature review seeks to determine whether these acoustic wave-based Q-switch elements, the AOMs, do generate high repetition rate pulse with high peak power [34]. Maximum diffraction occurs when the propagated acoustic wave satisfies the Bragg condition. AOMs are known for advantages such as affordability (low cost), small electrical power requirement (low voltages), weaker (insensitive to) polarisation and wavelength dependence. Their drawback though is that the pulse widths are usually long, especially at high repetition rates. Typically, values of 20 to 100 ns have been reported in the literature [35].

Several research reports that have been published over the past decades achieved different output values based on their desired applications. For this study, end-pumped AOM Q-switched laser research reports were selected for their suitability with compact size and high PRF output operation. Table D.1 in Appendix D lists several of these accounts.

27

Laser output with short pulse durations (2 ns) and considerably higher peak powers (~5 kW) was reported in 2007 at the PRF of 80 kHz and it was achieved with a 0.5 at.% doped Nd:YVO$_4$ crystal in a 20 mm long cavity [35]. Several other attempts were made where high PRF (100 kHz) operations yielded high peak power laser output while the pulse widths were at 10 ns [36] .

These results are comparable with the intended results of the current research, displaying the sought-after combination of short pulse duration, high peak power laser output at high PRFs, unlike the other techniques that have been discussed so far. However, it can be observed that in some accounts the output parameter values are slightly below (PRF, average power, pulse energy, and peak power) or above (pulse durations) the intended values. In such cases, the current research may be able to improve the results through optimisation. This already prompts us to investigate AOM active Q-switching further in this research. Literature does show AOM Q-switched lasers able to generate pulsed outputs that satisfy the conditions of a high repetition rate pulse with high peak power [34].

It can also be seen in some accounts that two parameters are satisfied while the others exhibit a huge difference. It such cases, it may be necessary to either scale the laser up or use other laser materials, such as active fibre gain media.

2.4.5.2   Electro-optic Q-switched lasers

This section seeks to indicate from the literature that is published in the recent past that Pockels cell based electro-optic (EO) pulsing technique is suitable to generate desired pulsed laser outputs. This is an active Q-switching technique that is implemented when an external active operation (e.g. voltage applied) is exerted to the fast switching Pockels cell in order to produce short pulsed outputs [37]. Table E.1 in Appendix E lists several research accounts on this technique while this sub-section highlights those that are similar and relevant together with properties that influence their performance. This sub-section also provides a basis to which the results of this research can be compared. This study enables us to identify the most reported capabilities and limitations that researchers are working on currently.

In addition, Table E.1 in Appendix E presents more details on several research accounts, focusing mostly on end-pumped and Nd^{3+} doped lasers that are Q-switched with different EO devices. The components listed there indicate how they influence the performance of the laser that is presented. For example, it can be seen that low (< 1% at.) concentration doping enabled high power pumping and gave rise to high energy and high peak power laser outputs with the Pockel cell Q-switch ([38], [39]). The cavity lengths for these lasers were ~70 mm and ~100 mm respectively. While these lengths were fairly long and therefore yielded pulses with slightly longer pulse durations (~10 ns), longer (10 and 7 mm) crystals with 0.3% at doping concentration made the Pockels cell Q-switched lasers generate high energy and high peak power pulses. Other accounts also show a combination of high PRF operations yielding short (nanosecond) and high peak power pulses [40]. These results show that an electro-optic (Pockel cell) Q-switched laser system can be optimised to generate the desired results. This can be achieved by adjusting design parameters such as crystal dimensions, the crystal's doping concentration, cavity length as well as the choice of the Pockels cell and output coupler mirrors.

2.4.6 Fibre Lasers

Fibre lasers are also worth mentioning. They are increasingly attracting interest as alternatives or substitutes for bulk solid-state lasers because they are cheaper, more efficient, possess better performing characteristics and have potential as sources of coherent light with guided output [41]. Research on fibre lasers is several decades old and few results ([42], [41]) were reported, but these generated low power outputs.

In our search for suitable pulsed fibre lasers that can be used for ranging applications, we found a commercial ytterbium doped fibre that can generate a high pulse repetition, short pulsed and high peak power output. This laser is manufactured on an industrial scale (1000 units a year) by a company in France, called KEOPSYS. Figure 2.4 shows a picture of this laser (sourced from their website). As seen here, the manufacturers stated that this ytterbium doped pulsed fibre laser is 1 m long, built to be compact and rugged so that it can operate

29

maintenance-free in hard environments. Its size (approximated by observation), appears to be 200 mm in diameter, and is the smallest size they can manufacture according to the fibre standards.

This ytterbium doped fibre laser stands out because of the pulsed output values it generates at the wavelength of 1.064 μm (which shows that fibre laser technology has significantly improved). It generates pulsed output in the 25 to 60 μJ energy range, with an average power that ranges from 3 to 10 W. The pulse durations and peak power range from 1 to 4 ns and 15 to 25 kW respectively, as the pulse repetition frequencies range from 50 to 400 kHz [43]. While these results are impressive, they were not specific in the actual combination of values.

Figure 2.4. A commercial ytterbium fibre pulsed 1.0 μm and high power transmitting laser built by KEOPSYS in France [22].

The manufacturers indicate on their website that the laser can be used in applications such as telemetry, range finding or detecting obstacles, airborne surveys, mapping or 3D scanning, and harmonic generation. The manufacturers also explain that the laser is packaged to comply with military vibration standards (MIL-STD-810F) and radiation certification [22]. However, its size remains bulky and would not fit into the limited space in which our laser is intended to be mounted. In addition, they do not disclose the pulsing technique they used or the repetition

frequency they operate in. As a result, an experimental investigation would be necessary to establish its operating conditions. For this research however, we did not investigate fibre lasers experimentally, and it will be set aside as future work.

The mass production of the laser indicates how well the technology has been established. However, while the laser system is small (in terms of fibre laser standards) and its output fits the application requirements of the current research, it is still too bulky to fit in the intended mounting location. At this stage, building a Nd:Fibre laser is part of the future plans of our research group.

2.4.7   Amplified lasers

If the desired objectives are not reached, laser materials and cavity properties can be optimised to scale lasers to achieve results that satisfy the design objectives. Brief discussions are presented in this sub-section to determine the feasibility of amplified lasers.

Fast switching and short pulsed outputs at high PRFs often require high power radiations that certain laser systems cannot reach, due to specific limitations. For this reason, this section seeks to study the scaling of some laser properties from literature. Power scaling for example is a systematic and distinct process that can be used to substantially and repeatedly increase the output power of lasers. Laser property scaling can be achieved by overcoming the known operational limitations of various laser materials without introducing or increasing negative effects such as excessive peak temperatures, optical damage or nonlinear effects [44]. Several techniques have been employed to get higher laser output powers and have been demonstrated in the past. Examples are the manipulation of laser system components to overcome limitations in performance as well as the master-oscillator-power-amplifier (MOPA) configuration, among others. Laser component manipulation can include choices such as laser material doping, dimension changes as well as adapting the cooling system, to name but a few. Successful component manipulation enables higher power pumping and therefore higher outputs can be reached. The MOPA configuration is implemented when a relatively low

31

power laser oscillator is used as a seed for a power-amplifier, or series of amplifiers, to effectively increase the brightness of the output [45]. The MOPA can be used to amplify the high repetition-rate seed laser to high power levels. This however makes the laser system a large and complex assembly [46].

Scaling laser outputs up can be achieved through the use of several techniques to overcome the characteristic limitations laser systems have. For example, major limitations in solid-state lasers are a result of negative thermal effects under end-pumping configuration; especially for high peak power lasers with short-pulsed output that at high repetition rates require high gain laser materials [1]. With regard to laser up-scaling, Table F.1 in Appendix F lists a report on the operation of an amplified laser where PRFs as high as ~80 kHz could be reached. However, to establish a stable amplitude pulsed output, the authors of this particular research reported a ~50 kHz PRF operation that yielded an output average power of over 5 W, pulse energies of 118 μJ, and a peak power of 6 MW could be calculated [47]. The major drawback of amplified lasers is their complexity. Further investigations on laser up-scaling will also be considered for future work, in which the goal would be to simplify the design.

2.5   Discussion and Conclusion

This chapter presented from literature the laser requirements for laser ranging and mapping applications. To do that, a study of ranging applications was presented that focused on LADAR devices. Central to the discussion of ranging applications on target objects that may not be cooperative, are the properties that can enable LADAR devices to operate in different and sometimes unfavourable conditions and still take reliable measurements. The target objects could include hard or soft irregular surfaces. It was established that operating LADAR devices under such conditions require pulsed laser radiation operating at high repetition rates, short pulse durations and high peak powers. This would enable LADAR devices to take readings at a longer range (high peak power), a high resolution (high PRF), and with high precision (short pulses). In addition, for ease of installation and stability during fast

measurement operations, the devices needed to be small (few centimetres), compact (can be packaged) and rugged (not fragile).

From a number of pulsed laser technology options, active Q-switching was chosen for a detailed investigation in this research because it can generate pulsed output with the combination of more stable nanosecond pulse energies, higher peak powers, lower temporal jitters [48], and it can be built to be very compact. With acousto-optic Q-switching, competing results were generated within a 20 mm long cavity where the authors obtained 2 ns duration pulses of 5.13 kW peak power at the repetition rate of 80 kHz. Certain techniques compete considerably well with these results on specific properties, but not on others. An example can be seen with cavity dumping, which generated good results – as shown by the high peak power, relatively short duration pulses and high PRFs (34 and 68 kW, with the corresponding 3.8 and 6 ns operating at 100 kHz). However, their cavities were long and not favourable for the small, compact and rugged requirement.

Active Q-switching as a result can prove suitable and useful for ranging applications in different practical conditions and provide reliable measurements. In general, Q-switched laser system design is firmly based on the Q-switch theory (discussed in Chapter 3). This determines the selection of gain material, cavity lengths, suitable feedback mirrors, etc., which will be applied in Chapter 4. These cavity components can be used for both acousto-optic (Chapter 5) and electro-optic (Chapter 6) Q-switching. The results obtained in these two investigations are compared with each other, as well as with the outputs generated by other techniques. The focus then shifts to the design parameters that influence the results that are closest to our experiments (Chapter 7).

Chapter 3

3. Theory of Q-switched Solid-State Lasers

In this chapter, the development of pulsed laser systems that are suitable for ranging applications is discussed. The focus is to provide their theoretical background, ranging from general laser operations to the specifically selected pulsing techniques.

3.1   Introduction

The importance of pulsed laser radiation and its uses in many industrial applications such as range finding prompted this research. Laser systems are transformed from the basic continuous wave (CW) into pulsed radiation-generating laser systems by employing different techniques such as Q-switching, cavity dumping, and mode-locking among others [49] (as reviewed in Chapter 2). Laser systems that are developed with these techniques are influenced by various of their laser properties at characteristic repetition frequencies. This causes them to emit outputs that are characterised by pulse widths, average and peak output power, as well as pulse energies. The desirable pulsed laser radiation properties for range-finding measurements at high repetition frequencies (~100 kHz) include short pulse durations (~1 ns) and high peak powers (~10 kW). In the literature review on all the laser pulsing techniques in Chapter 2, it was found that it is difficult to generate this combination of these output characteristics together. It was the actively Q-switched laser systems that were widely used in many applications that got closest to meeting these requirements. The industrial applications, for which active Q-switching is useful, require that energy be delivered on them in short intense pulses of laser output instead of delivering the same amount of laser energy over a longer period. Such applications include laser ranging, laser cutting, drilling, nonlinear optical studies, etc. [50], hence active Q-switching   was selected for further investigation in this research. This chapter looks at the background theory and principles that can influence the

34

ability of solid-state actively Q-switched laser systems to produce the desired results. The discussion here will influence the choice of the laser material, pumping system, the Q-switch element and the cavity properties that will allow the laser system that is developed in this research to produce stable, short, pulsed output with a high peak power at a high PRF.

Chapter 2 offered a motivation for the selection of the active Q-switching as a technique to develop the desired laser within this research. The current research focuses on two active Q-switches: the acousto-optic and the electro-optic modulators. Acousto-optic modulators (AOMs) use Radio Frequency (RF) sound waves to switch and are suitable when low modulation voltages, low insertion losses and high average powers are required. Electro-optic modulators (EOMs) for solid-state lasers are called Pockels cells, which use the Pockels effect to rotate the polarisation state of the laser. Together with the polarising element, the Pockels cell forms a Q-switch element that modulates the cavity loss. These devices are attractive for their short on-off time and high extinction ratios [51].

Chapter 3 presents a general overview of actively Q-switched lasers and covers the most important aspects one must consider when designing such systems. The chapter will also specify which parameters need to be optimised to develop a Watt level, nanosecond duration, Q-switched laser with pulse repetition frequencies in the range of 100 kHz. These lasers are suitable for applications such as remote sensing, ranging, micro-machining, marking, and more [52].

3.2   General Laser Operation

The word 'LASER', known as an acronym for Light Amplification by Stimulated Emission of Radiation, refers to devices that can produce and amplify intense, highly coherent and highly directional light beams at the infrared, visible, or ultraviolet frequency regions of the electro-magnetic spectrum [50]. At its most basic form, a laser system consists of three components: a gain medium, a pump (energy) source and a two-mirror resonator. Gain media can either be solid, liquid or gaseous, but must have strong absorption bands and sharp

35

fluorescence lines. Solid-state gain media, for example, consist of active ions hosted by solid materials such as crystals or glasses. Active ions get excited to higher energy levels and then relax to lower levels while they emit laser photons spontaneously and by stimulated emission. Exciting the active ions requires a pump source that emits optical radiation on the same wavelength as the absorption wavelength of the gain medium. To amplify the emission by stimulation requires the use of a feedback system such as a two-mirror cavity. A laser system in this form produces a continuous wave (CW) output.

Laser systems can also be built in more advanced forms to produce different kinds of pulsed outputs for specific applications. Such pulsed lasers include Q-switched, gain-switched, mode-locked lasers, etc. These laser systems are selected and developed for their characteristic pulse properties such as duration, energy, as well as average and peak power at specific repetition rates, depending on the desired outputs for specific applications, as discussed in Chapter 2. In this research, Q-switched laser system designs focus on the nanosecond pulsed laser output with high peak powers at high PRF. Figure 3.1 shows a typical Q-switched laser system that comprises a gain medium, a two-mirror cavity/resonator, a pump system, as well as a shutter. The first three are basic components required for CW output, while the shutter is responsible for switching the quality (Q) factor of the cavity to generate pulsed laser output. The pump sources excite active ions in the ground state to create population inversion in the higher energy levels of the gain medium. In bulk solid-state media, the pump energy can be delivered either from the side (side pumping) or along the optical path (longitudinal or end-pumping).
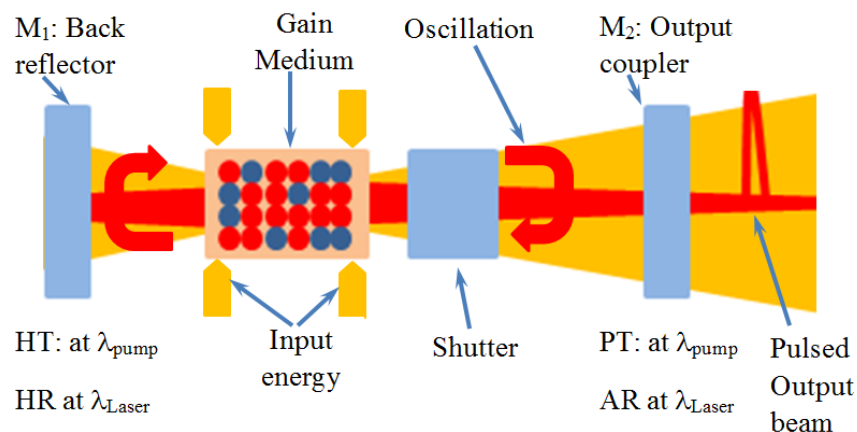
Figure 3.1. A typical general Q-switched laser cavity diagram consisting of four components: A gain medium, a pump (energy) source, an optical shutter and a two-mirror resonator. The gain medium possesses active ions which get excited to higher energy levels and then relax to lower levels while emitting laser photons spontaneously and by stimulated emission.

The two-mirror resonator or optical cavity consists of a back reflector that is coated for high reflectivity (HR) of laser light and high transmission (HT) of pump light, as well as an output coupler (OC) that was coated for partial transmission (PT) of the laser light and anti-reflection of pump light. This arrangement contains laser light that then oscillates in an optical path between the mirrors [53]. The gain medium amplifies this laser light via a stimulated emission process to provide gain, increasing the optical power in the cavity with each round trip. The process continues until the intracavity intensity saturates the gain, which leads to a steady state where the gain and the losses match. This results in a steady-state output from the OC and is termed continuous wave (CW) laser operation. The minimum gain that is required to initiate laser oscillation is called the threshold condition for laser oscillation [54]. By adding an optical switch or shutter to the system, one can obtain Q-switched output from the laser.

3.3   Laser Gain Materials

In addition to the pumping identification, lasers are also classified in terms of the laser materials or gain media they employ. In practice, a variety of laser materials have been used,

37

and they include solid-state materials (crystals, glasses, semiconductors and fibres), gases (atomic, ionic, molecular, and excimers), liquids (organic and inorganic solutes), as well as plasmas (for X-ray laser action) [49]. Laser materials (also known as gain media) are responsible for population inversion, spontaneous emission as well as stimulated emission. In their solid state, gain media are composed of crystalline or glass host materials doped substitutionally with active ions.

The active ions of interest in this research are the rare earth ions: Neodymiun (Nd^{3+}), Thulium (Tm^{3})$^{+}$ and Holmium (Ho^{3+}). Several other active ions exist and one can learn more about them from text books [1]. Active ions are used as dopants that replace some ions of the host material such as Yttrium (Y^{3+}), Lutetium (Lu^{3+}), and so on and introduce special characteristics to the gain medium. Because of active ions, gain media can be identified as either of three-level or four-level nature. In addition, active ions give gain media their characteristic absorption and emission cross-sections, as well as the corresponding spectra. These characteristics determine the choice of the gain media, their absorption and emission properties for use in specific laser systems. In addition, whether they are of a 3-level or 4-level nature, laser materials are also characterised by the absorption and emission wavelengths as determined by their spectra. In both energy level states of gain media/laser materials, active ions are first located at ground state. Upon absorbing sufficient input energy from an external source with a wavelength that matches the laser material's absorption wavelengths, the active ions are excited to higher energy levels [50].

Examples of active ions can illustrate how they function in laser materials. An Nd^{3+} active ion, for example, has an absorption wavelength around 800 nm that matches the emission wavelengths of some laser diodes that are suitable pump sources for 1060 nm lasers. It also has another important absorption line (around 880 nm). This makes Nd^{3+} ions excellent dopants for diode laser-pumped solid-state lasers [55] that emit continuous laser radiation at these wavelengths. Corresponding to the 800 nm absorption line, Nd^{3+} ions have three main lasing transitions that are ~930 nm (three-level), as well as the ~1060 nm and ~1300 nm, which are both of a four-level nature. The 880 nm absorption line is useful for direct pumping

38

(to be explained briefly in the next section) and corresponds to the ~1060 nm laser transition. These lasing transitions are characterised by high absorption and emission cross-sections [1].

Other active ions absorb and are pumped in a similar manner. For example, Tm^{3+} active ions absorb input energy and are pumped at wavelengths around 790 nm; their lasing wavelengths are in the mid-IR region, around 1900 nm. This wavelength is strongly absorbed by water and therefore does not have good transmission through the atmosphere. However, this wavelength is the absorption line of another active ion, the Ho^{3+} ion. With careful system design and assembly (that isolate the 1900 nm radiation from the atmospheric moisture), the Tm^{3+} radiation can be used as an input energy or pump for the Ho^{3+} doped laser material, which typically lases at wavelengths longer than 2050 nm, which fall outside the main water absorption band in the atmosphere. This makes Tm^{3+} doped lasers suitable to pump Ho^{3+} doped lasers.

The different types of solid-state host materials are vanadate (YVO_4, $GdVO_4$ and others), fluorides (YLF, $LiLuF_4$, and others) and oxides (YAG), to name but a few. The properties that characterise laser host materials are thermomechanical properties, stark splitting and crystal fields. When doped with active ions, and fabricated, gain media such as $Nd:YVO_4$, Tm:YLF, Ho:YLF, and $Ho:LiLuF_4$ are developed. A review of solid-state lasers can be found in [1].

3.4   Pumping of Laser Systems

Lasers are usually pumped optically, electrically or chemically. Optical pumping can be realised through continuous wave (CW), a pulsed radiation emitted by either flash lamps, laser diodes, or other lasers that are suited for solid-state lasers [56]. The electrical pumping method is obtained when a sufficiently intense electric discharge initiates a current flow through a conductive medium such as ionised gas or a semiconductor. The resulting narrow absorption bands can absorb the electric energy for active ion excitation. Furthermore, the pumping by chemical excitation occurs when highly reactive or explosive gas mixtures undergo an exothermic reaction that generates a large amount of energy. If a sufficient

39

fraction of this chemical energy can be transferred to laser energy, the process results in high power, and high-energy pulsed lasers [57]. Since this research is based on solid-state lasers, the focus will be on optical laser pumping.

In optically pumped solid-state lasers, a pump source emits light that is absorbed by the gain materials. In the process it increases the energy of active ions from the ground state, thereby exciting them to the upper laser level and thus creating a population inversion (N_{inv}).

Two commonly used energy level systems, the three and the four-level systems, are shown in Figure 3.2. Figure 3.2 (a) is a three-level system where the gain material absorbs a pump photon of frequency v_1, increasing its energy from the ground state (level 0) to an excited-state level (the pump level: level 3). The ion then rapidly decays non-radiatively to the upper laser level (the upper laser level: level 2). This creates a population inversion between the upper laser level and lower laser level. For three-level systems, the terminal state (level) of the stimulated transition is also the ground state and to maintain the population inversion in this case requires very high pump powers to continually pump more than half of its population into the excited state [50]. This is a draw-back of the three-level systems. Next is Figure 3.2 (b), a four-level laser system, where the pumping process and transitions are the same as the three-level laser system until the upper laser level.

However, the stimulated emission transition from the upper laser level (level 2) terminates at the lower laser level (level 1), which is at a higher energy level above the ground state (level 0). From level 1, the active ion population is rapidly evacuated to the ground state through a non-radiative transition.

Pumping can easily develop a positive population inversion with four-level lasers between levels 2 and 1, due to the rapid depletion of the lower laser level (level 1) to the ground state, which is not the case with the three-level lasers.
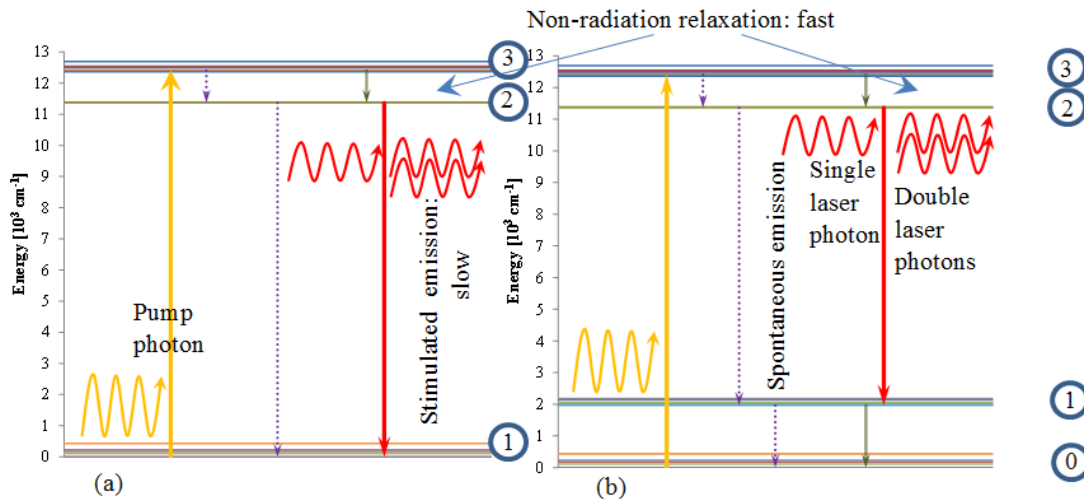
Figure 3.2. Two energy level diagrams that constitute general laser systems presented to show absorption and emission transitions for (a) Three-level and (b) Four-level laser systems.

Diode lasers are more efficient than flash-lamps for pumping solid-state lasers because they:

- Induce less heating in the gain medium, thus reducing the thermal problems [56]
- Lead to better beam quality solid-state lasers due to better overlap with laser modes
- Are widely available for a range of wavelengths and their outputs can be narrow enough to target specific active ions [58]
- Occupy small volumes
- Are lightweight
- Have long operational life and are highly efficient
- Have a low threshold
- Provide relatively high slope efficiencies to the lasers they pump ([59], [60])
- Are suitable for pumping Q-switched lasers that produce short-pulsed outputs at high repetition rates [61]

In practice, laser diode pumping can be applied along the optical axis (longitudinal or end-pumping) or from the side (side-pumping) [62]. End-pumping, however, offers better

41

mode matching. Laser diodes are the best candidates for end-pumping [57], because they produce outputs with high brightness compared to flash lamps. Also, end-pumping beams can be highly focused. Thus, laser diode pumping favours laser materials with high absorption coefficients, high gain, and short absorption lengths.

Consider a CW pump power (P_{pump}), longitudinally incident and traversing through a laser material of length L, its absorption length is defined by ([58], [63]) as in Equation (3.1),

$$l_{abs} = \frac{1}{N_{ai}\sigma_{abs}} \qquad \textbf{(3.1)}$$

where N_{ai} is the number density of active ions and σ_{abs} is the absorption cross-section of the laser material. Equation (3.1) shows that the higher the product $N_{ai}\sigma_{abs}$, the shorter the absorption lengths.

3.5   Choice of Laser Gain Material for Q-switching

Gain in a laser material originates from the amplification of the photon flux $\phi(z)$ as a result of stimulated emission. This causes the photon flux oscillating in the cavity, along the optical path z-axis, to increase exponentially from the noise level $\phi(0)$ [49]. For longitudinal optical pumping with diode lasers directed along the laser axis, focused to a spot the size of area A, and assumed to be constant along a length L, the overall gain can be estimated and expressed as in Equation (3.2) [63],

$$G(\nu) = \exp\left(\frac{P_{pump}}{h\nu}\frac{\sigma_{em}\tau_f}{A}\right) \qquad \textbf{(3.2)}$$

where τ_f is the fluorescence lifetime during which the gain is generated and σ_{em} is the emission cross-section. Equation (3.2) indicates that high overall gain can be obtained by using laser materials with large magnitudes of the product $\tau_f\sigma_{em}$. The main contributor to large $\tau_f\sigma_{em}$ product values is high σ_{em} values, which by direct proportion lead to high gain while short τ_f ensures that high gain is achieved in short intervals. This can indicate that

42

Equation (3.2) represents a gain that can hold at high PRFs. Furthermore, the mode size (area A) of the laser can be reduced to increase the gain, since high gain is needed for short pulsed laser output [1].

High gain laser materials are useful for different applications in both CW and Q-switched lasers. Q-switching, for example, is a repetitive process with characteristic (low or high) PRF, depending on the different intended applications. Low repetition rates $(\text{PRF} = (1/T) < 1/\tau_f)$ indicate that periods of repetition (T) are longer than τ_f, which then allows high gain to be generated. As discussed in Chapter 1, this research requires high repetition rates, which means that $\text{PRF} > 1/\tau_f$, and implies shorter repetition periods than the fluorescence lifetimes, thus limiting high energy storage. In such a case, to attain high gain and energy storage as well as extraction requires a proper choice of pump source and the laser material to generate and produce high gain, energy storage and extraction within the short periods of high repetition rates.

The Nd:YVO$_4$ crystal has a shorter upper level lifetime of 97 µs as compared to Nd:YLF and Nd:YAG, which have respective upper level lifetimes of 485 µs and 250 µs. As a result, this Nd:YVO$_4$ crystal's fluorescence lifetime, together with its high pump absorption and stimulated emission cross-section, makes it more suitable and at an advantage over other host materials to operate at high repetition rate Q-switched systems. When used in end-pumped Q-switched systems, laser materials with large stimulated emission cross-sections produce high gain, resulting in short duration output pulses even at high repetition rates of 50 kHz. The short upper state lifetimes benefit the Q-switching process by fast recovery of the excited-state population and allowing operation at higher repetition rates without loss of pulse energy [61].

3.6   Analysis of Laser Threshold

One of the goals of the current research is to obtain high power outputs. Equation (3.3) gives the threshold pump power of a four-level laser and is a mathematical tool that can be used to

43

calculate the absorbed pump power for a diode end-pumped Nd:YVO$_4$ four-level laser required to establish the threshold of oscillation that uses the values of the absorption and emission cross-sections, σ_{Abs} and σ_{Em}, of the laser wavelength respectively. It expresses the threshold of the laser with respect to absorbed pump power P_{th}, and the slope efficiency versus absorbed pump power η is given by

$$P_{\text{th}-4\text{level}} = \frac{\pi h \nu_p}{4\eta_{p-q}\sigma_{em}\tau_f}\left(\omega_l^2 + \omega_p^2\right)(T + L) \tag{3.3}$$

where η_{p-q} is the pump quantum efficiency, τ_{21} represents the excited-state lifetime, ω_L and ω_P are the laser and pump beam radii in the laser crystal, T represents the output coupler transmission loss, and L represents additional losses within the resonator. The laser system is designed for end-pumping since the pump beam and the laser modes are arranged to be of equal size ($\omega_L = \omega_P = \omega$). To express this, Equation (3.3) can be rearranged and approximated to Equation (3.4) as

$$P_{\text{th}-4\text{level}} = \frac{\pi h \nu_p}{2\eta_{p-q}\sigma_{em}\tau_f}\left(\omega^2\right)(T + L) \tag{3.4}$$

The threshold of the four-level (and even that of the three level) laser is inversely proportional to the product $\sigma_{em}\tau_f$ of emission cross-section and effective upper laser lifetime. This indicates that gain media that have high values of this product can be used to develop lasers with low-threshold pump powers. The low-threshold pump powers also correspond to high slope efficiencies. This also indicates that a low value of T favours the desired low pump threshold. Taking Nd:YVO$_4$ as an example, its product $\sigma_{em}\tau_f$ is roughly 1.6 times larger than that of Nd:YAG, which implies that its lasing threshold is characteristically lower, and its slope efficiency is higher.

3.7   Output coupling

Just like the threshold pump power, output coupling is very important in the generation of a laser beam. To determine how the choice of the output coupler influences the laser generation, we need to consider a number of things, such as the radius of curvature and its transmission or reflectivity [1]. In this study however, the focus is on a flat output coupler or a flat-flat cavity, so that its stability can depend on the thermal lens of the laser material. In this section, the focus is on the influence that the transmission/reflectivity of the output coupler has on the laser output.

Several techniques can be used to determine the optimum output coupling of a laser system. Koechner et al. (2013) discuss several laser properties such as output coupling (OC) transmission (%), OC reflectivity (≤ 1), and intracavity density (kW/cm^2) that influence the laser output. These independent parameters are said to influence the peak output power (kW), the internal flux (kW/cm^2), the output power, and the output pulse energy (mJ) respectively. By plotting the peak power against the OC transmission at a fixed pump power level (for example) – as the transmission increases, so does the output peak power until it reaches a maximum, and then begins to drop [1]. Thus, for a particular pump power there is an OC transmission percentage (where the output peak power is the highest) that gives the indication of optimum output coupling. This is true for internal flux vs OC reflectivity, output power vs intracavity power density, as well as output energy vs OC reflectivity.

However, as pump powers increase and, in turn, high intracavity laser intensity and peak power increase due to the high output coupler reflection, the intracavity components, including the laser material, are exposed to high temperatures [1]. It is the responsibility of the laser developer to strike a balance between obtaining the high values of these parameters and preventing optical component damage because of high intensities.

The properties of the laser output are the indication of its quality, which is also determined by the quality factor Q of the cavity, and this is introduced in the next section.

3.8   The Cavity Quality Factor

The quality factor Q of the cavity and the associated losses are the key properties of the Q-switching process. Equation (3.5) defines it as the ratio between the energy that the cavity stores, and the energy it loses per round trip. This is low when the losses are kept high and vice versa.

$$Q = 2\pi \times \left(\frac{\text{Energy stored in the cavity}}{\text{Energy lost per oscillation cycle}} \right). \tag{3.5}$$

Figure 3.1 in Section 3.2 demonstrates a cavity that can alternately switch from high-loss (low-Q) to low-loss (high-Q) states by modifying a continuous wave cavity that consisting of the gain-medium and two mirrors to a pulsed cavity consisting of the gain-medium, optical-gate and two-mirrors. As the cavity is pumped, the optical gate periodically closes and opens to respectively introduce and remove losses, giving rise to the concept of Q-switching.

3.9   Q-switching

Q-switching is a two-process cycle that spans two different time scales and generates pulsed laser output in each cycle. The first process is a high-loss interval, followed by a loss interval. The dynamics of the population inversion $N(t)$ and the photon populations $\phi(t)$ can be described by using the coupled differential rate equations given in Equations   (3.6) and (3.7) [64], [64]. While other lasers are pulse pumped with flash lamps, we discuss a continuous end-pumped wave and repetitively Q-switched laser.

$$\frac{d\phi(t)}{dt} = K\phi N(t) - \frac{\phi(t)}{\tau_c} \tag{3.6}$$

$$\frac{dN(t)}{dt} = R - \frac{N(t)}{\tau_f} - K\phi(t)N(t) \tag{3.7}$$

R describes the pump rate per unit volume, τ_f is the upper laser lifetime. τ_c is the photon cavity decay time and is given by Equation (3.8) as

$$\tau_c = \frac{2l_{\text{cav}}}{c} \frac{1}{\left[\ln \frac{1}{R_M} + L\right]} \tag{3.8}$$

where l_{cav} is the cavity optical length, R_M is the output mirror reflectivity and L is the roundtrip dissipative optical losses, but include scattering, residual transmissions of high reflectors, aberration due to thermal lensing and acousto-optic diffraction loss.

Equation (3.8) also indicates that the photon decay time is proportional to the photon transit time ($t_r = 2l_{\text{cav}}/c$), which in turn is proportional to the cavity length. Thus, photon decay times in short cavities are short. Furthermore it can be deduced that, for output couplers with a high reflectivity (R_M), more photons are reflected into the cavity for stimulated emission, thus resulting in long photon lifetime τ_c. In addition, shortened cavity lengths reduce the laser mode sizes and this is detrimental to the desired TEM$_{00}$ mode overlap with the pump volume [61]. This necessitates that a Q-switched laser designer properly balances the cavity length and the output coupler reflectivity.

Figure 3.3 graphically depicts the solutions to Equations (3.6) and (3.7) for the full Q-switch cycle during both high-loss and low-loss intervals. The high-loss process occurs first. The cavity is pumped while laser oscillation is blocked by introducing high losses to it. During this process interval, the quality factor (Q) of the resonator is significantly reduced [50], [50]. This interval can take place over one or a few upper laser lifetimes. This allows the population inversion or gain to build up, and energy to be stored in the upper laser level [53], [53]. Since there is no laser oscillation, the photon population is negligible or zero. Thus, Equation (3.6) plays no part, while Equation (3.7) becomes Equation (3.9):

$$\frac{dN(t)}{dt} = R - \frac{N(t)}{\tau_f} \tag{3.9}$$

and its solution is given by Equation (3.10) [37]:

$$N(t) = N_\infty \left[1 - exp\left(-t/\tau_f\right)\right] \qquad \textbf{(3.10)}$$

where $N_\infty = R_p \tau_L$ is the maximum and an asymptotic value of the population.

As illustrated in Figure 3.3, the population inversion builds up during the interval $0 < t < t_{hl}$ $(\sim 2\tau_f)$ and reaches the maximum $N_\infty = R_p \tau_f$ (the product of the pumping rate and the fluorescence lifetime). The second process interval is characterised by drastically reduced losses. This sudden switch to a high Q-state allows oscillation to take place. During this period, the following processes occur. First, the low-Q to high Q-switching takes place almost instantly.
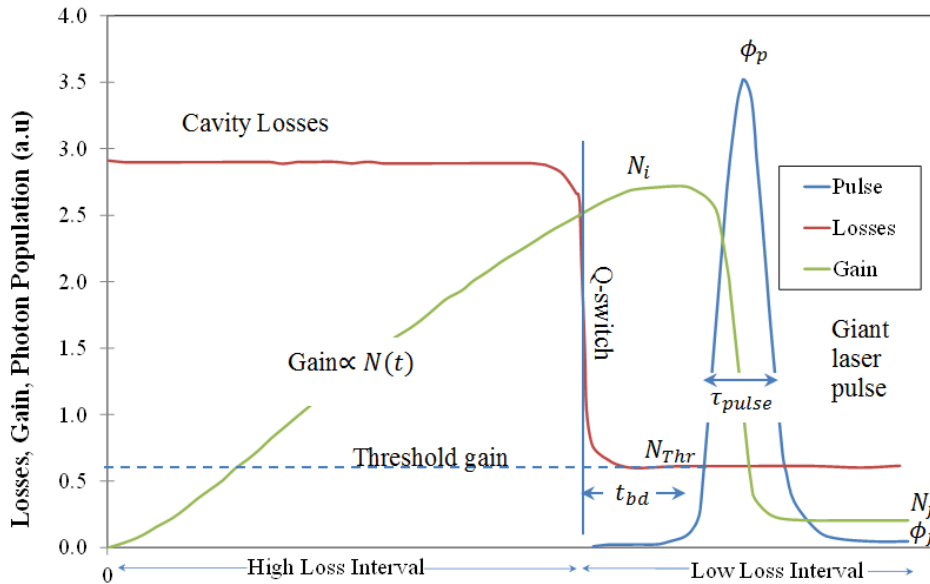
Figure 3.3. One pulse Q-switch cycle of two intervals of different time scales singled out from a train of cycles. The first interval of about one or two upper laser lifetimes illustrates the increase of gain and population inversion to values far higher than threshold. The second interval is in the order of cavity photon lifetimes and it illustrates the variation of the population inversion as well as the laser intensity over the time during which a single pulse is released [50].

48

This switching is followed immediately by a build-up of photon population into a giant pulse emission, while population inversion gets depleted from the upper laser level. This period is almost always so short that no significant pumping or relaxation can be considered [65]; therefore the pumping and relaxation terms in Equations (3.7) and (3.8) can be removed. This gives rise to Equations (3.11) and (3.12) for the low-loss period [50]:

$$\frac{d\phi}{dt} = K(N - N_{th})\phi(t) \tag{3.11}$$

$$\frac{dN(t)}{dt} = -K\phi(t)\,N(t) \tag{3.12}$$

where N_{th} is the active ion-population inversion at threshold level to which the losses will drop.

The solution of Equation (3.11) describes the photon population that begins to build up from the time the losses drop lower than the gain and is given by Equation (3.13) as:

$$\phi(t) \approx N_i - N(t) - \frac{N_i}{r}\ln\left(\frac{N_i}{N(t)}\right) \tag{3.13}$$

where N_i is the initial population inversion and $r \equiv N_i/N_{th}$ is the ratio that describes by how much N_i exceeds N_{th}.

A giant pulse is released at the end of the build-up time when the photon population is sufficiently high. At this stage, the photon population begins to rise sharply and rapidly depletes the population inversion from its initial maximum value N_i, as long as the gain is greater than the threshold level. When the population inversion reaches threshold ($N_{th} = N_c$), the photon population reaches its peak ϕ_p and stops growing after several hundred round trips. At this instant the gain diminishes, as the laser exhibits a net loss of less than the threshold. Consequently, the number of photons drops and the pulse diminishes down to noise level. Simultaneously, the population inversion decreases further to a final value (N_f), which remains in the active medium. Unlike the high loss period, which is related to the upper state

49

level and in the millisecond range, the pulse release period is related to the photon decay time and is in the nanosecond range [37]. Because the period during which all this happens is so short, the effect of continuous pumping is negligible.

3.10   Q-switched Laser Output Parameters

Laser pulse parameters such as pulse energy U_{pulse}, peak power (P_{peak}) and pulse width (τ_{pulse}) are dependent on the properties that characterise the two intervals of each of Q-switched laser cycle. For the high loss interval, the important cycle properties are the interval duration and the final amount of gain or energy stored in the upper laser level. For the low-loss interval, the most important properties are primarily the switching speed and the final loss value.

The pulse energy, defined by Equation (3.14), is simply the amount of upper-state population that has been depleted to be converted to optical energy.

$$U_{pulse} = U_i - U_f = \left(N_i - N_f\right)\hbar\nu_a \tag{3.14}$$

U_i is the initial energy stored as potential energy in the upper laser level, U_f is the remaining energy after the pulse has been released at the far edge of the pulse, and ν_a is the atomic transition frequency. Experimentally, this energy can be determined (approximated) by dividing the average power by the pulse repetition frequency (PRF) [50]. Equation (3.15) describes this as:

$$U_{pulse} = \frac{P_{ave}}{PRF} \tag{3.15}$$

where U_{pulse}, P_{ave} and PRF characterise the output pulse with energy in Joules, average power in Watts, and the pulse repetition frequency in Hertz. The right-hand side of Equation (3.15) indicates that to generate high-energy pulsed laser output while operating at

high PRF, requires high average output power. The desired high PRF would normally and undesirably reduce gain, as well as limit the energy of the output pulses.

In addition, the CW laser regime can be used to estimate or predict the value of the maximum pulse energy that can be extracted from the CW-pumped Q-switched pulse energies as expressed in Equation (3.16) ([66], [67]):

$$U_{pulse} = P_{\text{ave-cw}}(\tau_f \xi)\left(1 - \exp\left(-\frac{1}{\text{PRF} \times \tau_f}\right)\right)$$

(3.16)

where $= \frac{N_i - N_f}{N_i - N_{th}}$ is the numerical factor that can be approximated to values greater than or equal to 1 for high repetition rates. Equation (3.16) provides a way to theoretically calculate the pulse energy and average power in relation to the pulse repetition frequency. Figure 3.4 shows the theoretical values of the average power and energy per pulse of a continuously pumped and repetitively Q-switched Nd:YVO$_4$ laser versus repetition rate, according to Equation (3.16). The fluorescence lifetime was taken to be 97 μs [68].

51
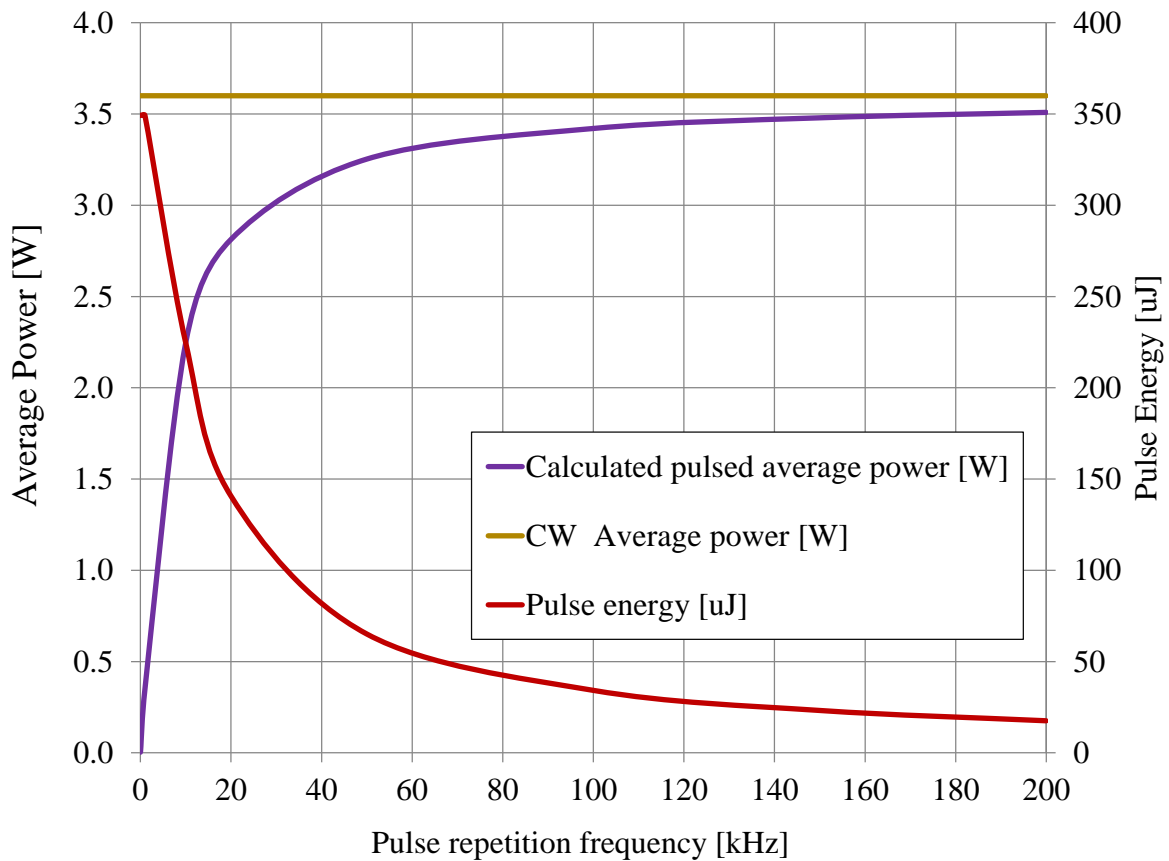
Figure 3.4. Theoretical approximation of the pulsed average power and the pulse energy that can be obtained with Q-switched Nd:YVO$_4$ laser in comparison to CW average power.

It should be noted that the average power increases with the increasing PRFs, such that they approach the CW values at high PRFs. It is common knowledge that the CW pumped and repetitively Q-switched Nd:YVO$_4$ laser, with a short fluorescence lifetime, operates favourably at high PRFs. Figure 3.4 also shows that high pulse energies are easily reached at low PRF values and get reduced at high values. This implies that obtaining high pulse energies at high PRFs is difficult.

Another parameter of practical importance to Q-switched lasers is the pulse widths (τ_{pulse}). Equation (3.17) defines this parameter, as derived from several textbooks [1], and expresses it

as a product of τ_c and a function of N_i, N_f, N_{th}. For the purposes of this work it is expressed as:

$$\tau_{pulse} = \tau_c f(N_i, N_f, N_{th}) \tag{3.17}$$

Equation (3.17) shows that laser pulse widths are dependent on the photon decay time that was shown earlier to be proportional to the cavity length (Equation (3.8)). Thus, short photon decay times lead to short pulse widths.

Peak power of an output pulse is another of the important Q-switch laser output parameters and Equation (3.18) defines it as:

$$P_{peak} = \phi_{pk} \frac{\hbar \nu_a}{\tau_c} \tag{3.18}$$

where ϕ_{pk} describes the peak photon population and τ_c is the photon decay time described in Equation (2.6). Experimentally, pulse widths and energy are measured and used to calculate (approximate) the peak powers of the laser as shown reliably in Equation (3.19) [69]:

$$P_{peak} = \frac{E_{pulse}}{\tau_{pulse}}, \tag{3.19}$$

P_{peak}, E_{pulse} and τ_{pulse} characterise the output pulse, with peak power in kilowatts, energy (which is the same as that defined in Equation (3.15)) in joules, and pulse widths at full-width half-maximum in nanoseconds. This means that obtaining short duration pulsed output, which can be achieved with short cavities and reduced losses when operating at high pulse repetition frequencies, leads to high peak powers [70]. Other contributing factors to short pulse widths are high gain and short fluorescence lifetimes [1]. Thus, laser materials with high gain, such as Nd:YVO$_4$ crystals, can be favourable for short pulse laser output at high pulse repetition frequencies (HPRF) because of their relatively short upper-state lifetimes.

53

3.11   Switching Speeds

Switching in the operation of Q-switched lasers initiates the processes that take place during the low-loss interval, such as pulse build-up and pulse emission. For Q-switch devices to generate the desired short output pulses with high energy extraction, their switching times must be significantly shorter than the build-up time [50]. Typically, practical switching times must be one order of magnitude longer than the pulse width [71]. However, available Q-switches sometimes open slower than desired and in the process reduce the quality of the intended outputs. Switching times start at $t = 0$ when the switch is opened, making the high cavity losses to drop drastically, and end at the time when these losses reach the minimum value. The speed at which the switch opens has a significant effect on the development of a pulsed output in Q-switch lasers.

Figure 3.5 (a) to (c) illustrate why slow Q-switch speeds are problematic. Figure 3.5 (a) demonstrates an optimised laser where the switching and the build-up times are equal; thus the cavity losses reach the minimum value when the output pulse is released. In this case, the gain remains almost constant throughout the build-up time and drops sharply as the pulse is released [1]. In Figure 3.5 (b) the build-up time is slightly shorter than the switching time, but the initial population inversion is still mostly depleted. However, since the losses are still above threshold values by the time the pulse is released, extra losses (still remaining but continuing to drop) cause the pulse energy to be reduced. The case presented in Figure 3.5 (c) is extreme. It illustrates the case when the build-up time is much shorter than the switching time. The gain drops in a slow stepwise manner, causing two or more pulses to be released. The first released pulse is much larger and depletes most of initial population inversion and gain. The fact that the cavity losses are not near the minimum at the time of the pulse release, reduces its energy. After this pulse, a smaller but significant amount of upper-level population and gain remain. While this happens, cavity losses continue to drop and soon fall below this residual gain, leading to the build-up and causing the release of an additional pulse within the same Q-switch open time [1]. Such a pulse may be weak or more prominent, depending on the switching time. Multiple pulse laser outputs are a disadvantage of slow switches, because

54

they reduce the overall energy and the average and peak powers of the first pulse [1]. These lasers exhibit poor pulse-to-pulse stability. Lasers that possess these secondary pulses can create timing errors when deployed in optical RADARs, measurement errors in scientific experiments, and a number of other different difficulties in practical applications [50].

(a) Switching time = Build-up time

(b) Switching time > Build-up time

(c) Switching time >> Build-up time
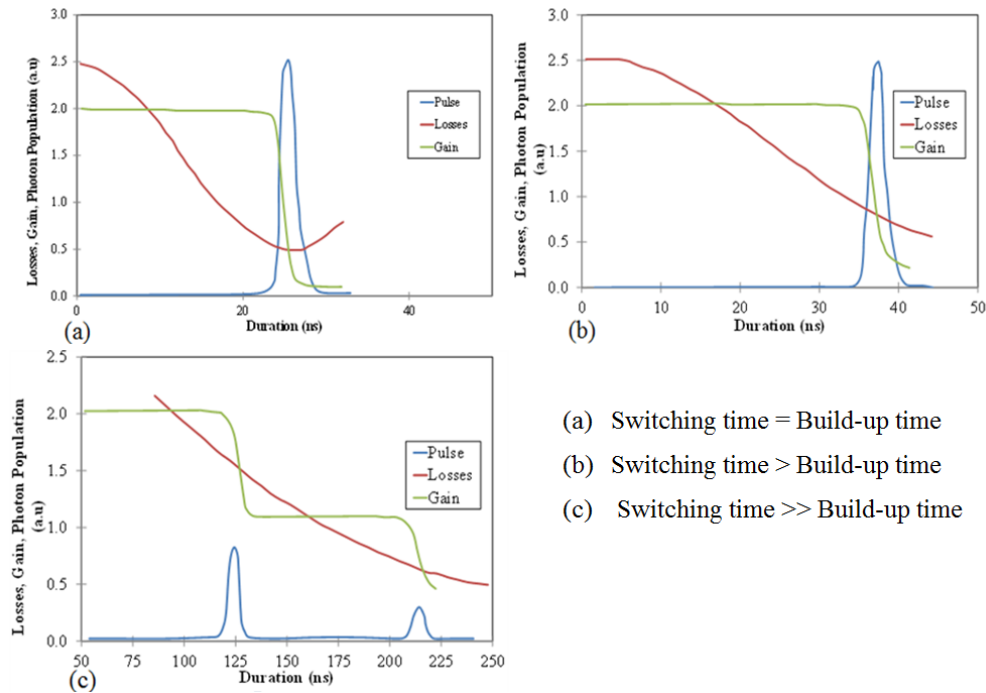
Figure 3.5. Gain, losses and pulse intensity are presented for three slow-switching scenarios. In (a) the switching time and the build-up time are equal, a state that allows the depletion of most of the initial population inversion. In (b) the switching time is slightly longer than the build-up time, in which case extra losses are introduced. In (c) the switching time far exceeds the build-up time, leading to the generation of undesired multiple pulses [1].

Various Q-switching techniques have been developed to find fast-switching techniques that are useful in industry. The two most implemented Q-switch techniques are based on acousto-

optic and electro-optic effects. These techniques are discussed in Sections 3.13 and 3.14 respectively, and evaluated based on their switching speeds.

3.12   Different Types of Active Q-switching

Laser pulsing by Q-switching is categorised into two classes, passive and active Q-switching. While passive Q-switching has a simple design because of its self-switching radiation that requires no high voltage and is operated at low cost, its drawbacks are the lack of precision capability to trigger the switching process and lower output. This makes it an unsuitable choice for the applications intended for this research. Instead, active techniques such as acousto-optic and electro-optic Q-switching are competing because of the results they can generate. While it is true that they too have their own drawbacks, this must be catered for by the laser designer.

3.13   Acousto-optic Q-switching

Active Q-switching has been realised with acousto-optic modulators (AOM) in both 4- and 3-level lasers at different wavelengths and for various applications. An AOM is a device that is made of a combination of an optical material (a crystal or glass of particular index of refraction), and a piezoelectric transducer that is tightly attached on one end and driven by a radio frequency (RF) oscillator [37]. Figure 3.6 shows a schematic diagram of an AOM. When an RF driving voltage is applied, the piezoelectric transducer converts electric energy into ultrasonic energy and launches a sinusoidal acoustic wave that propagates through the optical component of the AOM [1]. This creates a phase grating with a wavelength (Λ) equal to that of the travelling acoustic wave.

Equation (3.20) gives the condition of constructive interference for Bragg diffraction [72]:

$$n\lambda_L = 2\Lambda(\text{Sin } \theta_B)$$

(3.20)

λ_L and $\Lambda = v_{acoustic}/f$ (the ratio of the speed of sound to the frequency by which it is driven) are the respective optical and acoustic wavelengths. The symbol θ_B represents the Bragg

56

angle that is realised when the incident angle θ_{inc} equals the angle of diffraction θ_d such that $\theta_{\text{inc}} = \theta_d = \theta_B$. For the Bragg condition, all angles are described with respect to the acoustic wavefronts. The symbol n is the index of refraction of the AOM optical medium.
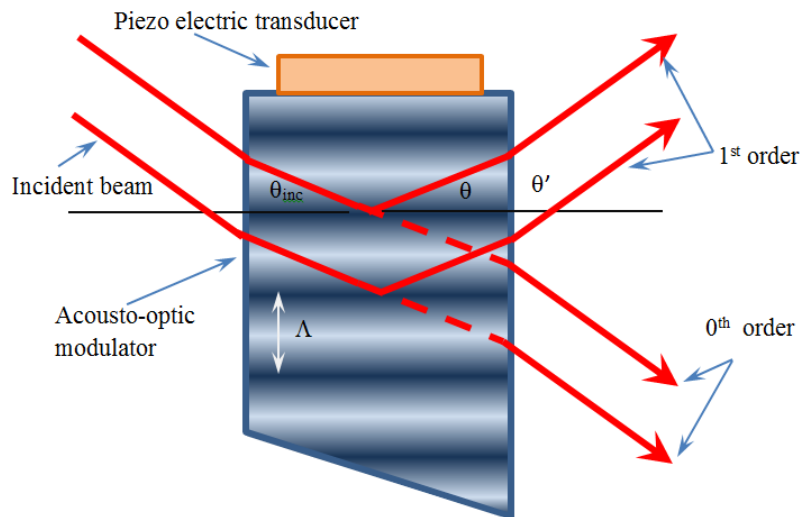
Figure 3.6. An AOM, shown here as a complete switching element that illustrates the diffraction of laser light from 0th order to the 1st order when the acoustic wave generated by the piezoelectric transducer forms a Bragg grating.

While it is possible for light to be diffracted into different orders off the optical path (0th order), the condition that all diffracted light be on the 1st order requires that the deflection angle (between the initial optical path and final optical path after the AOM) be twice the angle of diffraction, or $\Theta = 2\theta_d$ [72]. The AOM therefore must be aligned until the intensity is in the first order.

To develop an actively Q-switched laser, an AOM is placed inside a laser cavity together with the gain material. Figure 3.7 illustrates the two cases, the low and high Q-cavity conditions. When successive acoustic wavefronts interfere constructively, they periodically scatter or diffract a portion of the incident light passing through this transparent optical part of the AOM out of the optical path, thus causing a low-Q cavity and preventing laser oscillation

[37]. When the RF driving voltage on the transducer is off, the AOM transmits the beam and the 1st order receives no light.
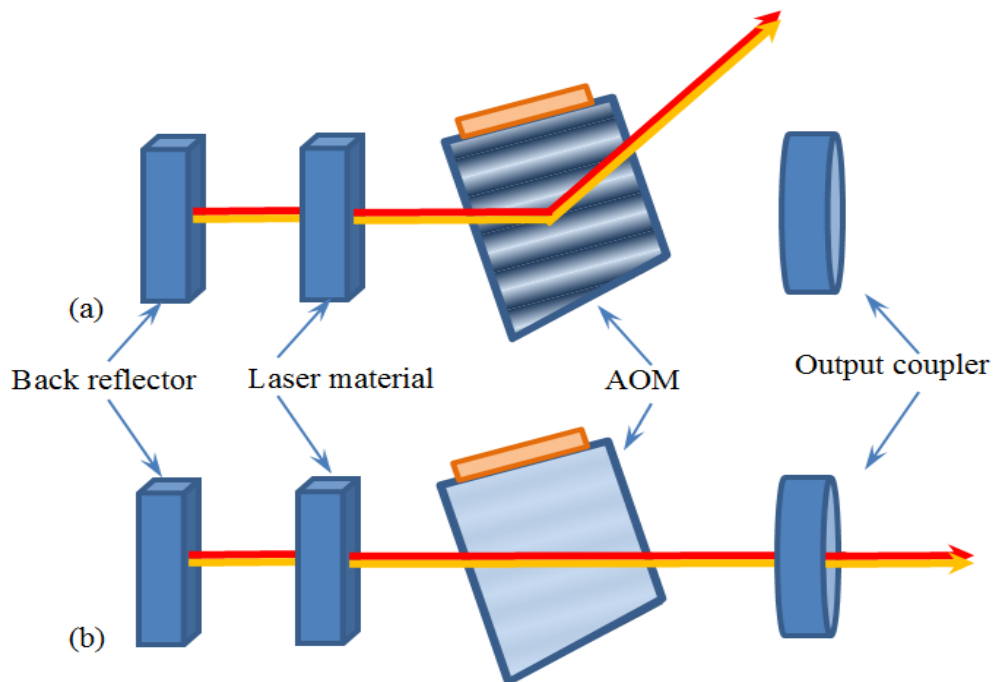
Figure 3.7. (a). (Top) The AOM Q-switched cavity when the beam is reflected out of the cavity by an acoustic wave compression. (b). The AOM Q-switched cavity when the beam oscillates in the cavity because it interacted with an acoustic wave rarefaction or no acoustic wave is propagated through the AOM.

The measure of the diffraction efficiency of the acousto-optic material is density ρ, acoustic velocity v, and photo-elastic coefficient p, and is defined by the diffraction figure of merit (FOM) of the material, M at a given acoustic power level. Equation (3.21) defines the figure of merit of an AOM crystal:

$$M = \frac{n^6 p^2}{\rho v^3} \tag{3.21}$$

Table 3.1 gives properties of few materials that are commonly used for acousto-optic Q-switching. The symbol $M_w = M/M_w$ represents the FOM of the material with respect to that of water.

Table 3.1. The properties of few crystals that can be used for light diffraction in acousto-optic modulators [73].

Material	ρ[kg/m^3]	v [m/s]	n	p	M_w
TeO$_2$	5.99	1.36×10^8	2.2	0.09	5
SiO$_2$	2.2	2.05×10^8	1.46	0.2	0.006
LiNbO$_3$	4.7	7.4×10^8	2.25	0.15	0.012

This can be used to calculate the ratio $I_{\text{diffr}}/I_{\text{inc}}$, which is the fraction of the incident power that is transferred in a distance L into the diffracted beam and is given by Equation (3.22).

$$\frac{I_{\text{diffr}}}{I_{\text{inc}}} = \sin^2\left(\frac{\pi L}{\lambda}\sqrt{\frac{MI_{ac}}{2}}\right) \tag{3.22}$$

L is the interaction length between the acoustic wavefront and AOM crystal, λ is the optical beam wavelength, and $I_{ac} = P_{ac}/$(acoustic wave active area) is the acoustic power. By using Equations (3.20), (3.21) and (3.22), the AOM can be characterised. It can be noted that the higher the product MI_{ac}, the larger the $I_{\text{diffr}}/I_{\text{inc}}$ will be, thus indicating higher diffraction efficiency. As a result, the AOM crystals with a high figure of merit are a better choice for efficient acousto-optic Q-switching.

The advantages of using AOMs for Q-switching applications include low cost, low voltage requirements, and smaller sizes that are suitable for robust, short cavity as well as polarisation and wavelength insensitive lasers. Furthermore, AOMs have desirable properties, such as very low optical insertion losses, relatively simple RF drive circuitry, and ease of use [50]. With these advantages, AOMs have been used for the generation of short, high peak power pulses

59

although there are limiting factors such as switching speeds and modulation depths that are difficult to optimise unless carefully designed.

Switching speed is a major disadvantage of the acousto-optic modulators due to the vast difference between the speed of light and that of an acoustic wave. It is determined by the time an acoustic wave takes to traverse a laser beam in the material [37]. For better results, AOM optical components such as TeO_2 crystals with high figure of merit are selected because they are highly efficient when compared to other crystals such as Quartz. For example, an acoustic wave that travels through an AOM crystal with the speed of 0.62 mm/μs, it would take about 320 ns to traverse a laser beam of diameter of 200 μm. For some lasers this is much longer than the build-up time, leading to the problems of slow switching discussed in Section 3.11. Unless design measures are implemented, such as reducing the interaction area of the laser beam and the acoustic wave, multiple pulses can be expected in AOM Q-switched lasers.

3.14   Electro-optic Q-switching

3.14.1 Electro-optic Q-switch Elements

Apart from using acousto-optic modulators, active Q-switching can also be achieved with electrically controlled electro-optic modulators (EOMs), by exploiting their ability to rotate the polarisation of light. This ability is referred to as an electro-optic effect. Well-known electro-optical effects are the Pockels or Kerr effects. Both operate under the periodic influence of applied voltage (or an electric field). Unlike the quadratic (or E^2 dependent) Kerr effect that has high voltage requirements, the Pockels effect is linear (or E dependent) and requires lower voltages [1]. For this reason, only EOMs utilising the Pockels effect will be discussed henceforth.

A conventional Pockels Q-switch consists of one or two polarisers, a wave plate and a Pockels cell. A polariser is an optical filter that permits light waves with a specific

polarisation to pass through, while blocking any part of the incidental light that falls outside its axis of transmission [74]. Wave plates are birefringent optical elements (characterised by fast and slow axes) that can rotate the polarisation of light. Two types of wave plates are used in practice, the half-wave and quarter-wave plates. Wave plates are mounted such that a linearly polarised beam of light would pass through with its polarisation at 45º with respect to both axes. The beam then gets resolved into equal components that experience different indices of refraction. For a half-wave plate, its slow axis retards one component of light passing through to create a phase difference of π, which results in 90º polarisation rotation and the beam remaining linearly polarised. The quarter-wave plate creates a $\pi/2$-phase difference and a linear to circular polarisation rotation.

Pockels cells are made of crystals that lack a centre of symmetry [75] when an electric field (or simply voltage) is applied across them [50], which momentarily creates slow and fast axes, making them voltage-controllable wave plates. When voltage is applied, the associated electric field shifts the principal axes from the natural i to $(i' = x', y',$ and $z')$, thus changing their refractive indices to n_i, [76] along new principal axes. Equation (3.23) describes the new axial and electric field dependent refractive indices as:

$$n_{i'}(E) \approx n - \frac{1}{2} n_i^3 r_i E \tag{3.23}$$

where the proportionality constant r_i is a general electro-optic (Pockels) coefficient [75]. The applied electric field is a function of the high voltage of Pockels cell operations, which can either be half-wave ($\lambda/2$) or quarter-wave ($\lambda/4$) voltage. The half-wave voltage $(V_{\lambda/2})$ is usually large when compared to the quarter-wave voltage $(V_{\lambda/4})$. As a result, the quarter-wave Pockels cell configuration requires lower high voltages and is more desirable and preferred for high repetition-rate operations.

Pockels cells are carefully selected based on their material properties and ability to operate at the lower end of the high voltage requirements. The main parameters that determine the voltage required are the electro-optic (Pockels) coefficients. Both $V_{\lambda/2}$ and $V_{\lambda/4}$ are inversely

61

proportional to the crystal specific electro-optic coefficients ([1], [75]). This indicates that Pockels cells with low voltage requirements are those with large coefficients. Table 3.2 depicts the rotation of light when the half-wave and quarter-wave voltages are applied and when they are off.

Table 3.2. The effect of applying $V_{\lambda/2}$ and $V_{\lambda/4}$ on the Pockels cell when an initially linearly polarised light passes through it.
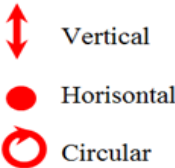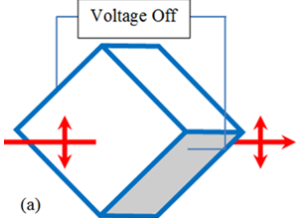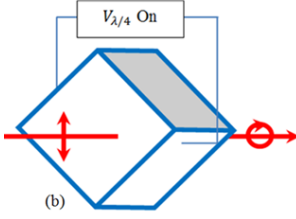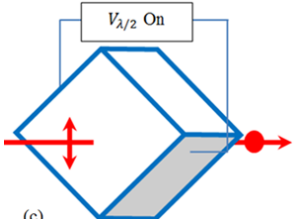
Voltage applied on the Pockels cell (V)	Retardation or phase difference (radians)	Polarisation after passing the Pockels cell	Resulting polarisation
0	non	Linear and same as the incident polarisation	
$V_{\lambda/2}$	$\dfrac{\lambda}{2} = \pi$	Linear but perpendicular to the incident beam	
$V_{\lambda/4}$	$\dfrac{\lambda}{4} = \dfrac{\pi}{2}$	Circular	

62

Table 3.3 lists the EO coefficients for a few crystals that are frequently used for Pockels cell fabrication [75]. Other important parameters that are also included are laser damage thresholds, large transparency ranges, large electric resistance, low dielectric constants, good physical and chemical properties, and ease of production [77].

Table 3.3. Basic Q-switching parameters to operate electro-optic materials [75]

Material	Quarter-wave or half-wave voltage [V]	Effective electro-optic coefficient [pm/V]	Insertion loss	Extinction ratio at $\lambda = 1.06\,\mu m$	Damage threshold [MW/cm^2], Pulse Width [ns] at $\lambda = 1.06\,\mu m$
RTP	$V_{\lambda/2} = \dfrac{\lambda d}{2n_e^3 r_{c2} L}$	$r_{c1} = 30.2$ $r_{c2} = 23.6$	< 1%	800:1	1800, 10
KTP	$V_{\lambda/2} = \dfrac{\lambda d}{2n_e^3 r_{c1}}$	$r_{c1} = 28.6$ $r_{c2} = 22.9$	< 1%	2000:1	900, 10
KDP ADP	$V_{\lambda/2} = \dfrac{\lambda}{2n_o^3 r_{63} L}$	$r_{63} = 10.6$ $r_{63} = 8.5$	4%	1000:1	600, 10
BBO	$V_{\lambda/4} = \dfrac{\lambda d}{4n_o^3 r_{22} L}$	$r_{22} = 2.2$	< 2%	>500:1	5000, 10

Other effects that need to be considered are their transmission ranges, symmetry and structure, as well as the natural indices of refraction (n_i) along the principal axes $i = x, y$ and z at specific wavelengths. Table 3.3 presents those properties of Pockels cell crystals that are useful to consider, namely, their characteristic voltages, EO coefficients, insertion losses, extinction ratios and damage thresholds. Because these properties are difficult to obtain, active research into new EO crystals is still relevant. For example, in the past, Pockels cells of choice for practical EO Q-switches were KDP crystals, because of their low half-wave voltages [1]. Since RTP crystals have larger electro-optic coefficients, they would require

63

lower voltage to achieve electro-optic Q-switching. As a result, they are the crystals of choice for Pockels cells that need to operate at high peak powers.

The Pockels cell crystals that have large EO coefficients may have a disadvantageous natural birefringence and suffer from thermal issues when exposed to high pump powers. However, by using a double-crystal scheme with crystals mounted in series and at 90º to each other (as shown in Figure 3.8), this can be compensated for, leading to an excellent thermal stability with even lower half- and quarter-wave voltages [75].
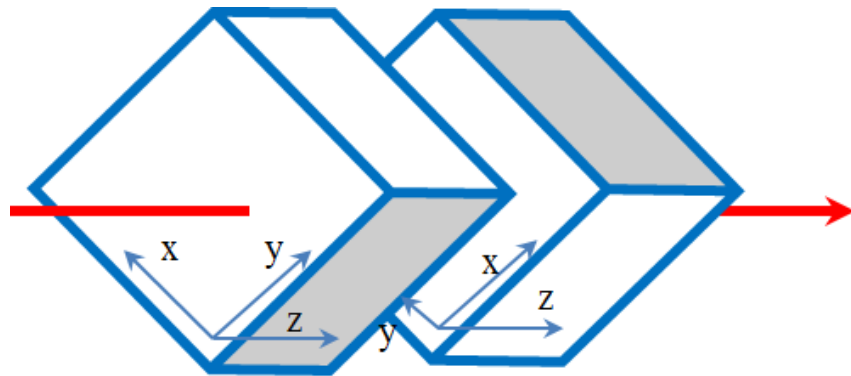
Figure 3.8. A double-crystal scheme with crystals mounted in series and at 90º that compensates for the natural birefringence and maintain thermal stability.

3.15   Pockels Cell Q-switch Operation

Figure 3.9 illustrates the combined effect of a Pockels cell, a wave plate and a polariser on a beam of light passing through it when voltage is applied and when it is not. When the voltage is off, only the wave plate rotates the beam polarisation. When a half-wave plate is used ($\lambda/2$-plate), the beam will be rotated by 90º, as in Figure 3.9 (a), and the polariser reflects the beam out of the optical path. However, when the half-wave voltage is on, both the Pockels cell and the half-wave plate rotate the beam. This causes a 180° single pass rotation, which restores the original polarisation and propagation of light along the optical path, as shown in Figure 3.9 (b).

64

In that regard, the polariser would be better placed on the left of the Pockels cell and the light beam will remain along the beam path when the voltage is on and coupled out when it is off.
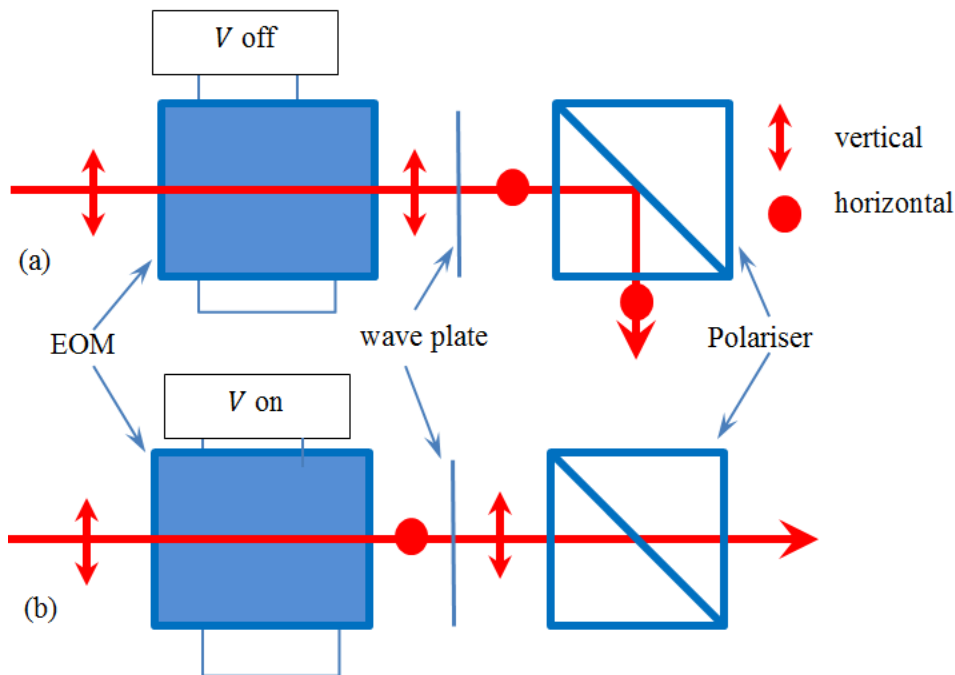
Figure 3.9. The EOM (Pockels cell) is presented as a Q-switching element. The two diagrams illustrate the interaction of laser light, which was initially linearly polarised, with the polariser, the EOM and the half-wave plate. When (a), the wave voltage is off, light is coupled out of the optical path and useless for any application. However, if (b) the wave voltage is on, light passes through the polariser and is useful for intended applications.

The voltage dependent ability of Pockels cell Q-switches to rapidly couple large percentages of laser light out of the optical path makes them highly suitable for Q-switching in laser cavities. This will be discussed in Section 3.16.

65

3.16   Pockels Cell Q-Switched Cavities

Electro-optic Q-switched laser cavities make use of Pockels cell Q-switches to realise high-loss and low-loss intervals. Figure 3.10 illustrates the interaction between the intracavity radiation with the Q-switch consisting of a polariser, Pockels cell and a λ/4-plate. First, when the λ/4-wave voltage is off, the Pockels cell does not have any effect on the beam. This leaves the λ/4-plate output-coupler combination to cause a λ/2-wave round trip phase difference, rotating the beam by 90° and resulting in a high-loss cavity state. During this time, the gain and the population inversion increase until the gain equals or exceeds the cavity losses. When a λ/4-wave voltage is then applied, the Pockels cell λ/4-plate output-coupler combination effects a full wave retardation of the beam components. This results in a low-loss state and the release of a giant pulse as the lasing conditions are restored during this shorter period.
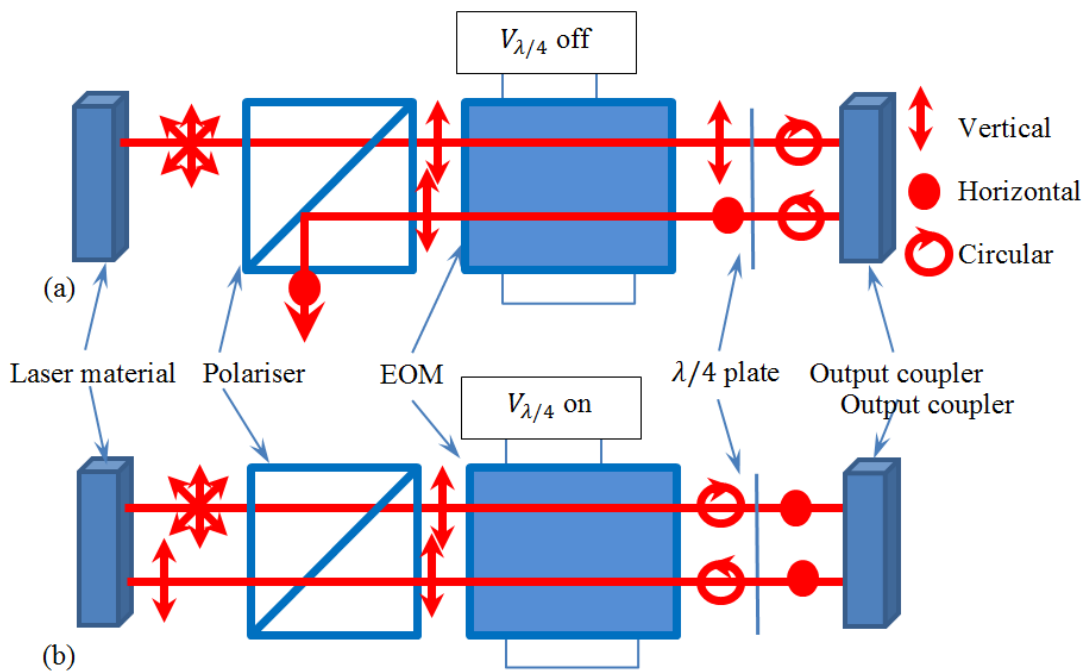
Figure 3.10. The conventional Electro-optic Q-switching cavity shows in (a), non-lasing conditions are reached when the λ/4 voltage across the Pockels cell terminals is off, and in (b) the lasing conditions are restored when the λ/4 voltage is on.

From the above discussion we can deduce that such switches always result in polarised output. It is also important to note that the complexity of a many component Pockels cell Q-switches is undesirable, because parasitic losses get introduced. In addition, most polarising elements that can handle high intracavity intensities are placed at angles that lead to naturally elongated cavities, resulting in longer pulse lengths. In Chapter 5 a solution to this problem is introduced.

3.17   Comparison between Acousto-optic and Electro-optic Modulators

Acousto-optic and electro-optic modulators are the most used active Q-switch elements. However, they differ in certain properties, which render them more favourable in some applications than in other. Jabczyǹski et al. (2007) [78] list several advantages of AOMs over electro-optic modulators (EOMs), such as much higher damage thresholds, a simpler radio

67

frequency (RF) supply, less dependence on beam quality, and higher pulse repetition frequencies (PRF). The desirable AOM Q-switch properties include low final losses, less requirement for temperature stability, high maximum PRFs (> 100 kHz), low radio frequency (RF) power supply requirements, and a high damage threshold ($> 1\,\mathrm{GW/cm^2}$). AOMs however have undesirable low contrast (>1:10) and slow switching times (>50 ns) [78].

For EOMs, desirable properties include high contrast (<1:200) and short switching times (2 to 5 ns). However, they also have undesirable properties that need to be mitigated, such as higher insertion losses, high demand for temperature stability and a lower damage threshold ($<1\,\mathrm{GW/cm^2}$) [78]. In addition, their relatively high background absorption makes them unsuitable for high average power switching.

In selecting either an AOM or an EOM to develop a Q-switched laser, desirable properties should be considered first and exploited, while undesirable ones are minimised in order to obtain the desired outputs for the intended applications. A simple example can be that of the EOMs, which offer favourable high contrast and fast switching times that can be exploited for high peak power and high repetition rate outputs. For such systems, the effects of rapidly switching high voltages and the resulting electromagnetic interference (EMI) need to be minimised. This will be shown in Section 6.2 where electric non-conducting mounting mechanics will be used. Furthermore, the photo-detector cable will also be shielded.

3.18   Summary

In this chapter, we presented the operation of a basic Q--switched laser system, focusing on gain media, pumping required as well as Q-switching background and popularly used active techniques. In discussing these laser system components, we considered properties that favour the high PRF generation of short pulsed laser outputs, characterised by high peak powers.

End-pumping with fibre-coupled laser diodes was discussed as most suitable to generate the desired high-gain media for high PRF Q-switched laser operations. This is because with proper choice of pump-focusing optics, the diode radiation can be easily made to match the

68

fundamental (TEM$_{00}$) resonator mode diameter, which allows the maximum energy from the laser diodes to be useful for absorption or active ion excitation. End-pumped solid-state lasers operate naturally and without intracavity apertures in the fundamental spatial mode.

The nature and properties of gain media that contribute to high gain were discussed. In doing so, we highlighted that gain media with larger values of the product $\sigma_{em}\tau_f$, not only provide high gain, but lower threshold values. Following this, a theoretical description of Q-switching and how it functions in the resonator to create large output pulses was presented. To achieve short pulsed laser outputs, we discussed contributing factors such as cavity lengths and photon lifetimes. We highlighted that the switching speed of the Q-switch elements is the important parameter that may affect the output.

The AOM and EOM based techniques were presented in this chapter as the two most used to realise active Q-switching and generate the desired results. These techniques were also described theoretically, highlighting factors that contribute to their performance. In comparing them, AOMs have been used successfully in industry but suffer from slow switching, thus severely limiting their ability to generate the desired outputs. The EOMs, however, have been found to offer an alternative because they switch faster. Having discussed the basic and Q-switched laser systems in this chapter, Chapter 4 looks at the general (common) Q-switched laser design that can be used to generate short pulsed and high peak power laser outputs at high repetition rates.

Chapter 4

4. Q-Switched Lasers Design

4.1   Introduction

Nanosecond pulsed laser outputs are characteristic of Q-switched lasers that are carefully designed by selecting components and procedures that contribute to the desired results. Chapter 2 introduced general laser operations in the CW and the Q-switched modes. This study seeks to develop a Q-switched laser that can generate nanosecond pulsed, high peak power laser output at high repetition rates. Chapter 2 discusses several research accounts where pulsed lasers were developed, including Q-switching and different levels of achievements that were reached. Two techniques stand out in all these attempts: the acousto- and electro-optic modulator-based Q-switching, with cavities that share a common architecture (component selection and cavity design), but that differ in respect of the kinds of shutters they employ. To achieve this, we investigated the Q-switch behaviour of both techniques with common design features (pump sources, gain media, and cavity length). While the two techniques differ with respect to the shutters used, the purpose is to generate nanosecond pulses. As a result, the general shutter used in this chapter's discussion must satisfy the output conditions. Chapter 4 therefore discusses the choices of shared (common) components such as pump, gain medium, and output coupling together with their properties, as well as cavity design and processes.

4.2   Common Q-switched Laser System

Figure 4.1 presents a general Q-switched laser system. Although similar to Figure 3.1 in Chapter 3, here the laser material was chosen to be $Nd:YVO_4$, the cavity configuration chosen

to be flat-flat, and the pump source to be laser diode end-pumping. The respective coating induced high reflection (HR) and partial reflection (PR) of laser by the back reflector and the output-coupler (OC) is responsible for the intracavity oscillation of the laser. The PR coating of the OC also transmits part of the laser light as laser output. Since the OC is only coated for laser light, we can deduce that it is insensitive to the pump light reflection, which is a benefit in heat management. Furthermore, the high transmission coating of the back reflector for the pump light exposes the gain medium to it and is responsible for the gain in the cavity.
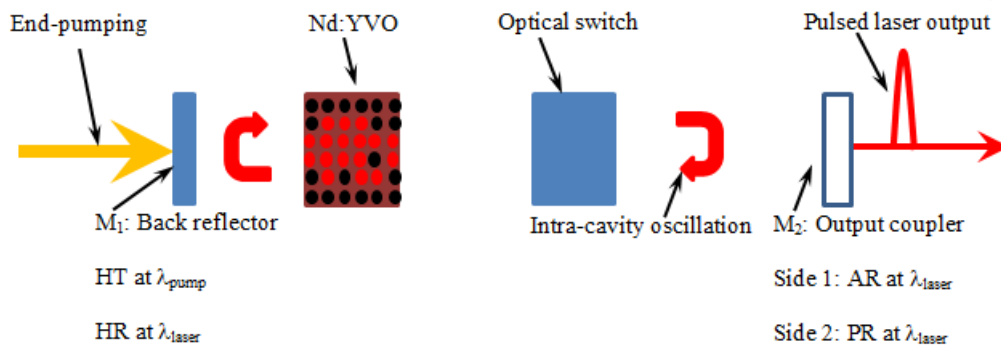
Figure 4.1. This is a common Q-switched laser system that shows end-pumping, as well as a Q-switched cavity. The back reflector was coated for high reflectivity (HR) of laser light and high transmission (HT) of pump light to transmit it into the gain medium. The output coupler (OC) was coated for anti-reflection of the pump light and partial reflection (PR) of the laser light.

The Q-switch element is selected for its ability to sufficiently hold off lasing during the low-loss period, to maintain a high switching speed, and to generate short-pulsed high peak power laser output. General properties that are common to different Q-switch elements will be discussed in a later section.

4.3   Nd:YVO$_4$ Properties

The choice of the gain medium is influenced by the desired output, which includes the wavelength, specific short pulsed, high peak power laser operated at high PRFs. Here Nd:YVO$_4$ was mostly chosen due to its high gain and strong absorption at diode wavelengths

71

of around 808 nm and its naturally polarised output. Nd:YVO$_4$ crystal is a uniaxial crystal with π polarised laser emission along the crystal c-axis. The oxide host crystal (YVO$_4$), has a zircon structure with a tetragonal space group [79].

4.3.1   Nd^{3+}:YVO$_4$ Energy Level System

The Nd^{3+} ions are characterised by weak crystal fields and sharp radiative and fluorescent transitions, and as a result they serve as dopants to hosts such as YAG, YLF, or YVO$_4$ crystals. In YVO$_4$, Nd:YVO$_4$ has been shown to surpass or is comparable to other Nd^{3+} hosting crystals in providing favourable properties such as large absorption and stimulated emission cross-sections, as well as natural birefringence [1]. As a result, Nd:YVO$_4$ crystals have relatively higher gain and emit polarised laser output. For a 1 at. %-doped Nd:YVO$_4$ for instance, both absorption and stimulated emission cross-sections at room temperature are more than double those of 1 at. %-doped Nd:YAG (see Table 3.1). Short crystals can therefore be used to extract significant gain, which is required for short pulsed Q-switched lasers. However, a drawback of the high absorption coefficient is a large temperature gradient and a resultant high thermal stress produced at the pump end of the crystal [80]. It is also important to consider Nd^{3+} dopant concentration to limit the absorption in order to avoid the strong thermal gradients and pump power dependent crystal fracture. Furthermore, Nd:YVO$_4$ is characterised by a much shorter upper laser lifetime compared to Nd:YAG, which then limits its energy storage [6] for low repetition rate, high energy applications.

Figure 4.2 shows the Nd:YVO$_4$ energy level system and incorporates Q-switch processes that take place, for example the high-loss (low-Q, closed) and the low-loss (high-Q, open) periods. The vertical dotted line (grey) is placed to differentiate the pumping and pulse output periods in a Q-switch laser. During the pumping interval the system is in a high-loss state during which the population inversion increases and energy is stored in the upper laser-level lifetime. The process is shown graphically in Chapter 3 and it starts with the transition $\left({}^4I_{9/2} \rightarrow {}^4F_{5/2} \right)$ of the ion population (left of the dotted), which occurs as a result of pumping radiation. The population inversion is caused by absorption of 808 nm light that

72

excites active ions from ground state $^4I_{9/2}$ to the $^4F_{5/2}$ pump energy level. This is followed by a rapid non-radiative transition $^4H_{9/2} \rightarrow \; ^4F_{3/2}$ from the pump energy level to the upper laser level $^4F_{3/2}$. This creates a population inversion between the $^4F_{3/2}$ and various lower laser levels. Due to high losses that are introduced at this stage, the population inversion accumulates in the upper laser level $^4F_{3/2}$ as gain increases, while no stimulated emission or laser action is taking place [50]. During this period, energy is stored in the upper laser level.
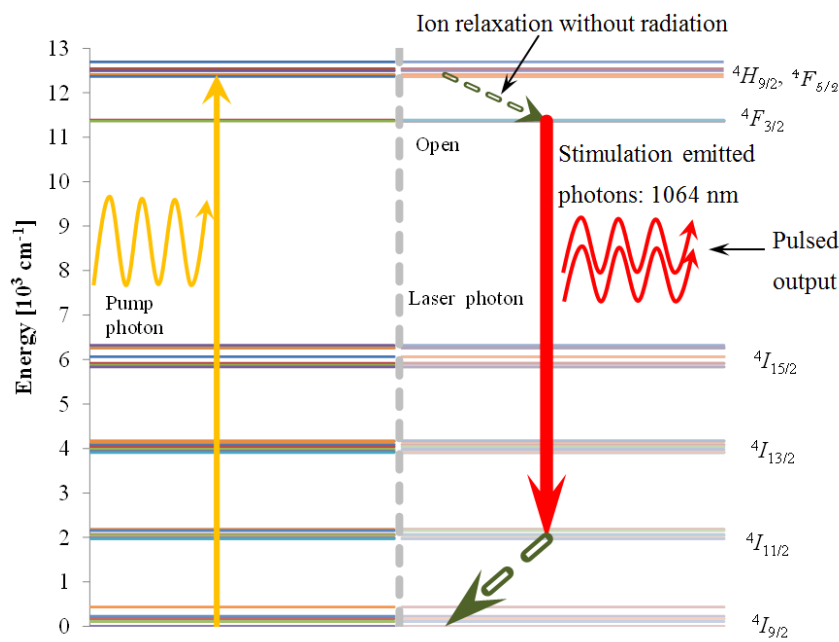
Figure 4.2. This is an Nd^{3+} energy level system showing the pumping/absorption process, non-radiative decays and lasing transitions at the 1064 nm wavelength [81].

When the losses are removed, laser action thereafter begins when the initial spontaneous-emission noise (few photons) stimulates ions in the upper laser level to relax to the lower laser level. This causes the emission of photons in the laser wavelength and in the process excites a cavity mode, as indicated to the right of the dotted line in Figure 4.2. The photon population suddenly builds up in the cavity, leading to the emission of a giant pulse [50]. Depending on the lasing wavelength of interest, Nd^{3+} can lase through different transitions by stimulating emission at different wavelengths. These lasing transitions include $^4F_{3/2} \rightarrow \; ^4I_{9/2}$, lasing at

73

914 nm (a quasi-three level laser transition), $^4F_{3/2} \to {}^4I_{11/2}$ lasing at 1064 nm, and $^4F_{3/2} \to {}^4I_{13/2}$ lasing at ~1342 nm. The last two are both high gain four-level laser transitions that are completed by the non-radiative decays $^4I_{11/2} \to {}^4I_{9/2}$, and $^4I_{13/2} \to {}^4I_{9/2}$ respectively.

Active ions spend much shorter times at the pump $\left({}^4F_{5/2}, \, {}^4H_{9/2} \right)$ and at the lower laser $\left({}^4I_{11/2} \right)$ levels than at the upper laser $\left({}^4F_{3/2} \right)$ level, before their respective rapid transitions to the upper laser level and the ground state. The energy differences between the pump level and the upper laser level, as well as between the lower laser level and the ground state, equal the same order of magnitude of phonon energy in the crystal lattice. In other words, energy released by the ions in transitions between these energy states is in the form of a phonon transferred to the crystal lattice.

4.3.2 Spectral properties of Nd:YVO$_4$ crystals: Absorption and emission spectra

The most important spectral properties that characterise laser gain materials are the absorption σ_{abs} and emission σ_{Em} cross-sections at different wavelengths (spectra) [1]. These properties are used to select and predict a material's performance in operational conditions and to select the absorption (pumping) and the lasing (emission) wavelengths.

The absorption and emission spectra indicate the transitions for Nd:YVO$_4$ crystals discussed in Section 4.3.1 and depicted in the energy-level diagram in Figure 4.2. These transitions are made possible by their strong absorption and emission lines at the said wavelengths. Figure 4.3 (a) and (b) show the relevant absorption and emission peaks of Nd:YVO$_4$ for pumping at wavelengths around 808 nm and lasing at a wavelength of 1064 nm ([69], [74] [95], [104]). The more prominent emission cross-section π-peaks of the two spectra indicate that Nd:YVO$_4$ crystals naturally emit a linearly polarised light along one axis, the c-axis, unless it is suppressed. Furthermore, Nd:YVO$_4$ absorbs π- polarised light at ~808 nm. Several Nd^{3+}

74

doped laser materials optimally absorb pump light (as a result they are pumped) at ~808 nm and lase at 1064 nm.
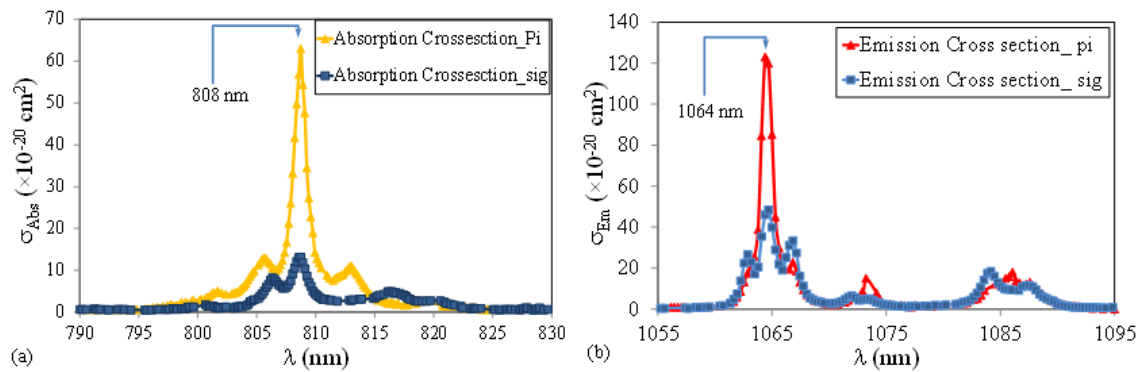
Figure 4.3. (a) Nd:YVO$_4$ Absorption Spectra showing transitions ^{4}I$_{9/2} \rightarrow$ ^{4}F$_{5/2}$ and ^{4}I$_{9/2} \rightarrow$ ^{4}F$_{3/2}$ at peaks 808 nm and 880 nm, which indicate the strong absorption lines of Nd:YVO$_4$ corresponding to excitation radiation of laser diodes. (b). Nd:YVO$_4$ Emission Spectrum for the ^{4}F$_{3/2} \rightarrow$ ^{4}I$_{11/2}$ 1064 nm transition [68].

However, they differ significantly in all other properties. Table 4.1 presents a summary of the comparison between the spectral properties of Nd:YVO$_4$ and Nd:YAG that influence the absorption (pumping) and the lasing processes. For example, Nd:YVO$_4$ has significantly higher absorption and emission cross-sections than Nd:YAG, making it an excellent material for high gain, short crystal/cavity lasers. The short crystal lengths are because the absorption cross-section of a laser material is given by the ratio of the absorption coefficient α to the number of active ions per unit volume, $\sigma_{abs} = \alpha/N$ [68]. From Equation (3.1), it follows that large absorption cross-sections lead to short absorption lengths. As a result, Nd:YVO$_4$ crystals, which have large absorption coefficients, have short absorption lengths at 808 nm and therefore shorter crystals suitable for miniature cavities can be used. While they have shorter fluorescence lifetimes, its product when multiplied with the high emission cross-section of Nd:YVO$_4$ crystals still remains high, resulting in high gain (Equation (3.2)), which in turn results in shorter pulsed laser outputs.

75

Table 4.1 shows that Nd:YVO$_4$ crystals can be pumped at 808 and 880 nm wavelengths, both of which have significant advantages. At 808 nm wavelength, end-pumping is favourable because of the highly efficient laser diodes available for four-level laser operation. This has been shown to have an advantage over the conventional three-level laser operation which requires hard pumping to maintain population inversion [1].

Table 4.1. The Nd:YVO$_4$ and Nd:YAG laser crystal spectral properties.

Optical Properties	Nd:YVO$_4$	Nd:YAG	References
Pump wavelength (nm)	808, 880	807.5	[68]
Lasing wavelength (nm)	1064, 1342, 914		[82]
Absorption coefficient (% cm^{-1}) at 808 nm [68].	60(π) 12(σ)	7.9	[68]
Emission cross-section ($\times 10^{-20}$ cm^2) at 1064 nm [68].	123(π) 52(σ)	29	
Intrinsic loss ($\times$cm^{-1}) at 1064 nm	0.02	0.003	[82]
Fluorescent lifetime (μs)	97	250	[68]

The 880 nm pumping creates an opportunity for direct pumping into the upper-laser level, thus by-passing the pump to upper laser-level transition that inflicts thermal problems on the laser operation [68]. The table also shows that Nd:YVO$_4$ is characterised by large absorption coefficients and emission cross-sections, as well as a short fluorescence lifetime. These are the favourable characteristics for a high repetition rate laser operation that generates outputs with short pulse widths and high peak powers [83].

4.4   Optical and Physical Properties of Nd:YVO$_4$ Crystals

Table 4.2 presents Nd:YVO$_4$ optical polarisation properties. Nd:YVO$_4$ is not only birefringent, but uniaxial, meaning that at 1064 nm two of its three perpendicular axes share the same index of refraction (n_o), while the third axis has a different index of refraction (n_e). In addition, $n_e > n_o$, which indicates that the crystal is dense along its c-axis as compared to

76

its a-axis, as indicated by the shorter interatomic distances [53]. Since the crystal's thermal conductivity (k_{th}) is inversely proportional to the inter-ionic distances, it can be deduced that the material plains with shorter inter-ionic distances are more heat conductive, that is, they can transfer heat or heat can be extracted from them more efficiently. Faster heat flow, or simply larger thermal conductivity, can occur through the crystal face with this more densely packed c-axis. Nd:YVO$_4$ also emits linearly polarised light with an electric field parallel to the c-axes.

Table 4.2. Nd:YVO$_4$ optical properties.

Nd:YVO$_4$ Crystal Properties	Along a-axis	Along c-axis	Ref.
Light Polarisation	E $\parallel$ a-axis: σ	E $\parallel$ c-axis: π	[84], [1]
Index of refraction, n at 1064 nm	$n_o = 1.958$	$n_e = 2.167$	[85]
Inter-ionic distances [nm]	0.71192	0.62898	[84]

4.4.1 Mechanical Properties of Nd:YVO$_4$ Crystals

Mechanical properties of laser materials (such as tensile strength, hardness and fracture strength) are a useful criterion in selecting a crystal suitable for a laser ion host. They are important in laser design because they determine the maximum thermally induced strain that the crystal can handle in operational conditions, and if the crystal can operate in high average power operation. In addition, the hardness must be high enough to resist breakage during normal fabrication processes [1]. Table 4.3 gives the mechanical properties of Nd:YVO$_4$ in comparison to Nd:YAG crystals. An Nd:YAG crystal is therefore still a popular gain material for applications where very high amounts of pump power (and therefore heat) is required. It is a hard, dense, and isotropic crystal with high tensile strength and elasticity that can be grown to possess high optical quality [1].

77

Table 4.3. The mechanical properties of Nd:YVO$_4$ in comparison to those of Nd:YAG.

Crystal Properties	Nd:YVO$_4$	Nd:YAG	References
Hardness [Mohs]	4.5	8.5	[6]
Density [g/cm3]	4.22	4.55	
Tensile Strength [MPa]	53	200	[1]
Modulus of elasticity (GPa)	133	310	

The Nd:YVO$_4$ crystals were initially difficult to grow, and as Table 4.3 shows, they are softer, less dense, have a lower tensile strength and lower elasticity, resulting in them being discarded by researchers. However, their large stimulated emission cross-section and high absorption of the pump wavelength have made it an important crystal. Its growth problems have also been solved by the use of small crystals in diode pumping [1]. In laser design these factors must be considered. That means that when using small Nd:YVO$_4$ crystals effective cooling must be provided and the crystal must be mounted in such a way that it is free to expand under high temperature conditions.

4.4.2   Thermal Properties of Nd:YVO$_4$ Crystals

During the pumping process, pump light deposits energy into the gain media to excite ground-state active ions into higher energy levels, as discussed in the earlier chapters. Part of that energy does not get converted into laser light, instead it generates heat inside the laser material. This happens due to quantum defect (the energy difference between the pump and the laser photon energies of optically pumped lasers), the pump absorption into energy levels other than the pump level, up-conversion processes [86], and the non-radiation energy released during the pump to upper laser level transition. To avoid the resulting thermal problems that give rise to negative thermal lensing and thermal birefringence, which limit the power scaling of solid-state lasers, effective heat-removing techniques from laser materials should be implemented [87].

78

Table 4.4 lists a few thermal properties of Nd:YVO$_4$ in comparison to Nd:YAG. An important property to consider when designing high power bulk lasers is the gain material's thermal conductivity (k$_{th}$), because it determines how efficient the gain medium is at dissipating heat [88]. For instance, gain media with high thermal conductivities can dissipate heat or be cooled easily.

Table 4.4. The thermal properties of Nd:YVO$_4$ in comparison to those of Nd:YAG

Thermal Properties	Nd:YVO$_4$	Nd:YAG
Melting point [ºC]	1825, [52], [1]	1970, [52], [1]
Thermal conductivity [W.m^{-1}.K^{-1}]	8.9: (a-axis) 12.1: (c-axis), [87]	10.1, [87]
Thermal Expansion coefficient [$\times 10^{-6}$ K^{-1}] at 298 K	$\alpha_a = 1.69$ [89] $\alpha_c = 8.19$	6.4 [90]
Thermo-optic Coefficient [$\times 10^{-6}$ K^{-1}]	$\frac{dn_o}{dT}$ =8.5 (σ: a-axis) [91] $\frac{dn_e}{dT}$ =2.9 (π: c-axis)	8.4 [90]
$f_{therm} \propto 1/\frac{dn_o}{dT}$ (σ: a-axis)	Stronger: (shorter f_{therm})	
$f_{therm} \propto 1/\frac{dn_e}{dT}$: ($\pi$: c-axis)	Weaker: (longer f_{therm})	
Thermal fracture limit [MPa)]	53 [46]	138 [44], 120 to 240 [92]

The thermal conductivity of a particular laser material is inversely proportional to the inter-ionic distances, which means that shorter distances indicate higher heat conductivity of the

79

material, resulting in more efficient heat transfer. For Nd:YVO$_4$ crystals the thermal conductivity is larger (and the inter-ionic distances are shorter) along the c-direction than the a-direction. This makes the crystal faces that include the c-axis the better choice to cool the crystal, since they will provide a more efficient heat extraction [84]. Notably also, the uniaxial Nd:YVO$_4$ crystals have larger and different thermo-optic coefficients along their c-and a-axes, and as a result strong thermal lens effects are always experienced under laser operations, especially along the a-axis. The thermal fracture limit of a gain material is of particular importance, as was discussed in the previous section. It is also inversely proportional to the absorption length, which implies that it can be managed by varying the doping and/or the pump wavelength.

The thermal lens of the gain medium is a major contributor to the quality and the power of the laser output. In end-pumped lasers, pump light is focused into the small area of the crystal face, thus generating intense localised heat that induces a refractive index gradient, which causes a thermal lens due to the parabolic phase profile [1].

The strength of a thermal lens ($1/f_{therm}$) is proportional to the temperature dependence of the refractive index (dn/dT) and the absorbed pump power P_{Abs}, while being inversely proportional to the thermal conductivity and the pump area [93] as shown in Equation (4.1).

$$\frac{1}{f_{therm}} \propto P_{Abs} \frac{dn/dT}{k_{th}} \frac{1}{\omega_{Ps}^2} \tag{4.1}$$

Since (dn/dT) is different along the a and c-axes, the focal length of the thermal lens f_{th} is also different for different polarisations. The thermo-optic coefficient (dn_o/dT) of the crystal along the a-axis is about twice that of the c-axis (dn_e/dT) [4]. As a result, the thermal lens strength in the a-axis is also roughly half that of the c-axis, since it is largely dependent on the thermo-optic coefficient of the axes' gain medium [3]. The thermal lens could also contain significant spherical aberrations that reduce the beam quality and fundamental mode output power.

80

One way to manage the thermal effects is to choose more thermal-optimal crystal geometries such as slab and thin disks that provide large cooling surfaces, thus limiting thermally induced strain and aberration, instead of cylindrical rods.

4.5   The Common Nd:YVO$_4$ Crystal used in this Study

The choice of a gain medium depends on the required outputs as well as operational conditions. For example, to meet the requirements of laser output this system seeks to produce, as stipulated in Chapter 3, would require a laser material that is characterised by high gain (to support the high peak power requirements), short upper laser life times (to support the high pulse repetition rates), and short pulse emission. In addition, some laser pulsing techniques require a polarised laser light; as a result, a uniaxial high gain laser material is the medium of choice. As shown in Table 4.1, Nd:YVO$_4$ fits all these requirements because of its high absorption, large emission cross-sections and short fluorescence life times. While this crystal is also uniaxial, it is limited to low power operations by its low thermal fracture limit, as shown in Table 4.4.

The selection of a Nd:YVO$_4$ crystal as the gain medium for the experiments that follow in this research was done to exploit the benefits it provides while preventing the problems that come with its limitations. The crystal was a-cut and mounted to exploit its large absorption and emission cross-sections along the c-axis, along which it was made to emit. As a result, in all experiments in this study an a-cut, 1% doped and 2 mm thick Nd:YVO$_4$ crystal with transverse dimensions of 3 mm × 3 mm was used (Figure 4.4 (a) to (c)). The 1% at. doping and 2 mm length were chosen from a selection of other Nd:YVO$_4$ crystals that were available, with thicknesses ranging from 1 to 3 mm and doping from 1% to 2% at. These choices were made to reduce the chances of thermal fracture and to allow enough pump absorption in the crystal. The 2 mm length of the crystal was chosen to cater for the need to achieve high absorption (which requires a long crystal) during the pumping process, while remaining small enough to satisfy the small crystal requirement for diode pumping. This is also important because the crystal is long enough to absorb the pump light and dissipate the heat that

81

develops, while remaining short enough to allow a pump beam of poor quality, short Rayleigh range and higher divergence than that of the laser to match its mode within a short active region [1].

To achieve high laser performance, the Nd:YVO$_4$ crystal was received from Crystech Inc., China, and selected for its input face (S1) coating of 808 nm pump light high transmission (HT) and 1064 nm laser light high reflection (HR) [82]. This made it possible to use S1 as one of the end mirrors of the laser cavity while the other face (S2: output face) of the crystal was coated to be anti-reflective (AR) to 1064 nm laser light, as shown in Figure 5.4. This selected the main 1064 nm lasing wavelength.

Figure 4.4 (d) shows that the crystal input face was mounted against a 3 mm thick copper plate (high heat conductivity), using a Scotch-weld structural adhesive primer (EC-3801) as an interface between them in order to cool S1. The copper plate was thick enough to accommodate channels for water circulation. Through this water-cooled copper plate, a pin-hole of 0.5 mm in diameter was drilled through which the crystal was end-pumped.
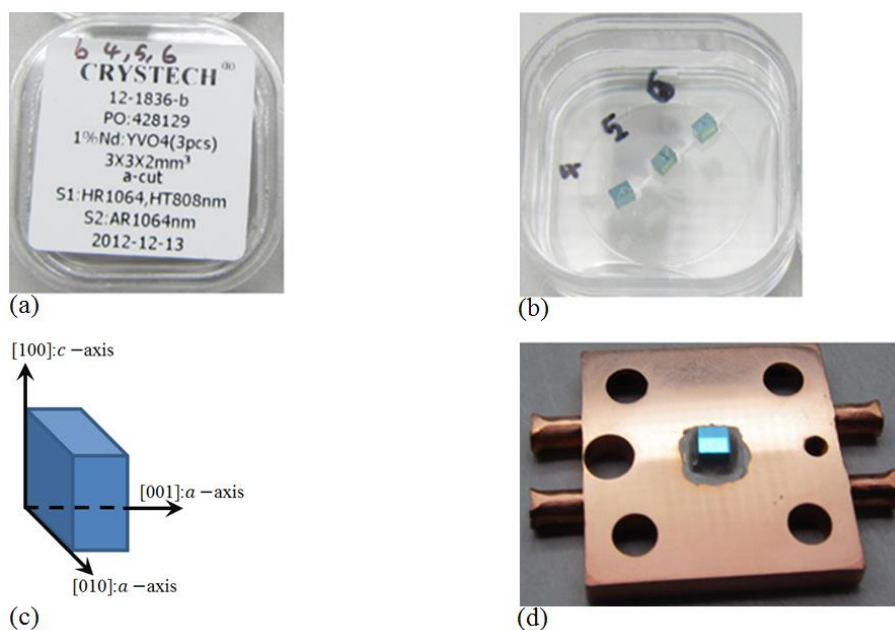
Figure 4.4. The specifications of the gain medium and its mounting format are presented here. (a) Crystal casing showing the manufacturer and labelling [82]. (b) The actual crystal batch from which the crystal was chosen. (c) The schematic diagram of a gain medium indicating its crystal axes as well as orientation. (d) The copper mount that is designed for water cooling and has a 0.5 mm hole drilled at the back through which to end-pump the crystal.

4.6 Common pump and relay system

4.6.1 Fibre-Coupled Laser Diode

End-pumping with laser diodes is a trusted technique in achieving pump light symmetry for solid-state lasers such as those based on Nd: vanadates (Nd:YVO$_4$, Nd:GdVO$_4$, etc.) operating in CW or Q-switched states at high repetition rates of tens to hundreds of kHz ([66], [94]). This is because it offers high coupling efficiency and high pump-laser mode matching in a short laser active distance [1]. Typically, laser diode end-pumping can be achieved with radiation from a stack of diode bars [1], but passive fibre coupling provides laser diodes with

83

advantages such as emitting a symmetric and randomly polarised pump light with uniform intensity distribution (into a rough top-hat shape). The rough flat-top profile of the emitted pump beam is known to reduce thermal aberrations in materials that have strong thermal lens effects [66]). Furthermore, the fibre apertures emit pump light that can be easily collimated and subsequently refocused with a lens system into different radii. The fibre-coupled laser diode system was also chosen for (end-) pumping the laser system because it provides the capacity to separately maintain and replace the pump source (or its components) when necessary. This can be done without disturbing the laser alignment and other components. These advantages make the fibre-coupled laser diode the best choice for use as a pump source, thus giving rise to highly efficient good quality laser system outputs.

The fibre-coupled laser diode, that was developed and used as a pump source in this research, was bought from Focuslight Technologies in China, with the unit number FL-FCSE01-7-808. It was made of a diode head with a passive fibre attached to it. In mounting this pump system, the diode head was placed on a water-cooling system. This laser diode was specified to operate at temperatures of 20 to 30 °C, with a wavelength temperature coefficient of 0.28. It was also specified to emit a maximum of 7 W of pump radiation at the centre wavelength of 808 nm from the 200/220 µm core/cladding diameter of the fibre aperture with numerical apertures (NA) of 0.22 and a power conversion efficiency of 43% [95].

Figure 4.5 shows a schematic diagram on the left and a photo of the actual lab-constructed laser diode on the right, mounted on a customised water-cooling heat sink designed in-house. This laser diode emitted 7 W of pump radiation at 808 nm from a 100 µm radius fibre aperture with numerical apertures (NA) of 0.22.

The cooling system components were mounted to fulfil the following functions:

1. The Ostech laser-diode and temperature controller (power supply)
2. A 7 W fibre-coupled laser diode emitting a randomly polarised continuous wave at 808 nm, used as a pump source
3. Thermocouple

84

4. Graphite foil

5. Top copper plate

6. Peltier

7. The negative (black) and positive (red) power cables

8. Water in- and out-lets connecting the water pipes to the copper block

9. Bottom copper block with water-cooling channels

10. Polymer block for thermal insulation
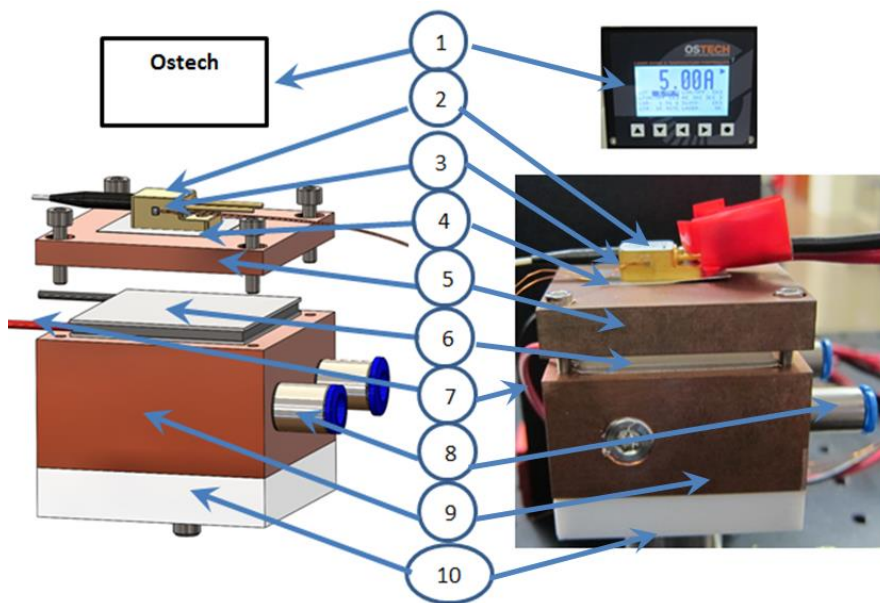
Figure 4.5. The assembly of the pump system, which includes the laser diode mounted on the copper plate that, together with a bigger copper block, sandwiches the Peltier cooler. This block has a water channel to allow cold water to flow through it to extract heat out of the system.

In addition to the fibre-coupled laser diode that is required to provide high pump coupling efficiency, the pump relay system (the collimating and the focusing lenses) was designed into a one-to-one image system using the Paraxia software and mounted to direct and focus the pump beam at the geometric image plane of the fibre aperture. This image (100 µm radius spot size) can be matched to coincide with the dimensions of the TEM_{00} fundamental laser

85

mode, which is the benefit of the end-pumping configuration of allowing maximum use of the pump light from the laser diodes [1].

4.6.2 Fibre-Coupled Diode Laser output

To design the one-to-one pump relay system, the divergence of the pump beam was determined with the help of the numerical aperture (NA) of the delivery fibre. The NA is defined as the measure of light that can be collected by an optical fibre and is related to the acceptance angle θ (outside the fibre). This angle corresponds to the critical angle $θ_c$ (inside the fibre) and describes the size of light cones the fibre can accept (or emit). Equation (4.2) describes this for small angles [49].

$$NA \approx n\sin θ \approx \tan θ \approx θ_{Div} \tag{4.2}$$

n is the index of refraction of the material (air) outside the fibre and $\tan θ \approx θ_{Div}$ is the approximated half divergence angle.

Figure 4.6 shows the measured beam divergence as it emerges from passive fibre. A knife edge was used at set intervals from the fibre tip. The fibre-coupled laser diode emitted a rapidly diverging beam. An insert of the laser beam profile is included to show the nature of the laser beam as it emerged from the fibre. From this measurement it was determined that the beam had a divergence of 85 mrad from an initial waist of 100 μm at the fibre tip.
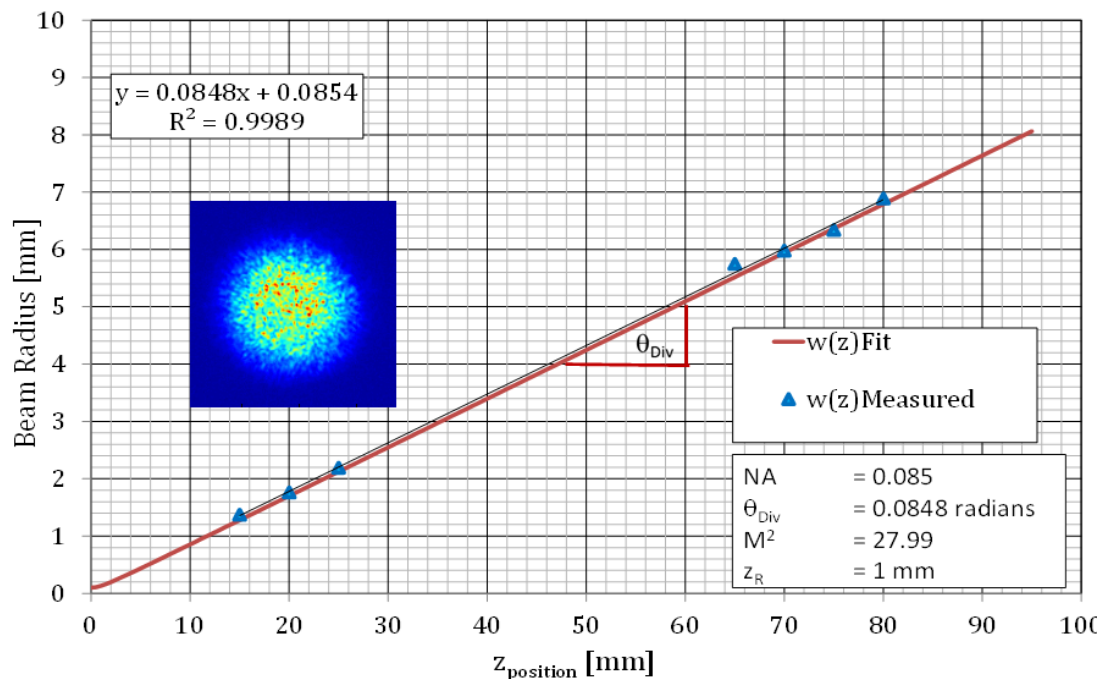
Figure 4.6. The beam emitted by fibre coupling is characterised using the knife edge method to determine the divergence and M^2 value of the pump beam.

From this it was determined that the fibre had a NA of approximately 0.085, which was much lower than what had been specified by the supplier (0.22).

4.6.3 Designing a Pump Relay System

The pump beam emitted by the fibre aperture diverged and a two lens ($f_1 = f_2 = 40$ mm) one-to-one image system was used to relay it to the crystal (the Nd:YVO$_4$ laser material). Figure 4.7 shows the designed pump relay system using an in-house, custom-written ABCD matrix EXAG program [96]. The first lens (L1) was positioned 40 mm (its focal length) away from the fibre aperture to collimate the beam where its size was approximately 3.4 mm, while the second lens (L2) focused and imaged the beam to the same size and intensity distribution when it was emitted by the fibre.

87
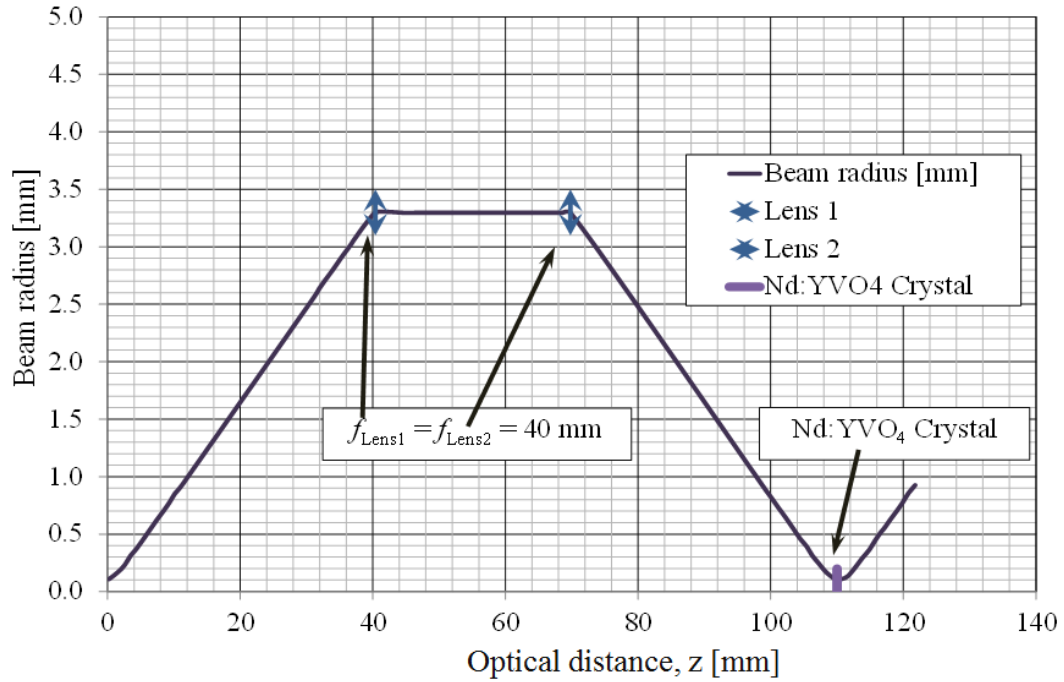
Figure 4.7. A one to one beam imaging or relay system consisting two lenses of equal focal length. The first lens collimates the diverging beam, and the second lens focuses it to a radius of 100 μm.

4.6.4 Pump Beam Waist Positioning and M^2 Measurements

The pump beam was measured by a CCD camera around the waist position where the crystal was to be placed. The results are illustrated in Figure 4.8. By fitting the Gaussian beam propagation equation (Equation (4.3) [68]) onto the data, we were able to obtain the M^2 of 32.0. The beam waist size ω_0 was measured to be 0.09 mm and the beam had a resulting Rayleigh range of 1.1 mm.

$$\omega(z) = \omega_0 \sqrt{1 + \left(\frac{M^2 \lambda (z - z_0)}{\pi \omega_0^2}\right)} \tag{4.3}$$

$\omega(z)$ is the beam size during its propagation.

88

The position of the beam waist is where the crystal was to be placed, so it was located using a pin-hole experiment. To do this the copper mount, without the crystal attached to it, was moved along the optical path while allowing pump light to pass through the pin-hole that clips it along its path. During this process, the clipping was measured as a function of position. The amount of transmitted pump power is illustrated as purple diamonds (right axis) in Figure 4.8. It shows that the waist position of the pump beam corresponds to the maximum pump power that goes through the copper mount pin hole. This ensured that no pump power was lost due to clipping when the assembly was placed between 32.4 and 34 mm from the back end of the lens mount of L2. The beam profile at the focus (insert in Figure 4.8) was roughly flat top, as highlighted in red, due to the imaging of the fibre-coupling output.
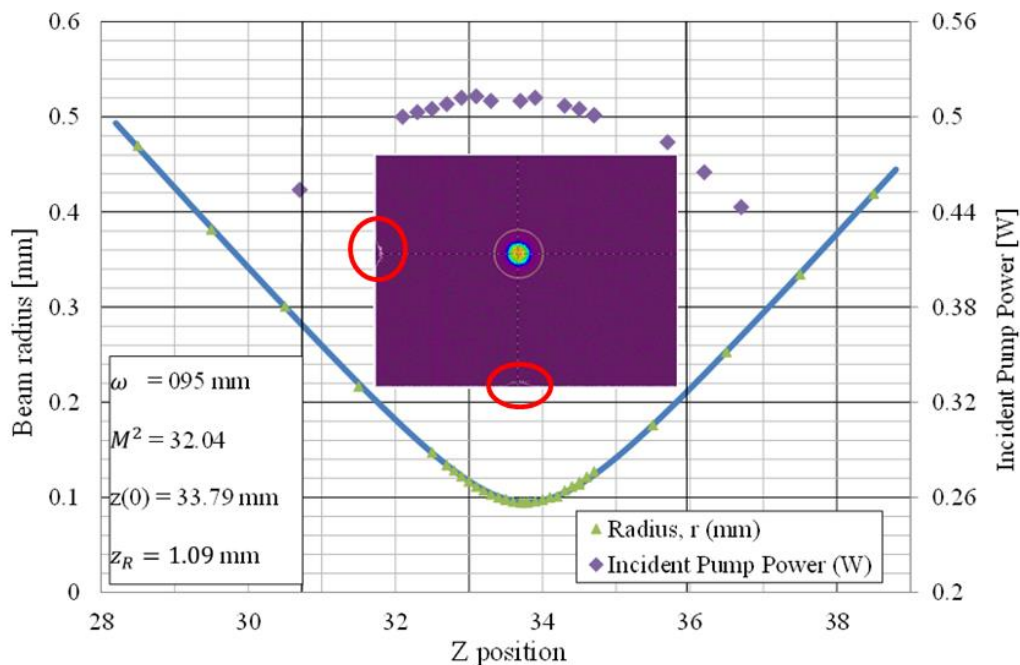
Figure 4.8. Measuring the M^2 value and the power of the pump beam as it passes through a pin hole was done to determine its waist position.

Figure 4.9 is a schematic diagram and photo that shows the fibre-coupling experimental setup incorporated with pump relay optics as well as a mounted $Nd:YVO_4$ crystal. The picture shows the fibre aperture, the lens image system and the gain medium during the construction

89

of the CW laser cavity. The diagram shows an 808 nm pump beam passing through the crystal into the cavity, some of which is absorbed (see absorption spectrum in Figure 4.3) and is responsible for the gain and population inversion of the gain medium, while the other is transmitted and lost.

Fibre Aperture   Lenses L1, L2 NdYVO₄ Crystal
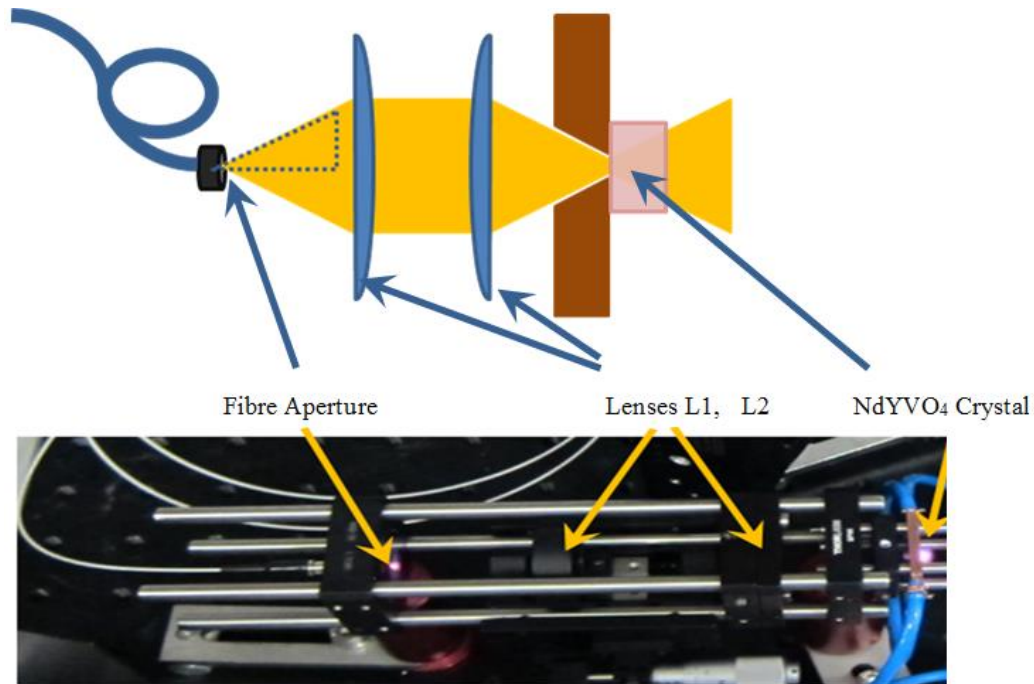
Figure 4.9. The pump optics for this laser were designed in a one-to-one imaging setup to match the beam size emitted by the fibre onto the gain medium.

4.6.5   Pump Power Measurements

Figure 4.10 presents the output power measurements of the pump beam, after pump optics, to determine how much of it was available to pump the laser crystal (with respect to input diode current). The diode threshold was at a current of ~1 A and the crystal incident pump power thereafter increased linearly to 4.8 W at a current of 5.5 A.

The pump wavelength was simultaneously measured by an Ocean Optics 2.2 Spectrometer. The diode was specified for the centre wavelength of (808 ± 3) nm, the maximum output

90

power of 7 W, the spectral width (full width at half maximum: FWHM) of $\leq$ 3 nm, wavelength temperature coefficient of ~0.28, operating currents of $\leq$ 8.5 A, and operating temperature range of 20 to 30°C.

Figure 4.10 illustrates the measurements of the laser diode output wavelength, the incident power. The power absorbed (green curve + stars) by the crystal was also calculated from the difference between the incident power (the brown curve + triangles) and the transmitted power (not shown) through the crystal. Measurements were taken from the operating diode current of 1.0 A at 19.01°C to 5.5 A and 19.45°C, after which a temperature runaway took place, such that when the 6.0 A measurement was taken, the diode temperature was 23.1°C.

The chart contains the following annotations:

$\lambda_p = 0.55_{op} + 803.48$
$R^2 = 0.98$

$P_{p\text{-Inc}} = 1.02 I_{op} - 0.99$
$R^2 = 0.99$

$P_{p\text{-Abs}} = 0.76 I_{op} - 0.98$
$R^2 = 0.99$

Legend:
— Ppump_Absorbed [W]
— Ppump_Incident[W]
— Wavelength [nm]

Axes: Pump power [W] (left), Wavelength [nm] (right), Current, I_{op} [A] (bottom)
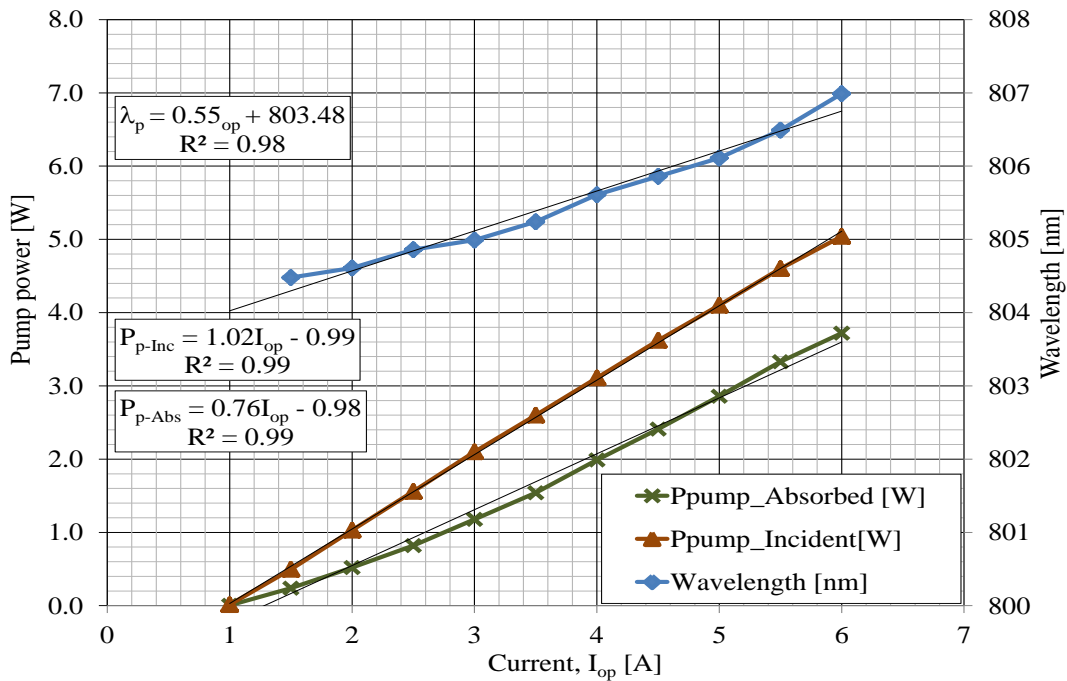
Figure 4.10. Pump power measurements taken after the pump optics, first when no pin hole is in place, when the beam passes through the pin hole at its waist and when the crystal is mounted in the pin hole. The resulting curves show the effects of the components on the beam.

91

Measurements were stopped after this, and the analysis shows how the diode output wavelength, the incident and the absorbed pump power vary with the pump operational current. The effect of this operational current forced the diode to operate off the spectral peak of the spectrum shown in Figure 4.3. The incident pump power graph also shows that the specified pump power could not be reached.

Power was also measured after the crystal was mounted. The absorbed pump power was calculated by subtracting the measured pump power after the crystal had been mounted from the crystal incident pump power. It is shown in green triangles in Figure 4.10. The pump power of 3.72 W was absorbed by the crystal at 6 A of incident pump power.

4.7   Common Switch Operation

The difference between CW and Q-switched lasers is the presence of an optical switch that is installed in the latter to introduce periodic losses in their cavities. In Chapter 5 we shall investigate an AOM-switched laser experimentally, while in Chapter 6 we investigate an EOM-switched laser. In that chapter we also present a new EO Q-switch technique that can be used as an alternative and developed further.

A Q-switch element in general must successfully prevent (hold off) laser oscillation during the off-period and permit it during the on-period, with each period being long enough to allow for their respective processes to take place. Apart from the gain medium and other components, Figure 4.1 shows a general cavity with an optical switch that represents switches such as AOMs, EOMs that all perform the same function, albeit differently. A Q-switch can either be one component or made of several components. As shown in Chapter 3, in Figure 3.6 and Figure 3.7 respectively, an acousto-optic Q-switch is a single component with the piezoelectric transducer attached to it and driven by an RF driver, while an electro-optic Q-switch is a combination of a few components. The electro-optic Q-switch components include a polariser, a Pockels cell, a wave plate, and are driven by a high voltage driver providing a high voltage. The high voltage can either be a $\lambda/2$ voltage or $\lambda/4$ voltage, depending on the

92

wave plate used [1]. Both switches have been discussed at length in Sections 3.13 and 3.14 respectively. The specific switches used in this study are discussed and presented in the following relevant chapters.

4.8   General Flat-Flat Cavity and Stability Considerations

In this study a cavity consisting of two flat mirrors was employed. The first HR mirror was one of the surfaces of the laser crystal, while the second was the output coupler that had a partially reflectivity of 70% for 1064 nm light. Normally, flat-flat cavities are on the stability boundary. Stability can be determined from the cavity g parameters, which are given by Equation (4.4) as,

$$g_1 = \left(1 - \frac{L}{R_1}\right), g_2 = \left(1 - \frac{L}{R_2}\right) \tag{4.4}$$

where L is the cavity length and R_1 as well as R_2 are the radii of curvature of the two cavity mirrors [97]. Cavities are only stable if their g-parameters are such that their product is enclosed by the branches of hyperbolic plot of $g_1 g_2 = 1$ [97]. When operated in this stable region, the intracavity beam oscillates without spreading out noticeably, but satisfies a stability condition given by Equation (4.5).

$$0 < g_1 g_2 < 1 \tag{4.5}$$

This is the case where R_1 and R_2 are both less than infinity.

4.8.1 Stability of a Flat-Flat Cavity due to Thermal Lens

In a flat-flat cavity, R_1 and R_2 are both infinity and they are known to be severely sensitive to perturbations; this easily makes them unstable [1]. However, if a positive thermal lens is generated within the laser crystal, the g-parameter product becomes less than 1 [98]. Hence, the stability of a flat-flat cavity is made possible by the presence of the thermal lens, making it possible to design it to efficiently generate high quality laser output (the thermal lens can be

93

approximated by a thin lens close to the pumped side of the laser material). To illustrate this fact, Figure 4.11shows how the presence of the thermal lens in the cavity influences its stability, where L_1 and L_2 are the spaces between the cavity end mirrors and the thermal lens.
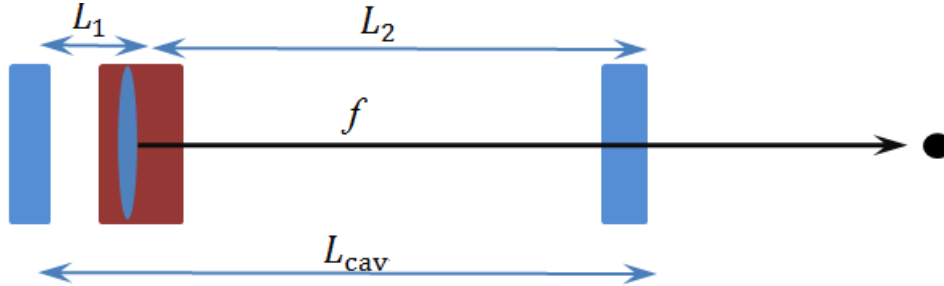
Figure 4.11. The geometry and stability of a flat-flat cavity where the thermal lens has much influence.

In that case, Equation (4.5) is replaced by Equation (4.6).

$$g_1 = \left(1 - \frac{L_2}{f_{th}} - \frac{L_0}{R_1}\right), \quad g_2 = \left(1 - \frac{L_1}{f_{th}} - \frac{L_0}{R_2}\right) \tag{4.6}$$

In this equation $L_0 = L_1 + L_2 - (L_1 L_2 / f_{th})$. In the event that the flat pump face of the gain medium replaces mirror 1 (the back reflector), then L_1becomes zero, thus making $g_2 = 1$. The resulting thermal lens resonator stability condition is given by Equation (4.7).

$$0 < \left(1 - \frac{L_2}{f_{th}}\right)(1) < 1 \tag{4.7}$$

Now, consider what happens when $f_{th}$is greater or less than L_2. For the case where the crystal has a weak thermal lens and $f_{th} > L_2$, the cavity remains stable. For the case where the thermal lens is strong however, that is where $f_{th} < L_2$, the cavity becomes unstable because the stability condition (Equation (4.7)) is not satisfied. This can be realised with uniaxial or birefringent gain media that have different thermal lens effects along their two axes that are perpendicular to the optical axis. In such gain media, one axis (the c-axis where the crystal emits π-polarised light) has a weak thermal lens with focal length $f_{th-c} > L_2$. Thus, when the

94

intracavity light interacts with this weak lens along the *c*-axis, the stability condition is satisfied and the cavity remains stable. However, when the thermal lens focal length becomes shorter than the cavity length ($f_{th-a} > L_2$), which occurs on the *a*-axis where the thermal lens is strong, the cavity becomes unstable or quenched. Quenching can be observed when the laser output begins to decrease as the input pump power increases [84].

Different thermal lens effects also introduce different resonator stability limits for the same cavity. This means that a cavity with a strong positive thermal lens will quench at lower pump powers, while the one with a weak thermal lens will quench at higher pump powers.

In uniaxial gain media, like the vanadate crystals, the two cavity stability states exist in one cavity and can be exploited. For example, a stable flat-flat cavity can be achieved when the intracavity beam interacts with the weak thermal lens axis of the crystal, and the opposite is true when the beam interacts with strong thermal lens axis. In Chapter 6, the influence of the different thermal lens effects are investigated experimentally in an effort to introduce a new method of Q-switching.

4.8.2 Output Coupling of a Flat-flat Cavity

The two mirrors that constitute a laser cavity, the back reflector and the output coupler, are responsible for the intracavity oscillation. Because of the coating on both these mirrors (already discussed earlier), pump light has full access to the laser material for pumping. In addition, the laser light oscillates continuously inside the cavity while its fraction is coupled out as laser output through the output coupler that is coated for its partial transmission. This process forms part of laser generation. As a result, it is important to select the optimum partial reflection or transmission percentage for the output coupler coating, a measure that will prevent the exposure of intracavity components to high peak powers and subsequent optical damages.

A laser is considered to have good performance if it has a high slope efficiency and a low pump threshold where lasing is initiated. However, Equation 3.3 relates the output coupler transmission *T* to the threshold pump power by direct proportion, which indicates that a high output-coupler

95

transmission gives rise to undesirably low slope efficiency. For this research, we did threshold calculations using Equation 3.4 to determine the reflectivity of the output coupler that we can use. The transmission of the output coupler was varied from 10 to 50% in steps of 10%, which corresponded to its 90% to 50% reflectivity. The lowest threshold pump power was observed with the 10% transmission, and the highest was observed with the 50% transmission. The implication of the 10% transmission is that 90% of intracavity intensity is reflected back at the crystal. While this favours high gain, operation at high peak power and high pulse repletion frequency, the exposure of the gain medium to extreme heat can cause damage, especially to $Nd:YVO_4$ with its low thermal fracture limit. So, the highest slope efficiency that can be obtained as a result of low threshold pump power cannot be sought at the risk of losing the gain medium. Conversely, the 50% output coupler transmission is an indication of 50% reflectivity and less intracavity flux, less gain and less suitability of the system for high peak power laser generation at high repetition rates. The laser designer therefore has to balance between the two extremes.

4.9   Summary

In this chapter, we introduced a common design for a general Q-switched laser. We discussed, in detail, all the components of a common laser system that had been employed to develop both AOM and EOM Q-switch lasers in this research. The laser system components that were discussed include the laser materials, the pump system, the common Q-switch element, and the laser cavity properties. With laser material, the physical properties such as the mechanical, optical, spectral and thermal properties were discussed. The study of the pump system conducted in this chapter included its assembly and cooling, as well as the propagation and characterisation of the pump beam. Following this, a common Q-switch element was briefly discussed to introduce the intended effect of its inclusion in the laser system, whether it is of the AOM or the EOM variety. On laser cavity properties, output coupling was discussed to determine the choice of the optimum output coupler for our experiments. Also, the laser cavity stability requirements of a flat-flat cavity were discussed as being dependent on the thermal lens of the laser material. In the following two chapters, two different Q-switching

techniques are introduced to this common setup in order to generate short pulsed laser outputs.

Chapter 5

5. Acousto-Optic Modulator-Based Active Q-switching

5.1   Introduction

There is a growing demand for lasers with a stable nanosecond pulse length and high peak power that operate at high repetition rates for applications such as materials processing, and high resolution or high speed ranging [99]. The required pulse lengths for such applications are in the low nanosecond range, which in turn require high gain and short cavity life time to achieve [100]. One approach for generating such short pulsed laser outputs is employing acousto-optic modulators (AOM) in Q-switched diode-pumped solid-state lasers [1], because they can generate a train of high peak power pulses at high repetition rates [35]. Active Q-switching with AOMs is reported to be favourable to generate stable pulses with high peak powers, while providing the advantages of low modulation voltage and low insertion loss, thus making it suitable for these applications [51].

Miniature, short pulse lasers have been demonstrated in literature, as introduced in Chapter 2 and listed in Appendix D. In some of these cases however, short pulses were obtained while peak powers were low, indicating the difficulty in obtaining short pulsed high peak power laser output at high repetition rates.

This chapter, however, presents a compact acousto-optic modulator Q-switched laser that is suitable for the generation of high peak power, nanosecond pulses at PRFs of ~100 kHz or more. Specifically, a $Nd:YVO_4$ laser system, Q-switched with a TeO_2 crystal AOM was designed and operated, and has been demonstrated to function at 140 kHz. This laser system produced pulses of < 2 ns durations, ~ 3 W average power, ~ 20 μJ energy and ~ 10 kW peak power. According to our knowledge, similar lasers in this class of high peak power, short

98

pulsed lasers, have not previously been reported. This shows that with careful cavity design, short pulse laser outputs with high peak powers can be obtained with compact AOM Q-switched laser systems, even if the laser is operated at high pulse repetition frequencies. However, while reporting on this range of parameters, this chapter will also demonstrate the limitations of high gain, AOM Q-switched lasers, such as double pulsing and thermal effects.

5.2 Developing a Nd:YVO₄ Acousto-Optic Q-switched Laser: AOM Characterisation

Designing and characterising a laser system requires informed selection of the individual components by considering properties that can contribute to their performance in realising the desired results. Central to the development of Q-switched lasers are the properties of the gain medium, the Q-switch element and the resonator. For example, the laser material influences the selection and performance of suitable pump sources as well as the structure of the cavity required [53]. For CW and Q-switched lasers alike, spectral properties (absorption and emission spectra and cross-sections) and gain requirements are used to select suitable gain media and their pump sources. Properties such as upper laser lifetimes (influencing energy storage), together with mechanical and thermal properties of the gain medium are discussed in Chapter 3, and are uniquely important in relation to the damage resistance of the gain medium and other optical components, as well as stability conditions of the cavity [1].

Short cavity lasers with reduced round-trip times that favour high gain, high repetition rates and short pulse widths have been realised with miniature lasers, but sometimes at the expense of achieving high mode matching (e.g. [101]). For this reason, the aim was to maximise the laser waist size, while avoiding obtaining higher order modes $\omega_{\text{laser}} \leq \omega_{\text{pump}}$. Furthermore, the output coupler can be aligned, and the cavity length adjusted, for the lowest possible threshold pump power.

99

5.3 AOM Q-switched Laser Experimental Setup

Q-switched laser cavities consist of several components that help achieve their desired pulsed results. Apart from the traditional laser material, the high reflectivity back reflector and the output coupler for CW laser systems, an AOM is an additional element in AO Q-switched lasers. In this subsection we discuss the laser system design, focusing on the component specifications, their mounting and orientation as well as their operational behaviour in experimental environments. Since our experiments were carried out with the same $Nd:YVO_4$ crystal, as introduced in Chapter 4, only the AOM is discussed in this chapter in relation to the cavity design.

5.3.1 AOM Manufacturer Specifications and Laser Design

The primary criterion for the selection of the AOM that was used in our experiments was size, in order to keep the ranger device small and the cavity length short for the generation of short pulses. A TeO_2 crystalline acousto-optic modulator (AOM) manufactured by Gooch and Housego (Model No.: I-QS150-0.4C2G-E-NL7) and specified for 1030 to 1064 nm was bought for the first Q-switched experiments. This AOM was one of the smallest that Gooch and Housego offered to fit our size requirement.

Table 5.1 lists factory measured specifications of the AOM we used in our experiments. A TeO_2 crystal-based AOM is highly preferred because of its high damage threshold ($50\,MW/cm^2$ for 10 ns as listed in Table 5.1), its high figure of merit [102], and high compressional wave speed [41]. It was chosen as a Q-switch element for our experiment because of the desired high performance and envisaged high peak power exposure. Ideally, the laser mode should under-fill the AOM ($\omega \leq (1/3)D$) for more than 99% of the beam intensity to pass through an aperture D to maximise diffraction efficiency. For our experiment, a 10 mm long AOM was specified to operate with 1064 nm laser beams of up to 0.16 mm beam diameters. It was specified to interact with laser beams of up to the maximum

beam diameter of 0.16 mm. The AOM we used for these experiments was specified for high (99.5%) transmission of laser light and high (85%) loss modulation.

Table 5.1. The specification of the manufactured AOM we used in our experiments.

Measurement	Specifications
Inter-action material	Tellurium dioxide (TeO_2)
Housing	Aluminium
Cooling	Through the base
Damage threshold	> 50 MW/cm^2 (assuming 10 ns pulse widths)
AR coating	$< 0.2\%$ per surface
Voltage standing wave ratio (VSWR)	$<1.2{:}1$ at 0 dBm
Transmission [%]	$>99.5\%$
Frequency	150 MHz
Optical polarisation	Insensitive
Active aperture	0.4 mm
Acoustic mode	Acoustic
Separation angle	36 mrad
Acceptance angle	8 mrad
Rise time (10-90%)	153 ns/mm
Loss Modulation [%]	$\geq 85\%$
Maximum RF power	2 W

A well-designed AOM is used to diffract a large percentage of laser light when the RF power is on and to allow all light to pass through the AOM when the RF power is off. An AOM's maximum power rating is determined by the size of the piezoelectric transducer, which must not be exceeded during operation, otherwise it will distort the acoustic wave and reduce diffraction efficiency. Our AOM was rated for the maximum RF power of 2 W, in keeping with the small size of its piezoelectric transducer. As is evident later on (see Figure 5.2 in Section 5.4.2), the 2 W RF power limits our small AOM's ability to hold off lasing at high

pump powers. The AOM selection is therefore a compromise between physical size (length and active aperture) and the maximum diffraction power at high cavity intensities.

5.3.2   RF Driver Specifications and the Function Generator Settings

The AOM RF Driver (Part number: 508A00169) that was used in our experiments was an A-35 Series model (A35 150-S-1/50-p4k7u) manufactured by Goosh and Housego and specified for an adjustable maximum RF output power of 5 W, with an output RF frequency of 150 MHz. For digital modulation, the RF On/Off ratio was specified for greater than 100 dB. Also, for both the digital and analogue modulations, the RF rise/fall times between 10 and 90% of RF power in the RF output frequency range between 140 to < 200 MHz, was specified to be less than 10 ns (because 150 MHz is within this range).

5.4   Nd:YVO$_4$ Laser Cavity Diagnostics

Q-switched laser cavities require additional components in the cavity to introduce pulsing effect. The resonator configuration implemented in this experiment was a simple linear flat-flat Q-switched cavity, where the pulsing effect was provided by the AOM that is introduced above. The flat-flat cavity was chosen because the thermal lens that is generated within the Nd:YVO$_4$ crystal was sufficient to stabilise the cavity [98] without additional mirror curvatures.

5.4.1   AOM Cavity Design and Implementation

Figure 5.1 shows a three component Q-switched flat-flat resonator in our lab, which includes the gain medium, an AOM as well as an output coupler. The cavity was designed with the aid of the Photonics Simulation Software for Teaching (PSST) [103] package. Figure 5.1 (a), (b) and (c) show the picture of the cavity as assembled in our laboratory, its complete schematic diagram, and a PSST simulation screen shot showing the complete cavity. The PSST cavity design was such that the cavity would be short (23 mm), with the laser mode matched to the

102

pump mode (at ~100 μm), as shown by Figure 5.1(c), by adjusting the cavity length. The thermal lens, which influences the modes size, was modelled as a thin lens in the software.
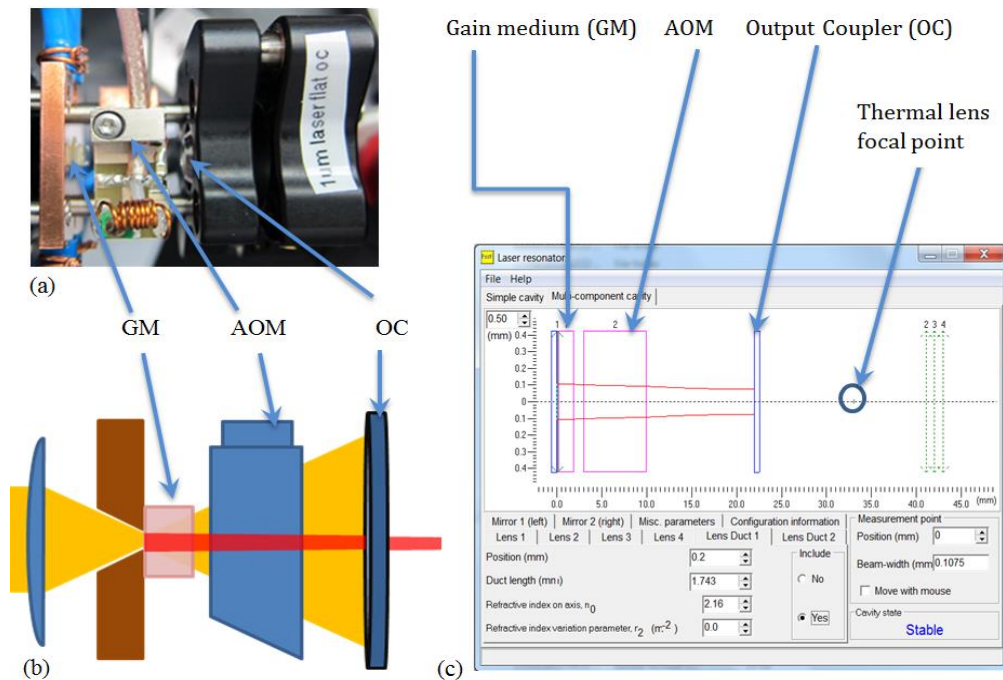
Figure 5.1. A complete AOM Q-switched laser system. (a) The lab snapshot of the short flat-flat AOM cavity. (b) The schematic diagram. (c) A screenshot of the CW laser cavity design within PSST [103].

While this is the case, in the lab the Figure 5.1 flat-flat cavity was constructed first by mounting a 1% at. doped Nd:YVO$_4$ laser material with dimensions $(3 \times 3 \times 2)$ mm^3 in position (at the waist of the incident pump beam) against a water-cooled copper mount with a pin-hole for pump light crystal access. This laser material is the same as the one introduced in Chapter 4. It is mentioned here again as a reminder and to illustrate the design of the cavity. The input face of the crystal served as the back reflector, hence it was coated for 1064 nm high reflection and 808 nm high transmission, while the second face was an AR coated for the intracavity oscillating 1064 nm laser light as shown in Figure 4.4.

103

Next, the AOM was mounted and aligned for maximum transmission under lasing and a high threshold for non-lasing conditions, and connected to its driving system, the RF Power supply and RF driver. To complete the cavity, a flat output coupler (OC), coated for 70% partial reflection of a 1064 nm laser beam, was mounted at the position where lasing was first observed. Upon investigation, the OC reflectivity that was chosen was found to be optimal because it generated less double pulsing at high PRF.

Double pulsing could not be avoided however, as is shown in this research. In addition, 70% OC reflectivity is a balance between high reflectivity (over 90%, which would return a large number of laser photons in the cavity and optically damage the components in the cavity), and low reflectivity (where there would not be enough photons in the cavity to effect stimulated emission).

While taking advantage of the thermal lensing effect of the crystal to stabilise this flat-flat cavity, the cavity length was physically measured to be $l_{cav-air}$~16 mm, or if we consider the optical distance $l_{cav-optical}$ that the intracavity light travels through the crystal and the AOM, it would be even shorter. While the shorter cavity would favour short pulse generation, the pump and the laser modes would be slightly mismatched. However, the experiment was successfully carried out under the circumstances.

5.4.2 Hold-off Threshold

The AOM that we used was specified for design transmission and loss modulation so that it would transmit more than 99.5% of light through the AOM when the RF was off and hold-off, and more than or equal to 85% of light when the RF was at a power of 2 W. The hold-off measurements of this AOM Q-switched laser system were taken as a diagnostic tool to predict its ability to effect the high-loss state when deployed in lasing conditions. The hold-off ability of this laser was obtained by measuring the CW threshold power at different radio frequency (RF) powers. The RF threshold pump power describes the ability of the cavity to hold off oscillation during the off-period of the Q-switched laser. Since hold-off determines how high

104

above the threshold the Q-switch can operate, higher hold-off threshold pump powers are desirable. In this case, where the laser was operated at high repetition rate operation (indicating limited time for the gain to rise and for the losses to be kept high), the hold-off pump powers may be expected not to rise high enough. However, because of the short fluorescence life time and the large absorption cross-sections, the limited off period may be balanced.

Figure 5.2 shows the hold-off threshold pump power of the AOM as a function of a Q-switch driver RF output power. It was measured as the RF power was varied in steps of 0.5 W from 0 to 2 W. The graph shows that at low RF powers the hold-off pump powers were low, but they increased with the increasing RF powers until the RF power of 2 W.
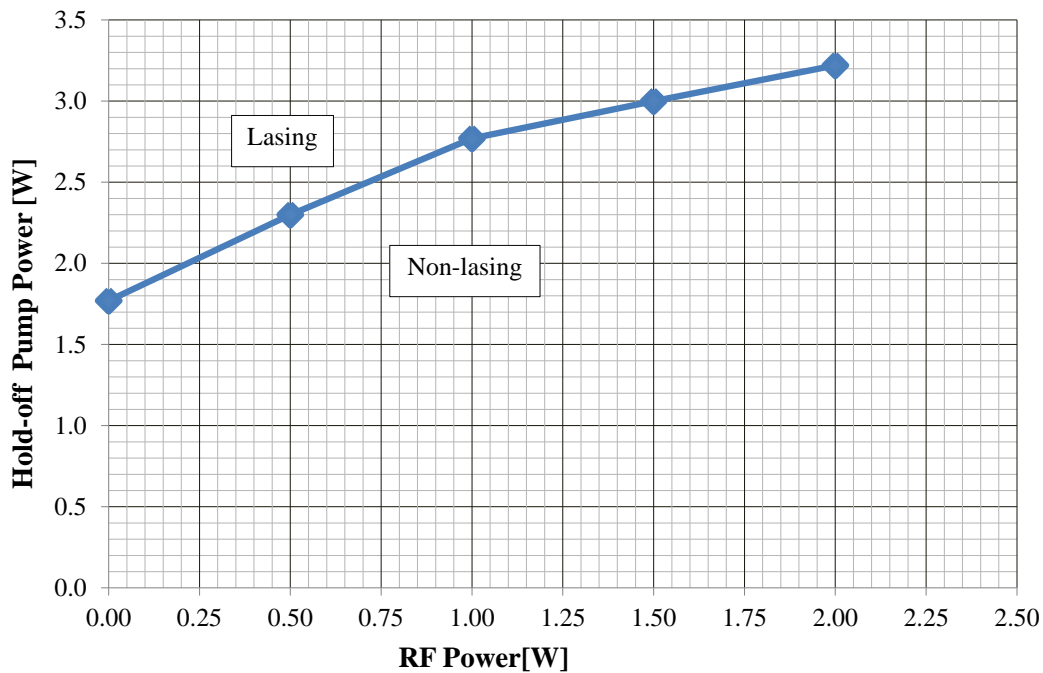
Figure 5.2. Hold-off pump power measured as a function of the RF power.

Firstly, it can be concluded that the AOM induced cavity loss was scaled with the RF power. This is seen by the steady increase of the CW lasing threshold with the AOM RF power. Also, it was observed that at maximum RF power, the AOM could hold off 3.2 W of pump power.

105

This raised concern about whether the AOM would be able to hold off lasing during Q-switching at a maximum pump power of over 6.5 W. However, considering that at high PRFs pulsing would periodically reset the gain to zero, the lasing hold-off would then be better at high pump power.

To prevent the leak of CW beam during the Q-switch off period, the hold-off must be sufficiently high. However, that may not be possible under real laboratory conditions. Figure 5.2 shows that the maximum CW hold-off pump power of 3.22 W, thus blocking 1 W of CW laser oscillation, was measured at the RF power of 2 W. From this, we can deduce that at low RF powers, the cavity losses are low, and that gives rise to low threshold pump powers.

The values of the hold-off pump powers, which increase as the RF power increases, indicate the extent the AO Q-switch we used would hold off lasing between two successive Q-switched pulses. Low hold-off is one of the disadvantages of AOM Q-switching [100]. When a Q-switch cannot sufficiently hold off lasing during the off-period, it is normally due to the high gain generated in the laser medium as well as the slow switching time of Q-switch AOMs [86]. The choice of a laser crystal (Nd:YVO$_4$) with high gain and short fluorescence life times as well as the Q-switch element (see Table 3.1), an AOM with high loss-modulation (see Table 5.1) contributed to having the laser operate successfully.

5.5   Acousto-optic Experiment's Results

This research covered several areas in order to determine the performance of an AOM Q-switch to generate short pulsed, high peak power laser output at high pulse repetition frequencies. First the AOM insertion losses were determined by measuring the slope efficiencies of both the CW and Q-switched laser. Following this, pulse width and peak powers were measured as functions of input pump power. The quality of the AOM Q-switched laser beam was also measured. Lastly the nature of the pulses was investigated at low and high pump powers. While the pulse energies could also be presented, the following results were sufficient to characterise this Q-switched laser.

106

5.5.1   Laser Output: The CW Laser Performance

To obtain maximum output as set by the research objectives, the cavity must be designed such that the pump mode matches the laser mode and is stable for the shortest possible flat-flat cavity length. The laser performance was evaluated by measuring the M^2 value and output power values to compare CW and AOM Q-switched lasers. The pulsed laser output was measured with the oscilloscope and controlled by a function generator. The Q-switched laser results are presented below.

5.5.2   Slope Efficiencies and AOM losses

The slope efficiencies of the CW and the AOM Q-switched lasers were measured with the same cavity and are presented in this section. In other words, the AOM was inserted in both measurements. For the CW laser, the AOM laser Q-switching system was off and it was switched on for the Q-switched laser, thus making both lasers have the same base loss in the cavity. The Q-switched laser measurements were taken at the high PRF of 140 kHz. At such high PRFs (PRF $>> 1/\tau_f$) it would be expected that the difference between the CW and the Q-switched lasers' average power should be small, as predicted by Figure 3.4.

Figure 5.3 shows the average power measurements taken to characterise these two laser systems, the CW and the AOM actively Q-switched laser under the same operational conditions. The optimum diode pumping was conducted up to approximately 6.5 W to measure the slope efficiencies for both lasers. A Spiricon camera was also used to show the beam profiles of the laser under investigation and to determine the nature/ behaviour of the beam as pump increased.
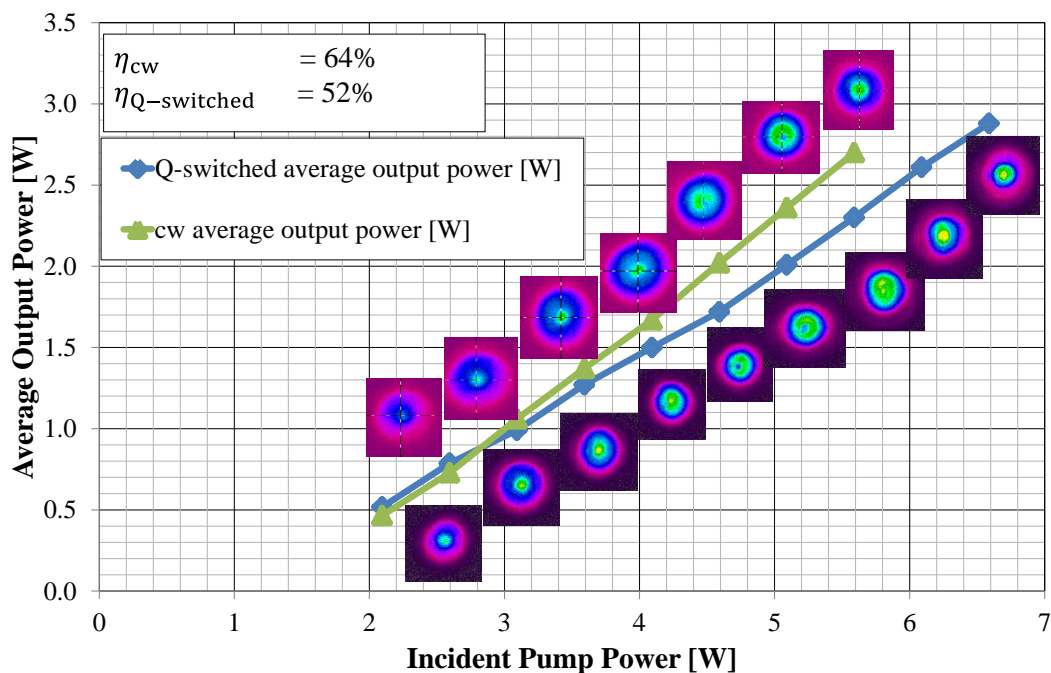
Figure 5.3. The average power output measurements for the continuous wave and AOM Q-switched laser operations. The difference between the CW and Q-switched laser output indicates that the insertion of the AOM in the cavity introduced losses.

Comparing the CW and the AOM Q-switched laser outputs was done by subtracting the Q-switched from the CW power and a notable difference was observed. At low pump powers (~1.6 W) the difference was ~0.2 W, while at high pump powers (~6.6 W) the difference was 0.73 W. The difference between CW and Q-switched lasers' average power at high PRFs, where they are expected to be similar, indicates losses in the Q-switched laser and that energy was dissipated somewhere. The difference (the losses) can be attributed to the gain reaching the CW levels before the end of the fluorescence life time and to the possible dissipation of energy through pre-lasing. The former may cause low energy extraction, and the latter occurs due to a limited diffraction loss that the AOM introduces, thus causing the hold-off capability of the AOM to be limited at high pump powers [104] and resulting in low peak power. Another possibility could be double pulsing, as observed in our results in Figure 5.6 (b)

108

below, which occurs due to the slow switching of the Q-switch element as explained in Chapter 3, Figure 3.5 (c).

This can also occur more at high pump powers as a result of short build-up times. Lastly, the Q-switched average output power could have been reduced by the active Q-switch losses during a pulse, which can occur as a result of the narrow open time window. In that case, an AOM may have limited rise and fall times, leading to a situation where a degree of AOM loss may still be present during the pulse. This affects the diffracted beam and reduces the laser output and efficiency. Both can be prevented by inspection and monitoring the AOM diffracted beam for the output pulse. However, in our case this could not be done because of the short cavity and space limitations.

To explain the results, we observe that the laser output behaves differently at different pumping zones as pump power is increased to the maximum. This behaviour is observed by how the peak power and the pulse widths of laser change during the pumping process at the low, intermediate and high-power zones.

At the low-power zone, for example, which starts from the threshold pump power of 1.1 W to the intermediate pump power of 3.6 W, pure Gaussian beam profiles with increasing intensity were observed. However, severe thermal lens effects created small cross-section mode areas at higher pump powers, which lead to mode-mismatching and thus generates higher order modes to oscillate and significantly reduce the beam quality.

With these results, the AOM Q-switch used in this research can be expected to perform with little or no negative influence from its optical properties when generating the expected short pulsed laser output at high PRFs.

5.5.3 Pulse Width, and Peak Power

The major characteristics of a Q-switched laser include pulse widths, pulse energies, average and peak powers, and are useful for various applications. Figure 5.4 shows the measured

pulse widths, the calculated pulse energies, and the peak power of the AOM Q-switched Nd:YVO$_4$ laser developed in this research.
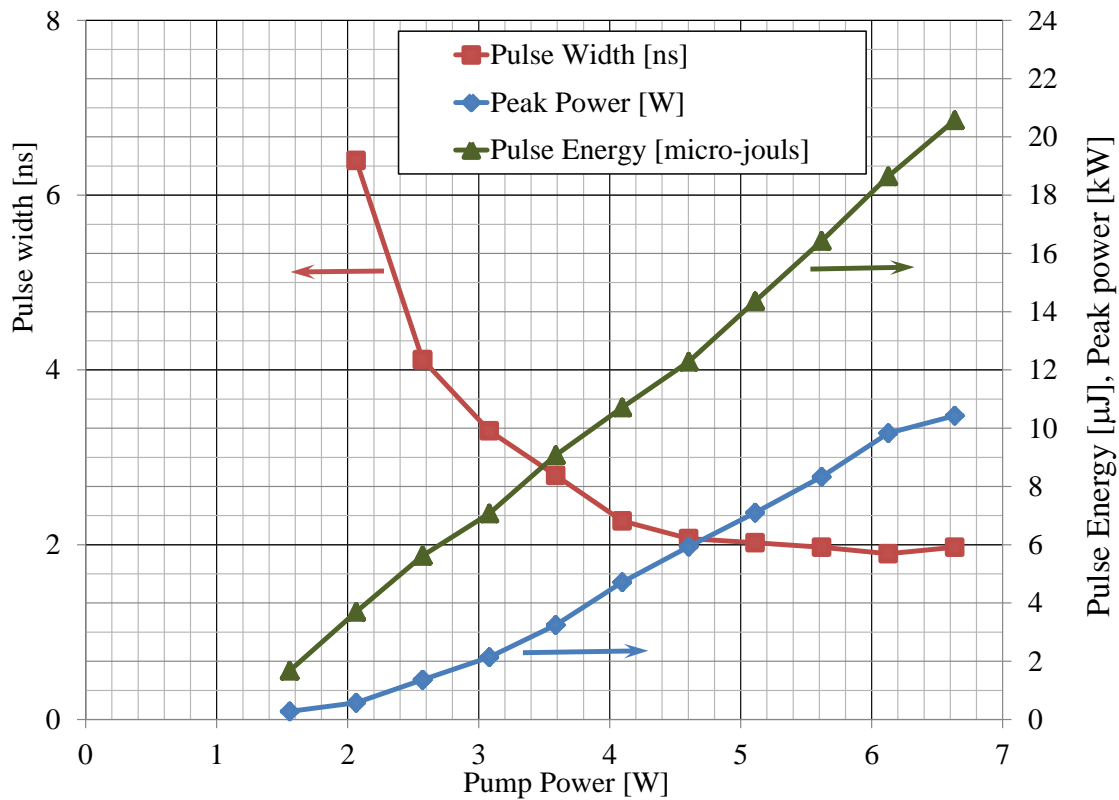
Figure 5.4. The peak power, the pulse width and the pulse energy results of the AOM Q-switched Nd:YVO$_4$ laser measured as functions of incident pump power.

The pulse width curve showed a decrease from the highest value of 6.4 ns at low pump power of 2.2 W to the lowest (shortest pulse width) obtained of 1.89 ns at the high pump power of 6.1 W. This corresponded to the increase of peak power from ~0.3 kW to 10.43 kW. Meanwhile, the pulse energies increased from 1.7 μJ and reached a maximum of 20.6 μJ.

Pumping laser higher than this leads to the increase of pulse widths to about 2 ns at the pump power of 6.4 W. However, a higher peak power of 10.48 kW was reached at this pump power, yielding a slightly longer pulse width of 1.97 ns. This indicated that the cavity was becoming unstable at high pump powers.

110

5.5.4 Q-switched M^2 Measurement

Performing an M^2 measurement requires the use of a distortion free lens and a high-resolution camera with ND filters on a translation stage that passes through the beam's waist. This then measures how the beam focuses and how it diverges. The ND filters are affixed to the camera to prevent beam saturation on its sensor. As the camera moves through the waist, its beam widths are measured at each location from the lens.

Figure 5.5 shows the measurements taken to characterise the AOM pulsed laser beam when an optimum diode pumping of approximately 6.5 W was employed. A Spiricon camera (with pixel pitch of 4.5 μm) was used to show a circular Gaussian beam profile of the $Nd:YVO_4$ laser under investigation, from which the quality of the beam, the beam waist size and its position were determined. The insert beam profile shows that the beam measurements can be trusted. This is because the specified pixel pitch of the camera implies that a sufficient number of pixels were present over the beam area.

A stable TEM_{00} laser beam profile was obtained, and by measuring its beam widths at various positions after passing through a $f = 100$ mm lens, and determining its M^2 factor, its quality was determined. The M^2 obtained was 1.32, while its waist size was 38 μm. The M^2 value obtained is an indication of a good quality beam, and this leads to the deduction that a near single mode oscillation was achieved.

111
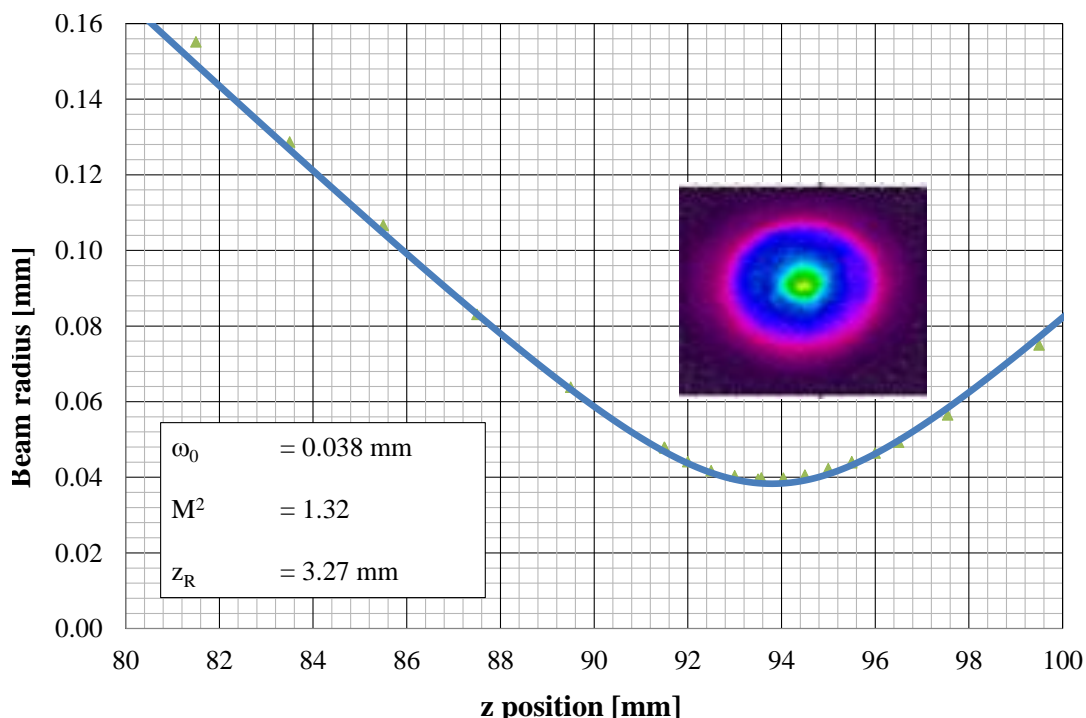
Figure 5.5. The M^2 measurements of a CW laser are presented here together with the beam waist radius, its position and the Rayleigh range.

The waist size was quite small and reduced from the pump beam waist size. This was in favour of the desired faster switching of the AOM [21].

5.5.5 Double Pulsing in AOM Q-switched Lasers at High PRF

When operating in the AO Q-switch regime, from the pump power of 4.5 W to 6.4 W, giant pulse formations were established in the laser. Within this pump power range, Figure 5.6 (a) shows that at lower pump powers, the pulse traces were well defined and the pulse width of 2.273 ns was achieved at the PRF of 140 kHz. In comparison with the higher pump powers, however (Figure 5.6(b)), other pulse traces began to develop as shown by the second pulse profile. This is described in Chapter 3 Figure 3.5 (c), which indicates that it is much slower than the build-up time. This is the major drawback of acousto-optic Q-switching. So, even when high peak powers (10.84 kW) and shorter pulses (1.972 ns) were achieved at the PRF of

112

140 kHz, the other pulse will generate a measurement conduction when the laser is deployed in ranging applications.
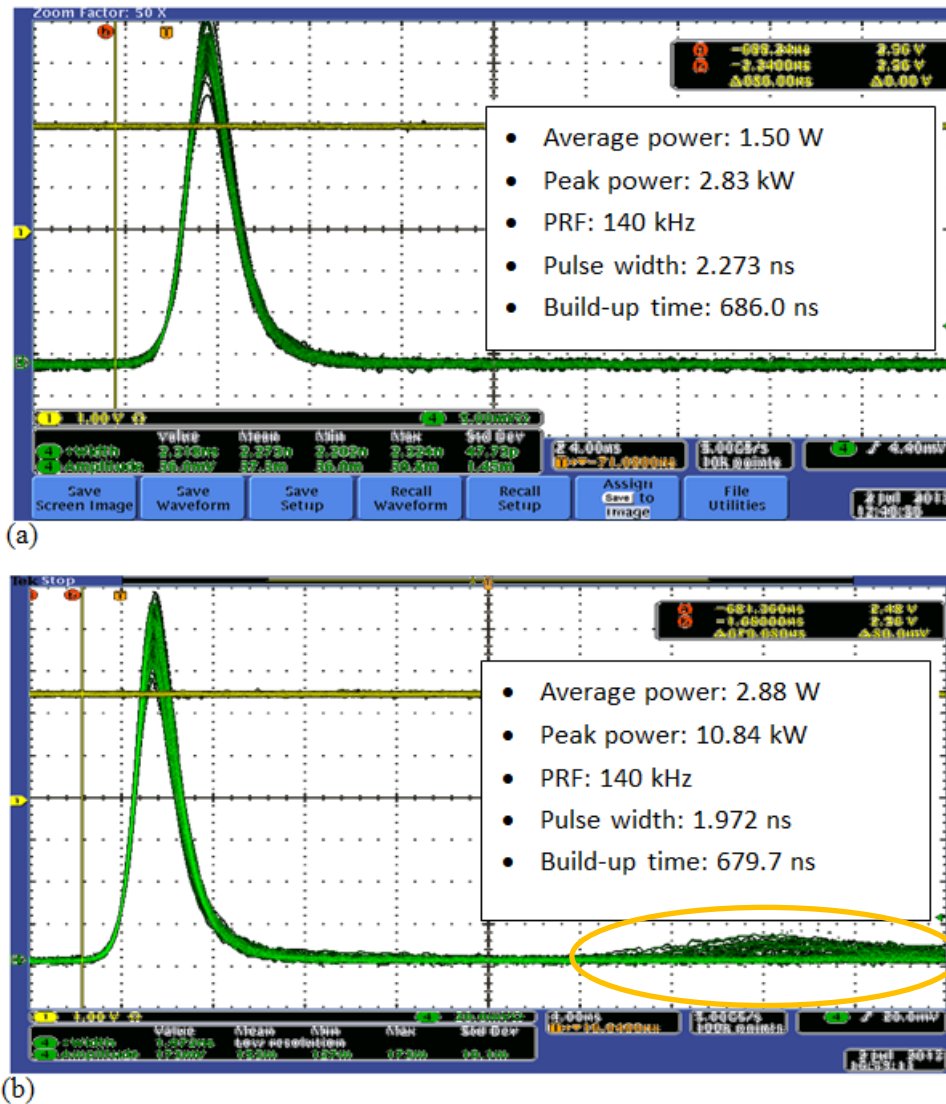
Figure 5.6. (a) The pulse trace of the laser output at low pump powers when being Q-switched at a pulse repetition frequency of 140 kHz, and (b) the pulse trace of the Q-switched laser at high pump powers.

With AOMs we have shown that high stable output peak power can be obtained with pulse widths over 2 ns. By increasing the pump power, shorter pulse traces (the shortest was 1.89 ns) could be obtained – however, parasitic additional pulses developed. The phenomenon

113

that was observed is called double pulsing, and it shows the instability of the laser when generating laser output peak powers greater than 10 kW. This reduces the laser efficiency at high incident pump power. Of the three cases of slow switching presented in Chapter 3, the double pulsing observed shows that it is the third case, where the switching time is much longer than the pulse build-up time, such that it is not instantaneous.

As the first pulse is bigger, it is an indication that a greater percentage of population inversion is depleted with the emission of a greater percentage of photon energy extracted through the first pulse. While the energy of the second pulse is much lower and useless, it robs the first of much needed energy.

5.6   Discussion

The findings of this chapter suggest that short (nanosecond) pulsed laser outputs with high peak powers can be obtained by a carefully designed compact AOM Q-switched laser system at high PRFs. Such a design includes selecting laser material, pump source and scheme, the Q-switch element as well as cavity properties such as length and mirror reflectivity to favour the desired results. To determine if the results obtained in this chapter are novel, both the design and the results were compared to the best AOM Q-switch results that were selected from the literature review presented in Chapter 2 and the appendices.

The design was compared to the designs of other lasers that produced similar results. Table 5.2 summarises the results of the laser we developed in this research together with two other research reports on acousto-optic Q-switching with comparable results. One was conducted by Ogawa et al. (2005). Part of their research included Q-switching a $(3\times3\times5)$ mm^3 1% at. a-cut Nd:GdVO$_4$ with an unspecified AOM at 100 kHz repetition rate and direct pumped at 879 nm with a 11.7 W CW laser diode. Their laser design was optimised for high beam quality, and as a result they extended the resonator length to 40 mm and increased the gain volume for cavity-mode matching. With that design, they observed no saturation of the output power, although it was slightly at the expense of the slope efficiency and optical-to-optical

conversion efficiency [36]. The laser output they obtained involved a pulsed beam of $M^2 = 1.1$, which was better than what we obtained ($M^2 = 1.32$), a higher average power and almost double the pulse energy we obtained. The pulse durations, however, were quite long (more than five times the value we obtained) and the peak power was lower (less than half of what we received). Because short duration pulses at this PRF are more important, our laser system did well.

Table 5.2. Comparison of the laser Acousto-optic results produced in this research with fewother AOM results produced elsewhere.

Authors, Year	Pump source/ scheme, wavelength [nm], Power [W], radius [µm]	Gain medium + Doping [%]	Crystal Dimensions [mm^3]	Q-switch device	Cavity length (mm), OCR	PRF [kHz]	Pulsed Average power [W], M^2	Pulse Energy [µJ]	Pulse Width [ns]	Peak Power [kW]	Ref.
E. L. Maweza, this thesis, 2018	End, 808, 6.5, 100	1% at. Nd:YVO$_4$	3×3×2	10 mm TeO$_2$ AOM	16, 70	140	2.8, 1.32	20.6	1.97	10.43	This work
T. Ogawa et al., 2005	Direct, 879,	1% at. a-cut Nd:GdVO$_4$	3×3×5	Length not specified TeO$_2$ AOM	40, 80	100	4, 1.1	40	10	4	[36]
Y. Wang et al., 2007	End, 808, 4, 50	0.5 at.% Nd:YVO$_4$	3×3×5	13.8 mm Not specified	20, 10	80	0.82, 1.3	10.3	2	5.13	[35]

Wang et al. made a compelling case in 2007 when they developed a Q-switched 2 ns pulse duration laser of 5.13 kW peak powers at 80 kHz of PRF with an unspecified 13.8 mm long AOM. Since they wanted to generate short pulses, the authors designed their laser such that the cavity length was reduced and had high gain. To reduce the cavity length, they used a short AO Q-switch. The authors also used a small radius oscillating mode, which they deemed crucial for high gain as well as fast AO Q-switching laser systems. The latter are dependent on the transit time of the sound wave across the oscillating beam. To achieve high gain, they used a Nd:YVO$_4$ crystal as a laser material, thanks to its large stimulated cross-section. It was indicated however that the laser system cannot be optimised for short pulse durations and high repetition rate simultaneously, because of the low gain at high pulse rates. They pointed out that because of low gain at high repetition rates, it was difficult to achieve short pulses. As a result, they used a longer crystal $(3\times3\times5)$ mm^3 to allow high absorption of the pump, end-pumped at 808 nm wavelength and low doped 0.5% at. a-cut Nd:YVO$_4$ to curb thermal problems in a 20 mm long cavity [35]. Compared to the AOM laser we developed with a 16 mm long cavity and reported on in this chapter, their cavity length was longer. While they obtained pulsed output of comparable durations (2 ns) to the 1.89 ns pulses we obtained, they obtained half the peak power we obtained. This was so even though we operated our laser at a much higher PRF (140 kHz). Meanwhile, they had to operate at lower PRFs to reach these laser parameters, which were not suitable for our applications.

In our research, we sought to improve the results obtained earlier by other researchers. To do so under an acousto-optic modulator-based Q-switch operation, this work reported on the design and the factors that influenced the performance of the laser, such as the hold-off and accounts of intracavity losses. We also reported the output parameters (results) obtained in this work, such as the CW and Q-switched average power, peak power, pulse energy and pulse width, as well as the beam quality. Our results also account for the drawbacks of this technique as we assess the performance of AOM Q-switched high peak power lasers.

117

As observed and presented in Figure 5.2, the low hold-off pump powers (minimum of 1.7 W thresholds to the maximum of ~ 3.2 W at 0 and 2 W RF powers respectively) indicate a significant influence of factors such as the high gain generated in the $Nd:YVO_4$ crystal, as well as the slow switching time of the AOM Q-switch. Measuring the slope efficiency in the CW and Q-switched conditions, a maximum of ~0.4 W insertion loss can be calculated, thus indicating the quality (high transparency and damage threshold) of the TeO_2 based AOM used. This also showed that optically the AOM had the least negative influence. The results that are presented in Figure 5.4 demonstrate a successful development of an acousto-optic modulator-based Q-switched laser with outputs reaching peak powers of 10.84 kW. This was double the peak power our group obtained earlier (5.5 kW), which indicated a significant improvement from earlier demonstrations.

Figure 5.5 shows that the laser emitted near single mode laser beam profiles of symmetric pulses at both low and high pump powers, indicating equal rise and fall times. However, at high pump powers, double pulsing was identified at pulses that correspond to the output peak powers > 10 kW. This can be attributed to the slow switching speeds of the AOM and led us to investigate Q-switching based on electro-optic modulators that switch much faster. Obtaining short pulsed laser output with increased efficiency at high peak powers and high PRFs was the ultimate goal. That may require improving even the conventional electro-optic Q-switch techniques.

By comparing our results with the existing and recent literature, we have shown that our laser is a better candidate to be used in LADAR applications. The double pulsing however needs to be addressed. From these studies we can optimise the cavity for high energy values by taking advantage of direct pumping for shortened pulse duration and beam quality, balance between cavity length, mode size and output coupling. The average power can also be improved by selecting an AOM with high hold-off.

118

In the next chapter we explore the use of fast-switching electro-optic modulators (EOM) to generate short duration pulsed laser output, with high peak powers. In the EOM investigation, the cavity will be optimised for the shortest possible cavity, while using the same laser material and output coupler. With regard to cavity length we also introduce a technique that seeks to advance their current operations and curb the problems that exist with AOMs.

5.7   Conclusion

With an AOM Q-switched laser we managed to obtain less than 2 ns duration pulses with peak powers of more than 10 kW at the high pulse repetition frequency of 140 kHz. When we compared our laser design and results with other similar lasers in literature, we were able to determine that our system was unique in that it delivered laser parameters close to the required ones, while having a small physical footprint. While good and well-defined pulses were obtained at the lower pump powers and even shorter pulses were obtained at higher pump powers, double pulsing was observed at the latter. The double pulsing observed confirms a known fact, namely that AOMs are slow in switching. This prompted further attempts (making shorter cavity design) to obtain as short pulse widths as possible with better mode matching at higher pump powers. The work in hand highlights the problems that are traditionally associated with AOM Q-switching and prompts us to develop a new technique in the faster Q-switching regime.

Chapter 6

6. Developing a New Electro-Optic Q-Switched Laser

6.1 Introduction

Electro-optic Q-switching offers fast switching speeds, high efficiencies and stability in generating high peak power, nanosecond pulsed outputs at high repetition rates. In the previous chapter it was demonstrated that it is difficult to achieve this combination of parameters with AOM Q-switching due to slow switching speeds. EOM Q-switching, on the other hand, can be fast enough to avoid all these negative effects. In addition, another advantage it has over AOM-based switching is better hold-off ability, which may result in higher pulse energy lasers [83]. However, to achieve this, EOM Q-switching generally requires additional polarisation elements.

This investigation aimed to use EOM Q-switching to generate nanosecond pulses at 100 kHz repetition rates and thereby avoid the slow switching issues of AOM Q-switching. A new concept that was developed is a technique to reduce the number of polarisation elements in EOM Q-switched cavities. With this new technique, we produced 2.21 ns pulsed laser output with 10 kW of peak power at 100 kHz, although the main aim was to demonstrate its feasibility.

6.2 Conventional Electro-Optic Q-Switched Laser Components

The focus of this chapter is on electro-optics-based Q-switching. In this section, we discuss the insertion of various EOM Q-switch assemblies to Q-switch the lasers. The aim was to produce a short duration (ns) pulsed laser output at high (~100 kHz) PRF. To do that, a

120

conventional but short cavity was designed. Apart from the laser material (the Nd:YVO$_4$ crystal), additional components were part of the laser system, namely the Pockels cell, high voltage driver, wave plate and the polariser [17].

The operation of a conventional electro-optic Q-switch is described in Sections 3.15 and 0 in Chapter 3. Figure 6.1 shows the implementation of this technique in the general and conventional laser setup that was discussed, using a reflective polariser as example.
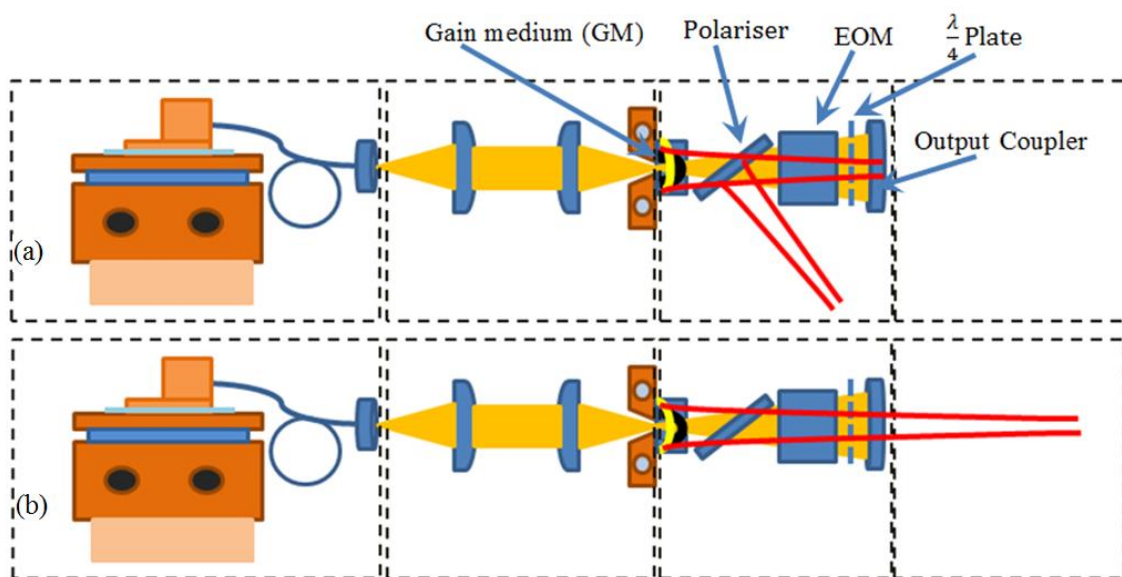
Figure 6.1. Conventional Electro-Optic Q-switching cavity process where the polariser, the Pockels cell, the λ/4 plate and the OC are involved: (a) The high-loss state occurs when high voltage is off and only the λ/4 plate, OC combination rotates the beam such that the polariser introduces cavity losses as shown by laser light reflected outward. (b) The low-loss states where the polariser allows light to pass through with little or no losses.

To design a short cavity, all the components needed to be short – including the Pockels cell and the polariser. The polariser is responsible for introducing losses in the cavity during the high loss-state of Q-switching. In Figure 6.1 (a) the polarisation of the intracavity beam is

121

rotated such that it is reflected out of the cavity by the polariser, and no lasing would take place. while in Figure 6.1 (b), the polarisation is such that the beam is allowed to oscillate in the cavity.

6.2.1   The Pockels Cell Design Considerations

Pockels cells are selected for electro-optic Q-switched laser design by considering certain properties that satisfy certain requirements. Since this research sought to develop a high-power laser, the Pockels cell material (the RTP crystal) was chosen based on its high laser damage threshold. The electro-optic (EO) coefficients that characterise RTP crystals [75] are larger than those of other crystals listed in Table 3.3. Figure 6.2 shows first the Pockels cell that was bought from Raicol Crystal Ltd (Part number: 32812001) and used in our experiments. It was made of two x-cut 3 mm long Rubidium Titanyl Phosphate (RbTiOPO or just RTP) crystals that were factory fitted 1 mm apart and orientated with their corresponding axes perpendicular to each other for thermal compensation [75].
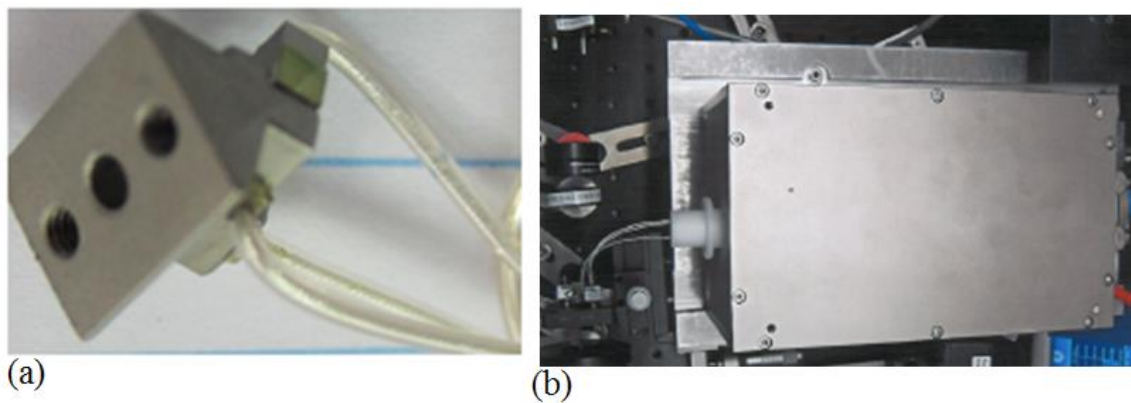
Figure 6.2 (a) The factory RTP crystal Pockels cell used from Raicol Crystal Ltd (Part number: 32812001) [105]. (b) The second photo is the Pockels cell driver, which itself is driven by a digitally controlled high voltage driver.

Because of the inverse proportion between them, the large EO coefficients of RTP crystals limit the voltage required to effect polarisation rotation to values low enough to save the components from high voltage exposure.

Both crystals had transverse dimensions of $2\,\text{mm} \times 2\,\text{mm}$ and occupied $7\,\text{mm}$ physical distance along the optical path. Furthermore, they were AR/AR coated for high transmission (99%) at 1064 nm. The Pockels cell was bought fitted with fluorinated ethylene propylene (FEP) insulated wire cables by the manufacturer across the Pockels cell terminals. These cables were used to connect the Pockels cell to a water-cooled Bergmann Messgeräte Entwicklung KG (BME) Pockels cell driver (PCD). The PCD was connected to a digitally controlled high voltage driver for the electric field to be transverse in the direction of the beam propagation. The BME PCD system was chosen for use in this research because of its ability to operate at high repetition rate, fast on-and-off switching, variable pulse durations, low jitter and its compatibility with high EO coefficient BBO, KD*P and RTP Pockels cells [106].

The digital control was made possible by a BME delay generator that was in the form of a PCI card (supplied with appropriate operating software to control the trigger generation and delays) that was installed on a desktop computer. The delay generator signals were first verified on an oscilloscope before the high voltage in the system was turned on for the driving process. This BME PCD system was used to drive the Raicol Crystals RTP crystal Pockels cell in our labs for the EOM laser Q-switching. This EOM mechanical assembly was put in place together with its electrical equipment and cooling connections. The system was shielded from electromagnetic interference (EMI), as its triggering system and the delay generator were set.

Table 6.1 lists voltages that were specified for the Pockels cells that could be used for EO Q-switching. The Pockels cell that was available for our experiments however was from Raicol Crystal Ltd. The Cristal Laser crystals are listed as an alternative and for comparison.

123

Table 6.1. High voltages for driving different Pockels cells made of crystals from two different companies, Raicol and Cristal Laser.

Material	RTP-measured [V]	RTP factory measured [V]	RTP Measured in our labs [V]
Source and place measurement	Raicol: factory-measured values	Cristal Laser: factory-measured values	Raicol Company: Measured in our labs
Half-wave voltage	2250	1200	2100
Quarter-wave voltage	1125	600	1050

As it was the desire of the designer to achieve polarisation rotation with sufficient but less voltage (1050 V), it was desirable to measure less voltage than the specified 1125 V. More than that, the Cristal Laser Pockels cell gives an alternative, which can be hoped to perform even better because of its low voltages that are specified for the beam polarisation rotation.

6.2.2   The Polariser Design Considerations

Polarisers are important components in conventional electro-optic Q-switching because they are used to select the lasing polarisation. Their function is to introduce losses to the cavity whenever the intracavity beam polarisation is rotated off its transmission axis. Figure 6.3 shows two versions of polarising elements, one reflective and the other absorptive as an alternative. It shows how the different polarisers operate, where one polarisation is transmitted with minimum attenuation, while the other planes of the initially unpolarised light are reflected outwards for a reflective polariser or absorbed for an absorptive polariser. The reflective polariser was made of BK7 and had circular dimensions of 3×1 mm^3. It was bought from Crystech Inc. and coated to transmit a linearly polarised 1064 nm laser beam. Absorptive polarisers are made of materials with different degrees of absorption for

124

perpendicular planes of incident beams. Reflective polarisers utilise special coatings near the Brewster angle to achieve high reflection of laser light for EO effect. For this research, we used an absorptive polariser that was bought from the Corning Company (Polarcor glass polarisers) with an extinction ratio of > 40 dB [107] and chosen for its high damage threshold. It was small and thin, and its dimensions are $10 \times 10 \times 2$ mm^3.
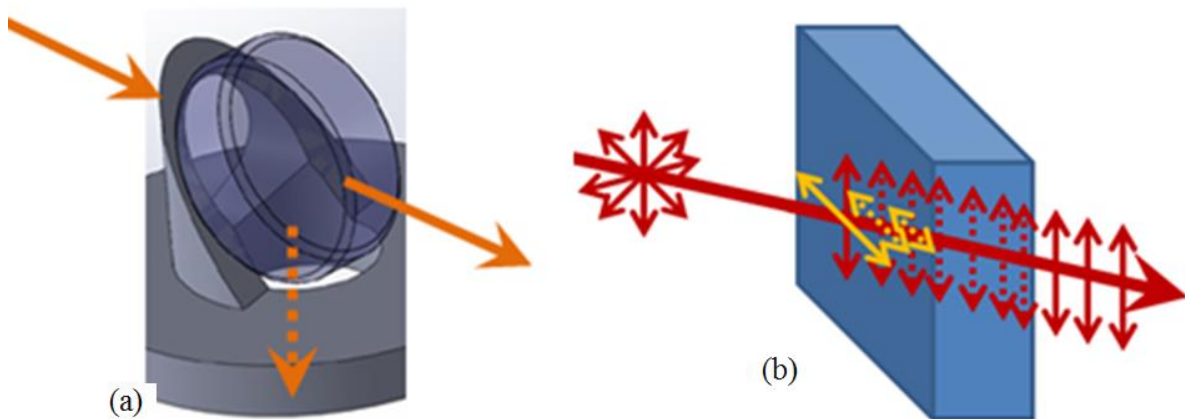
Figure 6.3. Two polarisers used in this research. (a) This is a reflective polariser, which functions by reflecting light out of the cavity, and (b) is an absorptive polariser, which functions by absorbing light when its polarisation is not parallel to the polariser transmission axis.

6.2.3 Quarter-wave Plate Design Considerations

The components of the intended laser system include a quarter-wave plate, which functions as a passive polarisation rotator. Figure 6.4 shows the quarter-wave plate that was utilised to rotate the polarisation by $\pi/2$ radians phase difference and lead to a linear-to-circular polarisation rotation for each pass. The plate was bought from Thorlabs.
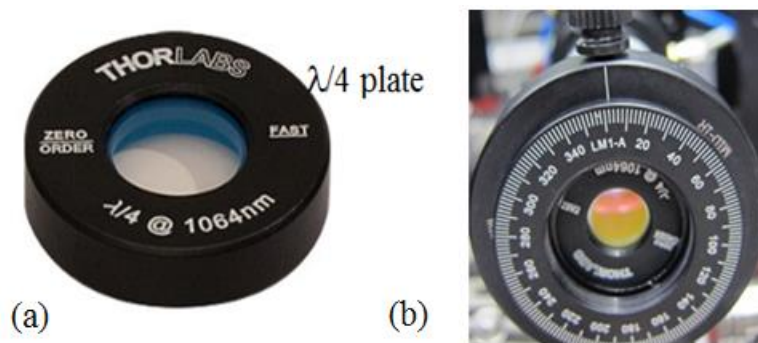
Figure 6.4. The Thorlabs quarter-wave plate that was used in our experiments. (a) Factory mounted. (b) Mounted in the rotational stage.

6.3   Conventional Electro-Optic Q-Switching Using Polarisers

The first conventional electro-optic Q-switching that we carried out involved using a thin film absorptive polariser that was chosen to occupy less cavity space and to produce short pulsed laser outputs. The thickness of this polariser was 1 mm and it was mounted on a rotation stage at an angle that transmits a linearly polarised beam as the lasing beam polarisation. The resulting laser system had a short cavity and operated at high repetition rates. Before the absorptive polariser was mounted inside the cavity at the position of the reflective polariser illustrated in Figure 6.1, it was first tested outside the cavity using a CW laser cavity.

Figure 6.5 illustrates an experimental optical setup to determine the ability of the polariser to prevent or allow transmission of laser light when the quarter- or half-wave voltages are applied to the Pockels cell. To achieve this, the polariser was set for maximum transmission of laser light when no voltage is applied to the Pockels cell and then placed on the path of the output beam.

126
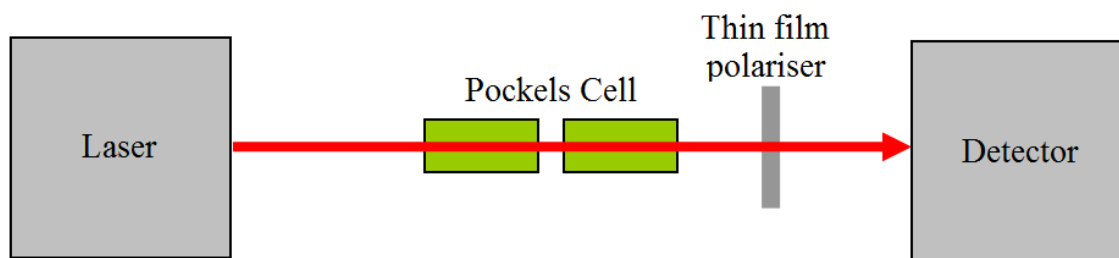
Figure 6.5. The extracavity polariser test setup serves to verify the operation of the absorptive polariser with the Pockels cell. It consists of the laser source, a Pockels cell, a thin film absorptive polariser and a detector, or a power meter. The function of the Pockels cell is to rotate the polarisation of the beam when specific voltage is applied, while the polariser permits a certain polarisation and blocks the other.

When a halve-wave voltage is applied on the Pockels cell, the linearly polarised beam is expected to undergo a rotation of 90° and get blocked by the polariser, indicating that the polariser is working properly. If it is the quarter-wave voltage that is applied to the Pockels cell, the linearly polarised light can be completely blocked when a quarter-wave plate is also mounted in front of the polariser. In such a setup, the beam undergoes a polarisation rotation from linear at 0° to circular by the Pockels cell and from circular to linear at 90° by the quarter wave plate.

In this research, an absorptive polariser was tested when the halve wave voltage was applied across the Pockels cell terminals. Upon switching the laser on, the measured output power increased with the increasing but low pump powers. However, when high pump powers were reached, the output powers transmitted by the polariser were lower than those measured without the polariser. This was an indication that the polariser was significantly attenuating the output beam. After observing this, we observed the absorptive polariser under a microscope and discovered structural damages (i.e. a crack and a burnt spot) as shown in Figure 6.6. We concluded that the absorptive polariser would not withstand the transmitted high average intensities that osculate in 1 μm resonators.

127
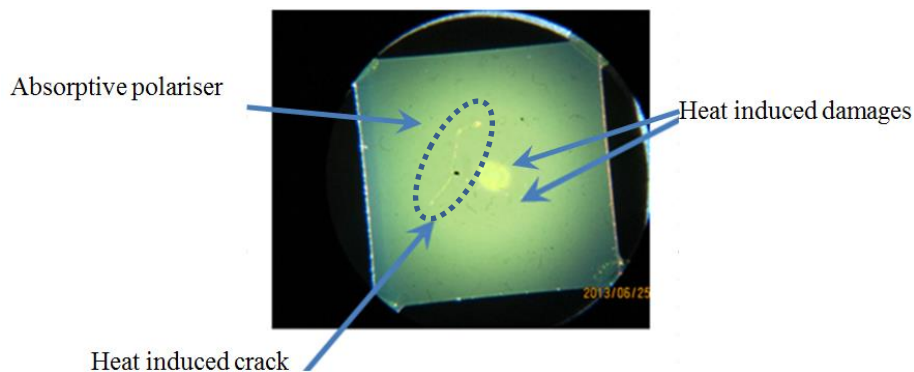
Figure 6.6. Testing the absorptive polariser outside the laser cavity. The polariser showed signs of damage, as shown by the circled crack and the white spot.

We subsequently switched to the reflective polariser which was mounted against a plastic mount (see Figure 6.3(a)) to eliminate electromagnetic interference (EMI) that would come as a result of the relatively high voltages that are involved in electro-optic Q-switching. However, we experienced difficulties in assembling the cavity as the material of the mount could not hold the polariser, because it could not handle stray pump light in the cavity. From this we deduced that this polariser would perform optimally in a different cavity configuration such as an L-shaped cavity, where pump light could be filtered to a different route. However, these cavities are significantly longer than linear cavities, with a corresponding increase in pulse lengths. Since a short pulse width was a crucial parameter that was pursued in this study, we decided to abandon this approach and develop a new Q-switching technique that does not require a polariser.

6.4   Cavity Instability Electro-Optic Q-Switching Technique

6.4.1   Theoretical Description of the Technique

In this section we introduce a technique that uses the gain medium's uniaxial nature and its different polarisation dependent thermal lenses along its axes, to emit a linearly polarised light

128

and to select the Q-switch lasing polarisation instead of a polariser. Nd:YVO$_4$ is well known for its emission of linearly polarised light [1]. The differing thermal lens of a uniaxial crystal has also been used to make the cavity stable for one axis and unstable for the other. In 2010, while reporting on scaling a diode-end-pumped Nd:YLF laser to higher average powers and higher energies per pulse, the authors designed their cavity such that is was stable for σ-polarisation and unstable for π-polarisation for the duration of their laser operation. This was done because there is a stronger negative thermal lens along the π-polarisation, which induces higher losses to the cavity than the σ-polarisation [66]. We used this same principle to show how the polariser can be eliminated at certain pump powers if the gain material is an *a*-cut uniaxial material with a significant difference in thermal lensing in the *a*-axis and the *c*-axis. The resonator in which the crystal resides must be designed so that, at a certain pump power range it is unstable when the intracavity beam interacts with one axis, while it remains stable for the other.

In order to understand this, one must recognise that the thermal lens strength can be drastically different for different polarisations. As seen in Equation (4.1), the largest contribution to the thermal lens effect in Nd:YVO$_4$ was from the spatially varying refractive index profile caused by a temperature gradient in the conversion of pump to laser light in the crystal. The focal length of the thermal lens is related to positive thermo-optical coefficients $\frac{dn}{dT}$ with the relation $f_{Th} \propto 1/\frac{dn}{dT}$. The coefficients that are unique to specific crystal axes of uniaxial laser materials – the ordinary and the extra-ordinary axes – are such that $\frac{dn_o}{dT} > \frac{dn_e}{dT}$. This means that the thermal lens along the ordinary axis is stronger than that along the extra-ordinary axis, in other words, the focal lengths of thermal lens effects along the ordinary axis are shorter than those of the extra-ordinary axis ($f_{Th-o} < f_{Th-e}$). According to Table 4.4 [91], the relation between the two focal lengths can be approximated as follows:

129

$$f_{Th-o} \approx \frac{1}{2} f_{Th-e} \qquad \textbf{(6.1)}$$

Therefore, the thermal lens along the ordinary axis is positive and roughly twice as strong as the extraordinary axis and it is normally not encountered because the extra-ordinary axis has a much higher gain. Lasing along the ordinary axis is therefore supressed, leading to the polarised output found in Nd:YVO$_4$ lasers.

The stability of flat-flat cavities is strongly dependent on thermal lens strength. Chapter 4 introduces two thermal lens dependent stability states. The first one occurs when the focal length of the thermal lens is shorter than the cavity length ($f_{Th} < L_{cavity}$), which results in an unstable cavity where no laser action takes place. The second state is when the focal length of the thermal lens is longer than the cavity length ($f_{Th} > L_{cavity}$), and it results in a stable cavity where laser action can take place. Furthermore, according to Equation (4.1), the focal length of the thermal lens is inversely proportional to the absorbed pump power. This implies that as pump power increases during the pumping process, the focal length of the thermal lens decreases (the thermal lens becomes weaker). As a result, the cavity will remain stable as long as the thermal lens focal length is still longer than the cavity length, which occurs at lower pump powers.

To add to this, electro-optic Q-switched cavities with uniaxial laser materials that have significantly differing thermal lens effects along their axes. In particular, Equation (6.1) describes the focal length of the thermal lens along the ordinary axis of a uniaxial Nd:YVO$_4$ crystal to be stronger and approximately half that of the extra-ordinary axis. As a result, such Nd:YVO$_4$ crystals, make the cavity to realise two stability states. One stability state occurs when the polarised intracavity laser radiation interacts with the axis with the strong thermal lens (the ordinary axis for the Nd:YVO$_4$ and similar crystals) after pumping above a certain pump power when $f_{Th} < L_{cavity}$ begins. The shorter thermal lens focal length leads to an unstable (quenched) cavity which can be seen in Figure 6.7. In practise, this is observed when

130

the output power begins to drop. For the axis with the stronger thermal lens, the output powers begin to drop at much lower pump powers.
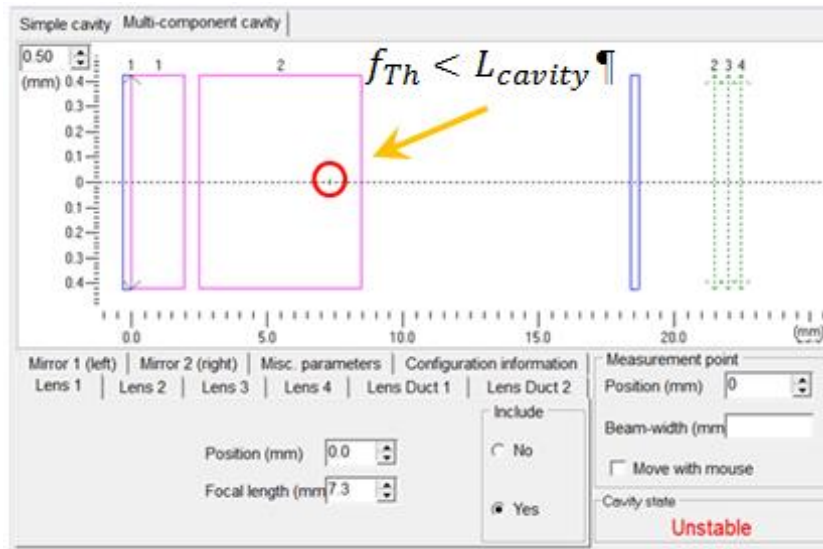
Figure 6.7. An unstable flat-flat cavity that is quenched by a strong thermal lens. The instability of the cavity is shown by the focal length of the thermal lens that is shorter than the cavity length.

The discussion is also true when the polarised intracavity radiation interacts with the weak thermal lens axis, as shown in Figure 6.8. When applying Equation (6.1) again, it can be deduced that the intracavity radiation interacts with the extra-ordinary axis that has a weak thermal lens (with a longer focal length f_{Th-e}). While the crystal is pumped and continues to absorb even higher pump powers, the cavity will remain stable and gets quenched after much higher pump values are reached. The quenching of the laser is observed when the output power begins to drop as pump powers are also increased at this stage. In this way the cavity can be designed to be stable along the high gain and weak positive thermal lens c-axis that emits a linearly π-polarised light, and to be unstable along the strong positive thermal lens a-axis for σ-polarisation.

131
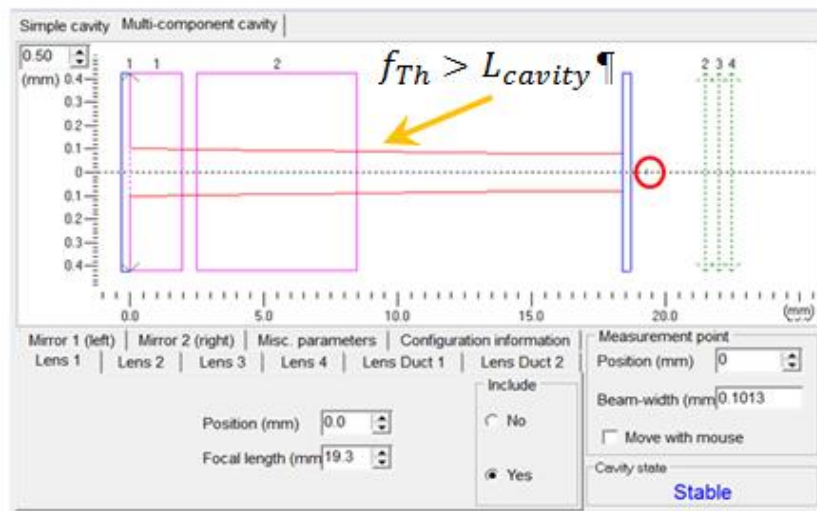
Figure 6.8. A stable flat-flat cavity that is NOT yet quenched by a strong thermal lens. The stability of the cavity is shown in the focal length of the thermal lens that is longer than the cavity length.

Equation (6.1) in connection with Equation (4.1) also implies that there are a range of pump powers where such a cavity is stable for the extraordinary axis (π-polarisation), but quenched for the ordinary axis. This is the situation that is exploited in this research to Q-switch the cavity.

6.4.2   The Expected Operation of the New Technique

In the absence of the polariser, this electro-optic (Pockels cell) Q-switching technique completely depends on the differing thermal lenses of the laser material and the remaining intracavity components. These components include the Pockels cell and the quarter-wave plate. By placing a quarter-wave plate in the flat-flat cavity, just before the output coupler, the polarisation of the polarised intracavity beam is rotated by a $\lambda/2$-wave (polarisation rotation: linear to circular) on every pass. Intracavity trapped photons therefore encounter different thermal lens strengths in the crystal during subsequent passes. On every second round-trip

132

photon encounter, the quenching grows stronger than the ordinary thermal lens, as shown by the beam represented by the black lines in Figure 6.9.

By introducing a Pockels cell to the cavity, the effect of the quarter-wave ($\lambda/4$) plate-mirror combination can be cancelled when a quarter-wave voltage is applied to the Pockels cell. The polarisation that encounters the non-quenching thermal lens will then oscillate, thus Q-switching the cavity.
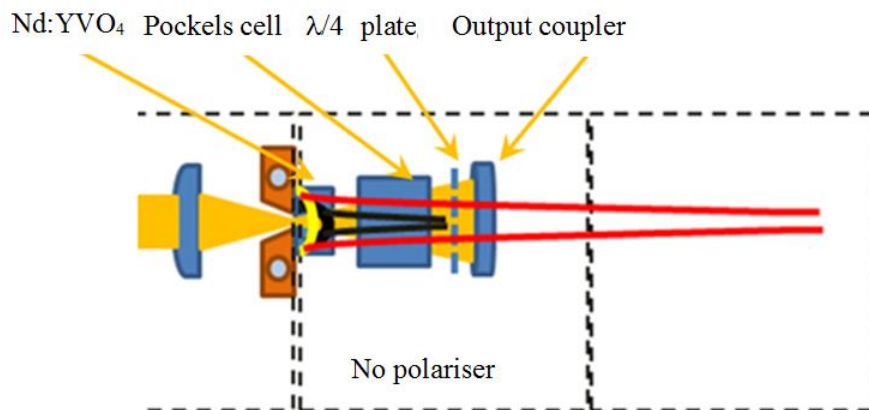
Figure 6.9. A flat-flat cavity containing a quarter wave plate. The cavity is quenched (black) on every second pass due to the losses introduced by the strong thermal lens along the a-axis. When the beam (read) interacts with the weak thermal lens the cavity becomes stable.

This concept was tested in the laboratory by adding both a quarter-wave plate and EOM Pockels cell to the cavity described in Chapter 4. The resulting setup is shown in the photo in Figure 6.10. The RTP Pockels cell was placed ~1 mm in front of the AR-coated (output) face of the Nd:YVO$_4$ crystal. The ($\lambda/4$) plate, mounted in a rotational stage from Thorlabs, was placed after the Pockels cell. The cavity was completed with a flat output coupler (diameter of 6.35 mm and coated for a 70% partial reflectivity) resulting in a 22 mm long cavity.

133
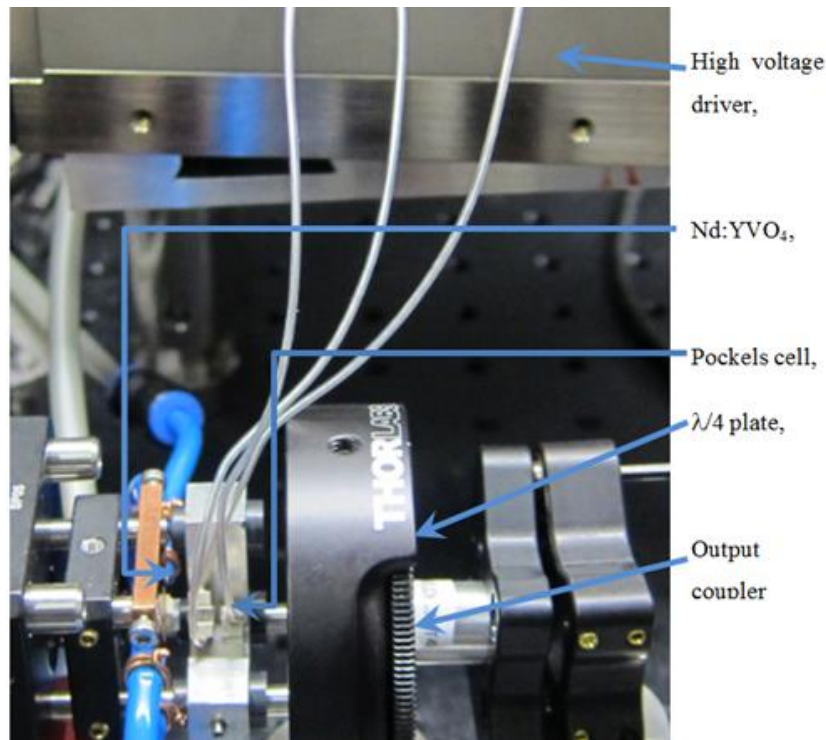
Figure 6.10. A photo of the quenching Electro-Optical Q-switching setup. It shows the Nd:YVO$_4$ crystal (mounted on the water-cooled copper mount), RTP Pockels cell, quarter-wave plate and the OC cavity.

6.4.3   Verification of the Losses on every Second Pass

The interaction of the intracavity beam with the two crystal axes with different gain and thermal property values resulted in high-loss and low-loss cavity states. These states were determined by observing the pump powers where the CW average power began to drop, which were different for the two axes. The pump power where the average output power began to drop indicated where the cavity quenched for that particular crystal axis. The pump powers were measured under CW (non-pulsing) conditions for both the high-loss and the low-loss state. Figure 6.11 graphically illustrates both states that are accessed by means of

134

beam rotation using a λ/4-wave plate. First the λ/4-wave plate was set at an angle so that it had no influence on the polarisation (low-loss state). This occurred when the cavity was operated on the high gain, weak thermal lens c-axis of the laser crystal interacting with the π-(vertical) polarisation of the beam. The resulting CW output power, as a function of incident pump power, is shown as blue diamonds on the graph. The low-loss state showed that the weaker thermal lens only quenches the cavity at an incident pump power of 7.2 W, much later in the pumping process.
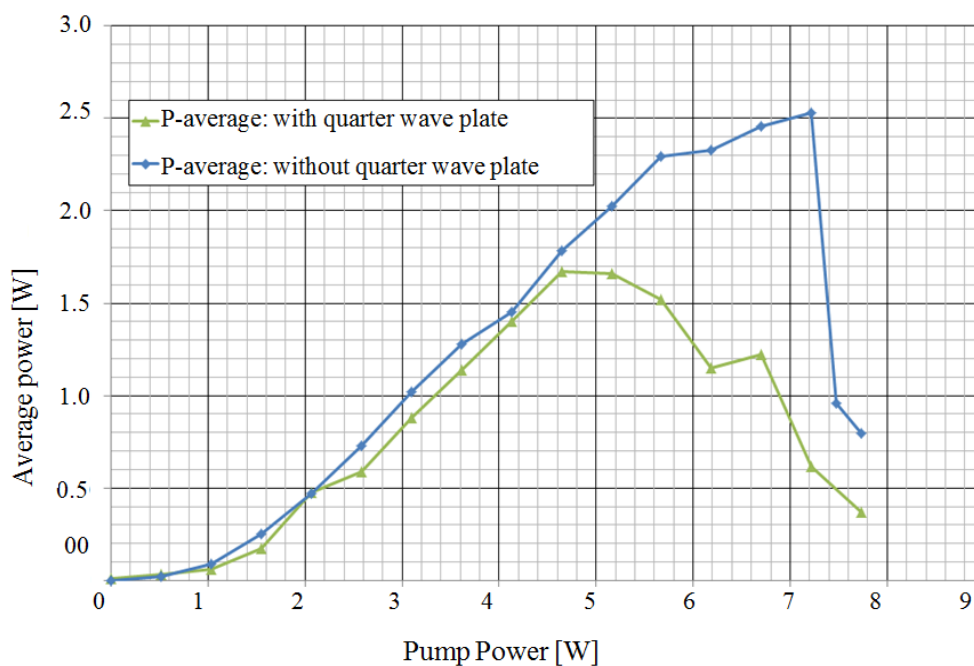
Figure 6.11. The continuous wave laser output when a wave plate is mounted in the cavity such that it has no influence on the beam polarisation (blue diamonds) and when it is set to give a λ/4-wave retardation resulting to a 90° rotation on every second round-trip.

When operated at this state (low-loss) during the Q-switch process, the cavity would remain stable and allow oscillation and the release of a pulse at high pump powers. Subsequently, the λ/4-wave plate was rotated so that together with the mirror, they can rotate the beam

135

polarisation by a λ/2-wave on every roundtrip. This resulted in a 90° rotation of the beam polarisation such that it interacted with the strong thermal lens a-axis and gave rise to the high-loss state of the cavity. This is represented by the curve with green triangles, which illustrates the resulting quenching of the cavity by the strong thermal lens crystal axis. This interaction of laser light with the strong thermal lens a-axis occurs on every second round-trip, thereby quenching the cavity at a pump power of ~4.6 W – as shown by the lower power roll-over of the curve. The green curve also illustrates a strong constraint (hold-off) when laser light interacts with the strong thermal lens in the crystal, indicating the high-loss state or a non-lasing state. Operating the laser on this condition prevents laser action due to the high losses the strong thermal lens introduces into the cavity. The range where this significant difference in quality between the two cavity states was observed was from ~4.6 W to ~7.2 W, and is the region in which this technique was expected to work. In that case, the low-loss (oscillation) and high-loss (hold-off) states correspond to the interaction of the intracavity beam with the high gain and weak thermal lens, and the low gain and strong thermal lens crystal axes respectively. When these two states have high power differences, high energy extraction can be expected during the low-loss state and high hold-off during the high loss state.

6.4.4 Q-switching Using the Cavity-Quenching Technique

The new electro-optic Q-switch technique was demonstrated with a flat-flat cavity as illustrated above in Figure 6.9. The experiment was conducted with the λ/4-wave plate fixed at an angle (position) that would cause the intracavity beam to interact with the weak thermal lens (where cavity can become unstable only at high pump powers), as determined by Figure 6.11. Without the polariser in place, the λ/4-wave voltage for 1064 nm light that was applied to this Pockels cell was ~1050 V. It was measured in our laboratories and was chosen because it was lower and relatively suitable to operate the Pockels cell for the small transverse dimensions that we used. This λ/4-wave voltage was applied momentarily to the Pockels cell

136

to Q-switch it. For instance at a 100 kHz repetition rate, the $\lambda/4$-wave voltage was applied for 42 ns, but stable Q-switched pulses were only observed from ~5 W to 6.8 W, as expected – well into the pump power range established in Figure 6.11. At pump powers higher that 7.2 W, no stable pulses were observed, which showed that the concept is feasible for a specific pump power range.

Figure 6.12 shows the pulse durations (navy diamonds), peak power (brown diamonds), average power (green triangles), and the pulse energy (purple stars) of the EOM Q-switched laser as functions of incident pump power at a PRF of 100 kHz. At pump power lower than ~5 W, no stable pulses were observed because of the differing thermal lens effect observed along the perpendicular a- and c-axes of the uniaxial Nd:YVO$_4$ crystal, starting from low pump powers of ~4.6 W. At pump powers greater than 5 W, the differences between the two cavity states were high enough to prevent laser action during the high-loss state and emit pulses during the low-loss state.

137
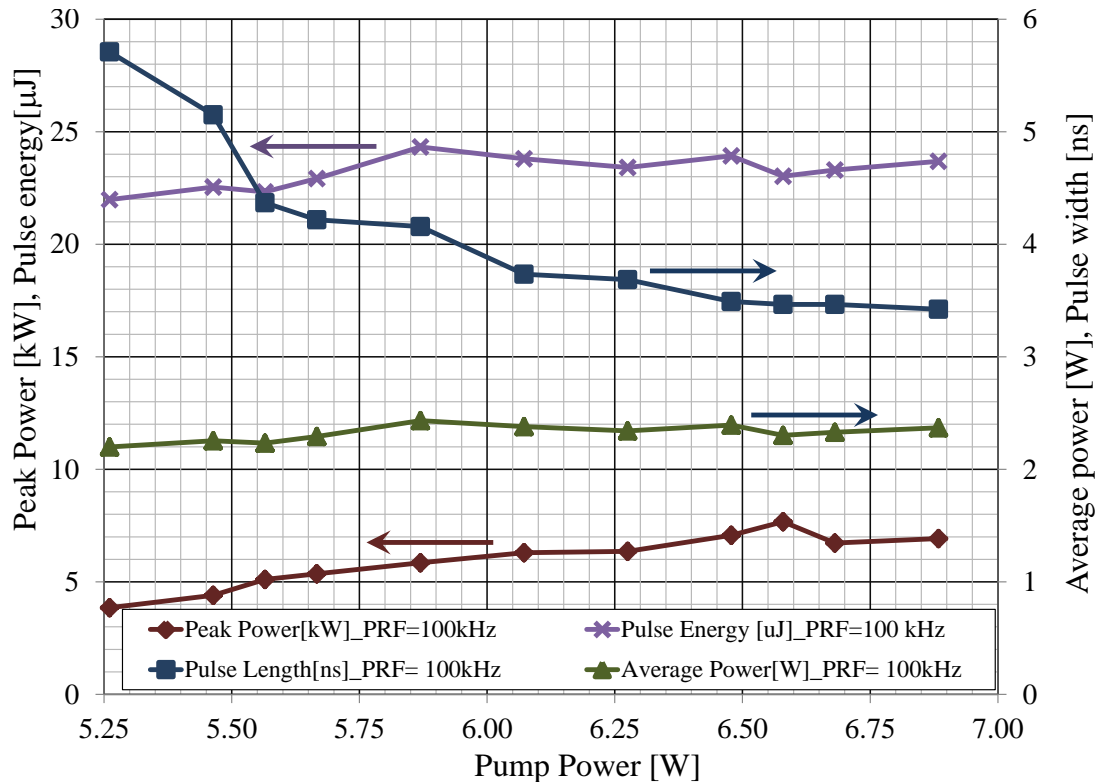
Figure 6.12. Pulsed average power, peak power, energy and pulse widths in the stable Q-switch pump power region measured at the PRF of 100 kHz. The arrows indicate the axes that describe the graphs displayed.

The results obtained exhibited an increase in average power from 2.2 W at the pump power of 5.25 W to 2.4 W at the pump power of ~5.9 W, after which it began to roll over, indicating that the high heat load in the Q-switched laser [18] was taking effect. This resulted in a slight decrease of the output power with the increasing pump power, which indicated that the cavity was becoming unstable. However, the roll-over effect is a lot less pronounced than what was observed for the CW measurements when the quarter-wave plate was set to introduce losses due to the λ/2-wave rotation for every second double pass in the cavity.

The average pulse duration decreased with increasing pump power from 5.7 ns at 5.25 W of pump power to a minimum of 3.4 ns at 6.8 W of incident pump power. This resulted in a

138

corresponding increase of peak power from 3.8 kW (5.25 W pump power) to 7.7 kW (6.6 W pump power), after which a roll-over was observed. This roll-over effect in the peak power dropped to only 6.9 kW at the pump power of 6.8 W.

At each measurement point, the pulse duration was measured using an oscilloscope. Figure 6.13 shows one of the pulse profiles obtained in this experiment. It shows a stable pulse that can be useful in ranging applications. This experiment was carried out at different pulse repetition frequencies and yielded different results.
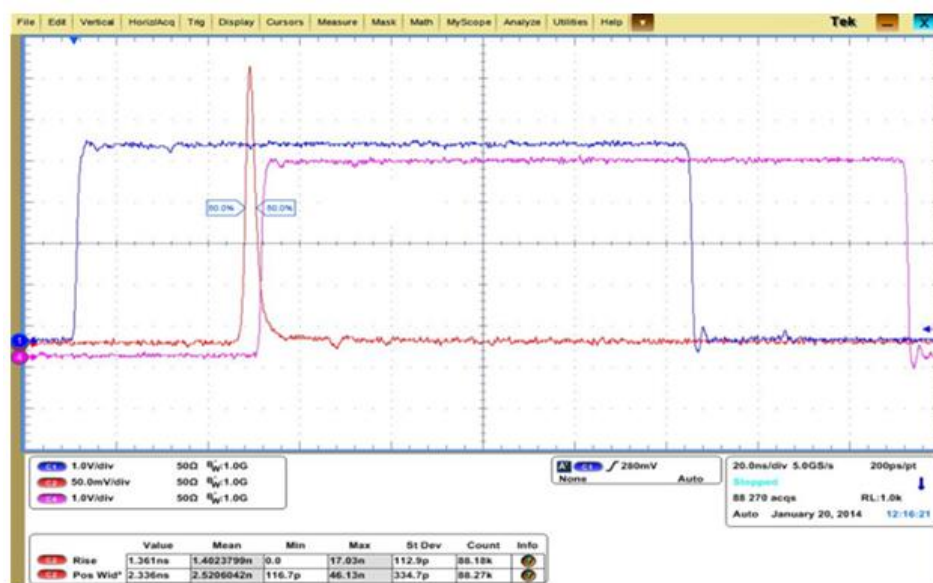
Figure 6.13. The typical optical pulse trace obtained during the Q-switch process. The lowest was 3.4 ns obtained at the incident pump power of 6.8 W. Also shown are the opening and closing pulses for the high voltage applied to the Pockels cell.

The results shown in Figure 6.14., are the average (green) and the peak powers, as well as the pulse energy as well asand the pulse widths (blue), that were measured at a pump power of 6.5 W for increasing PRFs, ranging from 75 to 150 kHz, in steps of 25 kHz. The graph reveals that the pulsed laser average power increases slightly as the PRF increases. In this case, since at 75 kHz the PRF was already high, and the average power (2.3 W) was already close to the

139

CW value of 2.61 W, it increased by just less than 12% – from ~2.2 W to ~2.53 W. The pulse energy increased from 22.6 to 25.3 µJ, by approximately the same percentage, which indicated notable in the photon population as the PRF increases. More significant was the pulse duration increase from 3.1 ns at 75 kHz to just over 4.5 ns at 150 kHz, which indicates less that at higher PRFs, the precision of ranging measurements is reduced.
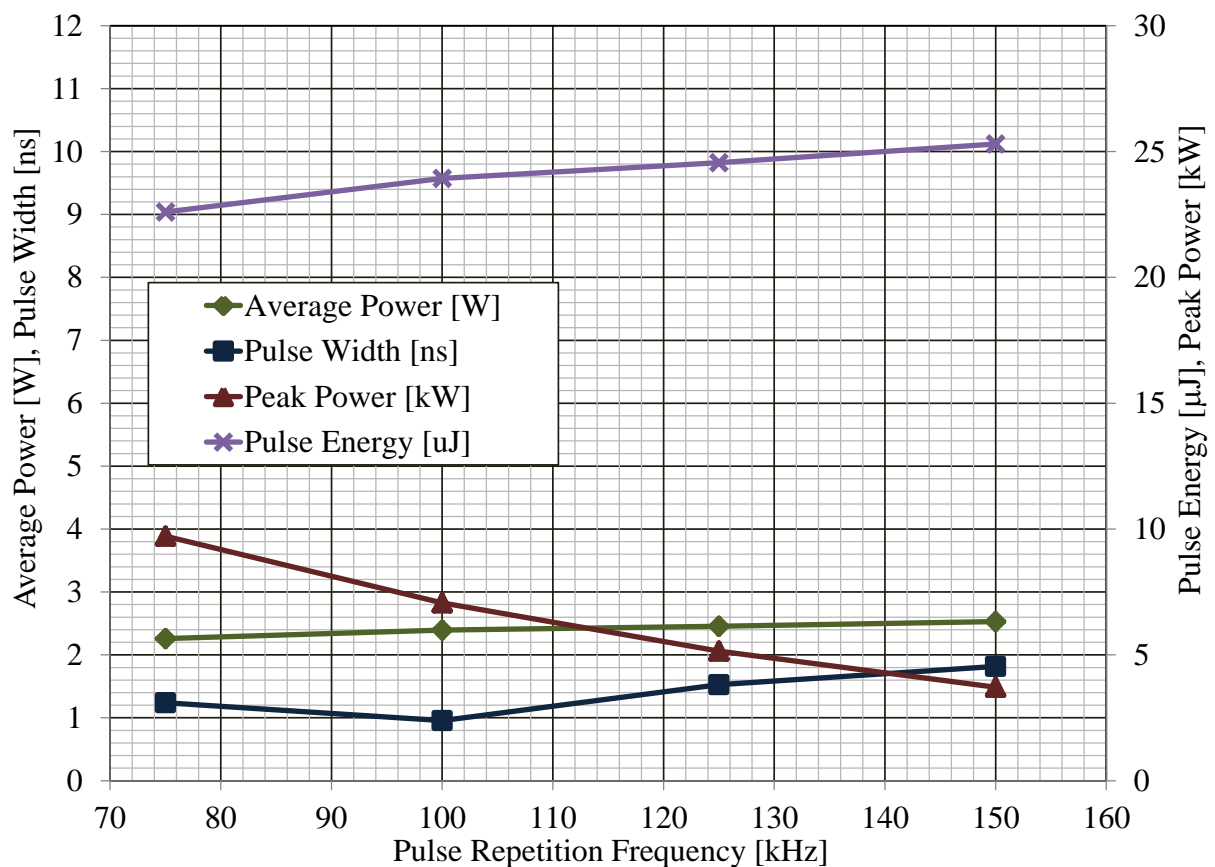
Figure 6.14. Pulse average power, pulse energy, pulse widths and peak powers measured for a stable pulse at the pump power of ~6.5 W, which lies within pump power Q-switch region.

The combined effect of this investigation is that the peak power was decreased by ~59% from 9 kW to 3.6 kW. While this decrease was significant, the peak power was still high even at

140

the PRF of 150 kHz. This confirms that Q-switched laser output with high peak powers and short pulse widths can be obtained at various pulse repetition frequencies with this technique. This also means that when the PRF is increased for higher resolution ranging measurements, both the precision and the range of the measurement will be compromised – as seen by the elongation of the pulse widths and the decrease of the peak powers.

6.4.5 Discussions

This section serves to account for the results we obtained in our research and compares them with similar research results that are already in the public domain. Table 6.2 summarises the designs and results of the EOM experiments carried out and presented in this chapter, together with the similar electro-optic Q-switched laser system. The laser that is considered for this discussion is the one that also omitted the polariser. The remainder of EOM research accounts are listed in Table E.1 and discussed in Appendix E.

A research account was reported in 2011, where the combination of the Pockels cell and the laser crystal with the output face cut at Brewster angle was used to Q-switch the laser [108]. Figure 6.15 illustrates their experimental setup. As was intended, the shorter cavity design in this research enabled the generation of short pulses. In their research Feng et al. (2011) demonstrated a compact E-O Q-switched 1 ns laser that was developed using a Pockels cell in the absence of a polariser. To achieve the electro-optic effect, the output face of the $Nd:YVO_4$ crystal was cut at a Brewster angle in order to select the lasing polarisation.

141
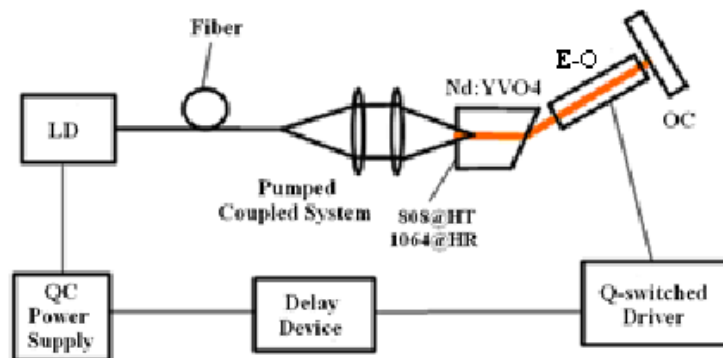
Figure 6.15. An electro-optic Q-switched laser systems using a Brewster angle as a polarisation selector [108].

The crystal was pumped with a pulsed laser and from this arrangement, desirably short duration (1.049 ns), high energy (0.32 mJ) and high peak power (300 kW) pulses were obtained [108]. However, the pulse repetition frequency at which the laser was operated was in the Hertz scale. That means that any measurement resolution that can be measured would be extremely low. The results they obtained far exceeded the results generated in this research, and even though the Brewster angle crystal cut concept they implemented was good, this laser could not be considered for ranging applications because of the low PRF. Low PRF gives rise to low resolution measurements.

Based on the above results, we can consider the EOM Q-switched Nd:YVO$_4$ laser developed in this research better suited and novel, because it was compact (22 mm long cavity), emitted short pulses of 3.4 ns and 7.7 kW peak power at the PRF of 100 kHz. This enables a LADAR device that can be built with this laser to take high resolution, high precision and long-range measurements. We achieved this by taking advantage of the high gain properties of the laser material; we employed effective cooling of the laser material, and selected a TeO$_2$ AOM that has high diffractive efficiency, as well as   an optimum output coupler.

142

With this work, we used the differing thermal lens effects of a uniaxial laser material to replace the traditional polariser in the cavity during the electro-optic Q-switch process. We demonstrated an advanced use of thermal lensing, where the intracavity laser polarisation was rotated by the Pockels cell toward the strong thermal lens to introduce losses during the high-loss, and rotated towards the weak thermal lens during low-loss state. This is the first time this was ever done, and it was done successfully. With this work we introduced a novel technique of Q-switching lasers with an electro-optic Q-switch, and the results showed that it is a viable and alternative technology that can be used in LADAR devices. We consequently presented the results of this work at an international conference on Advanced Solid-State Lasers that was held in Boston, in 2016.

Table 6.2. Laser design that is developed and the results that are generated in this research.

Authors, Year	Pump source/ scheme, Power [W], wavelength [nm], radius [μm]	Gain medium + Doping [%]	Crystal Dimensions [mm3]	Q-switch device	Cavity length (mm)	PRF [kHz]	Pulsed Average power [W]	Pulse Energy [μJ]	Pulse Width [ns]	Peak Power [kW]	Ref.
E. L. Maweza, 2018	End, 6.5, 808, 100	1 at.% Nd:YVO₄	3×3×2	RTP EOM	22	100	2.3	23	3.4	7.7	This work
Chi et al., 2011	End (semi CW), 200, 140 (Peak power), 808	1% at. Nd:YVO₄	3×3×2.6	Electro-optic Q-switcher	20	0.1		320	1.049	300	[108]

6.4.6   Conclusion and Future Work

In this chapter we discussed our development of a relatively high peak power (7.7 kW), short pulsed (3.4 ns) laser at the high PRF of 100 kHz. This was achieved with the new thermal lens dependent Q-switch technique demonstrated in this research. This chapter demonstrated our new technique with a uniaxial laser material, Nd:YVO$_4$, selected for its high gain properties and differing thermal lens effects along its axes. Two major advantages of this new technique for the laser cavity are the reduced cavity length and reduced intracavity losses. The advantage that designing shorter cavities provides is deduced from its direct proportion to the photon decay time in Equation (3.8). Shorter photon decay times in turn give rise to reduced pulse lengths. We strongly believe that the short cavity we designed contributed to the short duration pulses we produced, even though we did not reach 1 ns. Also, with the reduced number of components in the cavity (as the polariser was not used), associated losses were eliminated, thus enabling the laser to reach relatively high peak powers.

A few things could not be achieved with this research, namely a small and compact conventional electro-optic laser system could not be developed successfully, and the desired 1 ns pulse width output was not reached. The difficulty in reaching these desired outcomes was discussed, and still more efforts can be made/measures be explored in future to scale up the laser we demonstrated. Such measures will enable improved thermal management and pumping the laser system harder (high pump powers) to achieve high output peak powers and further shorten pulse lengths. The measures can include mechanisms to prevent stray pump light from heating up the optical elements [104] of the system, such as the laser material and Pockels cells at positions off the optical path, which can negatively affect the thermally stabilised Pockels cell.

The following concepts that have been drawn from the reviewed literature can be implemented in future work. The focus can be on improved thermal management for high power laser operation, on the gain achieved and on direct amplification.

The laser can be scaled up for improved thermal management as well as high gain in the following ways:

- Use composite laser material, where two crystals are bonded together, making one portion of the crystal to be doped while the other is not ([109], [35])
- Pump the crystal directly at its upper laser level of 880 nm [109]
- Consider the option of an amplifier

To increase the gain:

- Increase the crystal length slightly to allow for harder pumping, high absorption and high gain to obtain higher peak powers with similar or even shorter pulse widths

If all fails, and high peak powers are still required, the following can be done:

- Amplify the laser using amplifier crystals, including Nd:YVO$_4$ and Nd:YAG
- Explore different forms of laser amplification such as MOPA, side-pumped Nd:YAG amplifier, and fibre amplifiers

Chapter 7

7. Extended Results Analysis: Current Research vs Literature

7.1   Introduction

In this chapter, we seek to extend the comparison and discussion of the design and results of pulsed laser systems to the remaining techniques reported in literature. The chapter presents a critical comparison of the findings we observed in both the AOM and the EOM experiments in Chapters 5 and 6, with the most comparable results of other techniques that are reported in literature, as introduced and briefly discussed in Chapter 2. These techniques include gain switching, cavity dumping, passive Q-switching, fibre lasers and amplified lasers. The accounts that are presented in this chapter are selected from the broader reviews and summaries presented in Appendices A, B and C, because they can compete with our research for the intended ranging applications.

7.2   Summarised Parameters of the Competing Pulsing Techniques

Few other research accounts have come close or obtained better results than we are presenting in this research. Table 7.1 summarises the results that were obtained in Chapters 5 and 6 as presented in the earlier discussions, and includes them here for the sake of comparison. The first set of results with which we compare our results, are those obtained with gain switching. We selected the research account by Wang et al. (2007), because they conducted their research at high PRF and obtained kW peak power pulses. Typically, gain switched lasers operating at high PRFs (100 kHz) generate long low peak power (< 1 kW) and long duration ($\geq$ 40 ns) pulses. However, in this case they implemented intense pumping (1.1 W) to achieve high gain and short build-up times for the output pulses. This enabled them to generate > 3 kW peak power pulses, but they could not go lower than 30 ns in pulse durations [12].

147

Table 7.1. Laser design that was developed and the results that were generated in this research.

Authors, Year	Pump source/ scheme, power [W], wavelength [nm], radius [μm]	Gain medium + doping [%]	Crystal dimensions [mm³]	Q-switch device	Cavity length (mm)	PRF [kHz]	Pulsed average power [W]	Pulse energy [μJ]	Pulse width [ns]	Peak power [kW]	Ref.
E. L. Maweza, 2018	End, 6.5, 808, 100	1 at.% Nd:YVO$_4$	3×3×2	TeO$_2$ AOM	16	140	2.8	20.6	1.97	10.43	This work
				RTP EOM	22	100	2.43	24.3	2.21	10	

Table 7.2. Gain switching research account that has been selected for comparison with the current research.

Authors, Year	Pump source/ scheme, power [W], wavelength [nm], radius [μm], NA	E$_{pulse@Threshold}$ [μJ], P$_{peakpump}$ [W], PRF [kHz], pulse width [ns]	Gain medium + doping [%]	Crystal dimensions [mm³]	Cavity length (mm)	PRF [kHz]	Pulsed average power [W]	Pulse energy [μJ]	Pulse width [ns]	Peak power [kW]	Ref.
Y. Wang et al., 2007	- ,808, 50, 0.12	-, 1.1 W,	1.8 at.% Nd:YVO$_4$	Area × 1	1	100-1000	0.1	1E-04	32	3.063	[12]

148

Compared to our laser, these results still fall short. The peak power is more than three times lower than the values we obtained in both our AOM and EOM accounts and the pulse duration is much longer.

When we extend this discussion to cavity dumping and passive Q-switching in Table 7.3 and Table 7.4, stronger cases are observed. Cavity-dumped lasers have important advantages in favour of generating high peak and short pulsed outputs. Firstly, the absence of output coupling during the growth of the giant pulse within the resonator reduces the lasing threshold. Next, the short pulse widths that the laser system generates are in the order of the round-trip time of the resonator, thereby reducing the need for short cavity lengths and high round-trip gain when short pulses are required. Lastly, the peak power inside the cavity is not more than the output peak power, because the absence of a partially reflecting mirror allows not just partial transmission, but the entire pulse to be emitted from the cavity [110].

We reviewed several of cavity-dumped research accounts and selected from them those with results that are comparable to our research. Firstly, He et al. (2011) experimented with end-pumping the 0.3% at. doped 8 mm long Nd:GdVO$_4$ crystal, with a large mode (320 mm radius) high (21.9 W) pump power, in a cavity-dumped laser system. The crystal was chosen for its better thermal conductivity (two times higher) when compared to Nd:YVO$_4$ crystals; as a result they were able to pump harder and obtain high peak power pulses. However, the pulse widths that they generated would not go lower than 5.1 ns at the PRF of 50 kHz, and even at lower PRFs [18]. The next account we saw as comparable to our results, was a directly pumped composite Nd:GdVO$_4$ crystal, where an 8 mm long portion of the crystal was 0.3% at. doped and bound on the input pump side by a 2 mm long undoped GdVO$_4$ crystal. This work was done by Yu et al. (2012) and generated 3.8 ns pulses with 34.4 kW of peak powers at 100 kHz of PRF. These results show that cavity dumping is the best technique that can be used to generate pulses as we intended. But, in all cases that we looked at, the cavity length was long and would not fit the limited space in which the LADAR device needs to be mounted.

149

Table 7.3. Recent cavity-dumped laser design showing the shortest pulse widths that have been achieved with this technique.

Author, Year	Pump source/ scheme, power [W], wavelength [nm], radius [µm]	Gain medium + doping [%]	Crystal dimensions [mm³]	Cavity dumping device	Cavity length (mm)	PRF [kHz]	Pulsed average power [W]	Pulse energy [µJ]	Pulse width [ns]	Peak power [kW]	Ref.
P. He et al., 2011	End, 21.9, 808, 319	0.3 at.% Nd:GdVO$_4$	3×3×8	RTP Pockels cell	175	50	5.1	0.0001	5.5	18	[18]
X. Yu et al., 2012	End (Direct), 30, 879, 320	0.3 at.% GdVO4/ Nd:GdVO$_4$	3×3×(8+2)	RTP Pockels cell	175	100	13.1	0.0001	3.8	34.4	[109]

Table 7.4. Research accounts of Passive Q-switching in the past two decades including low and high PRF operations together with their corresponding outputs.

Authors, Year	Pump scheme, λ_p [nm], radius [µm], power [W]	Gain medium + Doping [%]	Crystal geometry [mm³]	Cavity length (mm)	Q-switch device, transmission [%], thickness [mm]	PRF [kHz]	Pulsed average, threshold power [W]	Pulse energy [µJ]	Pulse width [ns]	Peak power [kW]	Ref.
C. Li et al., 2000	End, 807.6, 350, 8.1	1.2at.% Nd:GdVO$_4$	Area × 2.5	140	Cr^{4+}:YAG, 80, 0.66,	69	1.4, 1.6	20	32	0.625	[111]
Y. G. Wang et al., 2006	End, 808 100, 1.6	1.0% at. Nd:YVO$_4$	3×3× 1.15	12	GaAs/ In0.25Ga0.75 As/ GaAs	2000	0.135	0.063	8.3	7.5	[112]

150

Passively Q-switched lasers were reviewed in this research and some have properties similar to those desired in this research. Table 7.4 presents the most competitive research account among the passively Q-switched lasers. The table shows that with laser systems of a cavity length as short as 12 mm and pulse durations of < 9 ns, comparable peak powers of 7.5 kW can be achieved at PRFs of up to the MHz range. Of the list presented in Chapter 2, two cases stand out. They are the Nd:GdVO$_4$ (1 mm long) and the Nd:YVO$_4$ (5 mm long) AOM Q-switched accounts with doping that is comparable to our research (1% at. and 1.1% at. concentrations).

Researchers used design parameters that included the selection of pumping schemes, the laser materials and the cavity dimensions. Most often, the longitudinal/ end pumping scheme preferred over transverse or side pumping, ~ 808 nm for the pump wavelength and ≤ 8.1 W pump powers have been reported. Mostly used laser materials include Nd:YVO$_4$, Nd:GdVO$_4$, Nd:YAG crystals with doping concentration ranging from 0.5 to < 2.0 at. % and lengths varying from < 1mm to ≤ 10 mm, and suitable crystal face coatings for pumping and laser wavelengths).   The selection of Q-switch elements (saturable absorber, coatings: laser wavelength transmission) and cavity parameters (length, mirror radii of curvature and coatings) ([30], [32], [33], [111]) are important in laser design. While the passive Q-switched laser operating at a PRF of ~70 kHz was the closest to the required ~100 kHz that we found in literature, and while it generated a comparable 20 μJ of pulse energy, the cavity length and the pulse durations were long and peak powers were low [111]. In another account, the peak power of over 7 kW with a short cavity of 12 mm was comparable to our results and the required 10 kW and ~8 ns pulse durations generated were long, but still less than 10 ns. However, the repetition rates were quite high. Apart from these accounts, a high energy (157 μJ), and high peak power (26 kW) passively Q-switched laser was reported in 2003, with pulse lengths of 6 ns, but it was generated at ~25 kHz of PRF [113], which was not suitable for our applications. This ruled out passive Q-switching as an alternative for the specific intended applications of our research.

With the lasers that we developed, we believe that we have revitalised active Q-switching as a laser pulsing technique. With AOM active Q-switching for instance, we managed to reach a

high PRF laser operation that generated a combination of short pulsed laser output with both high energy and high peak power pulses within a short cavity. This was so, even though double pulsing was observed at high pump powers. To curb this, the laser system can either be optimised to operate up to the highest pump power before double pulsing takes place or to reduce the low-loss (high-Q) window and close the second pulse out. This, however, would reduce output energy as well as the peak power.

With the EOM research, we established or exposed the difficulties and limitations that developing compact (small) actively Q-switched laser systems encountered when operated with conventional methods. This led to the development of a new electro-optic technique, which was demonstrated successfully. With this technique, we demonstrated a successfully operating compact device that can generate stable short pulsed and high peak power output at high repetition rates and compete well with devices developed through established techniques.

7.3   Conclusion

Our research, in both AOM and EOM Q-switches, managed to reach the combination of high PRF operation with short pulsed and high peak power output. Furthermore, the new technique that we demonstrated competed well and exceeded most results found in literature. This is a fact, even while we acknowledge that some reports would obtain higher energy, high peak powers at high PRFs but with long pulses [38]. Because other reports do not match our combined contribution of high PRF ($\gtrsim 100$ kHz) operation, short pulse ($\lesssim 2$ ns) and high peak powers ($\gtrsim 10$ kW), we believe we have made the right choice.

Part 2: Mid-IR Spatial Light Modulator Beam Shaping

Chapter 8

8. Mid-IR Modal Decomposition with Spatial Light Modulators

8.1   Introduction

The electromagnetic spectrum is an unlimited natural resource that is available to us to exploit for many applications without depleting it. As a result, light has been researched quite extensively and there is still room for more research. In particular, light in the form of lasers has been researched through laser development (see Part 1 of this research), laser beam shaping, etc. Beam shaping is one sector of laser research that has grown and matured over the past decades because it has attracted much interest. It is achieved by using optical elements to shape, transform, tailor, or structure a particular beam shape (such as a Gaussian beam) into any desired transverse profile [114], thus enabling that beam to be used for different applications. Optical elements can either be physical and use physical optics elements or digital and use dynamic screens. Physical optics elements that have been used to structure laser beams include spiral phase plates (SPP) to create beams with helical wavefronts and phase singularities at their axes, such as the Laguerre Gaussian beam [115], axicons to create Bessel beams [116], or a computer-generated hologram etched on a piece of glass to create any desired static beam shape. The digital optics elements involve mainly a dynamic spatial light modulator (SLM), which consists of a programmed and electronically addressed liquid crystal display [117].

Figure 8.1 (a) illustrates one example of beam shaping where a Gaussian beam on the left is shaped with an SPP into a Laguerre Gaussian beam LG_{lp}: LG_{00} [118]. Figure 8.1 (b) shows that the reverse is also true. For the LG_{lp} mode creation, beams take the shape of the SPP that is helical and is propagated as such. In this shape, the beam possesses a new property per photon, an orbital angular

momentum (OAM) described by $l\hbar$, where l is the same as the first index of the LG_{lp} mode and is called an unbounded azimuthal mode index [119]. This index indicates the order of the helical phase and the topological charge of the LG_{lp} mode [120]. The index $p \geq 0$ represents the radial index mode that indicates the number of radial nodes [121].
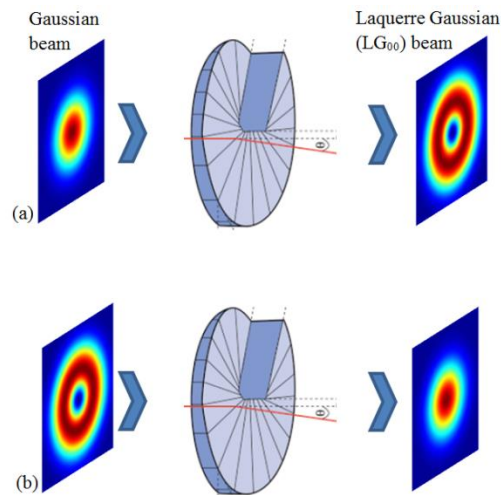
Figure 8.1. Beam shaping using a spiral phase plate [118]. (a) The creation of an LG_{lp} mode from a Gaussian beam. (b) The creation of a Gaussian beam from an LG_{lp} mode beam.

The shaping of laser beams into OAM-carrying Laguerre Gaussian beams can be sufficient by itself, because the phase structure that consequently rotates in space during propagation enables the beam to transfer its momentum. This capability can be used to spin microscopic particles, to optically trap and manipulate particles, and to manipulate as well as perform logical operations and free space communication with OAM states [120]. Instead, beam shaping has been taken further, to reconstruction and detection through a technique called modal decomposition. The shaping of laser beams into other beams (such Bessel beams, as well as several others) has unique importance and provisions, which have also attracted wide interest. While they will not be discussed in this study, information about them can be obtained from different other sources [118].

The concept of this thesis employs the modal decomposition of light into orthogonal basis functions, where the resolution is contained in the basis function and not in the finite coefficients needed to reconstruct the field. Modal decomposition decomposes an unknown light field into a superposition of orthonormal basis functions or modes, to determine the constituent components

154

that make up the optical field of interest [2]. The process is specifically achieved when the modes that underlie an optical field, such as its relative phases and amplitudes, are measured, thus inferring all the physical quantities associated with it – for instance its intensity, phase, amplitude, wavefront, beam-quality factor, Poynting vector and orbital angular momentum density. With physical optics however, such as the SPP, these advanced measurement techniques have been difficult to realise because they fail to provide the phase information that is important to characterise a laser beam. It has been the introduction of dynamic spatial light modulators that provided a solution to the challenge of characterising light with a number of advanced measurement techniques [122]. Modal decomposition using SLMs is discussed in detail in later sections.

8.2   The Structured Mid-IR Light Potential

We illustrate structuring (shaping) the mid-IR region by extracting the wavefronts via modal decomposition that we tested on a Ho:LiLuF$_4$ laser source. Mid-IR light provides a benefit of not only operating during the day, but also in the night [123]. It also has a superior transmission through the atmosphere and a better penetration through fog, thus enabling the creation of links for areas where there are adverse weather conditions ([124], [125]). Unlike at shorter wavelengths where conventional systems operate, the 2 µm wavelength region has attracted the attention of researchers because of its "eye safe" nature, which offers laser systems exceptional advantages to operate in free space applications.

Figure 8.2 shows how with a transmission curve of the mid-IR wavelength range, only from 2 to 2.5 µm, the available wavelengths can be exploited for atmospheric-based applications. Shaping light in the mid-IR region will introduce a number of new applications such as higher-bandwidth free-space communication. Areas where structured light has played a role with other wavelength ranges can be extended to the mid-IR region. Two kinds of modal decomposition are demonstrated in this chapter, namely the azimuthal (phase-only) and complex modulation (phase-and-amplitude) of the mid-IR regions. Research in azimuthal modal decomposition is motivated by the high interest in helically phased modes that carry orbital angular momentum [126]. Phase-and-amplitude modal decomposition is topical because of its ability to retrieve the full information about the investigated field by measuring the modal phases and amplitudes of the field of interest [127].

155
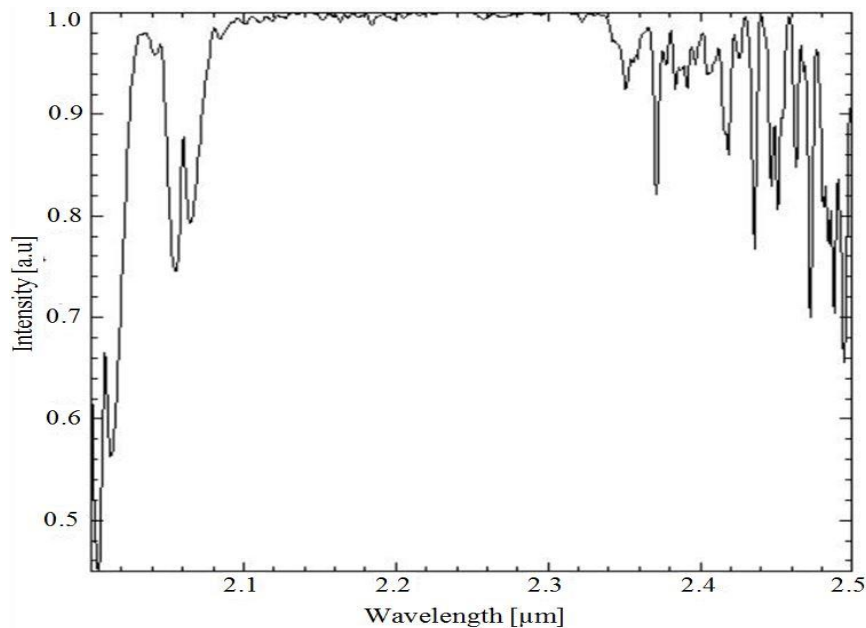
Figure 8.2. Atmospheric transmission at the wavelength range of 2.00 to 2.5 μm [128].

Since the manipulation or the shaping of laser light has so far been done extensively in the visible and near Infrared regions only, mid-IR beam shaping opens a window to a new sphere.

One of the instruments used to shape (or create) unique structured modes is a computer-generated hologram (CGHs) encoded on a spatial light modulator (SLM). With these CGHs we can create, reconstruct and detect structured optical fields via a process called modal decomposition.

8.3   Modal Decomposition Literature Review

The discovery of the importance that different light shapes have, has led to much interest in laser beam shaping. The latter has developed over the years from using diffractive and refractive optical elements, to using spiral phase plates and lately to the use of spatial light modulators (SLM). In addition, while all electromagnetic wave propagations support a multiplicity of modes, experimental techniques such as modal decomposition – with the known techniques at the time – failed to produce phase information [122]. SLMs, which are also employed in this research, provide a dynamic beam-shaping capability that opens the field up to more research and applications.

156

8.3.1   Earlier Light Characterisation: Passive Optical Windows

Characterising light (optical fields) dates back decades and has become a useful basis for applications of lasers and optical components. As a result, measurement techniques have been developed to provide information about the properties that these optical fields possess [129].

It was not until Shapira et al. (2005) that modal decomposition of light fields by implementing a non-interferometric approach at the output of a general waveguiding structure was introduced. This was done through the mapping of a two-dimensional field distribution onto the one-dimensional space and by using a phase-retrieval algorithm to extract the amplitudes and phases of all the guided modes. To validate their measurements, they used this approach on 16 modes at the output of a fibre output and examined their interactions [122].

Modal decomposition was developed further by among others Kaiser et al. (2009), where they presented a mode analyser (MODAN) based field reconstruction technique to obtain unambiguously an experimental solution to the modal decomposition problem. A MODAN is a special passive diffractive optical element, which is also referred to as an optical correlation analysis tool [130], on which a computer-generated hologram with a specific transmission function (to be defined later in the chapter) is etched. The advantages of the MODAN technique include simplicity, ability to perform modal decomposition in real time and to extract beam properties of interest without time-consuming numerical analysis. While satisfactory results could be obtained, the technique was limited by its static nature, low diffraction efficiency and low signal to noise ratio. It is also limited in that the intermodal phase cannot be measured with this method if the chosen reference (fundamental) mode is not excited sufficiently and a second reference mode is introduced on additional branches of the hologram [131]. Research on extracting beam properties continued with many researchers, including Schmidt et al. (2011), who used a computer-generated hologram in an all-optical measurement of modal amplitudes to determine the beam propagation ratio M^2 of laser beams in real time [132]. To do this, they measured modal weights, from which they calculated the beam propagation factor M^2 and compared their results to values obtained from traditional measurements. From this method, the measured M_x^2 deviated by 13% and M_y^2 by 5% from the expected values, which confirmed to the authors that the method was functional and could be used whenever good beam qualities are required. The capability of making real-time M^2

measurements was demonstrated by continually varying the alignment of the laser cavity. However, the reachable speed of the process was limited by the hardware used – such as a prefabricated diffractive optical element as part of the laser system. These techniques were soon replaced by spatial light modulators (SLMs) [133], which started to be used in optics research [134]. The next section looks specifically at research that has already been done with SLMs.

8.3.2 Recent Light Characterisation: Spatial Light Modulators

Liquid-crystal spatial light modulator (SLM) technologies have emerged recently as enabling on-demand tools for the creation of arbitrary optical fields. Beam shaping with SLMs has drawn much interest and has grown into a mature practice in the visible and near infra-red light in recent times. Its point of attraction is its dynamic properties and ability to generate the desired shapes in real time.

Such beams include, among others, laser beams that carry an OAM of $l\hbar$ per photon, namely Vortex, Laguerre-Gaussian, Bessel-Gaussian, and Airy beams [135]. To create vortex beams for example, an SLM must be programmed with a computer-generated hologram that is encoded with an l-fork dislocation (a fork hologram). A vortex beam with an index l is created in the first diffraction order when a Gaussian illuminates an l charged fork hologram at the centre of the dislocation. The index l represents the number of singularities in the hologram. Figure 8.3 illustrates three scenarios that result from illuminating a fork hologram with one dislocation ($l = 1$) at different positions. Figure 8.3 (a) occurs when the laser is well aligned, while Figure 8.3 (b) is not aligned at all, because the illumination of the hologram is completely off the singularity that is represented by the end of the half line of the hologram (the picture in the middle). Figure 8.3 (c) shows a case where the illumination is shifted slightly off the centre of the singularity in the hologram.

When the illumination is centred on the singularity of the fork hologram, that is at $(x_0, y_0) = (0, 0)$, the resulting beam is a symmetrical vortex beam with charge $l = 1$. The second case (Figure 8.3 (b)) occurs when the illumination is far away from the centre, when $(x_0, y_0) = (-\infty, -\infty)$ or (∞, ∞), which occurs when the laser is severely misaligned. In this case the beam is modified by the blazed grating only and the resulting beam is unintentionally Gaussian.

158
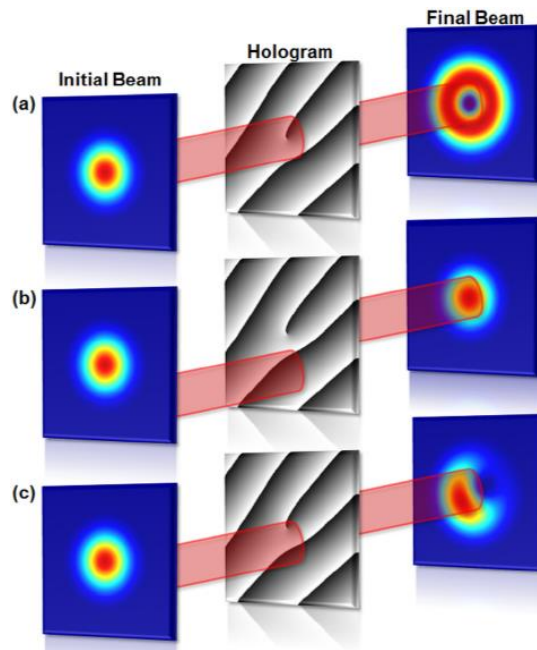
Figure 8.3. Illumination of a fork hologram with a Gaussian beam and transforming it into a (a) vortex, (b) Gaussian mode and (c) a mixture of the two [136].

In this third case (Figure 8.3 (c)), as the resulting beam can be represented on the complex plane, and controlling x_0 and y_0, which is subsequently described by r_0 and ϕ_0, and the illumination can be positioned at any point within the complex plane [136]. The beam that gets created in this case is undesirably not symmetrical. Scenario (a) is the desired one. Symmetric vortex beams, and other beams that carry OAM can be used in many applications such as holographic optical trapping and tweezing, quantum information processing, mode-division multiplexing, microscopy, 3D-holographic imaging, metrology and optical communication. The structured light that is used to perform these applications has been characterised by modal decomposition using the SLMs [2].

To study the transmission properties of controlled light propagation in a modally resolved manner requires, in general, modal tools to excite spatial modes and their superpositions, as well as the subsequent modal decomposition of such modes [137]. Modal decomposition has been known from when it was used for pattern recognition decades ago, and later it was used to study Hermite-Gaussian modes, waveguides, solid-state laser systems, and fibres with diffractive optical elements [2]. It is a powerful tool that is used to investigate in detail the power content and relative phase of the modes that comprise laser fields [120]. Modal decomposition is of interest in this discussion because it can be used for the detection of laser modes in free-space communication.

159

Two types of modal decomposition have been demonstrated recently, namely phase-only (azimuthal [133], [120]), as well as phase-and-amplitude modal decomposition.

Modal decomposition is performed with computer-generated holograms (CGH) that enable fast and accurate measurement of the mode spectrum. The CGH encodes the modes of interest, whose powers and relative phase differences are measured from the far-field diffraction pattern of the incident optical field with the hologram transmission function [120]. Litvin et al. (2012) demonstrated one of the early reports on azimuthal modal decomposition of an arbitrary laser source by using a dynamic and phase-only SLM. This was done without knowing the structure, the phases of its modes, or the scale of the amplitude distribution of the light field [133]. In this case the authors used a basis comprising of the angular harmonics that are independent of spatial scale and expressed the spatial distribution in terms of spatially dependent coefficients. They executed it in full by considering a superposition of OAM-carrying Bessel beams with relative phase differences, as well as an off-axis vortex beam. Among other components, the authors used two SLMs to conduct their experiments. These comprised the generation and the decomposition of the field. The first SLM (SLM$_1$) was programmed to generate various fields. In particular, they encoded SLM$_1$ with two annular rings modulated in their azimuthal phase to execute a superposition of two OAM carrying Bessel beams to generate the field $u(r, \phi)$ of interest. The fields that SLM$_1$ created were propagated through a telescope to SLM$_2$ for azimuthal decomposition. The superposition was done first for two identical and later with different Bessel beams with opposite handedness (m = 3 and n = -3) and (m = +3 and n = -2) respectively. In comparison, they found excellent agreement between the measurements of the experiments and the predicted theory. With these phase shift measurements, the comparison of the measured and the programmed phase shift had a 0.1% slope difference, confirming that the technique they used worked correctly [133]. The other results in this paper also show that the technique worked well. However, they are limited to operating at low power.

Modal decomposition was again demonstrated by Schulze et al. (2013), who used it to measure the OAM density of light, using a two SLM set-up and correlation filters from which the optical field was reconstructed [120]. To do this they generated Laguerre-Gaussian beams of a known OAM density that served as a reference to the modal decomposition results, by programming the first SLM with the coding technique that converts complex transmission functions into phase-only phase

functions. The second SLM, together with the lens and the camera, was used to perform modal decomposition. This was done by displaying a transmission function on SLM_2 and recording the inner-product at the Fourier plane with the camera. This process generated the modal powers ρ_l^2 and the phases $\Delta\varphi$, which gave rise to the optical field, the Poynting vector, and the OAM density [120].

Figure 8.4 characterises this beam, showing the measured near-field intensity. The donut shape in Figure 8.4 (a) indicates the phase singularity of the beam. Figure 8.4 (b) and (d) are their modal decomposition results, where the modal power spectra reveal only a correlation signal for the $LG_{0,1}$ mode, while all other mode powers in the range $p = 0$, 1, 2 and $l = 0$, 1, 2 are zero. All the phases are also measured to be zero [120]. Figure 8.4 (c) illustrates the reconstruction of the field from the measured modal powers and phases. Comparing the reconstructed Figure 8.4 (c) with the measured beam intensity, Figure 8.4 (a) shows very good agreement. When the experimentally measured and theoretically calculated OAM density were compared to each other, they yielded a good agreement. This OAM density is viewed as a characteristic of Laguerre-Gaussian beams.
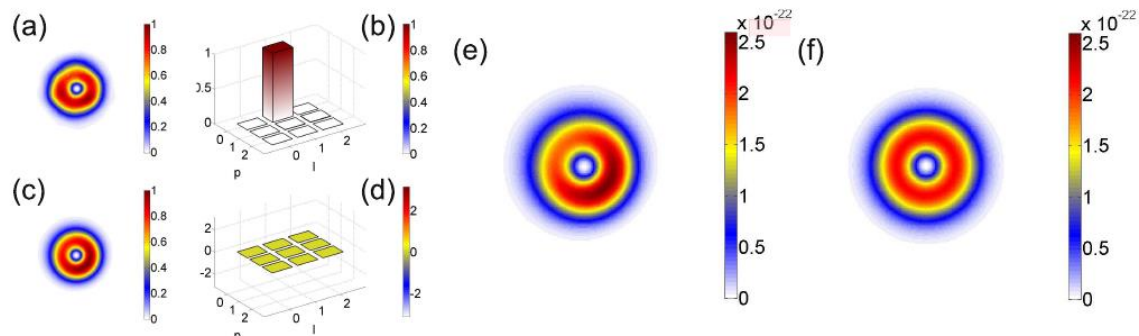
Figure 8.4. Characterising Laguerre-Gaussian LG$_{lp}$ mode beam by (a) measuring the intensity in the near field. (b) Modal power spectrum. (c) Reconstructed intensity. (d) Modal phase spectrum. (e) Measured OAM density. (f) Calculated OAM density. OAM densities in Ns/m^2 [120].

Modal decomposition has since been implemented for many purposes. One is wavefront reconstruction ([138], [139]), which will be investigated in Chapter 9. Other instances where modal decomposition has been used include measuring the orbital angular momentum [140], measuring (detecting) created Laguerre Gaussian modes [141], calculating the 'vectorness' of a field [142], and others.

8.4 SLM Theory and Calibration

In our research, we used an SLM that was specifically coated for the mid-IR region. As this implies, SLMs are wavelength specific. It is also customary that all SLMs are calibrated for their specific wavelength before use. The calibration principles that one would follow in the visible band can be followed in the mid-IR region as well. A basic overview of this mechanism will indicate why.

8.4.1 The Operation of a Spatial Light Modulator

An SLM consists of a liquid crystal micro-display, which is programmed and addressed by a circuit board through a flex cable. The display has a full high definition (HD) resolution of 1920×1080 pixels and an 8 µm pixel dimension leading to an active area of 15.36 mm $\times$ 8.64 mm and aspect ratio of 16:9 with each pixel of the SLM addressed by two electrodes. As the liquid crystal molecules tilt in the direction of the applied voltage, the refractive index seen by the light changes accordingly and, subsequently, its phase shifts or changes proportionally. The voltage increase is also related to the grey levels (or phase modulation) required for each pixel, which varies through the 256 levels from level 0 (i.e. zero voltage with no phase shift) to 255 (a maximum voltage with 2π phase shift) [126].

Figure 8.5 (a) illustrates the electrically controlled birefringent mechanism of the SLM where the molecules that constitute pixels are initially aligned parallel to the electrodes when no voltage is applied across them. However, in the case where the electric field is applied across the electrodes, it forces the molecules to tilt in the direction of the applied electric field, as shown in Figure 8.5 (a) and (b).
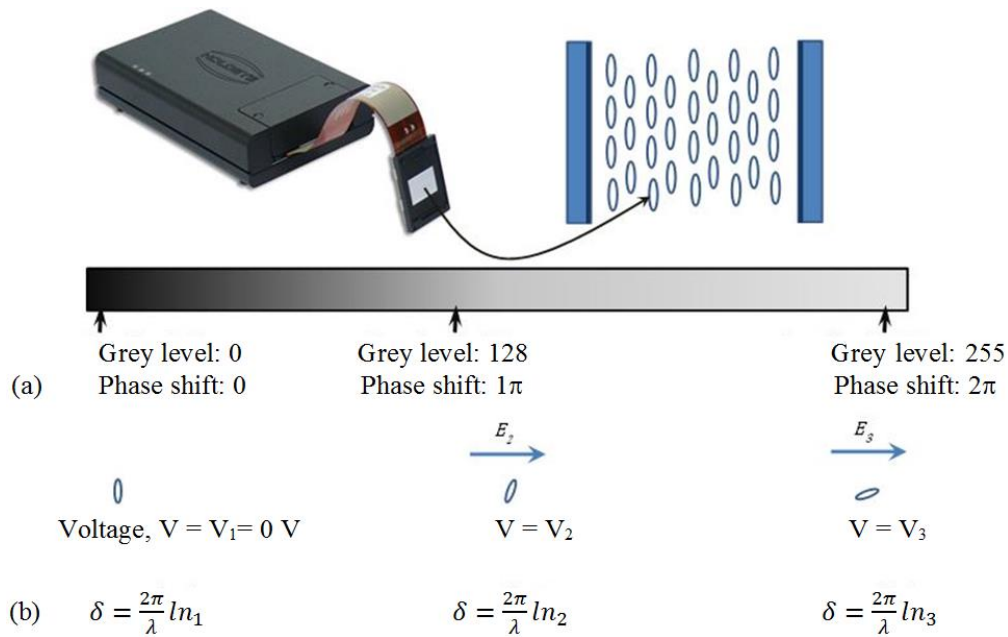
Figure 8.5. The liquid crystal display illustrating the operation of an electrically controlled birefringent SLM. (a) An SLM setup showing the liquid crystal display that is addressed by a circuit board (the insert represents an individual pixel in the display). (b). The grey scale varying from level 0 (black) to level 255 (white), corresponding to a 2π phase shift. (c) The three cases presented here illustrate the tilting of the molecules in relation to the applied voltage and the corresponding phase shift resulting in the changing of the refractive index of the liquid crystal pixel [118].

As seen in Figure 8.5 (b), the equation to determine the phase shift imparted to the incident field is dependent on its wavelength, λ. This therefore makes it necessary for an SLM to be calibrated for a specific working wavelength, in order for a 2π phase shift to be achieved across all 256 grey levels.

If the assigned grey levels fall outside this phase shift range, say 3π, it is an indication that the SLM was not calibrated correctly. To correct this and achieve the correct phase modulation, the voltages applied to the electrodes of the pixels will need to be adjusted appropriately. The procedure is well documented [118] and was also followed here.

8.4.2 Calibration of the SLM

In general, all SLMs that are coated for visible light are sold together with an automated calibration software programme called Phase-Cam. SLMs are first calibrated before use in order to verify that a

phase shift from 0 to 2π can be achieved in all of the 256 grey-levels. This is done for a particular wavelength by first measuring the phase modulation over all of them. To achieve this, the laser beam used for this purpose is expanded and collimated to overfill the SLM. The beam is passed through a mask containing two holes so that two identical beams, with amplitudes defined as $u_1 = u_2 = e^{i\phi_1}$, emerge separately and parallel to each another. The two beams are directed to and reflected off from the two halves of the SLM. One half is addressed with a constant grey level, while on the other half, the grey level varies from 0 to 255 (corresponding to black and white, respectively), as shown in Figure 8.6 (a). The two beams are then combined with the use of a lens, thus producing an interference pattern that is imaged onto a camera (see Figure 8.6 (b)). The beam that is reflected off from the half of the SLM that has a varying grey level undergoes a phase modulation over all 256 grey levels. As the grey level varies on the second half of the SLM, the shifting interference pattern is enlarged and imaged onto a camera. This is done in visible wavelengths with the help of a phase cam software programme that simultaneously varies the grey level on the SLM and monitors the locations of the maximum of the interference pattern as it shifts across the camera. However, since the mid-IR camera is not compatible with the phase cam software, the variation and the monitoring of the location of the maximum intensity points are done manually.
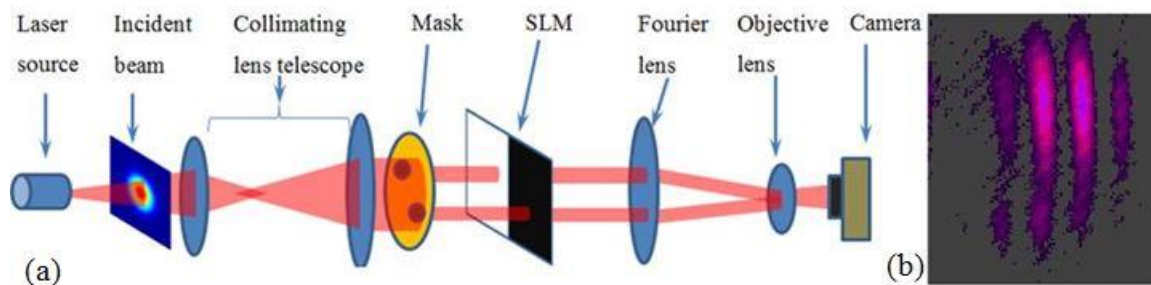
Figure 8.6. (a) A schematic setup for the calibration procedure whereby the grey level is kept constant on one half of the SLM and varied on the other half of the screen. (b) Typical fringes (interference pattern) that are seen on the laser wavelength compatible camera used.

Figure 8.7 illustrates the manual tracking and calculation of the intensity maxima respectively by taking images of the interference pattern as the grey levels on the hologram are varied through the entire grey scale. This is done by taking images in steps of 20 from grey level of 0 to 255. Figure

8.7 (a) marks the initial grey level state, which corresponds to the grey level 0 in both halves of the SLM. This state is shown in Figure 8.7 (c), at the top.
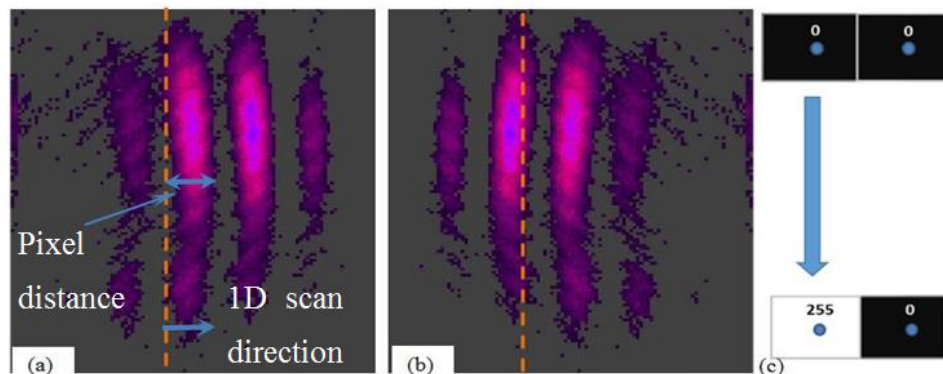
Figure 8.7. The illustration of how a change in a grey level produces a lateral shift in the interference pattern. (a) Mark the initial grey level state that corresponds to grey level 0 in both halves of the SLM shown in (c). (b) Mark the end of the grey level change that corresponds to an overall fringe shift across all 256 grey levels depicted in (c).

By varying the phase of one of the beams, the position of the interference pattern shifts, which is the principle used to measure the phase, shifts over all 256 grey levels.

8.4.3 SLM Calibration Results

Calibration of the SLM is done to verify that a 0 to 2π phase shift is achieved across all 256 grey levels for your working wavelength. To set the SLM response to the exact phase value and ensure the linearity of the phase response, a gamma correction is implemented that uses a wavelength specific to a supplier-provided EXCEL sheet gamma file [143]. A Matlab code is used to locate and trace the movement of the maximum as well as to measure the period between the phase patterns (fringes), as the grey scale is varied. This is done using one-dimensional intensity profiles across the fringe.

Figure 8.8 (a) is a plot that consists of 256 rows that contain one-dimensional (1D) intensity profiles of the interference patterns for each grey level. The white crosses mark the intensity maxima of the interference pattern for each grey level. Figure 8.8 (b) represents the one-dimension intensity profile

165

(the white line) in (a). showing the maxima and the minima and also illustrating the shift of the interference pattern by ΔT.
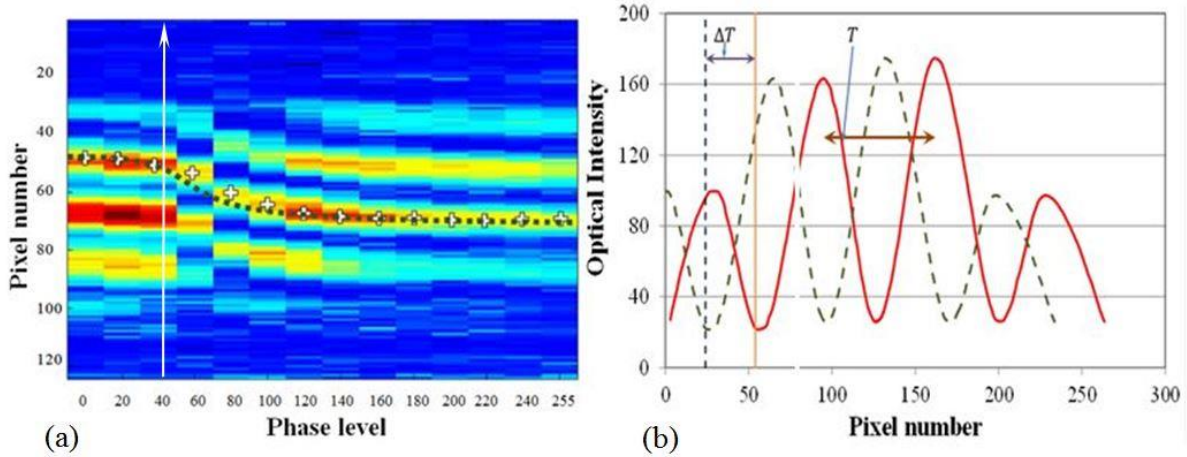
Figure 8.8. (a) A one-dimensional intensity profile plot of the interference pattern for a particular grey level, where a pre-selected fringe position is marked by the white crosses. (b) The one-dimension intensity profile.

Once the pixel positions of the maxima of the interference pattern (white crosses in Figure 8.8(a)) have been extracted, the associated phase modulation is determined by calculating the difference between the pixel position for a particular grey level and the pixel position for a neighbouring grey level, divided by half of the fringe period.

The shift of the interference pattern maxima is directly proportional to the phase modulation. The maximum phase shift that a particular grey level induces can be calculated using Equation 8.1.

$$\Delta\phi_i = 2\pi \frac{N_{pxl\_x} - N_{pxl\_i}}{T} \tag{8.1}$$

Here N_{pxl_x} is the pixel number for a particular grey level x, N_{pxl_i} is the number for the starting pixel, and T is the period between two peaks.

166

An example that uses the information Equation 8.1 provides is shown in Figure 8.6 (a) below. This is a plot of the pixel position of the intensity maxima, starting with pixel N_{pxl_i}= 20th and continuing to N_{pxl_f} = 43rd, where the period of the interference fringes was found to be 19. Once the calibration has been performed and the phase shift associated to each grey level has been determined, the voltages addressing the liquid crystal display are adjusted appropriately. This is where the PhaseCam software calculates the new voltages that need to be addressed to the electrodes. The calculation gives a maximum phase shift of 2.43π (Figure 8.9 (b)), which is higher than the expected 2π phase shift. This is an indication that the device is not correctly calibrated for this wavelength. To cater for such a situation, the process always creates a new gamma file that characterises the SLM for a 2π phase shift in real time. This gamma file is then saved as an old gamma file to be used for the next SLM calibration and gamma file correction, while discarding the initial old gamma file.

Next, the SLM is recalibrated using the new gamma file to obtain a 2π phase shift. The new gamma file needs to be saved and used the next time the 2 μm SLM is gamma corrected. The phase shift measurement is done again to verify whether the newly generated gamma file will produce the desired phase shift (i.e. 2π if the SLM is calibrated correctly). The process of recalibration involves adjusting the voltages in the Holoeye software to readdress the pixels in the SLM after the new gamma file has been loaded.
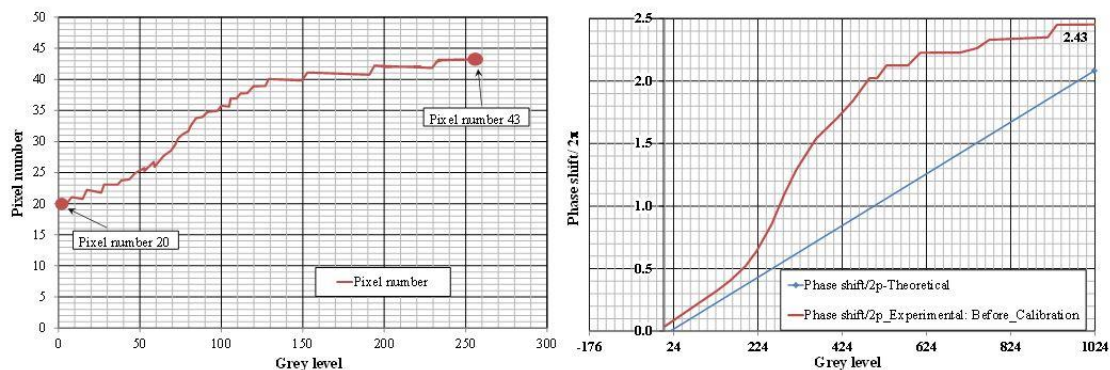
Figure 8.9. (a) Pixel number plotted against the grey levels. (b) The measured and the wanted phase shift against the grey levels indicating that this device (SLM) is not correctly calibrated for this particular wavelength.

167

Figure 8.10 illustrates a 1D intensity profile of the interference pattern taken through all its grey levels, again resulting in a new phase shift. The location of the maxima points along the line profile is measured again using a Matlab code. This code is used to determine where the phase shift has occurred and also to record the corresponding pixel values.
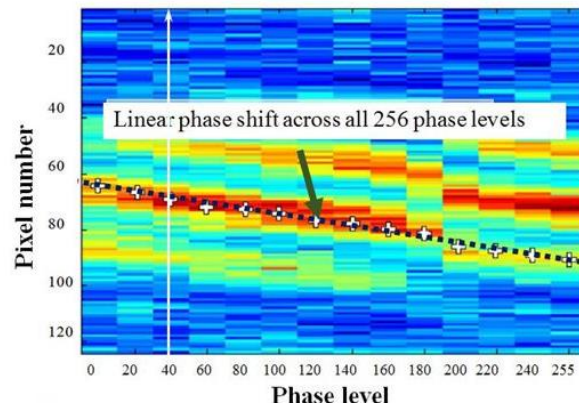
Figure 8.10. A one-dimensional intensity profile plot of the interference pattern for a particular grey level where a pre-selected fringe position is marked by the white crosses.

The interference pattern that resulted from the use of the newly created gamma file followed a linear shift (as expected and shown in Figure 8.11 (b)), when the SLM was configured with a gamma file that attains a 2π phase shift across all addressable pixels.
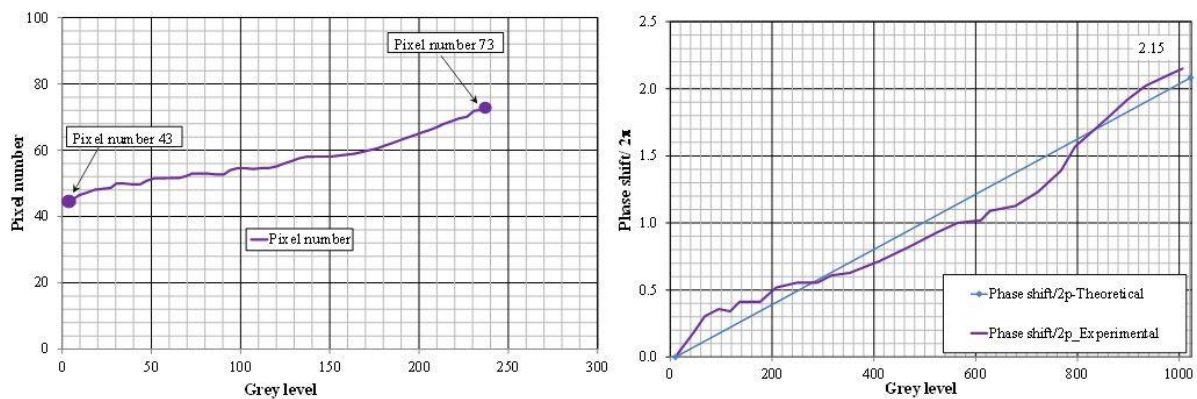
Figure 8.11. (a) This is a plot of pixel number vs grey level (purple curve) (b) The graph relates the measured phase shift (purple curve) after the voltages have been adjusted correctly.

168

Figure 8.11 (b) shows that the grey levels in the Mid-IR coated SLM have undergone a nearly linear phase shift that reaches approximately 2π. With the SLM correctly calibrated, it can be used to carry out various experiments with lasers of the wavelength for which it was calibrated.

8.5   Creation of Vortex and Laguerre Gaussian Beams

A fundamental mode (u_A) can be tailored into different shapes (u_B) that are defined by different basis functions (ψ_B) using several techniques for various intended applications. A digital match filter (hologram), described by a transmission function (t) and encoded on an SLM, is the technique used and discussed in this research. The two types of basis functions that are discussed in this research include vortex beams and Laguerre-Gaussian (LG_{lp}) modes. The azimuthal or 'fork' holograms are used to create vortex beams and the complex modulation holograms reported by Arrizón et al. (2007) [144] (as 'type 3') are used to generate LG_{lp} modes. Vortex beams are characterised by an azimuthal mode index (also called a topological charge) of the optical vortex, denoted by l, whose radius becomes larger at larger values of l. Laguerre-Gaussian modes are described by indices l and a radial index p, which denotes the number of concentric rings (as illustrated in Figure 8.12).
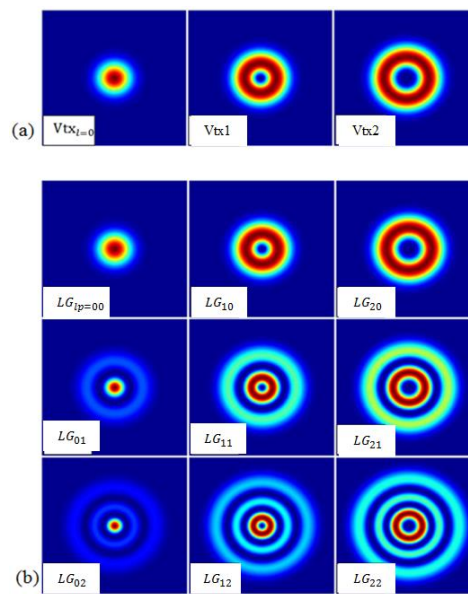
Figure 8.12. Two types of shaped light, (a) Vortex beams and (c) Laguerre Gaussian LG_{lp} beams.

169

Figure 8.13 demonstrates the creation of both the vortex and the LG$_{lp}$ beams. In both cases, a Gaussian beam illuminates a relevant hologram that diffracts the incident beam into many diffraction orders. At the 0th order, a Gaussian beam remains, while at either side of the 0th order, vortex beams of azimuthal mode indices $l_{\pm n}$ are observed where $n =$1, 2, 3, … The vortex beams obtained become symmetrical when the incident Gaussian beam is centred on the singularity of the fork hologram, which is recommended for all experiments. Figure 8.13 (b) is the reverse of the process in Figure 8.13 (a), where a vortex beam is incident on the hologram and the resulting diffraction pattern contains a Gaussian beam at the first diffraction order while vortex beams are diffracted to other orders, including the 0th order.

The same argument for the generation of vortex beams can be made for the LG$_{lp}$ modes in Figure 8.13 (c) and (d). The only difference is that, instead of a vortex beam, the complex modulation hologram (type 3) generates an LG$_{lp}$ mode. In the reverse case, a Gaussian beam is diffracted to the 1st diffraction order, while LG$_{lp}$ modes are diffracted to other orders, including the 0th order.
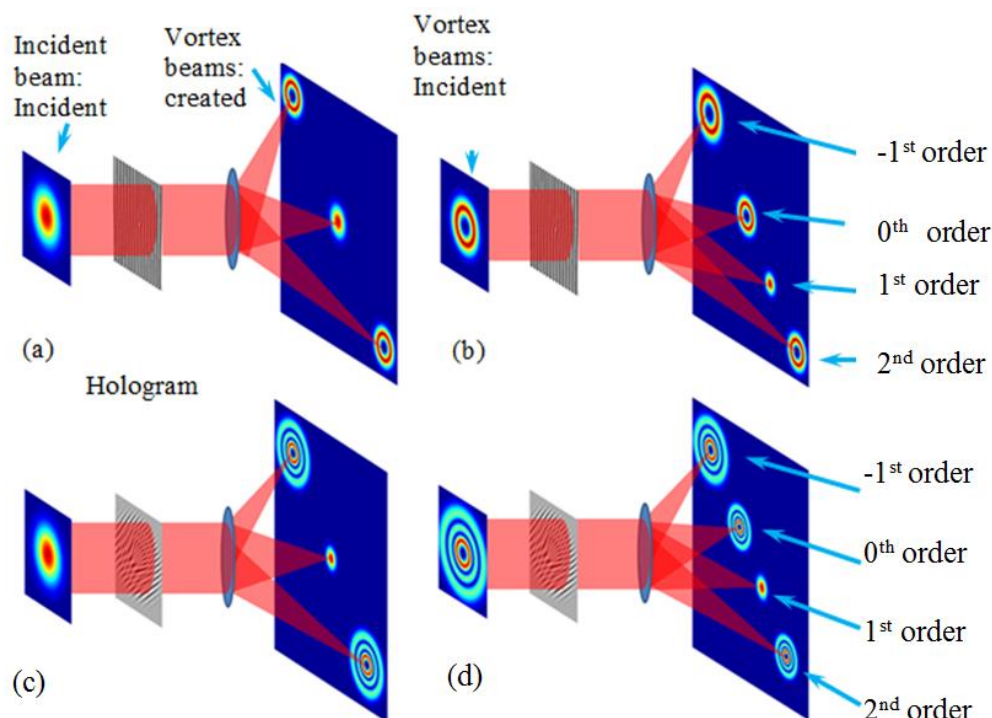
Figure 8.13. A diagram demonstrating the creation of different modes at the different diffraction orders when a Gaussian and a vortex beam are incident. (a) By reciprocity, an incident Gaussian beam produces a vortex beam at the 1st diffraction order. (b) The incident vortex beam produces a Gaussian beam at the 1st order and vortex beams elsewhere. (c) An incident Gaussian beam produces a Laguerre Gaussian beam (LG_{lp} mode) at the 1st diffraction order. (d) By recieprocity, the incident LG_{lp} mode beam produces a Gaussian beam at the 1st order and LG_{lp} mode beams elsewhere ([2], [144]).

8.6   Modal Decomposition

Modal decomposition is a powerful instrument that is used to investigate laser fields in detail by extracting their full information through measuring their amplitudes and intermodal phases [135]. To achieve this, match filters encoded on a SLM are used. Modal decomposition expresses an optical field as a linear combination of basis functions that can be conveniently selected from a set of orthogonal spatial modes. Equation (8.2) gives this linear combination of an arbitrary optical field, expressed in terms of the complex expansion coefficients c_l and basis function $\Psi_l(\vec{r})$ that can describe different modes, depending on the geometry in question. Typically, for rectangular

171

symmetry, $\Psi_l(\vec{r})$ would represent Hermite-Gaussian modes, and for circular symmetry, it would represent Laquerre-Gaussian modes [2]. Equation (8.2) represents any field:

$$U(\vec{r}) = \sum_{l=0}^{N} c_l \Psi_l(\vec{r}) \tag{8.2}$$

where $\vec{r} = (x, y)$ represents the spatial coordinates, $c_l = \rho_l \exp(i\Delta\phi_l)$, of which ρ_l is the amplitude of the mode and $\Delta\phi_l$ is the intermodal phase, or simply the phase difference between the mode in question $\Psi_l(\vec{r})$ and a reference mode, Ψ_0. The complex expansion coefficients (c_l) contain the information required to describe the phase only, or both the phase and amplitude of an optical field with respect to the reference mode.

Modal decomposition is mainly used to determine the complex coefficients (c_l) of an unknown field in terms of its constituent amplitudes and intermodal phases. To achieve this, an inner product (or overlap) between the field of interest and each individual mode is measured from $\rho_l^2 = \left| < U | \Psi_l^* > \right|^2$. This yields an on-axis intensity that is proportional to the power content of each mode in the Fourier plane and then normalised to 1, such that $\sum \rho_l^2 = 1$ [2]. The value of ρ_l can be calculated or measured from the product that results when the basis function Ψ_l is overlapped with a conjugate Ψ_k^* function (which can be the transmission function encoded on the SLM), given Equation (8.3):

$$\Psi_l \times \Psi_k^* = \rho_l \begin{Bmatrix} 1 \text{ for } l = k \\ 0 \text{ for } l \neq k \end{Bmatrix} \tag{8.3}$$

which can be measured experimentally.

Equation (8.4) describes the entire optical field of interest, and in this case, it can be used to describe the 2 μm laser light where the corresponding intensity profile can be calculated from Equation (8.2) :

$$I(\vec{r}) = |U(\vec{r})|^2 \tag{8.4}$$

Its phase can also be calculated as shown by Equation (8.5):

$$\Phi = \arg[U(\vec{r})] = \arg\left[\sum_{l=0}^{N} c_l \Psi_l(\vec{r})\right] \tag{8.5}$$

where Φ is the phase of the field $U(\vec{r})$. Modal decomposition involves correlating the field of interest with modes encoded in match filters so as to measure their modal powers and relative phases [140]. This is made possible with a particular transmission function encoded on the SLM, known as a match filter, and varies with the parameters needed to be measured (modal powers and relative phases). The transmission function required to measure the modal power of a specific mode Ψ_l, is defined by its complex conjugate $T(\vec{r}) = \Psi_l^*(\vec{r})$. This is encoded on SLM_2 and allows one to extract the amplitudes associated with the basis elements. By observing the intensity on the optical axis at far-field, the Fourier plane of the second SLM (where $I_l(0,0) = c_l^2$), the power of the mode ψ_l is measured.

8.7   Phase-Only Modal Decomposition

In this section we discuss the phase-only (azimuthal) modal decomposition that is achieved with azimuthal match filters (fork holograms). Taking the vortex modes as a basis, Equation (8.6) is a specific expansion of an optical field in Equation (8.2). While researchers have introduced a scale-invariant approach [133], it suffices to regard the process as involving decomposing even an unknown field into azimuthal modes where Equation (8.2) becomes,

$$U(r, \phi) = \sum_l c_l(r) e^{il\phi} \tag{8.6}$$

In this equation $e^{il\phi} (= \Psi_l(\vec{r}))$ represents orthogonal angular harmonics (basis functions) over the azimuthal plane or a helical phase term, with the weighting coefficients of the modes that contain the field's spatial distribution information [145] defined by Equation (8.7) as

$$c_l(r) = \frac{1}{\sqrt{2\pi}} \int_0^{2\pi} u(r, \phi)\, e^{i\Delta\theta_l} e^{-il\phi} d\phi \tag{8.7}$$

Figure 8.14 illustrates the azimuthal decomposition of vortex beams. This diagram demonstrates how a Gaussian beam, incident on SLM_1, is diffracted and propagated through a $4\text{-}f$ telescope. At the far-field of SLM_1, several vortex modes are created as shown first in Figure 8.13 (a) and in the

173

section left of the spatial filter in the middle of Figure 8.14. Following this, the vortex mode at the first order (carrying the field described in Equation (8.2) is selected and propagated further through the telescope to SLM_2. The $4\text{-}f$ telescope is used to relay an image of the azimuthal plane of SLM_1 onto SLM_2. SLM_2 further diffracts the incident vortex beam, according to Figure 8.13 (b). At the far-field of SLM_2 and at the first order, the original Gaussian beam is reconstructed as shown in Figure 8.13 (a). This occurs only if SLM_2 is encoded with the complex conjugate of the transmission function encoded on SLM_1 and it indicates that the mode under investigation is present in the incident field. If that is not the case, a zero-on-axis intensity is detected at far-field and at the first order of SLM_2, as shown in Figure 8.14 (b), indicating that the mode under investigation is not present in the incident field.
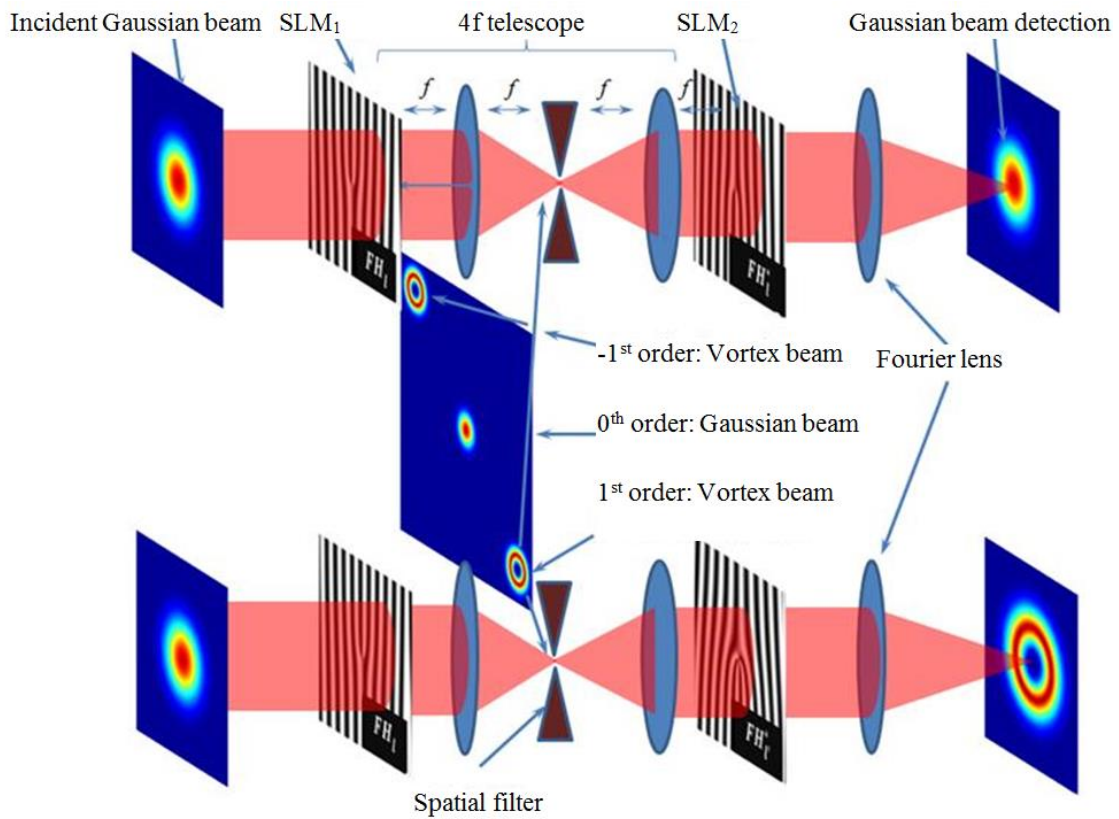
Figure 8.14. The Azimuthal hologram encoded on SLM_1 and SLM_2 for the creation and detection of the desired beams to perform phase-only modal decomposition [120].

174

8.7.1   Phase-and-Amplitude Modal Decomposition

The phase-and-amplitude modal decomposition relies on complex amplitude modulation expressed as Equation (8.8) [144]:

$$s(x, y) = a(x, y)\exp[i\phi(x, y)] \tag{8.8}$$

where amplitude $a(x,\ y) \in [0,\ 1]$, and phase $\phi(x,\ y) \in [-\pi,\ \pi]$. The tool that is required to encode this complex field $s(x, y)$, is a phase transmittance match filter that is expressed as a function $h(x, y)$. It has explicit dependence on the amplitude and the phase of the encoded beam, and is useful for hologram phase modulation $\psi(a, \phi)$ when represented by a Fourier series in Equation (8.9), in the domain of ϕ. This transmittance function is defined by Equation (8.9) [144]:

$$h(x, y) = \exp\{i[\psi(a, \phi)]\} = \sum_{q=-\infty}^{\infty} c_q^a \exp(ik\phi) \tag{8.9}$$

where Equation (8.10):

$$c_l^a \exp(ik\phi) =\ h_l(x, y) \tag{8.10}$$

and Equation (8.11):

$$c_l^a = (2\pi)^{-1} \int_{-\pi}^{\pi} \exp\{i[\psi(a, \phi)] \exp(-il\phi)d\phi\} \tag{8.11}$$

The resulting coefficients c_l^a depend explicitly on the amplitude $a(x,\ y)$ and implicitly on the coordinates $(x,\ y)$. A useful basis to determine the suitable match filter that recovers the signal $s(x, y)$ from the first order, is obtained by expanding Equation (8.11) and equating the real part of the integral to zero and the complex part to $2\pi c_1^a$. This signal encoding condition is expressed in Equation (8.12) as an identity:

$$c_1^a = Aa \tag{8.12}$$

where A is a positive constant that varies from 0 to 1. Different phase functions $\psi(a, \phi)$ satisfy these conditions, and thus correspond to different match filters.

Of interest to this research is the third phase function [144], the so-called type 3 phase function, because it accurately encodes complex fields and is expressed in Equation (8.13). This phase function describes the phase modulation of phase match filters that encode general scalar complex fields and can furthermore reconstruct the encoded fields, even when using SLMs with pixelated low resolution.

$$\psi(\phi, a) = f(a)\sin(\phi) \tag{8.13}$$

$f(a)$ increases with increasing amplitude a at a fast rate [144], and is obtained from inverting $J_1[f(a)] \cong 0.6a$, with the first-order Bessel function $J_1(x)$. We employ a sinusoidal grating to separate the orders and select the first diffraction order from the unwanted diffraction orders [126].

The phase distributions of the type 3 hologram as an example can be used to produce LG$_{lp}$ beams, which are mathematically described in polar coordinates (r, θ) by Equation (8.14):

$$u(r, \theta) = C \left(\frac{\sqrt{2}r}{\omega_0}\right)^{|l|} L_p^{|l|} \left(\frac{2r^2}{\omega_0^2}\right) \exp\left(\frac{-r^2}{\omega_0^2}\right) \exp(il\theta) \tag{8.14}$$

where $L_p^{|l|}$ denotes an associated Laguerre polynomial, ω_0 is the beam waist radius, p is the radial mode index, l is the phase singularity charge, and C is a normalisation constant [144].

The same mathematics presented in Section 8.6. (i.e. Equations (8.2) to (8.5)) is used here to perform a modal decomposition on complex amplitude modes (such as the LG$_{lp}$ modes). However, the LG function in Equation (8.13) is used to describe the basis function $\Psi_l(\vec{r})$. Figure 8.16 schematically illustrates modal decomposition as implemented with the complex field phase function encoded holograms. The same discussion used in the azimuthal modal decomposition also applies to complex modulation. However, instead of a vortex beam created at the far-field of the first SLM, a fundamental Gaussian beam incident on a complex modulation phase function encoded match filter gets decomposed into the set of LG$_{lp}$ modes, as shown in Figure 8.13 (c). Even with complex modulation, when the match filter that is encoded on SLM$_2$ is the complex conjugate of that encoded on SLM$_1$, on-axis intensity is reconstructed at the far-field of SLM$_2$. Similarly, if the zero-on-axis intensity is detected at the far-field of SLM$_2$'s first order, as shown in Figure 8.15 (b), this illustrates that the mode under question is not present in the incident field.
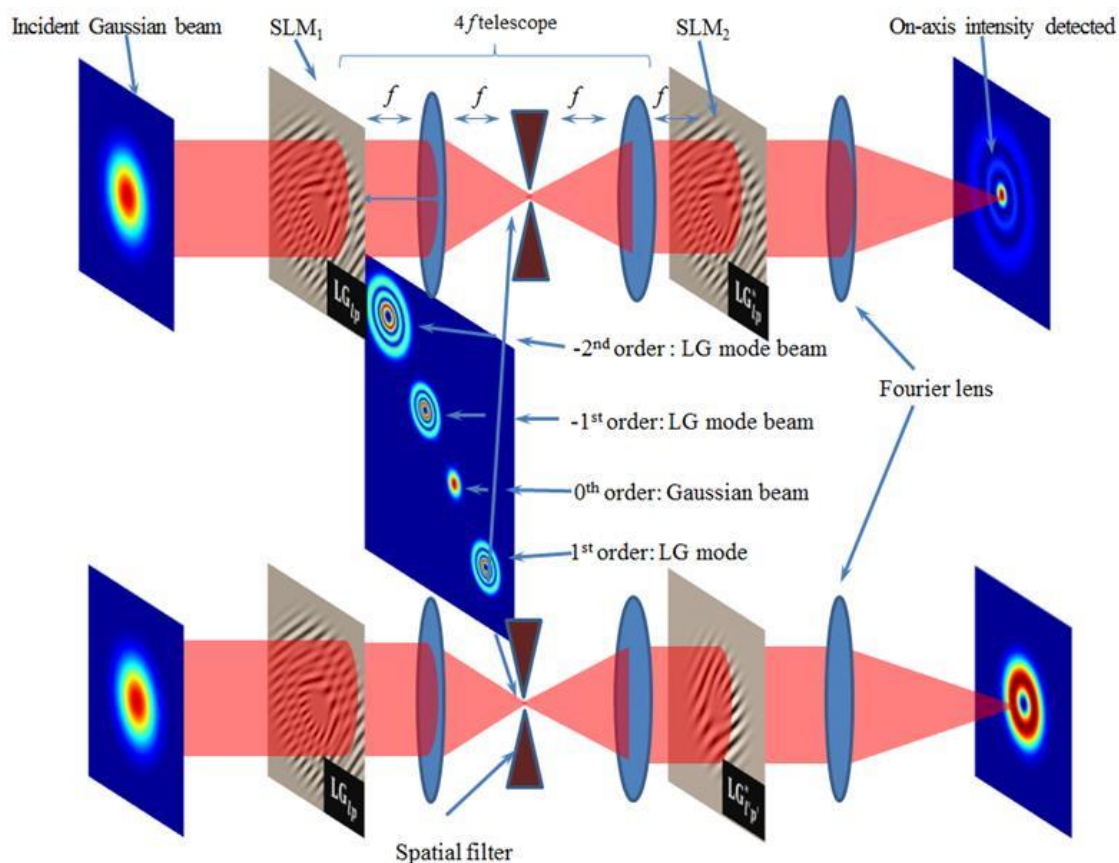
Figure 8.15. The type 3 hologram described by Arizon et al. [8] is encoded on SLM$_1$ and SLM$_2$, to generate LG$_{lp}$ modes and perform a modal decomposition (complex modulation) with and without the radial component [135].

8.8   Experimental Set-up

By employing an SLM and implementing computer-generated fork correlation filters to perform azimuthal modal decomposition, we expressed the spatial distribution of the selected modes in terms of spatially dependent coefficients. Following this, we performed a phase-and-amplitude modal decomposition in the same manner, but by generating a complex field with non-radial modes and then with radial modes.

The experiment that fulfilled the purpose of this research included the building of a 2 μm source, the Ho:LiLF$_4$ laser, filtering the linearly polarised output laser light from the pump and directing it

to the SLM with a telescope. The SLM is used here to generate the modes of interest and perform the modal decomposition for both azimuthal and complex amplitude modulation.

8.8.1   Developing a 2 µm Laser Source for Modal Decomposition

The mid-IR source that was developed to implement modal decomposition on was a Ho:LiLuF$_4$ laser system. The Ho:LiLuF$_4$ crystal (the laser material) with a 0.5 at. % doping concentration was mounted in thermal contact with a water-cooled copper mount. The crystal was coated for the 2 µm wavelength lasing and pumping with a commercial 80 W, Tm:fibre laser at 1940 nm that was manufactured by IPG Photonics. Figure 8.1 shows this laser source comprising the pump and the cavity, as well as the output that was linearly (π-) polarised.

Figure 8.16. Design of the Tm:fibre laser pumped Ho:LiLuF$_4$ laser source. The yellow colour represents the pump light and the red colour represents the laser light.

The laser output is shown in Figure 8.17.

178
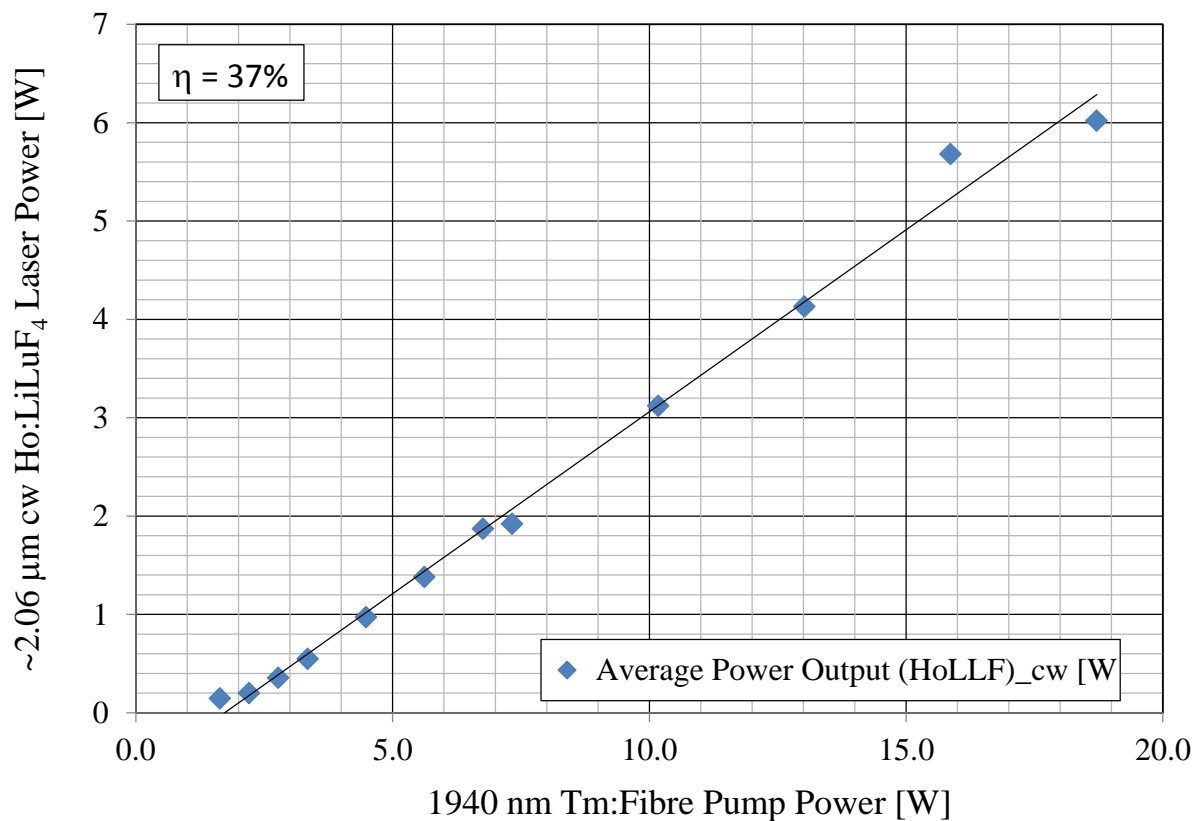
Figure 8.17. The output power of the Mid-IR laser used for the modal decomposition experiments versus the absorbed Tm:fibre laser pump power.

The power as reflected in Figure 8.17 is high in relation to the SLM damage threshold. A typical SLM such as those used by Beck et al. (2010) in their experiments, has power handling capabilities of 1 to 2 W/cm^2 and a damage threshold that limits its operation to a maximum of 3 W [146], which is also applicable to other wavelength calibrated SLMs.

8.8.2   Experimental Setup to Conduct Modal Decomposition

Figure 8.19 is a schematic of the experimental setup depicting the beam path during the modal decomposition process. The diagram also shows an SLM (Holoeye, PLUTO-Mid-IR) with 1920 × 1080 pixels of pitch 8 µm [147] and an active area of 17.66 × 10.60 mm^2 encoded with a hologram. The function of the SLM is to modulate light and introduce a phase change to it. The hologram that is encoded on the SLM shifts (diffracts) the modulated light off the optical path

[148]. The beam that was incident to the SLM was a Gaussian beam that was linearly polarised and parallel to the orientation of the SLM liquid crystals. The SLM was configured in such way that it was divided into two, thus a different hologram could be encoded on each half. This incoming beam was incident on the first half of the SLM for the creation of various modes, and then directed onto the second half of the SLM for their detection at the far-field of the second half of the SLM (see Figure 8.19).

The process starts with the interaction of the beam with the first half of the SLM, known as SLM_1. As SLM_1 reflects, it also diffracts the beam into many orders, which include 0th order (un-diffracted), the diffracted 1st order (where the OAM state is created [118]), 2nd order and so on. According to the illustration shown in Figure 8.13, the beams that get created in these orders are either a vortex (when a fork hologram is encoded on SLM_1) or a LG_{lp} mode beam if the complex modulation hologram of type 3 [144] is encoded. Figure 8.18 shows both holograms that have been used in this research: (a) the fork (azimuthal) hologram that is used to create vortex beams, and (b) the complex modulation hologram that is used to create LG_{lp} modes.
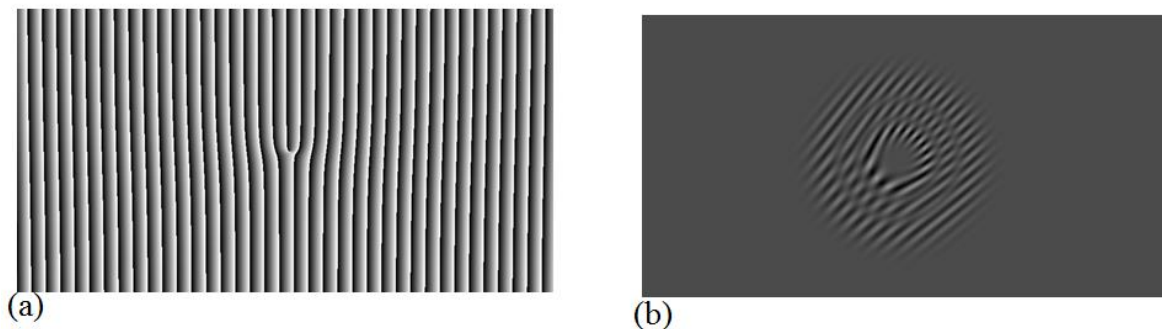
Figure 8.18. Typical holograms that were used in this research. (a) A fork hologram to create vortex beams and (b) a complex modulation (type 3) hologram used to create LG_{lp} modes.

Following the creation of modes, the light in the first order is singled out from other orders and made to pass through a $4-f$ lens imaging system that consists of a positive lens of focal length $f = 22.9$ mm and a 2 μm HR mirror. The lens was placed mid-way between the first half of the SLM and the mirror, at a distance that was equal to its focal length and aligned to the modulated light (that is diffracted) at the first order. Light then travelled a total distance of $4 \times f$ mm through the lens (L_2), reflected off the 2 μm HR mirror at the Fourier plane of the first half of the SLM. The

180

2 μm HR mirror was mounted to reflect the first-order beam at a narrow angle, so that light could pass through the same lens to the second half of the SLM, known as SLM_2. To completely isolate the light in the first order, a spatial aperture was placed in front of the 2 μm HR mirror, close enough to select it from the un-diffracted light and the other diffracted light of a higher order.
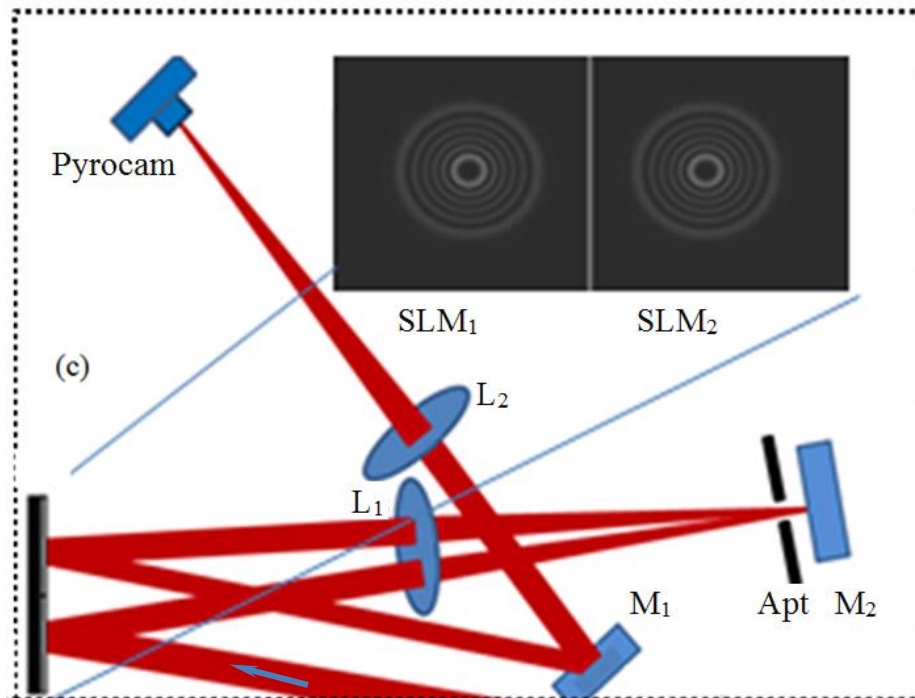
Figure 8.19. (a) The schematic diagram of the experiment illustrating the laser beam interaction with the SLM where the beam is reflected from the first half, propagated through a 4-*f* lens mirror system by a double pass through the lens L_1, and reflected of the first-order beam from mirror M to the second half of the SLM. The reconstructed beam is detected at far-field.

At SLM_2, the beam gets diffracted again into many orders. Because of the reciprocity shown in Figure 8.13, and whether the incident beam on SLM_2 was a vortex beam or an LG mode, it gets converted back to the on-axis high intensity Gaussian beam. Modal decomposition was implemented by detecting, selecting and measuring all modes that exhibit the on-axis intensities at the far-field of SLM_2.

181

8.9   Modal Decomposition Results

By performing modal decomposition measurements, we seek to infer the physical properties of vortex and LG$_{lp}$ beams by measuring their associated weighting coefficients. We seek to reconstruct the entire field $U(\vec{r})$, as described by Equation (8.2), by detecting the reconstructed modes at far-field and obtaining their superposition. The complex coefficient $c_l = \rho_l \exp(i\Delta\phi_l)$ can be quantified in the lab if the basis function is known. ρ_l is described by Equation (8.3) as the real amplitude and the intensity we measure at the far-field of the second half of the SLM, which is SLM$_2$.

To the best of our knowledge, this is the first occurrence of modal decomposition carried out with vortex and LG$_{lp}$ modes in the mid-IR region. In Chapter 9.3, the same will be done for wavefront reconstruction.

8.9.1   Azimuthal Modal Decomposition Results

To achieve azimuthal modal decomposition, a helical phase term $\exp(il\phi)$ is combined with a blazed diffraction grating to create an azimuthal (fork) hologram that was encoded onto the first and second halves of the SLM. The first half of the SLM (SLM$_1$) was used to create the vortex modes with the topological charge l_1 varying from -5 to +5. These modes were imaged via a 4-f lens telescope onto the second half of the SLM (SLM$_2$). Modal decomposition was then performed with SLM$_2$, where transmission functions were displayed and reconstruction takes place, a Fourier lens that mimics the far-field propagation and a Mid-IR beam sensor, the Pyrocam camera at far-field to display the on-axis OAM density. The process of reconstruction on the second half of the SLM is carried out for each topological charge (l_1) of the created modes from -5 to +5 in the first half, by varying l_2 from -5 to 5. In all the modes that are reconstructed for a particular l_1, only one will match the created mode and it is identified by on-axis intensity (detection). All others will yield modes with zero on-axis intensity (no detection). This occurs in an ideal situation when $l_1 = l_2$, that is, when the second half of the SLM is encoded with the complex conjugate of the transmission function encoded in the first half of the SLM. However, in real laboratory setup, the presence of the modal content where $l_1 \neq l_2$, also referred to as a cross-talk, is usually observed. This can be attributed to energy sharing between the adjacent modes, aberrations or system distortions.

Figure 8.20 (a) is a plot of the on-axis intensities detected at the far-field (the Fourier plane) of SLM_2. It illustrates the experimental azimuthal modal decomposition and shows the correlation of the created beam with the detected beam. In this experiment, a full set of modes was investigated using a fork hologram and given a combination of two sets of modes – l_1 (created) and l_2 (detected). Figure 8.20 (a) and (b) also show the experimental (observed) and theoretical (expected modal purity) on-axis intensity where the modal content is contained and where it is not. The inserted beam profiles actually represent the beam with the high on-axis intensity when $l_1 = l_2$, and null intensity when $l_1 \neq l_2$. In the diagram, the detected high on-axis intensities are plotted on the intensity/density plot and they occur along the diagonal.
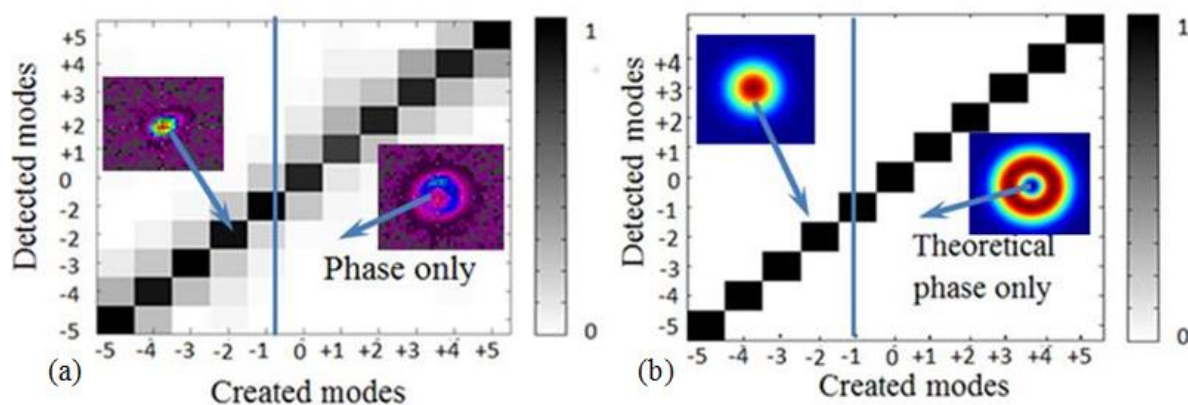
Figure 8.20. Normalised azimuthal modal decomposition – the correlation of the created beam with the detected beam, showing (a) the experimental and (b) the theoretical results. The strong diagonal terms show a high level of agreement.

This indicates the presence of the incident field's modal content. Outside the diagonal, the on-axis intensity is zero (or expected to be zero), and there is modal content on the neighbouring modes outside the diagonal. This is termed "cross-talk" among the modes and it is discussed below.

8.9.2   Non-radial Phase-and-Amplitude Modal Decomposition

In the same manner as above, the phase-and-amplitude modal decomposition was carried out, but with an encoding of a complex modulation hologram (the type 3 match filter [144]) on SLM_1 and SLM_2. The first phase-and-amplitude modal decomposition focused on non-radial modes ($p = 0$),

183

LG_{l0} modes, while SLM_2 varied l_2 from -5 to +5. The created LG_{l0} modes were relayed through a 4-f lens-mirror imaging system to SLM_2.
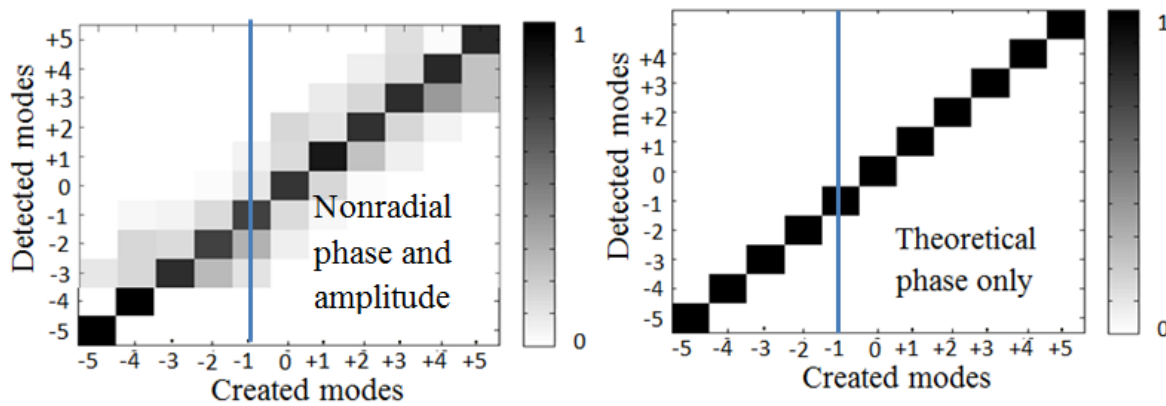
Figure 8.21. The normalised phase-and-amplitude modal decomposition obtained by complex modulation shows the correlation between the created beam at the input and the detected beam at the output. The strong diagonal elements indicate good agreement in the modal decomposition measurements.

While Figure 8.21 (b) shows a theoretical and expected modal purity, the reality is shown by the measured Figure 8.21(a) where cross-talk was also observed outside the diagonal. The azimuthal and complex amplitude density plots above in Figure 8.20 and Figure 8.21 can be compared to the theoretical prediction in terms of their cross-talks. This is illustrated in Figure 8.22, where the single column marked by the blue line in the density plots above (Figure 8.20 and Figure 8.21) is selected, and where the associated normalised intensities are plotted and presented. While this was an indication of agreement between theory and the experimental measurements of the mid-IR modal decomposition, a significant cross-talk with the neighbouring modes was observed. It was also noted that the cross-talk in the complex amplitude modulation (the type 3 match filter) was higher than in the azimuthal. The cross-talk observed can be attributed to an unintended mixture of the modes along the diagonal and neighbouring modes, and possible misalignment of the incident beam on SLM_2.

184
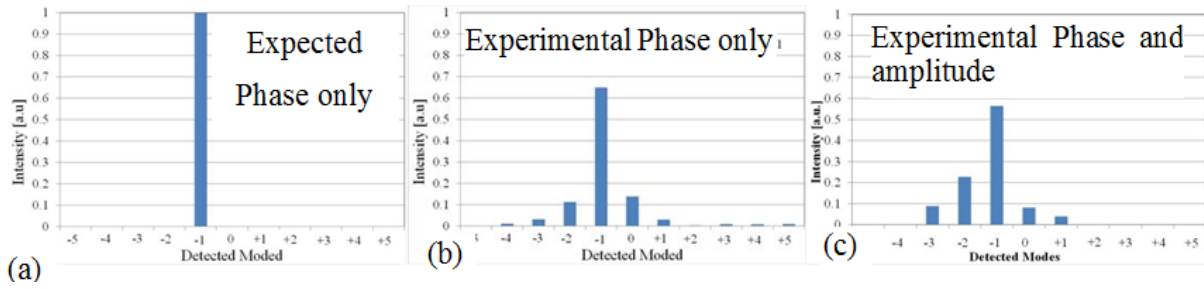
Figure 8.22. Cross-talk analysis for the azimuthal and the non-radial complex amplitude modal decomposition along one of the modal spectra. (b). In Azimuthal modal decomposition, less than 30% of modal power was lost to the neighbouring modes. (c) In phase-and-amplitude, approximately 40% of modal power was lost into the neighbouring modes.

8.9.3   Radial Phase-and-Amplitude Modal Decomposition: Higher Order

Phase-and-amplitude modal decomposition was also investigated for higher order radial modes. This is the demonstration of the creation of optical modes, as well as their detection at far-field. Both SLM_1 and SLM_2 were encoded with type 3 holograms to generate LG_{lp} modes as described in Section 8.7.1, where p_i may not be equal to zero. To achieve this, we fixed the radial and azimuthal modes of the first half of the SLM to l_1 = a and p_1 = b. In other words, SLM_1 was made to create LG_{ab} modes and the 4-f lens system then relayed them as seen in SLM_1 onto SLM_2 for reconstruction. This was done by varying the azimuthal and radial modes l_2 and p_2 of SLM_2 from 0 to 5. The results are depicted in Figure 8.23, Figure 8.24 and Figure 8.25 for LG_{21}, LG_{32} and LG_{43} respectively. In each case, the 3D plot axes represent the mutually perpendicular horizontal axes, the azimuthal and radial indices (l_2 and p_2) of SLM_2, as well as the vertical axis that represents the on-axis intensity at the far-field. As expected, we observed high on-axis intensity when $l_1 = l_2$ and $p_1 = p_2$, but null intensity when any of the two equalities were not satisfied. This indicated that the modes created by SLM_1 were correctly detected by SLM_2.

To illustrate how modal decomposition is achieved in this case, we applied Equation (8.2), where the field on the right-hand side may be unknown. The on-axis intensities represented by c_l were measured at the far-field and added together. Equation (8.15) shows that the superposition of the product of the measured intensities and basis functions reconstructs the entire field.

185

$$\boxed{?} = c_1 \ \boxed{\bullet} + c_2 \ \boxed{\odot} + c_3 \ \boxed{\circledcirc} + \dots \tag{8.15}$$

If there is only one high on-axis intensity (c_{21}), as shown in Figure 8.23 (a), and all others are zero, the reconstructed beam would be fairly similar to the theoretical profile shown in Figure 8.23 (c).
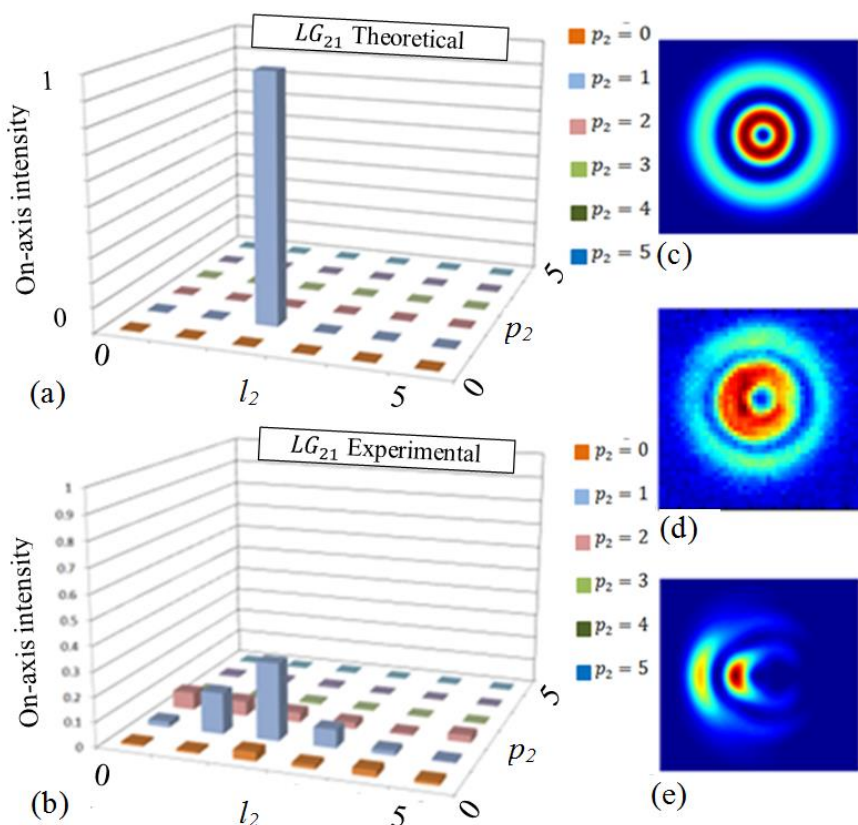
Figure 8.23. Phase-and- amplitude modal decomposition showing the LG$_{lp}$ mode with $l = 2$ and $p = 1$, as well as the 3 D plot of the modal spectrum. The diagram shows (a) the theoretical 3 D plot of the modal spectrum; (b) the experimental 3 D plot of the modal spectrum; (c) the theoretical representation of an LG$_{21}$ mode; (d) an experimentally measured beam profile of the LG$_{21}$ mode; and (e) the reconstructed profile of the LG$_{21}$ mode.

The measured LG$_{21}$ mode (d) was the incident beam onto SLM$_2$ that was encoded with the hologram of Figure 8.18 (b) nature, which is described by Equation (8.13). This beam (LG$_{21}$ mode) was almost identical to the theoretical beam. However, a slight deformation (loss of symmetry) along the horizontal could be observed, as shown by the stronger intensity towards the left of the inner ring. Figure 8.23 (b) is the modal spectrum that enables the reconstruction of the field at far-field. It

186

shows the presence of other modes such as c_{11} and c_{31} that were also observed, which indicates the existence of the cross-talk.

Comparing the reconstructed beam profile in Figure 8.23 (e) first with (c) and (d), the indices $l = 2$ and $p = 1$ are satisfied, but the reconstructed beam is not symmetrical. This is an indication of misalignment of the incident beam in relation to the singularity of the hologram. When comparing the reconstructed beam profile with the profiles in Figure 8.3 (c) that were created from deliberate misalignment, one can confirm that the incident beam at SLM_2 was unintentionally misaligned, that is to say it was illuminating an area slightly off the centre of the hologram. The misalignment could have occurred due to a single lens being used in the 4-f telescope between the two SLMs. This could easily lead to the beam illuminating SLM_2 not being perfectly centred on the singularity, which can construct a non-symmetric beam.

The investigation was extended to two other fields, and the reconstruction of the LG_{32} field was next in our discussion, as shown in Figure 8.24. All the figures from Figure 8.24 (a) through (e) are as described in Figure 8.23. First, the incident beam is clearly asymmetric. Next, the presence of modal content other than the expected LG_{32} is evident and is due to the misalignment of this beam in relation to the singularity of the hologram, as indicated earlier. The modal content in Figure 8.24 (b) managed to implement modal decomposition and to reconstruct the field that satisfies the indices $p = 3$ and $l = 2$, though with a highly asymmetric profile.

187
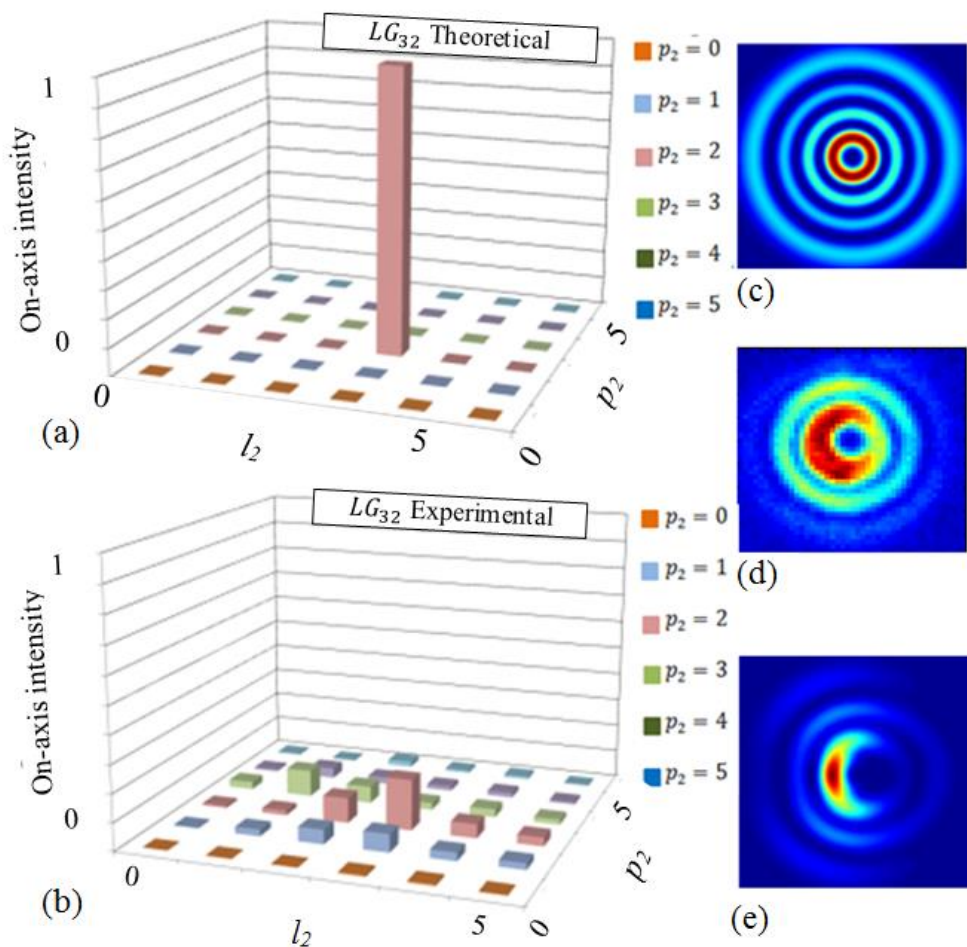
Figure 8.24. Phase-and-amplitude modal decomposition showing the LG_{lp} mode with l = 3 and p = 2 as well as the 3 D plot of the modal spectrum. (a) The theoretical 3 D plot of the modal spectrum. (b) The experimental 3 D plot of the modal spectrum. (c) The theoretical representation of an LG_{32} mode. (d) An experimentally measured beam profile of the LG_{32} mode. (e) The reconstructed profile of the LG_{32} mode.

Figure 8.25 presents the last case that is presented in this research. Figure 8.25 (a) through (e) are described as in the two earlier cases. While the incident LG_{43} mode clearly resembles the theoretical shape, its asymmetry is more defined than the one we discussed in Figure 8.24. The modal content for the LG_{43} mode can be seen in (b), along the index ranges $1 < l_2 < 4$ and $0 < p_2 < 3$ with the modal power dispersed more to the lower l_2 and p_2 values than to the higher l_2 and p_2 values.

188
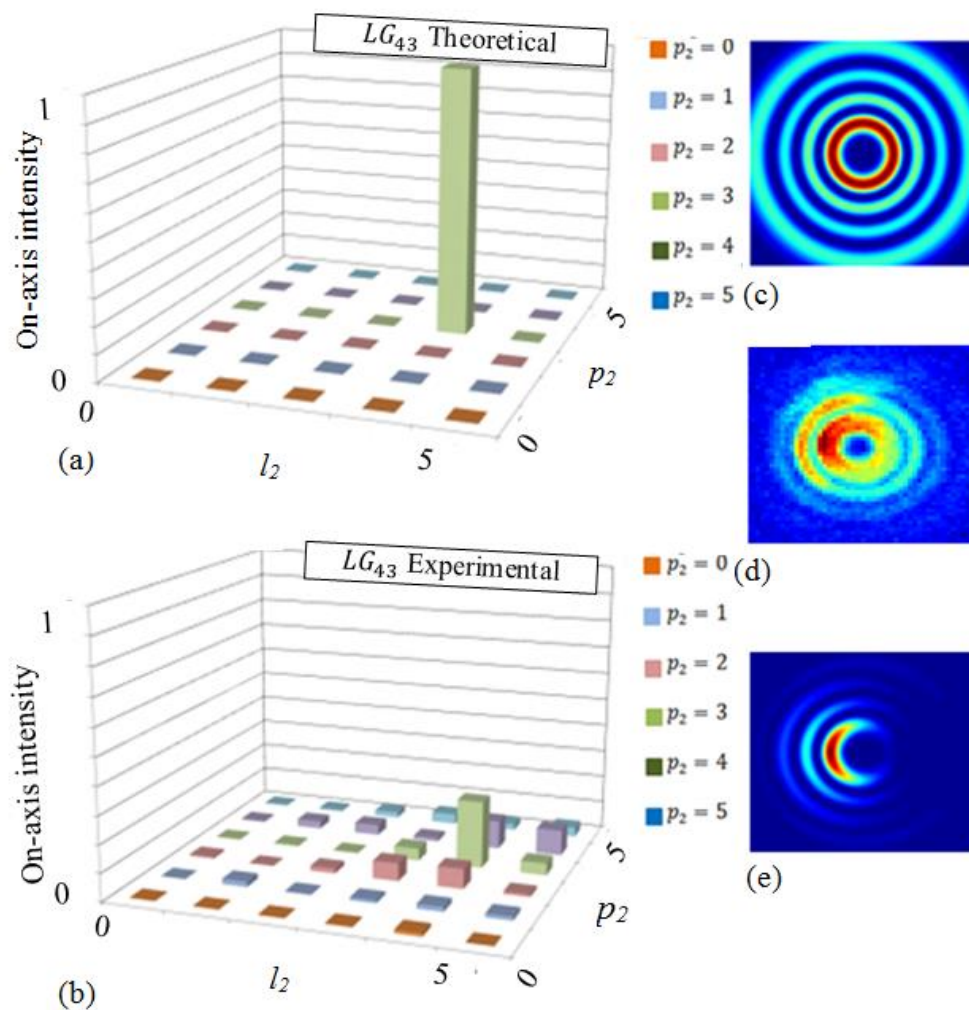
Figure 8.25. Phase-and-amplitude modal decomposition showing the Laguerre Gaussian LG$_{lp}$ mode with $l = 4$ and a non-zero radial index of $p = 3$, as well as the 3 D plot of the modal spectrum. (a) The theoretical 3 D plot of the modal spectrum. (b) The experimental 3 D plot of the modal spectrum as obtained in the lab. (c) The theoretical representation of an LG$_{lp}$ mode. (d) An experimentally measured beam profile of the LG$_{43}$ mode. (e) The reconstructed profile of the LG$_{43}$ mode.

Apart from this, we also observed that the beam was unsymmetrically reconstructed from the data we had obtained experimentally. We can attribute this to alignment inaccuracies resulting from the limited space that was available to assemble the system. For instance, the setup had only one SLM that we digitally divided into two halves and relayed-imaged the beam from one half to the other by employing a 4-f imaging system and a double pass through a single lens. With the beam clearly not aligned to pass through the centre of the lens, this resulted in the unsymmetrical reconstructed

189

beam. It can be seen in all the experiments that the reconstructed beam was unsymmetrical in the same way. The asymmetry of all the reconstructed fields is similar to that shown in the illustration in Figure 8.3 (c) and the laser was deliberately misaligned by shifting the singularity along the x-(horizontal) axis. Since we discovered that the misalignment leads to the beam being off-centre of the singularity, we strongly suspect that there was an unintended misalignment in our setup. This is so because all the experiments were conducted with the same setup and yielded reconstructed beam profiles that were not symmetric. All were shaped in the similar manner as the illustration in Figure 8.3 (c). thus confirming misalignment in our laser setup.

8.10   Discussion

It remains our responsibility to correct the alignment (the shift of the singularity on SLM_2 along the horizontal axis) problem with the current setup. Misalignment can also be avoided by conducting these experiments with two SLMs. The problem of misalignment, however, did not hinder the intended beam reconstruction as it was observed that every reconstructed beam agreed with the experimentally generated and the theoretical beam profiles. In addition, we can conclude that the observed cross-talk outside the mode that was intended for detection – together with the asymmetric beam profile contributed to the drop in the modal power of our results. Another factor that has contributed quite strongly to modal power drop is the low resolution of the 2 µm detecter (the Pyrocam). For example, resolution problems are not pronounced with visible light detectors (Spiricon camera) that have 4.5 µm pixel sizes, while the Pyrocam has ~ 30 µm pixels. This reduction in detection resolution also limits the correct acquisition of the modal weightings.

8.11   Conclusion

This chapter introduced beam shaping to mid-IR light. The literature review discussed the evolution of beam shaping from using static optical elements to dynamic SLMs. The literature review traces this evolution, using several studies which included modal decomposition of light fields, by mapping a two-dimensional field distribution onto the one-dimensional space and validating the results at the output on 16 modes. We also discussed the use of MODAN-based field reconstruction technique to obtain unambiguously and experimentally solve the modal decomposition problem. As the limitations of the MODAN technique were highlighted, with the literature study we discussed

190

the use of computer-generated holograms (CGHs) that were increasingly preferred in all optical measurement to determine the beam's M^2 values. The study showed that the later introduction of SLMs use solved many of the limitation of earlier components used in beam shaping had because they are dynamic and able to generate the desired results in real time. With SLM beam shaping, we looked at a few reports on modal decomposition.

The chapter sought to implement beam shaping (modal decomposition) on the mid-IR light. First, we discussed the calibration of the SLM that was quoted for a mid-IR source and later reviewed the theory of modal decomposition, both for the phase-only and phase-and-amplitude cases. With this research, we demonstrated – for the first time according to our knowledge – the creation and detection of mid-IR structured light fields, using vortex and LG_{lp} mode basis functions. Apart from the misalignment that resulted in unsymmetrical reconstructed fields, the shapes illustrated a good agreement between the experimentally generated and reconstructed (measured) modes and the theoretically expected modes. We believe that the work in hand can prove useful for beam shaping of 2 µm sources, in particular for high-bandwidth communication experiments.

191

Chapter 9

9. Mid-IR Wavefront Reconstruction Spatial Light Modulator

9.1   Introduction

Wavefront reconstruction is highly topical in academic and industrial research and has a wide market in industry. Wavefront measurements are sought after for applications that require high-resolution imaging such as terrestrial observation, communication and microscopy that rely on precise wavefront estimations. Wavefront reconstruction has been implemented extensively for these applications, with various techniques in the visible and 1 µm wavelength bandsbeing employed. Such techniques include laser ray tracing, pyramid sensors, interferometric approaches, and the Shack-Hartmann sensors (SHS). Adaptive optics are used to implement these techniques so as to correct measured wavefronts, yield enhanced beam qualities and therefore achieve improved spatial resolution [149].

Recently, in 2011, the capability of CGHs as wavefront sensors was investigated and the results obtained indicated that a wavefront that is distorted can be retrieved immediately through solving the amplitude of each coded mode [150]. After this, in 2013, the reconstruction of laser beam wavefronts from their mode spectra was demonstrated with SLMs. This enabled the investigation of the influence of defined wavefront distortions on the modes that compose the field in question [149]. In particular, applications that require high resolution rely on precise wavefront estimation. Noting the benefits of beam shaping, wavefront reconstruction in the mid-IR opens a wide research field that will enable one to precisely quantify wavefront measurements for different applications. Our concept is to use modal decomposition on an incident laser beam of unknown curvature to extract its wavefront. To demonstrate this technique of modal decomposition on wavefront reconstruction, we subjected the beam to three digitally encoded lens functions of different curvatures. The first was a blank grating ($f_1 = \infty$ m), the second a strongly curved grating ($f_2 = 200$ m) and the last a more weakly curved grating ($f_3 = 400$ m). The modal decomposition was used to reconstruct the wavefront of the resulting mid-IR optical fields.

9.2   Wavefront Reconstruction Literature Review

Wavefront reconstruction is one of the measurements that have existed for some time now to test various beam properties [126]. This section looks at few techniques to perform wavefront measurements. Such techniques include interferometric methods [151], laser ray tracing [152], pyramid sensors [62] and the widely used Shack-Hartmann sensor (SHS) [153]. The SHS has also been used in the mid-IR wavelength range (3.4-4.2 μm) [123]. In recent developments, CGHs have been used to encode specific aberrations to determine the Zernike coefficients [126]. A wavefront and phase measurement method − based on the correlation filter method that, together with an appropriate CGH, was used for complete modal decomposition of the light − is also reported [138].

Wavefront investigation covers quite a wide spectrum, and as a result the focus of this section is limited to wavefront reconstruction involving only some of the recent techniques, namely SHS, CGH and liquid crystal SLM. The research report that was selected on the basis of its relevance to the current research, was the report by Schulze et al. (2012), who compared measurements using a Shack-Hartmann wavefront sensor (SHS) and the reconstructed values from a decomposition measurement of just three modes. Several differences were noted. The Schultze work was noted because explains why a CGH-based wavefront measurement is preferable over SHS.

Figure 9.1 depicts the comparison of the intensities and differences. The SHS results are pixelated (Figure 9.1 (a) and (d)), whereas the modal results (b) and (e) by the CGH-based wavefront reconstructions are not. A CGH-based wavefront reconstruction was found to have several advantages over the SHS, namely the spatial resolution, the extension of the measurement area, and the measurable wavefront slope. The SHS is limited in spatial resolution due to the number of microlenses, where the resolution of the wavefront quantified by the CGH has no theoretical limit. Secondly, with SHS, wavefronts cannot be measured at points where there is little or no intensity − for example at phase singularities.

193
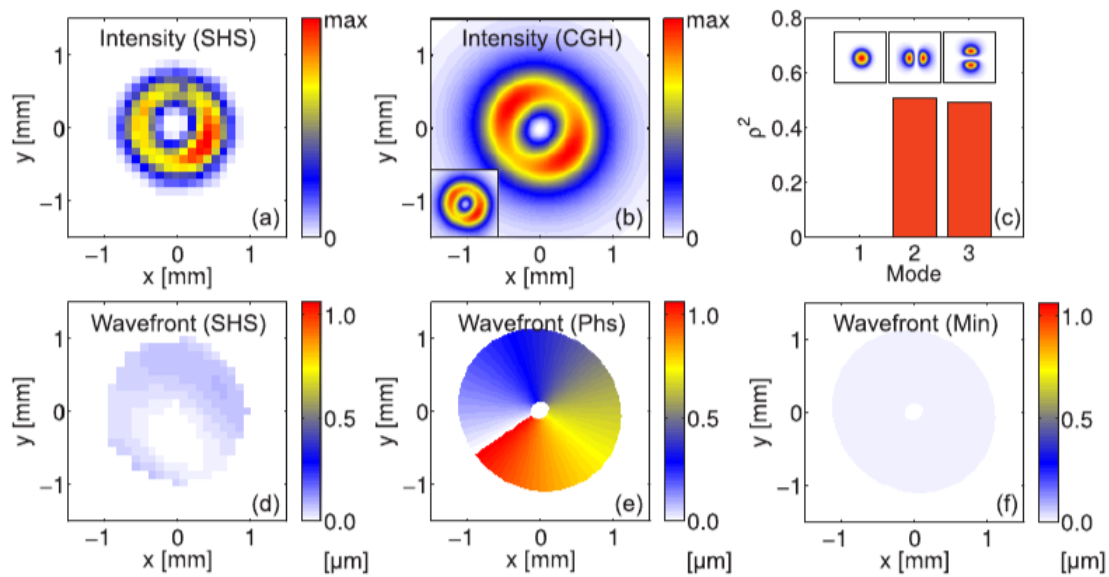
Figure 9.1. Donut beam wavefront reconstruction. (a) Intensity measured with the SHS. (b) Reconstructed intensity (inset depicts directly measured intensity with CCD camera). (c) Modal power plot. (d) Wavefront measured with SHS (scale in μm). (e) Wavefront determined from the phase reconstruction (scale in μm). (f) Wavefront from the minimisation of the weighted power density [138].

However, the phase of the beam that is determined by the CGH is defined everywhere, even in regions with no intensity. This means that with CGHs, wavefronts and phases are reconstructed in the entire frame, with no restriction to the depicted area. Lastly, the wavefront slope for the SHS is limited to the measurable slope, because the focus of one microlens can be shifted to the evaluation area of an adjacent lens. The wavefront reconstruction with the CGH shows no theoretical limit regarding the wavefront slope; even phase jumps can be detected easily [138].

In most recent works, wavefront reconstruction techniques are SLM based. In the work by Schulze et al. (2013) (which we report on here), the authors used the mode spectrum to demonstrate the reconstruction of a laser beam wavefront. They systematically investigated the influence of defined wavefront distortions (Zernike aberrations) on the modal composition of the beam. Figure 9.2 depicts the results of several aberrations with specific strengths that yield a similar impact on the mode spectrum [149].

194
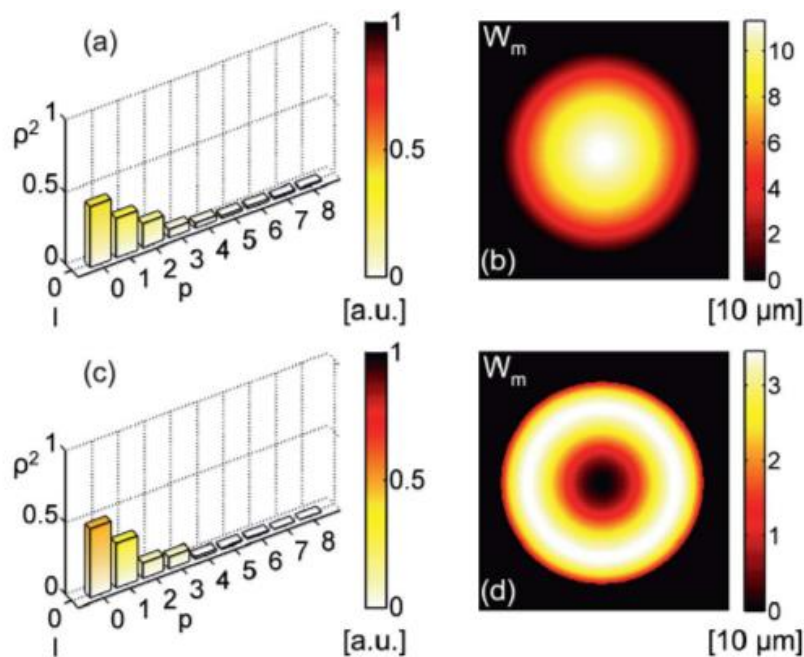
Figure 9.2. Modal decomposition of an aberrated Gaussian beam. (a) Modal power spectrum. (b) Reconstructed wavefront. (c) Modal power spectrum. (d) Reconstructed wavefront [149].

Figure 9.2 (a) and (c) present modal spectra that reveal a decay toward higher-order modes with $p \geq 0$ and $l = 0$. The measured wavefronts that are shown in Figure 9.2 (a) and (c) reveal the typical shapes for such aberrations [149]. They found that all the measured wavefront aberrations were in agreement with the theoretically expected deformations.

9.3 Wavefront Reconstruction by Modal Decomposition

Consider $U\exp(i\omega t)$ to represent a monochromatic optical field, where the time independent field $U(\vec{r})$ for the decomposition into a set of LG$_{lp}$ modes for free space is given by Equation (9.1) [149].

$$U(\vec{r}) = \sum_{p,l} \rho_{p,l} u_{p,l}(\vec{r}) exp(i\phi_{p,l})$$

(9.1)

195

$u_{p,l}$ is the LG_{lp} mode with radial and azimuthal indices (l, p) at $z = 0$, at its waist position. For wavefront reconstruction, we need to determine the modal powers $(\rho_{l,p})$ and phases $(\phi_{p,l})$ from a given set of orthogonal basis functions.

These above parameters (the modal powers $(\rho_{l,p})$ and intermodal phases $(\phi_{p,l})$) carry the information required to recover the optical field in terms of amplitude and phase, and finally to reconstruct the wavefront W by minimising the integral [149] given by Equation (9.2).

$$\iint |\vec{P}| \left| \frac{\vec{P}_t}{\vec{P}} - \nabla_t W \right| dA \rightarrow min \qquad \textbf{(9.2)}$$

$\vec{P} = [P_x, P_y, 0]$ is the Poynting vector or the vector distribution of the beam, and t indicates the transverse components $\nabla_t = [\partial x, \partial y]$. dA is the surface element of the wavefront. The Poynting vector is defined as the rate of electromagnetic energy flow per unit area. As a result, it has been invariably examined for waves with plane wavefronts ([140], [154]). Here, we refer to it as the wavefront reconstruction of LG_{lp} beams that have helical wavefronts. Since the Ho:LiLuF$_4$ crystal emits a linearly polarised beam, i.e. a scalar beam, its wavefront (W) is defined by its phase distribution $\Phi(\vec{r})$. Equation (8.4) describes this wavefront as:

$$W(\vec{r}) = \frac{\lambda}{2\pi} \Phi(\vec{r}) \qquad \textbf{(9.3)}$$

where $\Phi(\vec{r}) = -kr^2/2f$ is the phase of the optical field. However, this is only true if the beam wavefronts are continuous and have no phase jumps or phase singularities ([138], [149], [155]. To reconstruct the optical field (and consequently the Poynting vector distribution and wavefront), a correlation filter technique is used and a CGH acts as a match filter to correlate the investigated laser beam with a given set of modes. Consequently, this inner product measurement appears as an on-axis intensity $I = \iint T^*(\vec{r})U(\vec{r})d^2r$ in the Fourier plane of the hologram, where $T^*(\vec{r})$ is the complex conjugate of the transmission function $T_{p,l}(\vec{r}) = u^*_{p,l}(\vec{r})$ of the hologram required to measure the power content of the modes. The coefficient c_l, defined in Chapter 8 by Equation (8.2), describes the spatial distribution or the amplitude of the optical field. The phase of this optical field is described by the quantity Φ, as defined by Equation (8.5).

Furthermore, to measure the intermodal phase difference $\Delta\phi_l$ between mode ψ_l and a certain reference mode ψ_0 requires the two transmission functions expressed in Equations (9.4) and (9.5). They need to be encoded as match filters, with each representing an interferometric superposition of two modes ([140] [133]).

$$\text{Cosine term:} \quad T_l^{\text{Cos}}(\vec{r}) = \frac{1}{\sqrt{2}}[\psi_l^*(\vec{r}) + \psi_0^*(\vec{r})] \tag{9.4}$$

$$\text{Sine Term:} \quad T_l^{\text{Sin}}(\vec{r}) = \frac{1}{\sqrt{2}}[\psi_l^*(\vec{r}) + i\psi_0^*(\vec{r})] \tag{9.5}$$

By measuring the on-axis optical intensity signals from the inner product phase at the far-field where $I_l^{\text{Sin}} \propto \rho_0^2 + \rho_l^2 + 2\rho_0\rho_l\text{Sin}\,\Delta\phi_l$ [149] corresponds to $T_l^{Sin}(\vec{r})$ [120], and $I_l^{\text{Cos}} \propto \rho_0^2 + \rho_n^2 + 2\rho_0\rho_l\text{Cos}\Delta\phi_l$ corresponds to $T_l^{Cos}(\vec{r})$, intermodal phases can be calculated according to Equation (9.6) [140]:

$$\Delta\phi_l = -arctan\left[\frac{2I_l^{\text{Sin}} - \rho_0^2 - \rho_l^2}{2I_l^{\text{Cos}} - \rho_0^2 - \rho_l^2}\right] \tag{9.6}$$

In this equation, I_l^{Sin} and I_l^{Cos} indicate the intensity signals from the measurement of the phase (inner product) measurements [120]. To implement such filters, a phase-only (azimuthal) and/or a phase-and-amplitude match filter is encoded on the SLM [140].

Two types of modal decomposition are discussed in the following subsections, based on phase-only (azimuthal) holograms that generate vortex beams, as well as on phase-and-amplitude (complex modulation) that uses holograms encoded with the 'type 3' complex amplitude modulation technique reported by Arrizón et al. (2007) [144] to generate Laguerre-Gaussian LG_{lp} modes.

The phase difference is described by Equation (9.6) in terms of ρ_0, ρ_l, I_l^{sin} and I_l^{sin}. The following equations can simplify the measurements taken. Equation (9.7) evaluates ρ_0, the amplitude of the Gaussian basis function Ψ_0 such that

$$\Psi_o^* \times \Psi_0 = \rho_0 \tag{9.7}$$

197

where Ψ_o^* describes its complex conjugate representing a reference transmission function. The sine and the cosine intensity signals are given by Equations (9.8) and (9.9):

$$T_l^{\sin} \times \Psi_l \rightarrow I_l^{\sin} \qquad \textbf{(9.8)}$$

$$T_l^{\cos} \times \Psi_l \rightarrow I_l^{\cos} \qquad \textbf{(9.9)}$$

where $T_l^{\sin}$ and $T_l^{\cos}$ are the transmission functions for both the sine and the cos terms. Equations (9.7), (9.8) and (9.9) are evaluated with measurements in the lab. The phase difference $\Delta\phi_l$ can be calculated from Equation (9.6), and the entire field can be reconstructed.

9.4 Wavefront Reconstruction Method

A procedure similar to the phase-and-amplitude modal decomposition was followed for the wavefront reconstruction. The difference was that the first half of the SLM was encoded with a lens hologram, while the second half was encoded with the *LG* holograms via complex amplitude modulation (type 3, [144]).

The experimental set-up implemented here was the same as for the modal decomposition discussed in Chapter 8 in Figure 8.19. Figure 9.3 presents the schematic diagram that illustrates the modal decomposition for wavefront reconstruction. The mid-IR laser beam (possessing an unknown wavefront) was aligned to the center of SLM$_1$, which was encoded with lens functions of varying curvature.
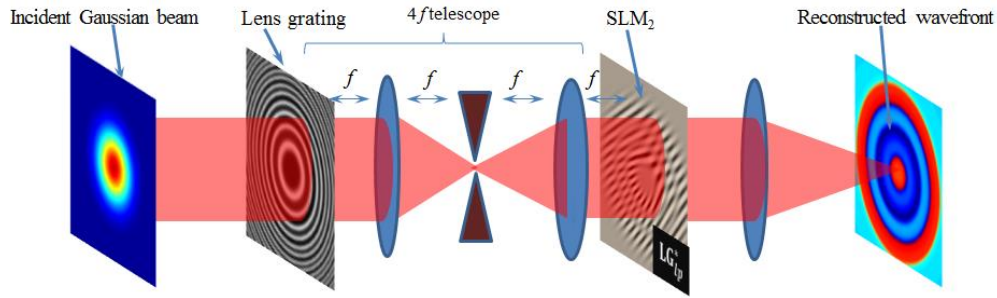
Figure 9.3. Wavefront reconstruction: The lens grating encoded on SLM$_1$ is used to induce a known curvature on an incoming beam of unknown curvature. The hologram on SLM$_2$ was the type 3 presented in Arizon's technique [144] and is used to reconstruct and detect the resulting wavefront.

Three lens gratings were encoded on SLM$_1$, namely the blank grating ($f_{gr1} = \infty$), the lens grating 2 ($f_{gr2} =$200 mm) and the lens grating 3 (($f_{gr3} = 400$ mm). A 4-f telescope (one lens and mirror combination) was mounted to relay the created image from SLM$_1$ plane onto SLM$_2$. An aperture was placed at the Fourier plane of SLM$_1$ to act as a filter to separate the desired (1st diffraction order) from the undiffracted light (0th diffraction order). The wavefront of the incoming beam was measured by displaying the transmission functions $T_{l,p}^{\rho}$, $T_l^{\sin}$ and $T_l^{\cos}$ on SLM$_2$, according to Equations (9.4) and (9.5). It also measured the intensities $I_{l,p}^{\rho}$ (amplitudes), $I_l^{\sin}$ and $I_l^{\cos}$ (the phase terms) according to Equations (9.8) and (9.9) for phase (as it varies from 0 to 2π) measurements, taken at the far-field of SLM$_2$.

First we encoded a blank screen (i.e. no curvature was encoded) on the first half of SLM (SLM$_1$) in order to reflect the incident laser beam with its original curvature and propagate it to SLM$_2$ to perform the modal decomposition. On SLM$_2$, we encoded the LG holograms via complex amplitude modulation (type 3, [144]) and looped through the indices $p_2 =\{0, 1, \ldots,5\}$ and $l_2 =\{-3, -2, \ldots, +3\}$ to extract the amplitudes and intermodal phases from this beam of unknown curvature. A camera was placed in the Fourier plane [$f(L_2) = 300$ mm] of SLM$_2$, enabling us to detect the modal powers and the phase distribution.

Two additional cases are also presented below for lens gratings encoded on SLM$_1$ with self-induced curvatures – that is, focal lengths of $f_{gr2} = 200$ mm and $f_{gr3} = 400$ mm respectively.

199

The same procedure that was undertaken on the blank grating was followed for each of these experiments. Taking advantage of the dynamic nature of SLMs, the transmission functions were displayed one after the other. Section 9.5 presents the results of each case.

9.5   Wavefront Reconstruction Results

This section presents the results of wavefront reconstruction carried out by encoding holograms with lens gratings of different curvatures. The results are contained in Figure 9.4, Figure 9.5, and Figure 9.6 respectively.

9.5.1   Wavefront Reconstruction with Different Lens Gratings

The results presented first were obtained when a blank grating was used to determine the unknown curvature of the incoming 2 µm light. Figure 9.4 presents the normalised intensities for the amplitudes, the intermodal phase (the sine and the cosine) terms, as well as the reconstructed wavefront.

The reconstructed beam wavefront is expected to show the original curvature of the beam as determined by its phase. It can be observed that the wavefront had a phase that alternated between ~0 and ~2π radians, which are equivalent. This indicates that the incoming beam also had a phase of ~0 or ~2π radians.
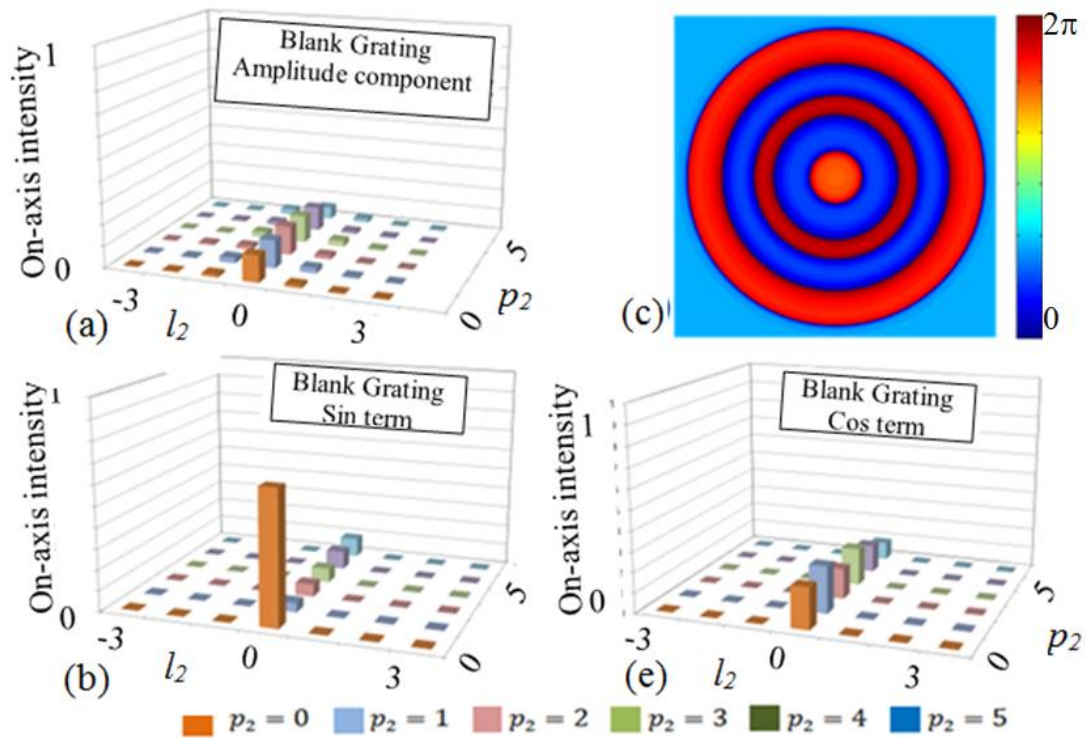
Figure 9.4. Wavefront reconstruction results when SLM$_1$ is encoded with a blank grating (i.e. no curvature). (a) The measured amplitudes. (b) Intermodal phases (relating to the Sine term). (c) Intermodal phases (relating to the Cosine term). (d) The reconstructed wavefront.

The same procedure was executed for lens gratings of focal length, $f_{\text{lens grating}}= 200$ mm in Figure 9.5, thus inducing a known curvature on the field.

For the $f_{\text{lens grating}}= 200$ mm, the resulting wavefront had a self-induced curvature varying between $0\ \pi$ and $2\ \pi$. The results indicate that the 200 mm lens grating successfully induced a curvature on the wavefront, as shown by the change of the phases on the beam.
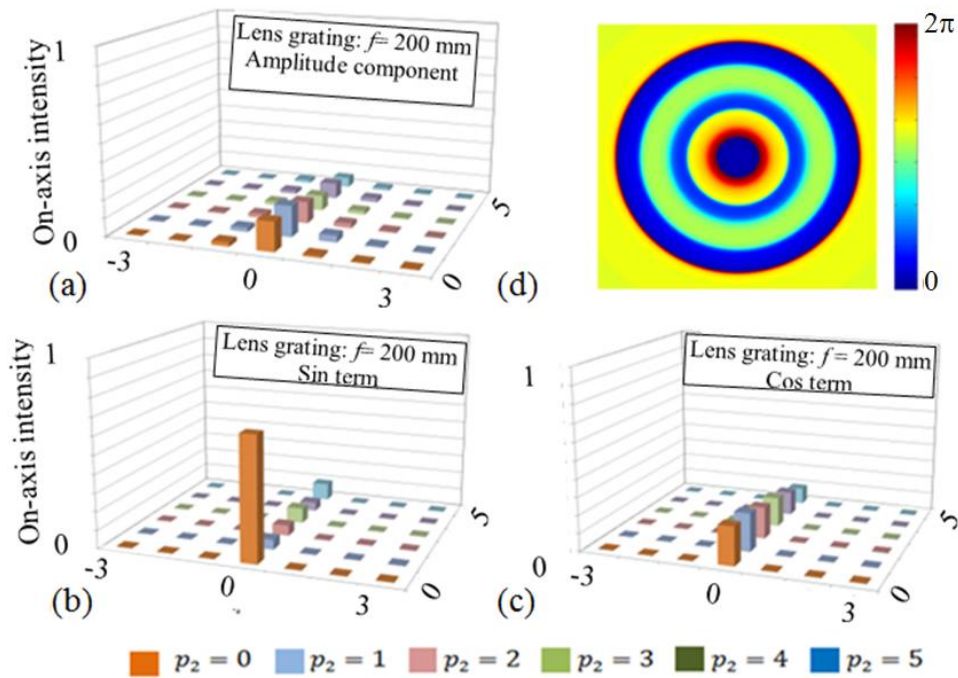
Figure 9.5. Wavefront reconstruction results when SLM$_1$ is encoded with a lens function with focal length of 200 mm. (a) The measured amplitudes. (b) Intermodal phases (relating to the Sine term). (c) Intermodal phases (relating to the Cosine term). (d) The reconstructed wavefront.

Figure 9.6 presents the normalised amplitude intensities, the intermodal phase intensities (the sine and the cosine terms), as well as the resonstructed wavefront for the lens grating of $f_{\text{lens grating}} = 400$ mm. The investigation is to detemine the resulting curvature of the lens grating.
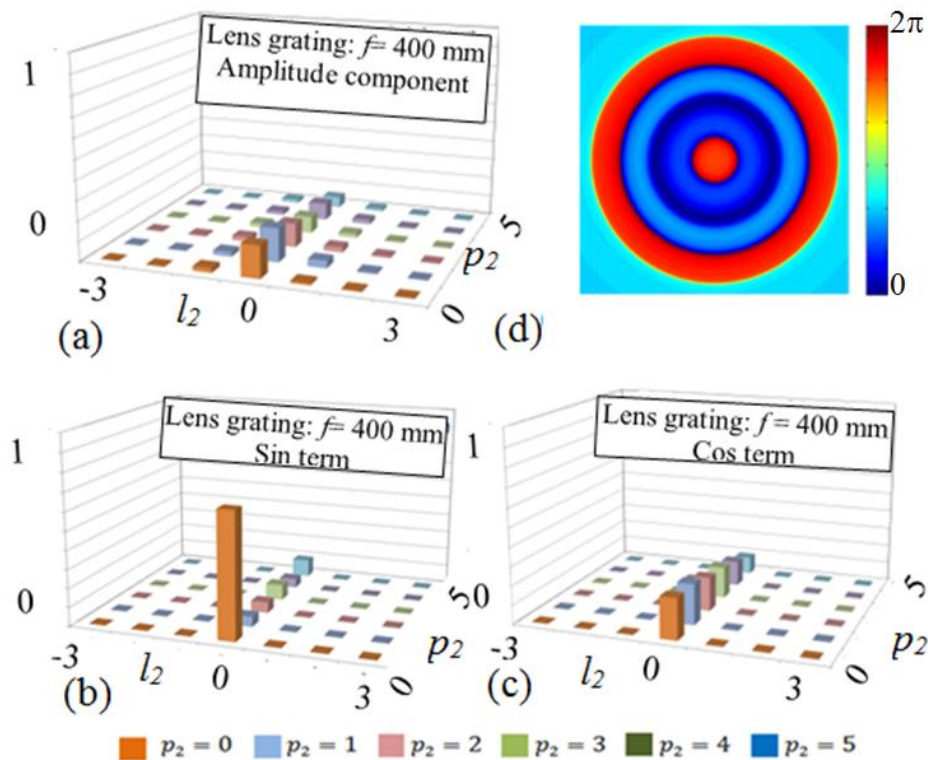
Figure 9.6. Wavefront reconstruction results when SLM1 is encoded with a lens function with focal length of 400 mm. (a) The measured amplitudes. (b) Intermodal phases (relating to the Sine term). (c) Intermodal phases (relating to the Cosine term). (d) The reconstructed wavefront.

The red outer ring indicates a phase that is ~2π, while the inner disc shows a phase that fluctuates close to 0 radians.

Figure 9.4 (d), Figure 9.5(d) and Figure 9.6 (d) represent the wavefront that was reconstructed based on the amplitudes and intermodal phases measured from the modal decomposition. From Figure 9.4 (a) and (d) it is evident that a degree of curvature exists in the field due to the detection of radial modes when performing the decomposition. This is also the case when a curvature of $f = 200$ mm and $f = 400$ mm is imparted onto the field of interest. It would have been ideal to verify this curvature against the wavefront measured from a Shack-Hartmann wavefront sensor. However, the Shack-Hartmann wavefront sensor does not operate within the mid-IR region.

203

The lack of uniformity of the phases of the beam can be attributed to the possible misalignment (see Chapter 8) that was present in this experiment and had an impact on the reconstruction of the wavefronts. This included alignment inaccuracies due to the construction of the system in a limited space and with limited equipment (only one SLM was used to both impart curvature and measure it with a double pass through a single lens that produces additional aberrations (curvatures)). In addition, the nonuniform curvature was caused by the additional (neighbouring) modes that mixed with the desired mode. The low resolution of the 2 µm detector (the Pyrocam) also had a negative impact on the detection procedure.

9.6   Conclusion

In this chapter we demonstrated how modal decomposition can be used to reconstruct the wavefronts of optical fields. Very limited work on wavefront reconstruction has been reported – in fact, only the work by Robert et al. (2012). However, the comparison between SLM and SHS-based measurements that was done by Schulze et al. (2012) showed that SHS is unable to measure wavefronts of mid-IR sources. This is – to the best of our knowledge – the first demonstration of extracting wavefronts of mid-IR light, and it was done with mid-IR coated SLMs.

While alignment was found to affect the results, the work in hand has shown that the wavefront of radiation of an unknown curvature can be extracted. By inducing known curvatures, the detected wavefront can be influenced or manipulated. The current state of results can be improved by using (at best) two SLMs with enough space to propagate the beam with no overlapping of modes, thus increasing cross-talk in our results. Thus, this work can prove useful for wavefront monitoring of 2 µm sources in terrestrial observation, communication and microscopy.

10. References

[1]   W. Koechner, *Solid-state laser engineering*, vol. 1. Springer, 2013.

[2]   A. Forbes, A. Dudley, and M. McLaren, "Creation and detection of optical modes with spatial light modulators," *Advances in Optics and Photonics*, vol. 8, no. 2, pp. 200–227, 2016.

[3]   T. H. Ngo, C. H. Kim, Y. J. Kwon, J. S. Ko, D.-B. Kim, and H.-H. Park, "Wideband receiver for a three-dimensional ranging LADAR system," *IEEE Transactions on Circuits and Systems I: Regular Papers*, vol. 60, no. 2, pp. 448–456, 2013.

[4]   R. Richmond and S. Cain, "Direct-detection LADAR systems," 2010.

[5]   A. Wehr and U. Lohr, "Airborne laser scanning—an introduction and overview," *ISPRS Journal of photogrammetry and remote sensing*, vol. 54, no. 2–3, pp. 68–82, 1999.

[6]   M.C. Amann, T. M. Bosch, M. Lescure, R. A. Myllylae, and M. Rioux, "Laser ranging: a critical review of unusual techniques for distance measurement," *Optical engineering*, vol. 40, no. 1, pp. 10–20, 2001.

[7]   C. S. Fox, "Active electro-optical systems," *The infrared and electro-optical systems handbook-IR/EO systems handbook, Bellingham: SPIE-The International Society for Optical Engineering and Ann Arbor, Michigan: ERIM-Infrared Information Analysis Center,| c1993, edited by Fox, Clifton S.*, 1993.

[8]   H.-S. Cho, C.-H. Kim, and S.-G. Lee, "A high-sensitivity and low-walk error LADAR receiver for military application," *IEEE Transactions on Circuits and Systems I: Regular Papers*, vol. 61, no. 10, pp. 3007–3015, 2014.

[9]   R. Sabatini, M. A. Richardson, A. Gardi, and S. Ramasamy, "Airborne laser sensors and integrated systems," *Progress in Aerospace Sciences*, vol. 79, pp. 15–63, 2015.

[10]   J. S. Massa, G. S. Buller, A. C. Walker, S. Cova, M. Umasuthan, and A. M. Wallace, "Time-of-Flight Optical Ranging System Based on Time-Correlated Single-Photon Counting." *Appl Opt*, vol. 37, no. 31, pp. 7298–304, 1998.

[11]   B. Li, J. Sang, and Z. Zhang, "A real-time orbit determination method for smooth transition from optical tracking to laser ranging of debris," *Sensors*, vol. 16, no. 7, p. 962, 2016.

[12] Y. Wang, L. Huang, M. Gong, H. Zhang, M. Lei, and F. He, "1 MHz repetition rate single-frequency gain-switched Nd: YAG microchip laser," *Laser Physics Letters*, vol. 4, no. 8, p. 580, 2007.

[13] L. Zenteno, E. Snitzer, H. Po, R. Tumminelli, and F. Hakimi, "Gain switching of a Nd^{3+} -doped fiber laser," *Optics letters*, vol. 14, no. 13, pp. 671–673, 1989.

[14] J. Zayhowski, J. Ochoa, and A. Mooradian, "Gain-switched pulsed operation of microchip lasers," *Optics letters*, vol. 14, no. 23, pp. 1318–1320, 1989.

[15] C. Larat, C. Feugnet, M. Schwarz, and J. Pocholle, "Gain-switched solid-state-laser pumped by high brightness laser diodes," in *Lasers and Electro-optics Europe, 1996. CLEO/Europe., Conference on*, 1996, pp. 57–57.

[16] E. Krüger, "High-repetition-rate electro-optic cavity dumping," *Review of scientific instruments*, vol. 66, no. 2, pp. 961–967, 1995.

[17] L. McDonagh, R. Wallenstein, and R. Knappe, "47 W, 6 ns constant pulse duration, high-repetition-rate cavity-dumped Q-switched TEM 00 Nd: YVO 4 oscillator," *Optics letters*, vol. 31, no. 22, pp. 3303–3305, 2006.

[18] P. He, H. Wang, L. Zhang, J. Wang, C. Mo, C. Wang, X. L and D. Chen, "Cavity-dumped electro-optical Q-switched Nd: GdVO$_4$ laser with high repetition rate," *Optics & Laser Technology*, vol. 44, no. 3, pp. 631–634, 2012.

[19] P. Urquhart, "Review of rare earth doped fibre lasers and amplifiers," *IEE Proceedings J (Optoelectronics)*, vol. 135, no. 6, pp. 385–407, 1988.

[20] Y. Wang and C.-Q. Xu, "Actively Q-switched fiber lasers: Switching dynamics and nonlinear processes," *Progress in Quantum Electronics*, vol. 31, no. 3–5, pp. 131–216, 2007.

[21] I. Abdulhalim, C. Pannell, L. Reekie, K. Jedrzejewski, E. Taylor, and D. Payne, "High power, short pulse acousto-optically Q-switched fibre laser," *Optics communications*, vol. 99, no. 5, pp. 355–359, 1993.

[22] K. the L. touch, "keopsys." [Online]. Available: https://www.keopsys.com. [Accessed: 2018]

[23] C. Larat, M. Schwarz, J.-P. Pocholle, G. Feugnet, and M. R. Papuchon, "High-repetition rate, short-pulse, diode-pumped solid state laser for space communications," in *Space Optics 1994: Space Instrumentation and Spacecraft Optics*, 1994, vol. 2210, pp. 565–571.

[24] X. Liu, Z Shi, Y Huang, Z Fan, J Yu, J Zhang, "Very high repetition-rate electro-optical cavity-dumped Nd: YVO4 laser with optics and dynamics stabilities,"

Optics Communications, vol. 336, pp. 273–277, 2015.

[25] W. Roberts, "Cavity-dumped communication laser design," 2003.

[26] Y. Ma, X. Yu, X. Li, C. Wang, R. Yan, and J. Yu, "High repetition rate electro-optical cavity-dumped Nd: GdVO 4 laser," in *The European Conference on Lasers and Electro-Optics*, 2013, p. CA_P_13.

[27] U. Keller, "Ultrafast solid-state laser oscillators: a success story for the last 20 years with no end in sight," *Applied Physics B: Lasers and Optics*, vol. 100, no. 1, pp. 15–28, 2010.

[28] J. E. Bernard and A. J. Alcock, "High-repetition-rate diode-pumped Nd:YVO4 slab laser.," *Opt Lett*, vol. 19, no. 22, p. 1861, 1994.

[29] B. Chichkov, C. Momma, S. Nolte, F. Von Alvensleben, and A. Tünnermann, "Femtosecond, picosecond and nanosecond laser ablation of solids," *Applied Physics A*, vol. 63, no. 2, pp. 109–115, 1996.

[30] J. Gu, F. Zhou, K.T. Wan, T.K. Lim, S.C. Tam, Y.L. Lam, D. Xu, and Z. Cheng, "Q-switching of a diode-pumped Nd: YVO4 laser with GaAs nonlinear output coupler," *Optics and lasers in Engineering*, vol. 35, no. 5, pp. 299–307, 2001.

[31] T. T. Nicolaie Pavel Jiro Saikawa H, "Diode end-pumped passively Q-switched Nd: YAG laser intracavity frequency doubled by LBO crystal," *Optics communications*, vol. 195, no. 1–5, pp. 233–240, 2001.

[32] Y. Chen, T. Huang, and C. Wang, "Passively Q-switched diode-pumped Nd: YVO_4/Cr^{4+}: YAG single-frequency microchip laser," *Electronics Letters*, vol. 33, no. 22, pp. 1880–1881, 1997.

[33] J. J. Zayhowski, "Passively Q-switched Nd: YAG microchip lasers and applications," *Journal of Alloys and Compounds*, vol. 303, pp. 393–400, 2000.

[34] T. Omatsu, M. Okida, A. Minassian, and M. J. Damzen, "High repetition rate Q-switching performance in transversely diode-pumped Nd doped mixed gadolinium yttrium vanadate bounce laser," *Optics Express*, vol. 14, no. 7, pp. 2727–2734, 2006.

[35] Y. Wang, M. Gong, and H. Zhang, "2 ns pulse width high repetition rate short cavity acousto-optically Q-switched Nd: YVO4 laser," *Electronics Letters*, vol. 43, no. 7, pp. 394–396, 2007.

[36] T. Ogawa, T. Imai, K. Onodera, H. Machida, M. Higuchi, Y. Urata, and S. Wada, "Efficient pulse operation of Nd:$GdVO_4$ laser with AO Q-switch," *Applied Physics B*, vol. 81, no. 4, pp. 521–524, 2005.

[37]   O. Svelto and D. C. Hanna, *Principles of lasers*, vol. 4. Springer, 1998.

[38]   K. Du, D. Li, H. Zhang, P. Shi, X. Wei, and R. Diart, "Electro-optically Q-switched Nd:YVO4 slab laser with a high repetition rate and a short pulse width.," *Opt Lett*, vol. 28, no. 2, pp. 87–9, 2003.

[39]   H. Tang, X. Zhu, and Y. Feng, "Comparison of 30kHz Q-switched Nd: YVO4 lasers with LGS and RTP electro-optic modulator," in *Conference on Lasers and Electro-Optics/Pacific Rim*, 2009, p. MD1_4.

[40]   J. J. Zayhowski and C. Dill Iii, "Coupled-cavity electro-optically Q-switched Nd:YVO(4) microchip lasers.," *Opt Lett*, vol. 20, no. 7, pp. 716–8, 1995.

[41]   I. Abdulhalim, C. Pannell, K. Jedrzejewski, and E. Taylor, "Cavity dumping of neodymium-doped fibre lasers using an acoustooptic modulator," *Optical and quantum electronics*, vol. 26, no. 11, pp. 997–1001, 1994.

[42]   R. Mears, L. Reekie, S. Poole, and Dn. Payne, "Neodymium-doped silica single-mode fibre lasers," *Electronics letters*, vol. 21, no. 17, pp. 738–740, 1985.

[43]   O. G. Okhotnikov, *Fiber lasers*. John Wiley \& Sons, 2012.

[44]   X. Peng, L. Xu, and A. Asundi, "Power scaling of diode-pumped Nd:YVO$_4$ lasers," *IEEE Journal of Quantum Electronics*, vol. 38, no. 9, pp. 1291–1299, 2002.

[45]   M. J. Yarrow, "Power Scaling of Laser Oscillators and Amplifiers Based on Nd:YVO$_4$," 2006.

[46]   X. Yan, Q. Liu, X. Fu, H. Chen, M. Gong, and D. Wang, "High repetition rate dual-rod acousto-optics Q-switched composite Nd:YVO$_4$ laser," *Optics Express*, vol. 17, no. 24, pp. 21956–21968, 2009.

[47]   M. Siebold, M. Hornung, J. Hein, G. Paunescu, R. Sauerbrey, T. Bergmann, G. Hollemann, "A high-average-power diode-pumped Nd: YVO$_4$ regenerative laser amplifier for picosecond-pulses," *Applied Physics B*, vol. 78, no. 3–4, pp. 287–290, 2004.

[48]   S. Ma, D. Lu, H. Yu, H. Zhang, X. Han, Q. Lu, C. Ma and J.Wang, "High repetition rates optically active langasite electro-optically Q-switched laser at 1.34 μm," *Optics express*, vol. 25, no. 20, pp. 24007–24014, 2017.

[49]   M. C. Teich and B. Saleh, "Fundamentals of photonics," *Canada, Wiley Interscience*, vol. 3, 1991.

[50]   A. E. Siegman, "Lasers. 1986," *P492 P*, vol. 1017, 1986.

[51] X. Yu, C. Wang, F. Chen, R.P. Yan, Y. F. Ma, X.D. Li, J.B. Peng, "Comparison of electro-optical and acousto-optical Q-switched, high repetition rate Nd:GdVO$_4$ laser," *Laser Physics*, vol. 21, no. 3, pp. 442–445, 2011.

[52] X. Li, X. Yu, F. Chen, R. Yan, J. Gao, J. Yu, D. Chen, "Comparison on performance of acousto-optically Q-switched Nd: GdVO$_4$ and Nd:YVO$_4$ lasers at high repetition rates under direct diode pumping of the emitting level," *Optics express*, vol. 17, no. 11, pp. 9468–9476, 2009.

[53] F. Träger, *Springer handbook of lasers and optics*. Springer Science \& Business Media, 2012.

[54] W. S. Koen, "End-pumped solid-state lasers," 2010.

[55] P. Milonni and J. H. Eberly, "Laser Physics.-J," 2010.

[56] R. L. Byer, "Diode laser-pumped solid-state lasers.," *Science*, vol. 239, no. 4841, pp. 742–7, 1988.

[57] B. Davarcioglu, "An overview of diode pumped solid state (DPSS) lasers," *Int Acad Arts Sci Technol*, vol. 1, pp. 1–12, 2010.

[58] W. T. Silfvast, "Fundamentals of Photonics," 2003.

[59] T. Y. Fan and R. L. Byer, "Diode laser-pumped solid-state lasers," *IEEE Journal of Quantum Electronics*, vol. 24, no. 6, pp. 895–912, 1988.

[60] B. P. Q. W. Caixia Wu and Y. Zhang, "The experimental study on 808nm LD end-pumped Nd:YVO4 laser," 2016.

[61] M. S. Keirstead, T. M. Baer, S. H. Hutchison, and J. Hobbs, "High repitition-rate, diode-bar pumped, Q-switched Nd: YVO 4 laser," in *Conference on Lasers and Electro-Optics*, 1993, p. CFM4.

[62] T. Y. Fan, "Diode-pumped solid state lasers," *Lincoln Laboratory Journal;(USA)*, vol. 3, 1990.

[63] D. Hughes and J. Barr, "Laser diode pumped solid state lasers," *Journal of Physics D: Applied Physics*, vol. 25, no. 4, p. 563, 1992.

[64] J. J. Degnan, "Theory of the optimally coupled Q-switched laser," *IEEE Journal of Quantum Electronics*, vol. 25, no. 2, pp. 214–220, 1989.

[65] J. Zayhowski and P. Kelley, "Optimization of Q-switched lasers," *IEEE journal of quantum electronics*, vol. 27, no. 9, pp. 2220–2225, 1991.

[66]   C. Bollig, C. Jacobs, M. D. Esser, E. H. Bernhardi, and H. M. von Bergmann, "Power and energy scaling of a diode-end-pumped Nd: YLF laser through gain optimization," *Optics Express*, vol. 18, no. 13, pp. 13993–14003, 2010.

[67]   N. Coluccelli, G. Galzerano, P. Laporta, D. Parisi, A. Toncelli, and M. Tonelli, "Room-temperature Q-switched Tm: BaY 2 F 8 laser pumped by CW diode laser," *Optics Express*, vol. 14, no. 4, pp. 1518–1523, 2006.

[68]   C. Czeranowsky, *Resonatorinterne Frequenzverdopplung von diodengepumpten Neodym-Lasern mit hohen Ausgangsleistungen im blauen Spektralbereich*. Shaker, 2002.

[69]   G. Li, S. Zhao, H. Zhao, K. Yang, and S. Ding, "Rate equations and solutions of a laser-diode end-pumped passively Q-switched intracavity doubling laser by taking into account intracavity laser spatial distribution," *Optics communications*, vol. 234, no. 1, pp. 321–328, 2004.

[70]   C. Wu, F. Chen, and Y. Ju, "Experimental study of the pulse energy of pulsed LD-pumped acousto-optically Q-switched Tm: YAG lasers," *Journal of Russian Laser Research*, vol. 34, no. 2, pp. 146–153, 2013.

[71]   X. Zhang, S. Zhao, Q. Wang, B. Ozygus, and H. Weber, "Modeling of diode-pumped actively Q-switched lasers," *IEEE journal of quantum electronics*, vol. 35, no. 12, pp. 1912–1918, 1999.

[72]   D. McCarron, "A guide to acousto-optic modulators," 2007.

[73]   A. Yariv and P. Yeh, *Optical waves in crystals*, vol. 5. Wiley New York, 1984.

[74]   K. J. Gåsvik, *Optical metrology*. John Wiley \& Sons, 2003.

[75]   M. Roth, M. Tseitlin, and N. Angert, "Oxide crystals for electro-optic Q-switching," *Glass Phys. Chem.*, vol. 31, pp. 86–95, 2005.

[76]   B. Kuhlow, "7.1 Modulators," in *Laser Fundamentals. Part 2*, Springer, pp. 85–110.

[77]   H. Kong, J. Wang, H. Zhang, X. Yin, S. Zhang, Y. Liu, X. Cheng, L. Gao, X. Hu, M. Jiang, "Growth, properties and application as an electro-optic Q-switch of langasite crystal." *Journal of crystal growth*, vol. 254, no. 3, pp. 360–367, 2003.

[78]   J. K. Jabczynski, W. Zendzian, and J. Kwiatkowski, "Acousto-optic modulation in diode pumped solid state lasers," in *Proc. SPIE*, 2007, vol. 6599, p. 65990B.

[79]   M. Bass, L. G. DeShazer, and P. P. Yaney, "Evaluation of Nd: YVO4 and Ho:Er:Tm:YVO$_4$ as pulse pumped Q-switched lasers," 1976.

[80] Y.-F. Chen, "Design criteria for concentration optimization in scaling diode end-pumped lasers to high powers: influence of thermal fracture," *IEEE Journal of Quantum Electronics*, vol. 35, no. 2, pp. 234–239, 1999.

[81] M. J. Weber, *Handbook of lasers*, vol. 18. CRC press, 2000.

[82] Crystech, "Crystech Inc." [Online]. Available: www.crystech.com. [Accessed: 2017]

[83] S. Ma, H. Yu, H. Zhang, X. Han, Q. Lu, C. Ma, R. I. Boughton and J. Wang, "Efficient high repetition rate electro-optic Q-switched laser with an optically active langasite crystal," *Scientific reports*, vol. 6, p. 30517, 2016.

[84] H. J. Strauss, "Thermo-optical effects in high-power end-pumped vanadate lasers," 2010.

[85] Y. Sato and T. Taira, "Thermo-optical and-mechanical parameters of Nd:GdVO$_4$ and Nd:YVO$_4$," in *Conference on Lasers and Electro-Optics*, 2007, p. JWA87.

[86] M. J. D. Esser, "Diode-end-pumped solid-state lasers," 2005.

[87] Y. Sato and T. Taira, "The studies of thermal conductivity in GdVO$_4$, YVO$_4$, and Y$_3$Al$_5$O$_{12}$ measured by quasi-one-dimensional flash method," *Optics express*, vol. 14, no. 22, pp. 10528–10536, 2006.

[88] K. Scholle, S. Lamrini, P. Koopmann, and P. Fuhrberg, "2 micron laser sources and their possible applications," in *Frontiers in Guided Wave Optics and Optoelectronics*, InTech, 2010.

[89] Y. Sato and T. Taira, "Thermal properties of Y3Al5O12, GdVO4, and YVO4," in *Conference on Lasers and Electro-Optics*, 2006, p. JThC30.

[90] H. Furuse, R. Yasuhara, and K. Hiraga, "Thermo-optic properties of ceramic YAG at high temperatures," *Optical Materials Express*, vol. 4, no. 9, pp. 1794–1799, 2014.

[91] Z. Ma, D. Li, J. Gao, N. Wu, and K. Du, "Thermal effects of the diode end-pumped Nd: YVO 4 slab," *Optics communications*, vol. 275, no. 1, pp. 179–185, 2007.

[92] R. Weber, B. Neuenschwander, and H. Weber, "Thermal effects in solid-state laser materials," *Optical materials*, vol. 11, no. 2, pp. 245–254, 1999.

[93] P. K. Mukhopadhyay, K. Ranganathan, J. George, S. Sharma, and T. Nathan, "Effect of Nd^{3+} concentration on CW and pulsed performance of fiber-coupled diode laser pumped Nd:YVO$_4$ laser at 1064 nm," *Pramana-J. Phys*, vol. 59, no. 1, 2002.

[94] N. P. Barnes, "Solid-state lasers from an efficiency perspective," *IEEE Journal of Selected Topics in Quantum Electronics*, vol. 13, no. 3, pp. 435–447, 2007.

[95] fl, "Focuslight Technologies Inc." [Online]. Available: http://www.focuslight.com. [Accessed: 2017]

[96] C. Jacobs, "Exag Propagation Software." [Online]. Available: www.csir.co.za/cobus-jacobs. [Accessed: 2016]

[97] V. R. Gagan Thakkar, "DEVELOPMENT OF CW AND Q-SWITCHED DIODE PUMPED Nd:YVO$_4$ LASER," *International Journal of Advance Research In Science And Engineering*, vol. Special Issue (01),, no. 4, 2015.

[98] J. Liu, X. Yu, X. Xu, X. Meng, H. Zhang, L. Zhu, J. Wang, Z. Shao and M. Jiang, "Diode-laser-array end-pumped actively Q-switched Nd:GdVO$_4$ laser at 1.06 μm formed with a flat-flat resonator," *Japanese Journal of Applied Physics*, vol. 39, no. 10A, p. L978, 2000.

[99] D. Wang, J. Zhao, K. Yang, S. Zhao, T. Li, D. Li, G. Li, W. Qiao, "Pulse characteristics in a doubly Q-switched Nd:GGG laser with an acousto-optic modulator and a monolayer graphene saturable absorber," *Optics \& Laser Technology*, vol. 96, pp. 265–270, 2017.

[100] H. Plaessmann, F. Stahr, and W. M. Grossman, "Reducing pulse durations in diode pumped Q-switched solid-state lasers," *IEEE photonics technology letters*, vol. 3, no. 10, pp. 885–887, 1991.

[101] Y. Wang, L. Huang, H. Zhang, X. Yan, Q. Liu, and M. Gong, "A fundamental mode miniature acousto-optically Q-switched Nd: YVO$_4$ laser with short pulse width at high repetition rates," *Laser Physics Letters*, vol. 5, no. 4, p. 286, 2007.

[102] H. Plaessmann, K. S. Yamada, C. E. Rich, and W. M. Grossman, "Subnanosecond pulse generation from diode-pumped acousto-optically Q-switched solid-state lasers," *Applied optics*, vol. 32, no. 33, pp. 6616–6619, 1993.

[103] M. Dunn, B. Sinclair, P. Lindsay, A. Gillies, "Photonics Simulation Software for Teaching (Psst!)." [Online]. Available: http://www.st-andrews.ac.uk/~psst/. [Accessed: 2017]

[104] M. Esser, "Mid-infrared diode-pumped solid-state lasers," 2010.

[105] "RaicolCrystals." [Online]. Available: raicol.com. [Accessed: 2017]

[106] "BME-Bergmann." [Online]. Available: http://www.bme-bergmann.de/pockel.htm. [Accessed: Aug-2018]

[107] "Corning." [Online]. Available: www.corning.com. [Accessed: 2018]

[108] C. Feng, Q. Li, M. Jiang, J. Wang, and W. Guo, "1 nanosecond EO Q-switched Nd:YVO$_4$ laser," in *International Symposium on Photoelectronic Detection and Imaging 2011*, 2011, p. 81920D–81920D.

[109] X. Yu, C. Wang, Y. Ma, F. Chen, R. Yan, and X. Li, "Performance improvement of high repetition rate electro-optical cavity-dumped Nd: GdVO 4 laser," *Applied Physics B*, vol. 106, no. 2, pp. 309–313, 2012.

[110] L. Harris, M. Clark, P. Veitch, and D. Ottaway, "Compact cavity-dumped Q-switched Er: YAG laser," *Optics letters*, vol. 41, no. 18, pp. 4309–4311, 2016.

[111] C. Li, J. Song, D. Shen, N. Kim, J. Lu, and K. Ueda, "Diode-pumped passively Q-switched Nd: GdVO4 lasers operating at 1.06 μm wavelength," *Applied Physics B*, vol. 70, no. 4, pp. 471–474, 2000.

[112] Y.-G. Wang, X.-Y. Ma, J.-Y. Peng, H.-M. Tan, and L.-S. Qian, "High-repetition rate Q-switched Nd:YVO4 laser with a composite semiconductor absorber.," *Appl Opt*, vol. 45, no. 25, pp. 6616–9, 2006.

[113] S. Han, Y. Liu, F. Zhang, H. Yu, Z. Wang, Q. Gu, X. Xu, "Sub-nanosecond passively Q-switched Nd: YVO$_4$/Cr^{4+}:YAG microchip lasers," *Infrared Physics \& Technology*, vol. 68, pp. 197–200, 2015.

[114] S. Ngcobo, I. Litvin, L. Burger, and A. Forbes, "A digital laser for on-demand laser modes," *Nature communications*, vol. 4, p. 2289, 2013.

[115] M. Beijersbergen, R. Coerwinkel, M. Kristensen, and J. Woerdman, "Helical-wavefront laser beams produced with a spiral phaseplate," *Optics Communications*, vol. 112, no. 5–6, pp. 321–327, 1994.

[116] V. Jarutis, R. Pa\vskauskas, and A. Stabinis, "Focusing of Laguerre-Gaussian beams by axicon," *Optics communications*, vol. 184, no. 1–4, pp. 105–112, 2000.

[117] "holoeye.com/spatial-light-modulators." [Online]. Available: https://holoeye.com/spatial-light-modulators. [Accessed: 2018]

[118] A. L. Dudley, "Superpositions of light fields carrying orbital angular momentum," 2012.

[119] A. Dudley, I. A. Litvin, and A. Forbes, "Quantitative measurement of the orbital angular momentum density of light," *Applied optics*, vol. 51, no. 7, pp. 823–833, 2012.

213

[120] C. Schulze, D. Flamm, A. L. Dudley, A. Forbes, and M. Duparr'e, "Modal decomposition for measuring the orbital angular momentum density of light," 2013.

[121] B. Sephton, A. Dudley, and A. Forbes, "Revealing the radial modes in vortex beams," *Applied optics*, vol. 55, no. 28, pp. 7830–7835, 2016.

[122] O. Shapira, A. F. Abouraddy, J. D. Joannopoulos, and Y. Fink, "Complete modal decomposition for optical waveguides," *Physical review letters*, vol. 94, no. 14, p. 143902, 2005.

[123] C. Robert, V. Michau, B. Fleury, S. Magli, and L. Vial, "Mid-infrared Shack-Hartmann wavefront sensor fully cryogenic using extended source for endoatmospheric applications," *Optics express*, vol. 20, no. 14, pp. 15636–15653, 2012.

[124] E. Luzhansky, F.-S. Choa, S. Merritt, A. Yu, and M. Krainak, "Mid-IR free-space optical communication with quantum cascade lasers," in *SPIE Defense+ Security*, 2015, pp. 946512–946512.

[125] S. Veronesi, Y. Zhang, M. Tonelli, and M. Schellhorn, "Efficient laser emission in Ho^{3+}: $LiLuF_4$ grown by micro-Pulling Down method," *Optics express*, vol. 20, no. 17, pp. 18723–18731, 2012.

[126] D. Naidoo, "High brightness lasers," 2015.

[127] D. Flamm, D. Naidoo, C. Schulze, A. Forbes, and M. Duparré, "Mode analysis with a spatial light modulator as a correlation filter," *Optics letters*, vol. 37, no. 13, pp. 2478–2480, 2012.

[128] "ukirt.hawaii." [Online]. Available: http://www.ukirt.hawaii.edu/astronomy/utils/atmos/atmos4.gif. [Accessed: Aug-2018]

[129] T. Kaiser, D. Flamm, S. Schröter, and M. Duparré, "Complete modal decomposition for optical fibers using CGH-based correlation filters.," *Opt Express*, vol. 17, no. 11, pp. 9347–56, 2009.

[130] M. R. Duparre, V. S. Pavelyev, V. A. Soifer, and B. Luedge, "Laser beam characterization by means of diffractive optical correlation filters," in *Laser Beam Shaping*, 2000, vol. 4095, pp. 40–49.

[131] T. Kaiser, S. Schröter, and M. Duparré, "Modal decomposition in step-index fibers by optical correlation analysis," in *Proc. SPIE*, 2009, vol. 7194, p. 719407.

[132] O. A. Schmidt, C. Schulze, D. Flamm, R. Brüning, T. Kaiser, S. Schröter, and M. Duparré, "Real-time determination of laser beam quality by modal decomposition," *Optics express*, vol. 19, no. 7, pp. 6741–6748, 2011.

[133] I. A. Litvin, A. Dudley, F. S. Roux, and A. Forbes, "Azimuthal decomposition with digital holograms.," *Opt Express*, vol. 20, no. 10, pp. 10996–1004, 2012.

[134] B. Boruah, "Dynamic manipulation of a laser beam using a liquid crystal spatial light modulator," *American Journal of Physics*, vol. 77, no. 4, pp. 331–336, 2009.

[135] A. Dudley, C. Schulze, I. Litvin, M. Duparré, and A. Forbes, "Quantitatively measuring the orbital angular momentum density of light," in *Optical Trapping and Optical Micromanipulation X*, 2013, vol. 8810, p. 88100E.

[136] A. Dudley, N. Majola, N. Chetty, and A. Forbes, "Implementing digital holograms to create and measure complex-plane optical fields," *American Journal of Physics*, vol. 84, no. 2, pp. 106–112, 2016.

[137] D. Flamm, C. Schulze, D. Naidoo, S. Schröter, A. Forbes, and M. Duparré, "All-digital holographic tool for mode excitation and analysis in optical fibers," *Journal of Lightwave Technology*, vol. 31, no. 7, pp. 1023–1032, 2013.

[138] C. Schulze, D. Naidoo, D. Flamm, O. A. Schmidt, A. Forbes, and M. Duparré, "Wavefront reconstruction by modal decomposition.," *Opt Express*, vol. 20, no. 18, pp. 19714–25, 2012.

[139] A. Dudley, G. Milione, R. R. Alfano, and A. Forbes, "All-digital wavefront sensing for structured light beams," *Optics express*, vol. 22, no. 11, pp. 14031–14040, 2014.

[140] C. Schulze, A. Dudley, D. Flamm, M. Duparre, and A. Forbes, "Measurement of the orbital angular momentum density of light by modal decomposition," *New Journal of Physics*, vol. 15, no. 7, p. 073025, 2013.

[141] C. Rosales-Guzmán, A. Trichili, A.L. Dudley, B. Ndagano, A.B. Salem, M. Zghal, and A. Forbes, "Free-space communication with over 100 spatial modes," in *Applications of Lasers for Sensing and Free Space Communications*, 2016, p. LTh1B–4.

[142] B. Ndagano, I. Nape, M. A. Cox, C. Rosales-Guzman, and A. Forbes, "Creation and characterization of vector vortex modes for classical and quantum communication," *arXiv preprint arXiv:1709.00736*, 2017.

[143] C. Font, F. Santiago, G.C. Gilbreath, D. Bonanno, B. Bajramaj, C. Wilcox, S. Restaino, and S. Mathews, "Implementation of a phase only spatial light modulator as an atmospheric turbulence simulator at 1550 nm," *Advances in Optical Technologies*, vol. 2014.

[144] V. Arrizón, U. Ruiz, R. Carrada, and L. A. González, "Pixelated phase computer holograms for the accurate encoding of scalar complex fields.," *J Opt Soc Am A Opt*

Image Sci Vis, vol. 24, no. 11, pp. 3500–7, 2007.

[145] A. L. Dudley, I. Litvin, F. Roux, and A. Forbes, "Complete azimuthal decomposition of optical fields," 2013.

[146] R.J. Beck, Parry, J.P., MacPherson, W.N., Waddie, A., Weston, N.J., Shephard, J.D. and Hand, D.P., "Application of cooled spatial light modulator for high power nanosecond laser micromachining, " *Optics express*, *18*(16), pp.17059-17065, 2010.

[147] "HOLOEYE Corporation." [Online]. Available: https://holoeye.com. [Accessed: 2017]

[148] D.-M. Spangenberg, A. Dudley, P. H. Neethling, E. G. Rohwer, and A. Forbes, "White light wavefront control with a spatial light modulator," *Optics express*, vol. 22, no. 11, pp. 13870–13879, 2014.

[149] C. Schulze, A. Dudley, D. Flamm, M. Duparré, and A. Forbes, "Reconstruction of laser beam wavefronts based on mode analysis," *Applied optics*, vol. 52, no. 21, pp. 5312–5317, 2013.

[150] L. Changhai, X. Fengjie, H. Shengyang, and J. Zongfu, "Performance analysis of multiplexed phase computer-generated hologram for modal wavefront sensing," *Applied optics*, vol. 50, no. 11, pp. 1631–1639, 2011.

[151] M. P. Rimmer and J. C. Wyant, "Evaluation of large aberrations using a lateral-shear interferometer having variable shear," *Applied Optics*, vol. 14, no. 1, pp. 142–150, 1975.

[152] R. Navarro and E. Moreno-Barriuso, "Laser ray-tracing method for optical testing," *Optics letters*, vol. 24, no. 14, pp. 951–953, 1999.

[153] R. Lane and M. Tallon, "Wave-front reconstruction using a Shack-Hartmann sensor," *Applied optics*, vol. 31, no. 32, pp. 6902–6908, 1992.

[154] L. Allen and M. Padgett, "The Poynting vector in Laguerre-Gaussian beams and the interpretation of their angular momentum density," *Optics Communications*, vol. 184, no. 1, pp. 67–71, 2000.

[155] C. Schulze, Naidoo, D., Flamm, D., Schmidt, O.A., Forbes, A. and Duparré, M., "Wavefront reconstruction by modal decomposition," *Optics express*, *20*(18), pp.19714-19725, 2012.

[156] S. Fang, C. Jun, and G. Jian-hong, "Controllable high repetition rate gain-switched Nd: YVO 4 microchip laser," *Journal of Zhejiang University-SCIENCE A*, vol. 6, no. 2, pp. 79–82, 2005.

[157] A. Ray, S. K. Das, L. Mishra, P. K. Datta, and S. M. Saltiel, "Nonlinearly coupled, gain-switched Nd: YAG second harmonic laser with variable pulse width," *Applied optics*, vol. 48, no. 4, pp. 765–769, 2009.

[158] X. Li, Yu, X., Gao, J., Chen, F., Peng, J., Yu, J. and Chen, D., "Improvement in the laser performances of an AO Q-switched Nd: GdVO$_4$ laser by direct-diode pumping into the emitting level," *Laser Physics*, vol. 18, no. 7, pp. 831–834, 2008.

[159] A. Agnesi and S. Dell'Acqua, "High-peak-power diode-pumped passively Q-switched Nd: YVO 4 laser," *Applied Physics B*, vol. 76, no. 4, pp. 351–354, 2003.

[160] S. Li, Z. Zhuo, T. Li, and J. Li, "Short-pulse-width and high-peak-power Q-switched YVO$_4$/Nd:YVO$_4$ laser with an acousto-optical modulator," *Laser Physics Letters*, vol. 6, no. 4, p. 275, 2008.

[161] Y. Wang, M. Gong, and L. Huang, "High-pulse-stability double-end continuous-grown YVO$_4$/Nd:YVO$_4$/YVO$_4$ acousto-optically Q-switched laser at high repetition rates," *Laser Physics*, vol. 20, no. 6, pp. 1316–1319, 2010.

[162] Y. Chen and Y. Huang, "Actively Q-switched Nd:YVO$_4$ laser using an electro-optic periodically poled lithium niobate crystal as a laser Q-switch," *Optics letters*, vol. 28, no. 16, pp. 1460–1462, 2003.

[163] Y. Yong-Ji, C. Xin-Yu, W. Chao, W. Chun-Ting, L. Rui, and J. Guang-Yong, "A 200 kHz Q-switched adhesive-free bond composite Nd:YVO$_4$ laser using a double-crystal RTP electro-optic modulator," *Chinese Physics Letters*, vol. 29, no. 2, p. 024206, 2012.

[164] Y. J. Yu, X.Y. Chen, C. Wang, C. T. Wu, M. Yu, and G. Y. Jin, "High repetition rate 880 nm diode-directly-pumped electro-optic Q-switched Nd:GdVO$_4$ laser with a double-crystal RTP electro-optic modulator," *Optics Communications*, vol. 304, pp. 39–42, 2013.

[165] W. Zhao, Zhang, L., Yu, H., Qi, Y., He, C., Zhang, J. and X. Lin, "Output characteristics of diode-end-pumped electro-optically Q-switched Nd:LuVO$_4$ laser at 1064 nm," *Optical Engineering,* , vol. 55(6), p.066103., 2016.

[166] J. Zayhowski and C. Dill, "Diode-pumped microchip lasers electro-optically Q switched at high pulse repetition rates," *Optics letters*, vol. 17, no. 17, pp. 1201–1203, 1992.

[167] X. Yan, Liu, Q., Fu, X., Wang, Y., Huang, L., Wang, D. and Gong, M., "A 108W, 500 kHz Q-switching Nd: YVO$_4$ laser with the MOPA configuration," *Optics Express*, vol. 16, no. 5, pp. 3356–3361, 2008.

217

[168] X. Fu, Q. Liu, X. Yan, J. Cui, and M. Gong, "120 W high repetition rate Nd:YVO$_4$ MOPA laser with a Nd:YAG cavity-dumped seed laser," *Applied Physics B*, vol. 95, no. 1, pp. 63–67, 2009.

[169] W. Wu, Li, X., Yan, R., Zhou, Y., Ma, Y., Fan, R., Dong, Z. and Chen, D., "100 kHz, 3.1 ns, 1.89 J cavity-dumped burst-mode Nd: YAG MOPA laser," *Optics express*, vol. 25, no. 22, pp. 26875–26884, 2017.

Part 3: Appendices

Appendix A

A.   Gain Switching

Table A.1 lists a number research accounts from the last three decades that investigated gain switching as a technique to generate pulsed laser outputs. Gain-switch laser techniques are well known for their ability to generate and control stable pulse widths and reproduce pulse amplitudes [23]. This appendix reviews several research accounts on this technique to determine if they can be considered for the purposes of this research.

The earliest account that we listed, had implemented gain switching with a 1 mm long Nd:YAG crystal, compared to 1 and 5 mm long Nd:YVO$_4$ crystals, and they operated their investigation at 100 kHz [23]. In their research they found that the Nd:YVO$_4$ crystal was favourable for shorter pulse widths (~40 ns) when compared to Nd:YAG (> 100 ns). They also observed that lengthening the crystal from 1 to 5 mm slightly reduced the pulse width from 45 to 40 ns. However, for the operation of this laser at 100 kHz (the intended PRF for our research), the pulse energy that this technique generated was low, that is, 10 nJ (Nd:YAG), and it decreased to 4 nJ and 2 nJ for the Nd:YVO$_4$ crystals respectively. In all their design conditions, the results they obtained fell outside the intended results range for our research. To improve their results, the same authors reported considerably higher peak powers (3 and 4 kW) when using a Gain-switched laser at low PRF (3 and 1.5 kHz) with a Nd:YVO$_4$ laser system, as demonstrated in 1996 [15].

Table A.1. Recent gain-switching laser designs and their corresponding laser results. Design parameters highlighted in the table include pump factors, laser material properties and the cavity length. These parameters provide the conditions that influenced the output parameters.

Authors, Year	Pump source/ scheme, power [W], pump wavelength (λ_p) [nm], radius [µm]	$E_{pulse@Threshold}$ [µJ], $P_{peakpump}$ [kW], PRF [kHz], pulse width [ns]	Gain medium + Doping [%]	Crystal dimensions [mm^3]	Cavity length (mm)	PRF [kHz]	Pulsed average power [W]	Pulse energy [µJ]	Pulse width [ns]	Peak power [kW]	Ref.
Larat et al., 1994	Diode pumped at 808, 100	P_{peak}=170 mW, NA=0.4	Nd:YAG	Area × 1		100	0.001	0.01	130	8E-05	[23]
			Nd:YVO$_4$	Area × 1			0.0004	0.004	45	9E-05	
			Nd:YVO$_4$	Area × 5			0.0002	0.002	40	5E-05	
Larat et al., 1996	Single high (1 kW) brightness component, 808, -		Nd:YVO$_4$		50	1.5	0.39	260	65	4	[15]
					7	3	0.306	102	34	3	
Feng et al., 2005	Diode pumped, 808		Nd:YVO$_4$	$\pi \times 10^2 \times 1$	1	25			16		[156]
Wang et al., 2007	808, 50	1.1,	1.8 at.% Nd:YVO$_4$	Area × 1	1	100-1000	0.1	1E-04	32	3.063	[12]

220

Ray et al., 2009	808, 100, side	1, 50-1, 000	40	Nd:YAG + SH for green laser	Area ×0.63	1435	50			409	0.04	[157]

The review noted that Gain-switched lasers have been operated at different pulse repetition rates, some from ~0.1 kHz to 25 kHz, and others from 100 kHz [23] to 1 MHz [12]. The ~0.1 kHz to 25 kHz operated lasers generated high peak power outputs [15]even though the pulse widths were long. This can be attributed to high energy pulses that were obtained. In contrast, the lasers that were operated at the 100 kHz to 1 MHz PRF range generated low peak power (tens of mW) and long pulse width (tens to over 100 ns) output 100 kHz [23]However, the kW peak power outputs and slightly reduced pulse widths (fewer tens of nano seconds), were obtained with micro-chip Gain-switched laser designs [12]. This indicated that one would have to trade one for the other.

It was also noted that shortening the cavity from 50 mm (for the 3 kHz, 4 kW laser) to 7 mm (for the 1.5 kHz, 3kW laser) favourably reduced pulse widths (65 ns to 34 ns). The subsequent and corresponding decrease of pulse energies from 260 to 102 μJ was however unfavourable [15]. While the decrease that was observed in peak powers (4 to 3 kW) [15] was unfavourable, the decrease in pulse energy was still high and could still yield the desired results if the pulse widths were shorter. With this knowledge one can deduce that gain switching should be the laser system of choice when high energy is required.

A shorter pulse (16 ns) was reported with gain switching in 2005, and was obtained through the use of a micro-chip laser setup that functioned at a low PRF range – 1 Hz to 25 kHz [156]. A relatively high peak power (~3 kW) was reported in 2007 for a high PRF range – 100 kHz to 1 MHz [12]. However, the pulse width for this laser remained long (32 ns). If high peak powers (~10 kW) were the only requirement for ranging applications – considering the respective 5 kW, 4 kW and 3 kW peak powers [15] obtained in 1996 – gain switching could be seen as a likely alternative.

Appendix B

B.   Cavity Dumping

Table B.1 lists a summary of several investigations into cavity-dumped laser systems that have been conducted over more than a decade ([25], [17], [18], [26] and [24]). Here we used the summary to compare their design parameters and results with the AOM and EOM active Q-switched laser systems presented in this dissertation. This summary seeks to determine several laser design parameters, like pumping, laser material choice, pulsing devices, cavity properties, all of which influence the results that are obtained. These features determine the gain, the thermal properties of the laser material, as well as the resulting laser outputs.

The laser system design parameters highlighted in the table include pump factors (source, scheme, power, wavelength and waist radius), laser material properties (kind, doping, geometry and size), the pulsing device and the cavity length (length and output coupling). These parameters provide the conditions that influence the outcome.

The pulse widths that were obtained ranged from 3.8 ns [109], [26] to 6 ns [25], while the peak power ranged from 0.6 kW [25] to 68 kW [17]. These were obtained at PRFs ranging from 50 kHz [18] to 1.5 MHz [25]. Particularly interesting were the results obtained at 50 kHz [18], where 5.5 ns pulse duration and 18 kW peak power were obtained ([26], [17]). This was very close to the intended ~1 ns, ~10 kW pulses at ~100 kHz PRF. The latter were obtained by hard pumping (21.9 W) a low concentration doped $Nd:GdVO_4$ at 808 nm with a relatively larger mode (320 μm) beam. Another comparable account reported in literature is the ~880 nm direct pumped laser (at the upper laser level) [26]. This was chosen to bypass the useless heat-generating and thermally limiting transition experienced by pumping the energy level of the laser material at 808 nm [158]. This resulted in reducing the quantum defect [109]. Furthermore, they employed an additional thermal compensation measure, which was to use a composite crystal. A portion of the laser crystal (2 mm) was undoped, while the other portion (10 mm) was doped with < 0.5 at. % concentration. The results generated were pulses of 3.8 ns duration and 34.4 kW peak power at the PRF of 100 kHz. On other laser systems, laser materials included long crystals (8 and 30 mm) [17], [18]

223

and composite crystals (consisting of doped and undoped portions bonded together) [109]. Long crystals favour high absorption and high gain, whereas composite crystals reduce the thermal lens effects [109] and thus provide the advantage of better heat dissipation.

In cases where the PRFs were 500 kHz [24] and 1.5 MHz [25] respectively, and where long crystals were used and short pulsed outputs (5 ns) were obtained, even longer cavities of 720 mm and 1500 mm and reduced peak powers 6 kW and 0.6 kW were obtained.

Table B.1. Recent cavity-dumped laser designs and their corresponding laser results.

Authors, Year	Pump source/ scheme, power [W], λ_p [nm], radius [μm]	Gain medium + Doping [%]	Crystal dimensions [mm3]	Cavity dumping device	Cavity length [mm]	PRF [kHz]	Pulsed average power [W]	Pulse energy [μJ]	Pulse width [ns]	Peak power [kW]	Ref.
Roberts, 2003		Nd:YAG		1064-nm PBS + (RTP) EOM	1500	1500	4.5	3	5	0.6	[25]
McDough et al., 2006	End (Direct), 30, 888, 200	0.5 at. % Nd:YVO$_4$	4×4×30	BBO cell		100	41	0.0004	6	68	[17]
He et al., 2011	End, 21.9, 808, 319	0.3 at. % Nd:GdVO$_4$	3×3×8	RTP Pockels cell	175	50	5.1	0.0001	5.5	18	[18]
Yu et al., 2012	End (Direct), 30, 879, 320	0.3 at. % GdVO$_4$/ Nd:GdVO$_4$	3×3×(8+2)	RTP Pockels cell	175	100	13.1	0.0001	3.8	34.4	[109]
Ma et al., 2013	End, 320, 808	0.3 at. % YVO$_4$/ Nd:GdVO$_4$	3×3×(10+2)	RTP Pockels cell:	190	50			3.8	30.8	[26]
	End, 320, 879	0.3 at. %			175	100				34.4	

225

		GdVO$_4$/ Nd:GdVO$_4$									
Liu et al., 2015	End (Direct), 30, 888, 675	0.5 at. % Nd:YVO$_4$	4×4×20	two 3×3×20 BBO crystals+λ/4 plate	720	500	10	20	5	4	[24]

226

From Table B.1, it can be deduced that cavity dumping could be a favourable alternative for obtaining short (~1 ns) pulsed, high (> 10 kW) peak power outputs at high PRF (~100 kHz). Since the pulse widths that have been reported were short ([25], [109]), the lasers can be used to take instant distance measurements and scan irregular objects with some reasonable level of precision and resolution. The peak powers that are accounted for in literature range from 0.6 kW at a high PRF of 1.5 MHz [25] to 68 kW through another 100 kHz operation (with a directly pumped 30 mm long laser crystal) [17]. In this range, many generated results are comparable or even better than the laser results we generated, except for the pulse widths. They can therefore be used in these instances to take long-distance measurements with the required resolution, but with slightly lower precision.

The major drawback is that the reported cavities of cavity dumped laser systems are long (close to 200 mm), which makes the laser systems too big to fit into or be transformed into the desired small and rugged ranging devices. In addition, long cavity length laser systems can easily become misaligned, which then reduces operation life of the device of taking quality and reliable measurements.

Appendix C

C.   Passive Q-switching

Table C.1 lists several investigations into passive Q-switching laser systems that were demonstrated in the past decade or two ([17], [19], [24], [26], [18]). The aim is to compare their design parameters and results with the intended design parameters and results of this dissertation. Various studies report that passive Q-switching enjoys several advantages apart from its simplicity and lower complexity, namely compactness [30], low cost [32] and reliability [31]. In addition, passively Q-switched lasers are small in size and operate with high power efficiencies [33]. However, Q-switched lasers are limited by their lack of an external precision-trigger system and have outputs that are lower when compared to electro-optic or acousto-optic versions of Q-switched lasers. The lower passive Q-switch outputs are caused by high insertion loss due to the residual absorption of the saturated passive Q-switch [1]. In addition, photo-chemical degradation is a

problem and the main drawback that dye-saturable absorbers suffer from when exposed to high intensities.

In 1997, Chen et al. reported a Cr^{4+}:YAG passively Q-switched 1 mm long Nd:YVO$_4$ single frequency microchip laser that obtained a short pulse width of 5.6 ns, with a peak power of 0.43 kW (low) at the repetition rate of 83 kHz. While the PRF (83 kHz) and pulse width (5.6 ns) obtained were comparable, the highest peak power they obtained was very low (430 W). In 2000, Li et al. demonstrated a passively Q-switched Nd:GdVO$_4$ laser with a Cr^{4+}:YAG crystal that had transmissions of 80% and 90% respectively at 1064 nm.

Table C.1. Passive Q-switching research accounts in the past two decades with laser system design and results parameters listed.

Authors, Year	Pump scheme, pump wavelength (λ_p) [nm], radius [µm], power [W]	Gain medium + Doping [%]	Crystal geometry [mm³]	S1, S2 or M1, M2 with R, T (%), for λ_{pump}, λ_{laser} [nm]	Cavity length (mm)	Q-switch device, transmission [%], thickness [mm]	PRF [kHz]	Pulsed average, threshold power [W]	Pulse energy [µJ]	Pulse width [ns]	Peak power [kW]	Ref.
Chen et al., 1997	End, 808, 100, 1.6	1.0 at. % Nd:YVO$_4$/ Cr^{4+}:YAG	Area × 1	S1:Flat,HR (R>99.8) @ 1064, AR (T>90%) @808, S2: Flat, AR (<0.2%)@ 1064	2	Cr:YAG with 80 and 90% initial trans	83	0.1992	2.4	5.6	0.43	[32]
Li et al., 2000	End, 807.6, 350, 8.1	1.2 at. % Nd:GdVO$_4$	Area × 2.5		140	Cr^{4+}:YAG, 80, 0.66,	69	1.4, 1.6	20	32	0.625	[111]
						Cr^{4+}:YAG, 90, 1.33	125	2.1, 1.2	17	45	0.373	
Gu et al., 2001	End, 808, 175, 3	1.0 at. % Nd:YVO$_4$	3×3×3	S1: Flat, HR@ 1060, HT@808 S2: AR 1064	7	OC: uncoated single crystal GaAs plate	4	0.048	12	2.2	5.6	[30]
Agnesi et al., 2003	21.5	0.5 at. % Nd:YVO$_4$	1×12×7	S1: Flat, HR@ 1064, HT @808.S2:θ_w=1°, AR 1064	40	Cr^{4+}:YAG, 80,	24.2	3.8	157	6	26	[159]

229

| Authors, Year	Pump scheme, λ_p [nm], radius [µm], power [W]	Gain medium + Doping [%]	Crystal geometry [mm3]	S1, S2 or M1, M2 with R, T (%), for λ_{pump}, λ_{laser} [nm]	Cavity length (mm)	Q-switch device, transmission [%], thickness [mm]	PRF [kHz]	Pulsed average, threshold power [W]	Pulse energy [µJ]	Pulse width [ns]	Peak power [kW]	Ref.
Wang et al., 2006	End, 808 100, 1.6	1.0 at. % Nd:YVO$_4$	3×3× 1.15	S1: Flat, HR@ 1064, HT @808. S2: HT 1064.	12	GaAs/ In$_{0.25}$Ga$_{0.75}$As/ GaAs	2000	0.135	0.063	8.3	7.5	[112]
						GaAs	420					
						Cr^{4+}:YAG	65					
Han et al., 2015	End, 808, 100, 3.96	2.0 at. %., a-cut Nd:YVO$_4$	3×3× 0.8	M1: Flat, HR@ 1060, AR @808	11.5, 8.9,	Cr^{4+}:YAG with T$_0$= 87%, 77%, and 65% and M3: AR@ 1064	16		20	0.693	30	[113]
		2.0 at. %, c-cut Nd:YVO$_4$	3×3× 0.8	M2: Flat, HR @ 808, AR @ 1064			5		29	0.897	32	
							2000	3.8	157	8.3	32	

230

The threshold was 1.6 W and at the incident pump power of 8.1 W, the average output power was measured to be about 1.4 W for the 80% Cr^{4+}:YAG transmission. The 90% transmission at the threshold was reduced to 1.2 W, while the output power was increased to 2.1 W. These indicate that the change (80% to 90%) of the initial transmission of the Cr^{4+}:YAG crystal had an effect on the threshold power (decrease) and the output parameter. This caused changes in the average output power (increase), the pulse energy (decrease), pulse widths (increase), and the peak powers (decrease) of the passively Q-switched lasers [111]. These results were obtained at different pulse repetition frequencies – 69 and 125 kHz respectively.

In 2003, Agnesi and Dell'Acqua exploited the high absorption efficiency of pump radiation that is polarised along the c-axis, by using an a-cut Nd:YVO_4 crystal with the output face also cut at an angle ($\theta_w = 1°$). They also investigated outputs at different cavity lengths. Figure C.1 shows their setup [159]. With the shortest (40 mm) flat-flat cavity they obtained the highest pulse energy (157 µJ) and the shortest pulses (6 ns), while the thermal lens kept the cavity stable. Apart from the PRF (~24 MHz) we calculated, which is far greater than the intended range (~100 kHz), these results were quite impressive.
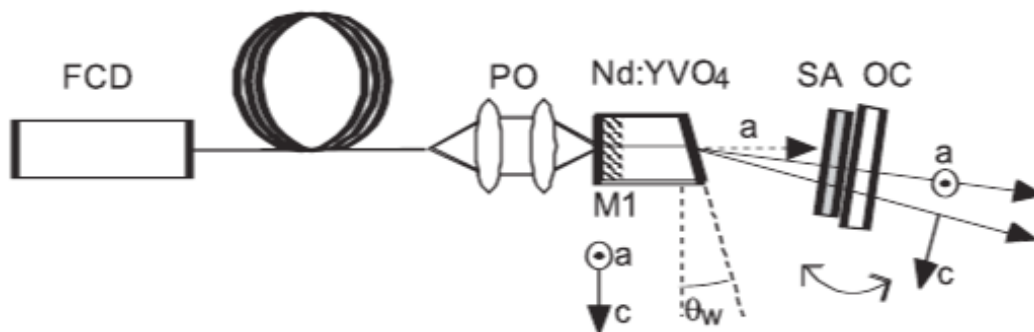
Figure C.1. The layout of a pumped fibre-coupled laser diode array in a passively Q-switched laser. The a-cut 7 mm long Nd:YVO_4 crystal, with one face cut at an angle, and a saturable absorber were used as gain medium and Q-switch element respectively[159].

Close to these results are those obtained in 2006 by Wang et al. with a setup shown in Figure C.2. The results, though obtained at 2 MHz (>> 100 kHz), included pulse widths of 8.3 ns (> 1 ns) and peak powers of 7.5 kW (<10 kW). Whereas the pulse widths and peak powers are comparable, the PRF is far higher. Although a-cut crystal lasers that emit π-polarised light have been the preferred high gain polarisation option for emission, the σ-polarised option was investigated for comparison.

231
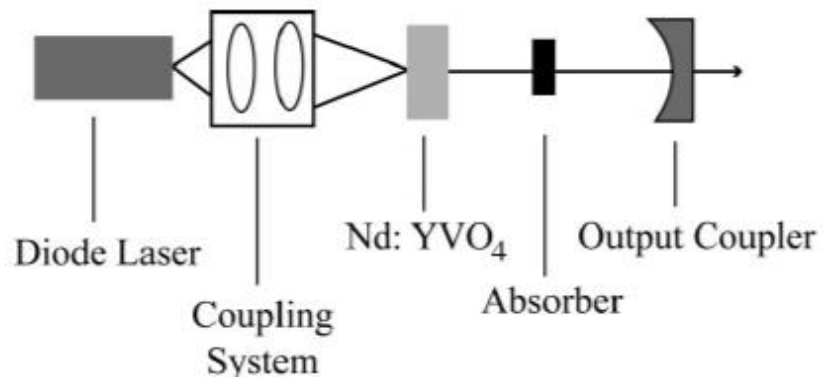
Figure C.2. A conventional passively Q-switched laser set-up with a 1.15 mm thick crystal in a cavity length of 12 mm [112].

Appendix D

D.   Active Q-switching: Acousto-optic Q-switched lasers

Several research reports have been considered in evaluating the work that has already been done by other researchers over the past decades, starting from 1993 to the recent past. They were selected when one of their parameters fell in the desired range, such as the 50 to 150 kHz range of PRF, lower than ten nanosecond pulse durations. or a peak power of approximately 10 kW and above. Plaessmann et al. (1993), for example [102], developed a 7 mm cavity length end-pumped 1.5 at. % Nd:YVO$_4$ laser, Q-switched with a TeO$_2$ acousto-optic modulator at 100 kHz of PRF that generated 0.5 µJ energy, 1.9 ns pulse width and 0.5 kW peak power pulses. They attributed the short pulse width (< 2 ns) that they obtained to the short photon lifetime they facilitated by designing a short cavity, as well as to their use of a small TeO$_2$ AOM that had a large figure of merit, a significant speed and loss modulation. However, the pulse energies and peak powers were low. This indicates that if this laser was used for a LADAR device, it would be accurate and provide high resolution, but it would be limited in the range it could measure.

In 2005, Ogawa et al. developed a compact, efficient (78% slope efficiency) AOM Q-switched 40 mm long cavity laser system with a direct diode pumped (879 nm) 1.0 at. % doped a-cut Nd:GdVO$_4$ crystal and an output coupler of 80% reflectivity. At 100 kHz of PRF, they produced pulsed output of significantly high 4 W average power and 40 µJ energy [36]. The pulse durations were short (10 ns), and the peak power (4 kW) was high, but not at the desired ~1 ns and ~10 kW values of this research.

Two years later, Wang, Gong and Zhang (2007) presented a short pulse width (2 ns), high repetition rate (80 kHz), short cavity (20 mm), acousto-optically Q-switched 0.5 at. % Nd:YVO$_4$ laser that was end-pumped with a 4 W fibre-coupled laser diode at 808 nm. However, they obtained a low average power of 0.82 W and the peak power was almost half the desired value [35]. This was due to the short cavity, long crystal and short intracavity beam radius. In 2008, Li et al. not only reduced the temperature of the thermal effects and prevented thermally induced thermal fracture of crystals with low concentration doping (0.5 at. %) and large dimensions respectively, they also used a YVO$_4$/Nd:YVO$_4$ composite crystal as a laser material. The undoped YVO$_4$ portion of the crystal functioned as a heat sink for the pumping face. With acousto-optic Q-switching at a variety of pulse

repetition frequencies, and in particular at 90 kHz, they produced a laser output with pulses of a 9.5 ns duration and an average power of 10.12 W [160].

Li et al. (2008) also used the equations $E_{\text{pulse}} = P_{\text{ave}}/PRF$ and $P_{\text{peak}} = E_{\text{pulse}}/\tau_{\text{pw}}$ to calculate the single-pulse energy E_{pulse} and the peak power P_{peak}, and they obtained 112.4 μJ and 11.8 kW respectively. These are extremely good results for long-range and high-resolution LADAR operations, and even though the pulses are long, they can provide the precision that is desired.

In 2009, acousto-optic Q-switching was demonstrated when it was implemented with direct pumping at 879 nm in a comparative study of the Nd:YVO$_4$ and Nd:GdVO$_4$ crystal lasers at the high repetition frequency of 100 kHz. While both crystals were shown to be efficient and promising under these conditions, Li et al. (2009) also demonstrated that Nd:YVO$_4$ crystals produced superior results because of their larger stimulated emission cross-section. The results obtained were the average powers that were nearly greater or equal to 20 W, with shorter pulse durations, higher pulse energies and higher peak powers for Nd:YVO$_4$ than for Nd:GdVO$_4$ respectively [52].

Having observed that when some techniques were used, the required parameters fell below (PRF, average power, pulse energy, and peak power) or higher than (pulse durations) those achieved with solid-state lasers. Thus it was deduced that it is sometimes necessary to either scale the laser up or use other laser materials, such as active fibre gain media. The following sections will discuss this.

Table D.1. Recent Acousto-optic Q-switched laser designs and results.

Authors, Year	Pump scheme, λ_p [nm], pump power [W], radius [μm]	Gain medium + Doping [%]	Crystal volume [mm³]	Q-switch element	Cavity length [mm], OC-R [%]	PRF [kHz]	Pulsed average power [W]	Pulse energy [μJ]	Pulse width [ns]	Peak power [kW]	Ref.
Plaessmann et al., 1993	End, -, 80	1.5 at. % Nd:YVO₄,	Area × 2.3	TeO₂	7, 25	100		0.5	1.9	0.5	[102]
Ogawa et al., 2005	Direct, 879,	1.0 at. % a-cut Nd:GdVO₄	3×3×5	TeO₂	40, 80	100	4	40	10	4	[36]
Wang et al., 2007	End, 808, 50	0.5 at. % Nd:YVO₄	3×3×5	Not specified	20, 10	80	0.82	10.3	2	5.13	[35]
Li & Zhuo, 2008	End, 808, 20, -	YVO₄/a-cut 0.5 at. % Nd:YVO₄	4×4×4/ 4×4×7	Gooch and Housego AO Q-switcher	65	90	10.1	112.4	9.5	11.8	[160]

235

Authors, Year	Pump scheme, λ_p [nm], pump power [W], radius [μm]	Gain medium + Doping [%]	Crystal volume [mm³]	Q-switch element	Cavity length [mm], OC-R [%]	PRF [kHz]	Pulsed average power [W]	Pulse energy [μJ]	Pulse width [ns]	Peak power [kW]	Ref.
Li et al., 2009	End, 879, 33, -	0.5 at. % Nd:YVO$_4$	4×4×8	Gooch and Housego AO Q-switcher	100	100	> 20 > 20	200	12.1	16.5	[52]
		0.5 at. % Nd:GdVO$_4$				> 20		15.6	15.6	12.8	
Wang et al., 2010	End, 45	YVO$_4$/Nd:YVO$_4$/YVO$_4$	3×3×(2+16+2)	ANEOS acousto-optical Q-switch	>120+140	60	32.9		19.6	27.7	[161]

236

Appendix E

E. Active Q-switching: Electro-optic Q-switched lasers

The laser designs in Table E.1 are mostly end-pumped Nd^{3+} doped lasers that are Q-switched with different electro-optic devices. The components listed indicate how they influence the performance of the laser that is presented. For example, from this table it can be deduced how the chosen pump sources and radiations, the laser material properties, the electro-optic Q-switches and the cavity lengths were manipulated to obtain the desired gains, oscillations as well as results for the applications. This section looks at whether the researchers obtained the intended results in their laser designs. Lastly, we look at how the results (average power, pulse energy, pulse width and peak power) that were obtained by the broader research world compare to our research.

Table E.1 lists a number of long and thin slab $Nd:YVO_4$ lasers, composite $YVO_4 + Nd:YVO_4 + YVO_4$ slab lasers, and $Nd:YVO_4$ slabs with one face cut at Brewster angles. Laser outputs with short (nanosecond) pulse durations, which are sought after for various applications, can be achieved with micro-chip and thin slab lasers. In 1992, Zayhowski et al. reported a diode-pumped electro-optically Q-switched 1.8% wt. Nd:YAG microchip laser with the geometry of cross-section area A $\times$ 0.44 mm^3 at PRFs varied from 5 to 500 kHz.

The microchip crystal was bonded to a 50% partially reflective A $\times$ 0.904 mm^3 $LiTaO_3$ crystal that doubled as an output coupler and a Q-switch element in a 1.436 mm long cavity. The results they obtained at the PRF of 150 kHz included 0.057 W average power, 0.38 µJ pulse energy, 4.2 ns pulse width and 93 kW peak power. In 1995, the same authors replaced the Nd:YAG crystal with a 1.1 wt. % $Nd:YVO_4$ crystal in almost the same arrangement and operated the laser at several pulse repetition frequencies, from 300 kHz to 2.5 MHz. At 300 kHz, in the 1.436 mm long cavity, they obtained pulses with 0.057 W average power, 0.38 µJ energy and 1.2 ns widths [10].

Table E.1. Recent Electro-optic Q-switched laser designs and their corresponding results laser are end-pumped by fibre coupling (FC).

Author, Date	Pump scheme, radius [μm]	Pump power [W], λ_p [nm]	Gain medium + Doping [%]	Crystal dimensions [mm³]	Q-switch device	Cavity length [mm], OC refl. [%]	PRF [kHz]	Pulsed average power [W]	Pulse energy [μJ]	Pulse width [ns]	Peak power [kW]	Ref
Zayhowski, & Dill, 1995	100	1.2, 808	1.1 at. % Nd:YVO₄,	A×0.44	Fabry–Perot etalon	1.44	300	0.36	1.2	1.2	1	[40]
Chen, & Huang, 2003	End,	4.5	2 at. % Nd:YVO₄, a-cut	3×3×1	b-BaB₂O₄ Pockels cell (BBO)	40	7	0.06	8.6	11.6	0.74	[162]
Du et al., 2003	end	248, 808	0.3 at. % Nd:YVO₄, a-cut	1×12×10	b-BaB₂O₄ Pockels cell (BBO)	67.5	50	83	1660	11.3	146	[38]
Tang, Zhu, & Feng, 2009	End, 200	24	0.3 at. % Nd:YVO₄	4 × 4 × 7	LGS	105	30	6.2	207	9.1	23	[39]
					RTP			6.7	223	7.8	29	

238

Authors, Year	Pump scheme, radius [µm]	Pump power [W], λ_p [nm]	Gain medium + Doping [%]	Crystal Dimensions [mm³]	Q-switch device	Cavity length [mm], OC refl. [%]	PRF [kHz]	Pulsed Average power [W]	Pulse Energy [µJ]	Pulse Width [ns]	Peak Power [kW]	Ref
Yongi-Ji et al., 2012	End, 400	30	0, 0.4 at. %, 0, a-cut YVO$_4$+ Nd:YVO$_4$ + YVO$_4$	3 × 3 × (4+7+4)	Double RTP crystal Pockels cell	100	200	11.8	57.7	16.5	3.5	[163]
			0.4 at. %, Nd:YVO$_4$	4 × 3 × 7				8.75				
Yu et al., 2013	End (Direct), 200	30, 880	adhesive-free bond (AFB) (0, 0.5, 0) at. % composite GdVO$_4$+ Nd:GdVO$_4$ + GdVO$_4$	3 × 3 × (2+8+2)	Double RTP crystal Pockels cell	100				14	8	[164]
Ma et al.,	End,	16.56	0.4 at. %	3 × 3 × 8	LGS	185	100	4.11	41.12	8.6	5.48	[83]

239

2016	100		Nd:LuVO$_4$								
Zhao et al., 2016	End, 105	8.8	0.4 at. % Nd:LuVO$_4$	$4 \times 3 \times 6$	BaB2O$_4$ (BBO)	135	50	2.88	56.96	17.8	3.2	[165]

While they managed to reduce the pulse width that they obtained in 1992, the average and peak powers were still very low, which then reduced the pulse energy. The high peak powers and short pulse widths produced at even higher PRFs make this technique a strong candidate for longer distance, high accuracy and high-resolution ranging applications. It also attracts interest in investigating how the laser would perform at 100 kHz PRF. Figure E.1 shows a configuration where the Nd:YAG microchip cavity is Q-switched, using the etalon effect with $LiTaO_3$ as its output face in a variable-reflectivity output coupler [166].
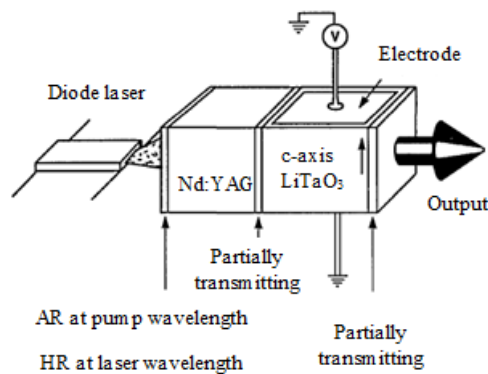
Figure E.1. The microchip diagram laser illustrates electro-optic Q-switching. The pump face is highly reflective (HR) to the laser wavelength and anti-reflective (AR) to the pump wavelength [166]. The mirror between Nd:YAG and $LiTaO_3$ reflects the 808 nm pump light to allow a double pass of its absorption by the laser material and with 95% reflectivity at 1064 nm, partially transmitting 5% of 1064 nm light.

Conventional electro-optic Q-switching requires the combination of an electro-optic Q-switch such as a Pockels cell, a polariser and sometimes a quarter-wave plate [1]. In 2012, Ji et al. used a composite $[3 \times 3 \times (4+7+4)]$ mm^3, $(0, 0.4, 0)$ at. % doped, a-cut $YVO_4 + Nd:YVO_4 + YVO_4$ laser (as shown in Figure E.2) to obtain peak powers of 3.5 kW, pulse widths of 16.5 ns and high pulse energies of 57.7 μJ.
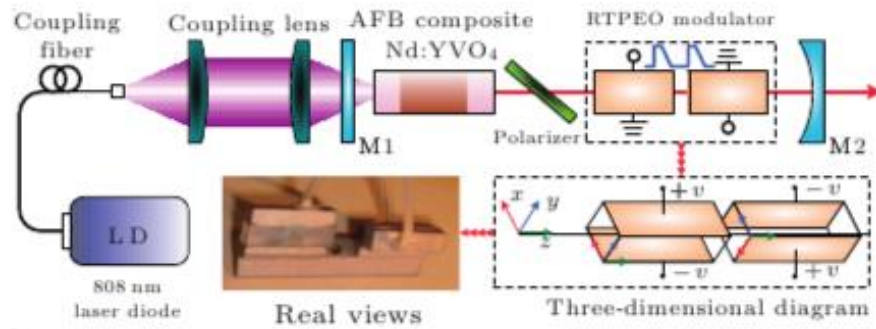
Figure E.2. Schematic results of an EOM Q-switched composite slab laser [163].

While the peak powers are relatively low and the pulse durations are long, the pulse energies are commendably high. The high energies obtained can be attributed to the thermal compensations the authors employed, both with the composite laser crystal and the use of two crystal Pockels cells.

Appendix F

F. Amplified lasers

Table F.1 lists specific cases that represent the research work done on laser scaling, focusing on regenerative laser amplifiers and MOPA.

Siebold et al. (2003) presented results for a 0.5 at. % doped Nd:YVO$_4$ crystal regenerative laser amplifier that they developed with 18 W dual end-pumping at 808 nm to exploit these properties. They combined this Nd:YVO$_4$ based laser amplifier with drivers for high pulse repetition rates of up to 110 kHz and 330 kHz for RTP Pockels cells. In this amplifier, 7 ps long seed laser pulses produced 19 ps of pulsed output evaluated at a pump power of 18 W and 45 kHz of PRF. A BBO Pockels cell (4 mm diameter aperture) was used to pulse it, while an RTP pulse picker was used to pre-select the pulses. Here we see that not only was the doping concentration kept at < 1 at. % with large apertures for longer pump beam radii, but a second Pockels cell was used in a 1400 mm long cavity. While higher PRFs (~80 kHz) could be reached, the authors decided to operate at 45 kHz to prevent amplitude fluctuations and thus obtained the average power of 5.3 W in the Q-switched operation. Under these conditions, the single pulse energies (118 μJ) and the peak powers (6 MW) could be calculated [47]. While the low PRF may yield low resolution, the cavity length was quite long and that made this laser not suitable for the intended applications.

Yan et al. (2008) [167] used a low doping concentration (YVO$_4$/ < 0.5 at. % Nd:YVO$_4$/YVO$_4$) in the end-capping of doped laser materials with undoped crystal host sections for a two-stage amplifier system. The crystal end-capping served as an additional heat sink, while the amplifiers contributed to the high average power, pulse energy and peak power when the laser was operated at 500 kHz of PRF. The properties that would make this MOPA not suitable for consideration are the long cavity length and the long pulse durations. In 2009, Yan et al. presented a fibre-coupled, dual-end-pumped MOPA laser with a composite crystal of rod geometry. The 500 kHz operation of this laser provided a high-resolution measurement, and while high energy (236 μJ) was generated, the peak power was slightly lower and the pulses were too long. The results they obtained had quite high average powers.

243

Table F.1. The amplified laser systems as well as MOPA configurations that have been scaled up, as reported in literature.

Authors, Year	Pump scheme, λ_p [nm] pump power [W], radius [μm], PRF [kHz], pulse width [ns]	(Oscillator + Amplifier) gain medium + Doping [%]	Crystal volume: oscillator + amplifier) [mm^3]	Pulsing technique (oscillator, amplifier)	Oscillator cavity length, amplifier [mm]	Seed + amplifier power [W]	PRF [kHz]	Pulse energy [μJ]	Pulse width [ns]	Peak power [kW]	Ref.
Siebold, et al., 2004	A dual-end pumped configuration, 18,	0.5 at. %, Nd:YVO$_4$		BBO EOM cell + l/4 plate	1400	5.3	45	117.8	0.019	6198	[47]
Yan, et al., 2008	Fibre coupled dual-end pumping, 808, 200,	YVO$_4$< 0.5 at. % Nd:YVO$_4$/YVO$_4$	A×18	Quartz AOM Q-switch	115	35	500	70	51	1.4	[167]
				MOPA	85	108		216	48	4.5	
Fu, et al., 2009	Fibre coupled, dual-end pumping, 808, 400, 345	0.4 at.% Nd:YAG rod + a-cut YVO$_4$/ 0.3 at.% Nd:YVO$_4$	(p×2^2×19), 4(3 ×3 × (2+16+2))	Cavity dumping,	70, -	5.4, 118	500	236	44.5	5.3	[168]
Wu, et al., 2017	Laser diode side-pumped	1.1 at.% Nd:YAG rod + 0.6 at.% Nd:YAG rod ×2	(p×1.5^2×75), 2(p×1.5^2×75)	burst-mode + cavity-dumped Q-switch technique	280, 220×2	18.9	100	1890000	3.1	2870	[169]

Comparative results were obtained in 2017, but on that occasion a technique was used that involved side pumping, composite crystals and the combination of burst-mode and cavity-dumped Q-switch pulsing. Since the PRF (100 kHz) and the pulse durations (3 ns) provided the resolution and the near precision required, the high energy and high peak power (~2 MW) for long range measurements were an added advantage. This laser can be considered for investigation. However, amplifiers do have limitations, since their complexity makes them difficult to design – which may result in huge losses and reduction of efficiency. The laser system as a whole is bulky, long and not suitable for the intended ranging applications.

Appendix G

G.1.   Publications: Conference Papers

- Maweza, E.L., King, G., Jacobs, C. and Strauss, H.J., 2016, October. Electro-Optic Q-switching using Thermal Lensing. In *Advanced Solid State Lasers* (pp. AM5A-4). Optical Society of America.

- Maweza, L., Gailele, L., Strauss, H., Litvin, I., Forbes, A. and Dudley, A.L., 2016, October. Shaping and detecting mid-IR light with a Spatial Light Modulator. In *Laser Applications Conference* (pp. JTh2A-15). Optical Society of America.

G.2.   Publications: Co-authorship

- Gailele, L., Maweza, L., Dudley, A., Ndagano, B., Rosales-Guzman, C. and Forbes, A., 2017, February. Multiplexing of spatial modes in the mid-IR region. In *Laser Resonators, Microresonators, and Beam Control XIX* (Vol. 10090, p. 100900Z). International Society for Optics and Photonics.

- Gailele, Lucas M; Maweza, Elijah L; Dudley, Angela L; Ndagano, B; Rosales-Guzman, C; Forbes, A (SPIE, 2017-02)

- Strauss, H.J., Esser, M.J.D., King, G. and Maweza, L., 2012. Tm: YLF slab wavelength-selected laser. *Optical Materials Express*, *2*(8), pp.1165-1170.

- Strauss, H.J., Esser, M.D., King, G. and Maweza, L., 2012, January. Volume Bragg grating wavelength selected Tm: YLF slab laser operating at 1890 nm. In Advanced Solid-State Photonics (pp. AW4A-20). Optical Society of America.